

AD-755 488

Nuclear Geoplosics

**a sourcebook of underground
phenomena and effects of nuclear
explosions Part 2
mechanical properties of
earth materials**

Agbabian Associates

prepared for

Defense Nuclear Agency

NOVEMBER 1972

Distributed By:

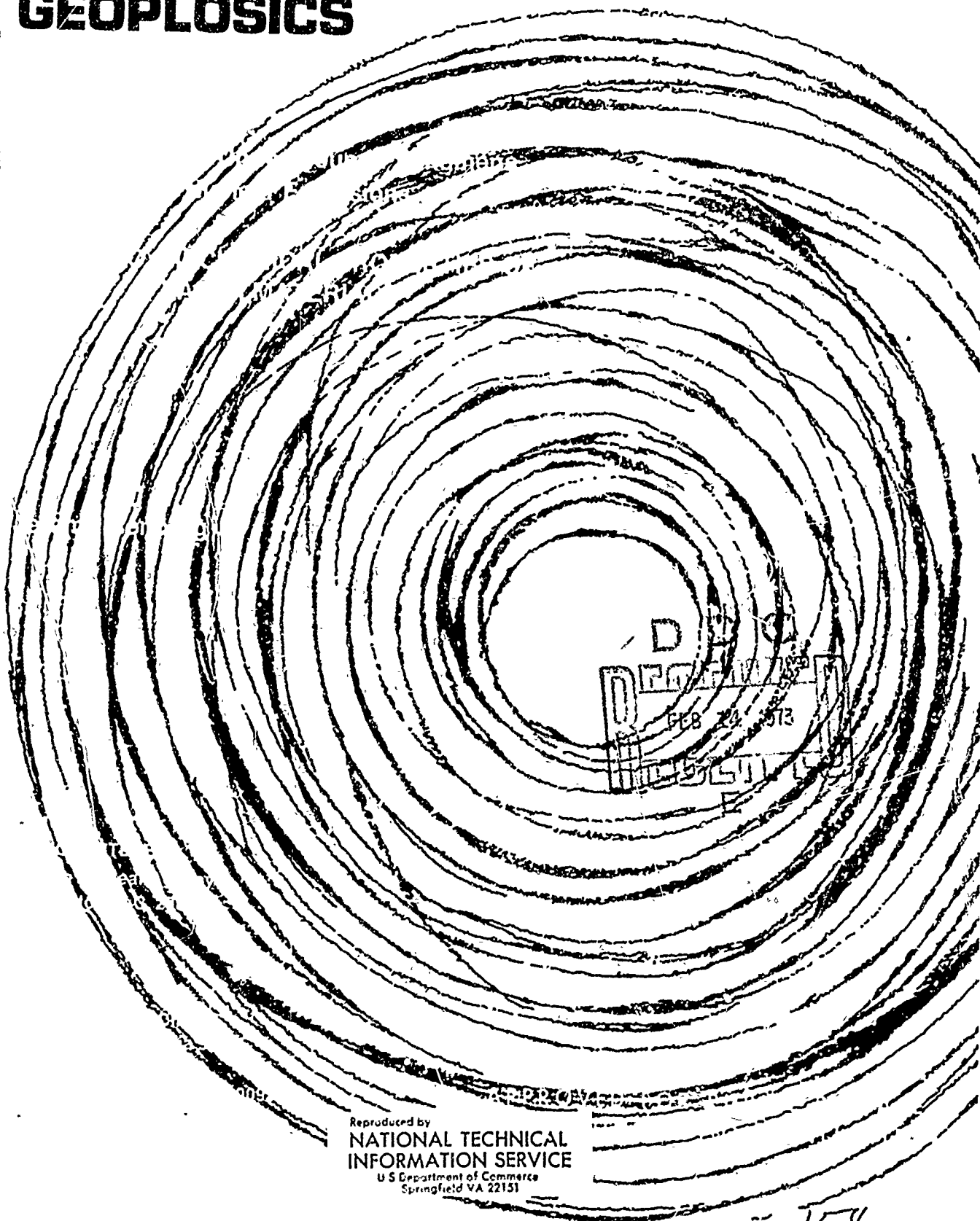
NTIS

**National Technical Information Service
U. S. DEPARTMENT OF COMMERCE**

AD 755488

NUCLEAR GEOPLOSICS

DNA 1285H2
(Formerly DASA 1285-2)
November 1972



Reproduced by
NATIONAL TECHNICAL
INFORMATION SERVICE
U S Department of Commerce
Springfield VA 22151

UNCLASSIFIED

Security Classification		
DOCUMENT CONTROL DATA - R & D		
(Security classification of title, body of abstract and indexing annotation must be entered when the overall report is classified)		
1. ORIGINATING ACTIVITY (Corporate author) Agbabian Associates 250 North Nash Street El Segundo, California 90245		2a. REPORT SECURITY CLASSIFICATION UNCLASSIFIED
		2b. GROUP --
3. REPORT TITLE Nuclear Geoplosics - A Sourcebook of Underground Phenomena and Effects of Nuclear Explosions. Part Two - Mechanical Properties of Earth Materials		
4. DESCRIPTIVE NOTES (Type of report and inclusive dates) Final Report		
5. AUTHOR(S) (First name, middle initial, last name) Jeremy Isenberg		
6. REPORT DATE November 1972	7a. TOTAL NO. OF PAGES 172	7b. NO. OF REFS 259
8a. CONTRACT OR GRANT NO. DASA01-71-C-0093	8b. ORIGINATOR'S REPORT NUMBER(S) DNA 1285H2 (Formerly DASA 1285-2)	
8c. PROJECT NO. NWER Code: XAXS		
c. Task and Subtask: B047		
d. Work Unit: 08	8d. OTHER REPORT NO(S) (Any other numbers that may be assigned this report) AA-R-7120-2000	
10. DISTRIBUTION STATEMENT Approved for public release; distribution-unlimited.		
11. SUPPLEMENTARY NOTES		12. SPONSORING MILITARY ACTIVITY Director Defense Nuclear Agency Washington, D. C. 20305
13. ABSTRACT Mechanical properties of rock and soil are described from the viewpoint of their effects on waves from explosive sources. Important variables which are commonly used in describing material properties are defined. Constitutive properties of rocks and soil are discussed and general and specific mathematical models of these properties are given. The role of laboratory and in situ experiments in measuring constitutive properties are considered.		

DD FORM 1473

REPLACES DD FORM 1473, 1 JAN 64, WHICH IS OBSOLETE FOR ARMY USE.

UNCLASSIFIED

Security Classification

1a

UNCLASSIFIED

Security Classification

14. KEY WORDS	LINK A		LINK B		LINK C	
	ROLE	WT	ROLE	WT	ROLE	WT
Properties of rock and soil under shock loading Mathematical models of earth materials						

UNCLASSIFIED

Security Classification

I6

DNA 1285H2
(Formerly DASA 1285-2)
November 1972

NUCLEAR GEOPLOSICS

**A Sourcebook of Underground Phenomena
and Effects of Nuclear Explosions**

PART TWO: MECHANICAL PROPERTIES OF EARTH MATERIALS

THIS WORK WAS SUPPORTED BY THE DEFENSE NUCLEAR AGENCY
UNDER NWER SUBTASK SB047-08

Jeremy Isenberg

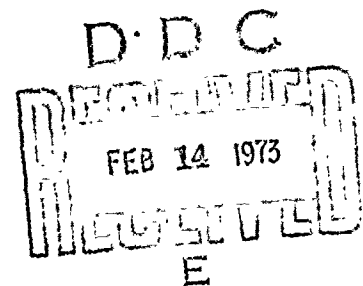
Prepared for

**HEADQUARTERS
Defense Nuclear Agency
Washington, D.C. 20305**

Prepared by


**AGABIAN ASSOCIATES
El Segundo, California 90245**

Contract No. DASA01-71-C-0093
Performed Under NWER Subtask B047



**APPROVED FOR PUBLIC RELEASE
DISTRIBUTION UNLIMITED**

IC

PREFACE

This sourcebook was written under contracts No. DASA01-71-C-0093 and No. DNA001-72-C-0045 between Agbabian Associates and the Defense Nuclear Agency, Washington, D. C. between March 1971 and April 1972. The DNA contract monitor was Clifton B. McFarland, Jr. The principal work of writing the sourcebook was performed by J. Isenberg. Major contributions to Section 2 "Properties of Rocks" were made by Wolfgang Wawersik and Ray Wilson of the University of Utah and Howard Pratt of Terra Tek, Inc., and to Section 3 "Properties of Soils" by Warren J. Baker of the University of Detroit. Parts of the sourcebook were reviewed by J. Zelasko of U. S. Army Engineering Waterways Experiment Station, M. L. Baron and I. Nelson of Paul Weidinger Consulting Engineer, and G. A. Young of Agbabian Associates. The first edition of "Nuclear Geophysics, Part Two-Mechanical Properties of Earth Materials," DASA-1285(II), was written by R. V. Whitman and G. B. Clark and was published in 1967. The present version considers primarily the results of research performed since then.

INTRODUCTION

AD-443590
✓

The objective of this sourcebook is to describe the mechanical properties of rock and soil from the viewpoint of their effects on waves from explosive sources. The reason for revising the sourcebook, whose first edition was published in 1964, is that nowadays much greater reliance than formerly is placed on computations of ground shock and interaction between structure and rock or soil. As a result, a new technology has developed for adapting properties of rock and soil for input to such computations. This new technology includes improved methods of testing in the laboratory and in situ as well as new mathematical methods of representing properties.

One important development in the area of material properties is widespread agreement that experiments and mathematical models should influence each other. Obviously, a mathematical model should mirror experimental relationships among stress, strain and internal energy. Here progress is marked by the ability of mathematical models to represent accurately a wide range of behavior within formal restrictions of thermodynamic laws. Only in the last few years, however, have the requirements of mathematical models influenced the types of experiments being made. Progress in this area is illustrated by many recent reports of laboratory experiments where complete states of stress and strain were measured. Until complete data became necessary for the development of general mathematical models, some measurements were usually omitted, often because of limitations on testing equipment. Although experimental studies still sometimes fall short of providing complete data for mathematical models, nowadays this can usually be traced to shortage of funds or the pressure of schedules.

Although there has been progress in laboratory measurements and their mathematical representation, important gaps remain in knowledge of in situ properties. In rock, cracks may occur on a larger scale than can be represented in the laboratory, and hence there is little firsthand, quantitative data on their effects. In soil, preservation of the in situ moisture content and void ratio in field samples is extremely difficult, and hence it is sometimes uncertain that the material being tested is the same as that in situ. Large scale field testing programs, such as Piledriver, have pointed out the need for determining in situ properties, and research programs to fill in some of the gaps are now underway.

Although inadequate measurement of in situ properties is the most frequently cited weakness in this technology, there are others. One of these is that little effort is made to reflect flow and fracture mechanisms in mathematical models of stress/strain relations. For example, plasticity theory is often used to represent both brittle fracture and ductile

flow, though the theory appears better suited to the latter. Also, studies of rate-of-loading effects are in their infancy. Sometimes materials are tested at the average rate or maximum rate of loading they experience during ground shock, and properties measured at those rates are modeled. Other times, however, the subject is treated haphazardly without proper coordination between those who perform the tests and those who use the results.

Although this progress is uneven, progress has been made since the first edition of Nuclear Geophysics was published. It is now possible to prescribe a series of field and laboratory measurements followed by mathematical representation of the properties and computation of ground shock effects within a factor of 2 to 3 of dynamic field measurements. Advances in measuring and mathematically representing material properties are responsible for an important part of the advance in overall ability to calculate ground shock effects.

The present sourcebook is divided into five main sections. The first section, entitled "Mathematical Aids in Defining Material Properties" discusses some of the important variables which are commonly used in describing material properties. These include stress and strain components and their invariants, specific internal energy and wave speed. The second and third sections, entitled "Properties of Rocks" and "Properties of Soils," respectively, describe the laboratory and in situ properties of rocks and soils and experimental methods used to measure them. The fourth section, entitled "General Mathematical Models of Earth Material," describes the mathematical framework into which models of specific materials are fitted. The fifth section gives several examples of models for specific materials.

This sourcebook follows the practice of discussing rock and soil in separate sections. However, the reader should be aware that a new viewpoint is beginning to emerge whereby for some purposes the familiar labels rock and soil are being replaced by more useful descriptions. For example, it is often useful to distinguish between sites whose overall behavior is governed primarily by joints and other large scale discontinuities and those whose overall behavior is governed primarily by homogeneous deformation. Under this scheme, some rocks and soils would be grouped together as being qualitatively similar materials or sites whose behavior is governed by the same basic properties which differ in value. Although this viewpoint is attractive as a system of classifying materials and in guiding the selection of properties to be defined by experiment, its value has not yet been proved. This sourcebook therefore maintains the orthodox distinction between rock and soil.

CONTENTS

<u>Section</u>		<u>Page</u>
1	MATHEMATICAL AIDS IN DEFINING MATERIAL PROPERTIES by J. Isenberg	1
	Stress	1
	Strain	2
	Elastic Moduli	4
	Wave Propagation	4
	Wave Propagation (Neglecting Internal Energy Changes)	6
	Wave Propagation (Including Internal Energy Changes)	6
	Summary	8
	References	8
2	MECHANICAL PROPERTIES OF ROCK by W. Wawersik, R. Wilson, H. Pratt, and J. Isenberg	9
	Introduction	9
	Mechanical Classification of Rocks	9
	Common Rock-Forming Minerals	10
	Geologic Classification of Rocks	10
	Mechanical Reclassification of Rocks	11
	Mechanical Rock Properties at Hydrostatic Pressure Below 10 kb and Strain Rates below 10^2 sec^{-1}	15
	Rock Mass Continua	15
	Constitutive Behavior of Competent Rock	15
	Yield Stress and Ductility	22
	Ultimate Strength	22
	Postfailure Behavior and Brittle-Ductile Transition	24
	Deformation and Failure Mechanism	26
	Effects of Anisotropy	29
	Discontinuous Rock Masses	30
	Mechanical Properties of Rocks at Strain Rates Above 10^2 sec^{-1} ..	32
	Laboratory Experiments	34
	Quasi-Static Experiments	35
	Dynamic Experiments	37
	Shock Wave Experiments	39
	Properties of the In Situ Rock Mass	43
	Preliminary Investigation	43

Preceding page blank

CONTENTS (CONTINUED)

<u>Section</u>		<u>Page</u>
2	Experimental Methods (Dynamic)	43
	Experimental Methods (Static)	48
	Summary	53
	References	53
	List of General Sources	57
	Texts	57
	References	57
	Journals and Abstracts	57
3	PROPERTIES OF SOILS by W. J. Baker and J. Isenberg	59
	Introduction	59
	Properties of Soils	63
	Effective Stresses in Soils	63
	Constitutive Behavior of Coarse-Grained Soils	66
	Constitutive Behavior of Fine-Grained Soils	76
	Experimental Techniques for Determining Soil Properties	87
	Laboratory Testing	87
	Static Triaxial Compression	89
	Static Uniaxial Strain	89
	Other Static Tests	90
	Dynamic Triaxial Testing	91
	Dynamic Uniaxial Strain	91
	Dynamic Direct Shear Testing	91
	In Situ Testing	92
	Summary	95
	List of General Sources	96
	Texts	96
	References	96
4	GENERAL MATHEMATICAL MODELS OF MATERIAL PROPERTIES by J. Isenberg	101
	General Equations of State (Fluid)	102
	General Equations of State (Solid)	104
	Variable Modulus	104
	Bulk Modulus	104
	Shear Modulus	107

CONTENTS (CONTINUED)

<u>Section</u>		<u>Page</u>
4	Plasticity Theory	109
	References	118
5	SPECIFIC MATHEMATICAL MODELS OF SELECTED EARTH MATERIALS by J. Isenberg	121
	Introduction	121
	Mathematical Models for Seven Rocks	121
	NTS Granite (Granodiorite)	121
	Cedar City Tonalite	124
	Mathematical Models for Several Soils	127
	Middle Gust Sandy Clay	127
	Distant Plain Alluvium	132
	References	133
6	CONCLUSION by J. Isenberg	135
	INDEX	136

ILLUSTRATIONS

<u>Figure</u>		<u>Page</u>
1-1	Stress Components in Cartesian Coordinates	2
1-2	Hydrostatic and Deviatoric Components of Stress	3
1-3	Strain Components in Cartesian Coordinates	3
1-4	Longitudinal Wave Propagation in a Laterally Constrained Rod	6
1-5	Principal Hugoniot Defined by Shock Wave Experiments	7
1-6	Relation Between Hugoniot and Release Adiabats	8
2-1	Stress/Strain Relation for a Shale	16
2-2	Stress/Strain Relation for Nugget Sandstone	17
2-3	Shear Stress/Axial Strain Relation for Coconino Sandstone	17
2-4	Stress/Strain Relation for Cedar City Granite	18
2-5	Stress/Strain Relation for Solenhofen Limestone	18
2-6	Stress/Strain Relation for Marble Subjected to Proportional Loading ($\sigma_3/\sigma_1 = 0.338$)	19
2-7	Stress/Strain Relation for Granite	19
2-8	Hydrostatic Loading and Unloading for Two Rocks	20
2-9	Biaxial Stress/Strain Relation for Westerly Granite	20
2-10	Stress/Strain Relation for Dunham Dolomite Under Constant $\sigma_3 (= 1.25 \text{ kb})$ and σ_2	20
2-11	Shear Stress/Axial Strain Relation for Berea Sandstone at Different Levels of Total Confining Pressure and Pore Fluid Pressure	21
2-12	Stress/Strain Relation for a Basalt at Different Temperatures	21
2-13	Stress/Strain Relation for Eureka Quartzite Under Confinement of $\sigma_3 = 5 \text{ kb}$ at 500°C and Subjected to Different Strain Rates	21
2-14	Ductility of Several Common Rocks Varies with Confining Pressure	22
2-15	Average Strength-Pressure Curves of Different Rock Types	22
2-16	Strength of Westerly Granite Under Triaxial Compression, Triaxial Extension and Intermediate Stress States	23
2-17	Strength of Dunham Dolomite Under Triaxial Compression and Triaxial Extension Stress States	23
2-18	Strength of Westerly Granite Under Different Loading Paths	24
2-19	Effect of Pore Pressure on States of Stress at Fracture, Effective Confining Stress Appears to Govern Strength of Sandstone	24
2-20	Dilatancy Hardening for a Typical Rock and for Specific Rocks	24
2-21	Variation of Strength With Strain Rate at Room Temperature and Pressure Except Where Noted. Numbers at the Left of Each Line Indicate the Slope of That Line	25
2-22	Differential-Stress/Axial-Strain Relation for Sandstone. Postfracture behavior	25

ILLUSTRATIONS (CONTINUED)

<u>Figure</u>		<u>Page</u>
2-23	Stress/Strain Relation for Westerly Granite, Including Postfailure Range	25
2-24	Sliding on Sawcuts in Granite, at a Confining Pressure of 2.1 kb. Dotted Parts of the Curve at 22° are Sudden Stress Drops. Actual Displacement Along the Sawcut During Sliding is Indicated by the 1-mm Bar Line	26
2-25	The Effect of Normal Stress on the Shear Stress at Fracture and on the Frictional Shear Strength of Westerly Granite	26
2-26	Relation Among Stress Level, Microfracturing Activity, Resistivity, Volumetric Strain, and Dilational Wave Speed	27
2-27	Effect of Fluid Pore Pressure on Wave Speeds	28
2-28	Velocity of Dilatational Waves Depend on Direction of Propagation Relative to Direction of Joints and Stress Across Joints	28
2-29	Velocity of Shear Waves Depends on Direction of Propagation Relative to Direction of Joints and Stress Across Joints	28
2-30	Strength of Beldens Marble Under 2 kb Confining Stress Depends on Orientation of Cleavage Planes Relative to Major Principal Stress	28
2-31	Anisotropy in Strength of Shale	29
2-32	Variation of the Modulus of Elasticity with Respect to Confining Pressures	30
2-33	Geometry of Block-Jointed Plaster of Paris Test Specimen	30
2-34	Typical Differential Axial Load-Axial Deformation Curves for Competent and Block-Jointed Plaster of Paris	30
2-35	Strength of Prefractured Nugget Sandstone Compared with Strength of Intact Specimens	31
2-36	Four Typical Modes of Joint Strength and Displacement (Percentages Based on 121 Direct Shear Tests of NX Cores from Auburn and Grand Coulee Projects)	31
2-37	Failure Envelopes Expected for Rock Masses	32
2-38	Velocities of Low Amplitude (Seismic) Dilatational Waves as Functions of Pressure	33
2-39	Seismic Compressional Wave Velocities as Function of Pressure	33
2-40	Hugoniot and Hydrostat for NTS Granite	34
2-41	Hugoniots and Release Adiabats for Dry and Wet NTS Tuff	35
2-42	Test Chamber (Load Cell Inside Chamber) for Triaxial Testing of Rock	37
2-43	Test Chamber for Triaxial Compression of Rock with Interstitial Pore Fluid Under Pressure	37
2-44	Instrumentation of Rock Specimen	37
2-45	Schematics of Direct and Double Shear Apparatus	38
2-46	Split-Hopkinson Bar Apparatus for Measuring Properties at Various Strain Rates	38

ILLUSTRATIONS (CONTINUED)

<u>Figure</u>		<u>Page</u>
2-47	Profiles of Axial Stress in Split-Hopkinson Bar Experiment, Showing Variation in Stress Due to Wave Effects Which Limit Range of Investigation by This Technique.	39
2-48	Apparatus for Measuring Sonic (Low-Amplitude) Dilatation and Shear Wave Velocities at Various Levels of Confining Pressures	39
2-49	Sequence of Events in Operation of a Light Gas Gun	40
2-50	Target Configurations for High Pressure Hugoniot Tests	40
2-51	Dynamic Properties of Rocks Measured Under Plane Shock Wave Conditions with Quartz Transducer Techniques	41
2-52	Diagrammatic Sketch of Two Shock Fronts in Rock Interacting with Buffer Material	41
2-53	Optical Methods of Measuring Properties Under Plane Shock Wave Conditions	42
2-54	Properties of Rocks Measured Under Spherical Shock Wave Conditions with Pressure-Sensitive Wires	42
2-55	Relation Between Arrival Time of Seismic Signals and Distance of Receiver from Source (Slopes of Lines Between Points are Average Sonic Velocities	43
2-56	Logs of Core Borings EL-01 and EL-02	44
2-57	Relationship Between Rock Quality Designation and Velocity Index	45
2-58	Relation Between Rock Quality Designation and In Situ Static Modulus of Deformation	45
2-59	Up-Hole and Cross-Hole Seismic Surveys	45
2-60	Relationship Between 3-D Sonic and Seismic Compressional Wave Velocities (Correlation Between Two Types of Experiments)	46
2-61	Relationship Between RDQ and Velocity Index	46
2-62	Relationship Between Rock Quality and Resistivity and Seismic Velocity	47
2-63	Technique of Emplacing Stress Gages In Situ (Sideways Mounting)	47
2-64	Technique of Emplacing Stress Gages In Situ (End-On Mounting)	48
2-65	Comparison Between Measurements and a Calculation of Radial Stress in a Spherical Shock Wave	48
2-66	Apparatus for Plate Jack Tests	48
2-67	Load/Deflection Relations from Plate Jack Tests	49
2-68	Uniaxial Jack for In Situ Measurements of a Deformation Modulus	49
2-69	Pressure Chamber for In Situ Measurement of a Deformation Modulus	50
2-70	Cedar City Stress Versus Strain, In Situ Test No. 6	50
2-71	Experimental Apparatus for In Situ Compression Testing of Large Rock Samples	50

ILLUSTRATIONS (CONTINUED)

Figure		Page
2-72	In Situ Shear Strength of Foliated Amphibolite	51
2-73	Shear Stress Versus Displacement for Specimens with a Single Joint at Angles from 30° to 75° to Axis of Loading	52
3-1	Stress/Strain Tests Adopted in Part	60
3-2	Relation Between Confining Pressure and Volumetric Strain for Sand at Two Different Initial Void Ratios	61
3-3	The Critical Void Ratio for Coarse-Grained Soil, at Which Shear Deformation Occurs at Constant Volume, is Uniquely Related to the Confining Pressure	62
3-4	Typical Behavior of Normally Consolidated and Overconsolidated Clay	63
3-5	Pore Pressure Parameters	64
3-6	Relationship Between P and $\sqrt{J_2}$ for Soils Reaching Different Degrees of Saturation During Loading in Uniaxial Strain	65
3-7	Pressure of Fluid in Pores Affects Shear Stiffness and Strength	65
3-8	Influence of Degree of Saturation on Stress/Strain Relations Under Uniaxial Strain	65
3-9	Influence of Effective Stress	66
3-10	Compressive Stress/Strain Relations for Elastic Spheres Subjected to Three Types of Loading are Similar to Those Generally Found for Coarse-Grained Soils	66
3-11	Loading and Unloading Compressive Stress/Strain Relation for Elastic Spheres Subjected to Uniaxial Strain	67
3-12	Bulk Properties of Dry Sand Under Hydrostatic Compression Depends Strongly on Initial Void Ratio or Relative Density	68
3-13	Pressure Versus Volumetric Strain Relations for Hydrostatic Loading of a Sand at Two Different Initial Void Ratios	69
3-14	Pressure Versus Volumetric Strain Relations for Hydrostatic Loading and Unloading of Sand at Two Different Locations	69
3-15	Pressure/Volumetric Strain Relation for Dry Ottawa Sand	69
3-16	Shear Stress/Strain Relations for McCormick Ranch Sand	70
3-17	Stress Paths for Investigating Deformation Paths Under Deviatoric Stress	70
3-18	Deviatoric Stress/Strain Relations for a Sand in a Test Where the Mean Normal Stress is Constant, Test B, Figure 3-17	71
3-19	Shear Modulus of Sand Increases with Confining Pressure	71
3-20	Volumetric Strain Versus Deviatoric Stress for a Coarse-Grained Soil Subjected to a Constant Mean Normal Stress of 15 psi	72
3-21	Volumetric Strain in Coarse-Grained Soils Subjected to Proportional Loading May Increase or Decrease Depending on Principal Stress Ratio	72
3-22	Breakdown Stress is Associated with an Increase in Poisson's Ratio and a Linear Relation Between Stiffness and Confining Stress	72

ILLUSTRATIONS (CONTINUED)

Figure		Page
3-23	Minnesota Sand Under Uniaxial Strain	73
3-24	McCormick Ranch Sand Under Uniaxial Strain	74
3-25	Relationship Between Lateral and Axial (σ_1) Stresses for Minnesota Sand under Dynamic Loading in Uniaxial Strain	74
3-26	Effect of Loading Rate and Initial Void Ratio on Axial Stress/Strain Relations of a Sand Subjected to Uniaxial Strain	75
3-27	Wave Velocities in Ottawa Sand	76
3-28	Stress and Strain Mechanisms in Soils	77
3-29	Shear Strength/Moisture Content Relationship for Compacted Partially Saturated Soil	77
3-30	Effective and Total Stress Paths for Overconsolidated and Normally Consolidated Undrained Soils Subjected to Triaxial Compressive Stress	78
3-31	For a Fine-Grained Soil, an Apparently Unique Relation Exists Among Octahedral Shear Stress, $\sqrt{J_2}$, Octahedral Shear Strain, and Effective Preconsolidation Stress, P_o	79
3-32	Shear Stress (Normalized to Effective Confining Stress) Versus Shear Strain for a Fine-Grained Soil Depends on the Previous History of Loading, Which is Measured in This Example by the Overconsolidation Ratio (OCR)	79
3-33	Secant Young's Modulus of a Clay as a Function of Shear Stress (Normalized to Shear Strength) and Overconsolidation Ratio	80
3-34	Ratio of Lateral Stress to Axial Stress (k_o) Which Develops in a Fine-Grained Soil Subjected to Uniaxial Strain as a Function of Over-Consolidation Ratio and Plasticity Index	81
3-35	Tangent Constrained Modulus Versus Axial Stress Relation for Fine-Grained Soils Subjected to Uniaxial Strain is Influenced by the Plasticity Index	81
3-36	Pressure Versus Volumetric Strain for Watching Hills Clay Subjected to Hydrostatic Compression	82
3-37	Shear-Stress/Strain Relations for Watching Hill Clay	82
3-38	Shear Strength Depends on Confining Stress and Degree of Saturation	83
3-39	Stress/Strain Relation for Partially Saturated Fine-Grained Soil Subjected to Uniaxial Strain	83
3-40	Stress/Strain Relations for Sandy Clay Subjected to Uniaxial Strain	84
3-41	Stress Paths During Loading of a Clay in Uniaxial Strain	84
3-42	Pressure/Volume Relationships for Watching Hills Sandy Clay Subjected to Different Loading Conditions	85
3-43	Deviatoric Stress/Strain Relation for Watching Hills Brown Clay Subjected to Uniaxial Strain	85
3-44	Deviatoric Stress/Strain Relations for Watching Hills Brown Clay Subjected to Different Loading Conditions	85

ILLUSTRATIONS (CONTINUED)

Figure		Page
3-45	Effect of Loading Rate on Shear Strength of Cohesive Soils	86
3-46	Influence of Time to Failure on the Normalized Secant Moduli at an Axial Strain of 1 Percent	87
3-47	Tangent Shear Modulus of Fine-Grained Soils with Increasing Mean Stress, Decreases with Increasing Void Ratio	87
3-48	Radial Stress and Strain Distribution in a Triaxial Compression Experiment as Indicated by Finite Element Analysis	88
3-49	Triaxial Cell	89
3-50	Lateral Deformeter	89
3-51	Schematic Diagram of True Triaxial Test Apparatus	90
3-52	Dynamic Oedometer	90
3-53	MIT Apparatus for Rapidly Loaded Triaxial Tests	91
3-54	Drawing of Basic Assembly, WES Dynamic Oedometer	92
3-55	Soil Vibration Mechanisms for Shear Wave Apparatus (a) and Compression Wave Apparatus (b)	93
3-56	Apparatus for Ultrasonic Wave Propagation Through Soil	93
3-57	Schematic Drawing of Pressure Meter Equipment	94
3-58	Schematic of Bore-Hole Shear Device	94
4-1	Idealized Hydrostat and Release Adiabats Illustrating the Effect of Hysteretic Compaction on P_{s1}	102
4-2	Typical Laboratory Data on Soil and Rock from Which Models of Solid State Behavior are Derived	103
4-3	Bulk Modulus (K) Versus Pressure (P) for a Compacting Soil	106
4-4	Pressure Versus Volumetric Strain for a Compacting Soil	107
4-5	Variable Moduli Models Versus Data	108
4-6	Continuity Condition Applied to a Variable Modulus Model with Different Shear Moduli in Loading and Unloading	109
4-7	Yield Criteria	110
4-8	Octahedral Shear Strength is Not Uniquely Related to Mean Stress in Two Rocks	111
4-9	Parameter Y, Containing J_2' , J_3' , and J_3 at Fracture, is Uniquely Related to Mean Stress for Two Rocks	111
4-10	Hardening Material Having Nested, Subsequent Yield Surfaces	112
4-11	Mathematical Model Having a Fixed Fracture or Failure Criteria (f_1) and a Movable or Strain-Hardening Cap (f_2)	113
4-12	Method of Correcting Final Stress State From a Trial State	115
4-13	Iteration Scheme to Evaluate Stresses	116
5-1	Tangent Bulk Moduli for Various Granites and a Model for NTS Granite	122
5-2	Model Hugoniot and Hydrostat for NTS Granite Compared with Data	123

ILLUSTRATIONS (CONTINUED)

<u>Figure</u>		<u>Page</u>
5-3	Model Hydrostat and Release Adiabats for NTS Granite	123
5-4	Shear Modulus as a Function of Pressure for NTS Granite	124
5-5	Models for Yield Strength of Granite as a Function of Mean Stress (Various States of Stress and Degrees of Initial Cracking)	125
5-6	Rock Cap Model.	125
5-7	Typical Behavior of a Compactible Material Under Hydrostatic Loads	128
5-8	Shear Stress Versus Mean Stress Under Uniaxial Strain for Layer 3 of Event Middle Gust 1 (Alluvium)	128
5-9	Stress/Strain Relations Under Uniaxial Strain for Layer 3 of Event Middle Gust 1 (Alluvium)	128
5-10	Event 1A, Operation Distant Plain, Layer III, Wet Sand, Silt, Subjected to Uniaxial Strain	131
5-11	Capped Model for Layer 5 of Middle Gust Site Subjected to Uniaxial Strain	131
5-12	Capped Model for Layer 5 of Middle Gust Site Subjected to Uniaxial Strain	133

TABLES

<u>Table</u>		
1-1	Relationship Among Elastic Moduli	5
2-1	Common Rock-Forming Minerals	10
2-2(a)	Sedimentary Rock Classification	11
2-2(b)	Igneous Rock Classification	12
2-2(c)	Metamorphic Rock Classification	12
2-3	Mechanical Classification of Rock	13
2-4	Numerical Ranges of Mechanical Classification Parameters	14
2-5	Examples of Rock Types in the Mechanical Classes	14
2-6	Rock and Soil Mechanics Experiments	36
2-7	Available Experimental Data	52
3-1	Maximum and Minimum Void Ratios Coarse-Grained Soils	61
4-1	Advantages and Disadvantages of Each Model	118
5-1	Equation-of-State Parameters and Variables	126
5-2	Loading Hydrostat for Middle Gust Alluvium, Layer 2	129
5-3	Permanent Excess Compression as a Function of Maximum Excess Compression for Middle Gust Alluvium, Layer 2	129
5-4	Unloading Hydrostat for Middle Gust Alluvium, Layer 2	129

TABLES (CONTINUED)

<u>Table</u>		<u>Page</u>
5-5	Hydrostat for Middle Gust Alluvium at Pressures Above Laboratory Data	130
5-6	Yield Strength of Middle Gust Alluvium, Layer 3	130
5-7	Material Parameters for Capped Model of Middle Gust Site	131
5-8	Soil Layers at Site of Event 1A, Operation Distant Plain	132
5-9	Material Constants--Distant Plain 1A Model	132

NOMENCLATURE

$A_0, A_1 \dots A_n$	Empirical parameters in yield function
\bar{A}, \bar{A}_1	Pore pressure parameters relating change in J_2^I or maximum shear stress to change in pore fluid pressure (Figure 3-5 and Equation 3-3)
a_0	Constant in equation of state for perfect gas, equal to ratio between specific heat at constant pressure to that at constant volume minus 1 (Equations 4-6, 4-7)
a_n	Terms in polynomial expression of Grüneisen ratio (Equation 4-5) ($n = 1$ to 4)
B	Constrained modulus or tangent to stress/strain relation in uniaxial strain (Equation 1-15)
\bar{B}	Pore pressure parameter measured in hydrostatic compression (Figure 3-5)
b_1, b_2, b_3	Constants in high pressure equation of state (Equations 4-6, 4-7)
c	Empirical coefficient in expression for temperature-dependent bulk modulus (Equation 4-10)
C	Matrix of coefficients relating incremental stress and strain (Equation 4-38)
\bar{C}	Pore pressure parameter measured in uniaxial strain (Figure 3-5)
C_p	Specific heat at constant pressure (Equation 4-3)
c_b	Velocity of compressional waves in an unconfined bar (Equation 1-18)
c_f, c_l	In situ seismic and laboratory sonic wave velocities, respectively (Figure 2-57)
c_p	Velocity of dilatational waves (Equation 1-17) (subscript f = field measurement; l = laboratory measurement)
c_s	Velocity of shear waves (Equation 1-16)
D	Empirical coefficient in capped model (Equation 5-18)
D_r	Relative density of soil (Equation 3-1)
d	Relates loss of porosity to pressure in variable modulus representation
E	Tangent Young's modulus (Equation 1-13)
\bar{E}	Secant Young's modulus (Equation 1-13)
E_s, E_d	Young's modulus of rock measured in situ by static means (Figure 2-57)
e	Specific internal energy (Equations 1-22, 4-1, 4-2)
e_m	Specific internal energy at which melting occurs (Equation 4-10)
e_{mo}	Specific internal energy at which melting occurs at normal density (Equation 5-1)
e_{mm}	Specific internal energy at which melting occurs regardless of density (Equation 5-1)

e_K	Specific internal energy at 0° Kelvin (Equation 4-2)
e_o	An empirical parameter related to the high pressure, high temperature equation of state (Equation 4-6)
e_v	Void ratio of soil (Equation 3-1)
e_{max}, e_{min}	Maximum and minimum void ratios of soil (Equation 3-1)
e_{v0}	Initial void ratio of soil (Figures 3-23, 3-25)
e_c	Void ratio after consolidation (Figure 3-3)
F	Sum of the derivatives of yield function with respect to components of direct stress (Equation 4-39)
f	Yield criterion (Equation 4-23)
G	Shear modulus (Equation 1-12)
G_o	Initial shear modulus (Equation 4-18)
G_{max}	Intrinsic shear modulus (Equation 4-18)
$g(e_v)$	A function of initial void ratio for a soil to which the tangent shear modulus, as measured in vibration, is uniquely related (Figure 3-47)
G_l, G_u	Shear modulus in loading and unloading respectively (Equations 4-21, 4-22)
G_{nl}, G_{nu}	Empirical parameters ($n = 0$ to 3) in variable shear modulus representation
J_3	Third stress invariant (Equation 1-6)
J'_3	Third invariant of stress deviator (Equation 1-5)
H	Strain hardening function (Equation 4-39)
I_1	First strain invariant (Equation 1-7)
I'_2	Second invariant of strain deviator (Equation 1-9)
I_3	Third strain invariant (Equation 1-10)
J_1	First stress invariant (Equation 1-1)
J'_2	Second invariant of stress deviator (Equation 1-4)
K	Bulk modulus (Equation 1-11)
K_l	Bulk modulus for loading in variable modulus representation (Equation 4-16)
K_m	Intrinsic bulk modulus of consolidated material (Equation 4-9)
K_{max}	Intrinsic bulk modulus at room temperature (Equation 4-10)

K_o	Initial bulk modulus
K_n	n^{th} coefficient in polynomial expression for bulk modulus (Equation 4-15)
K_u	Unloading bulk modulus in variable modulus representation (Equation 4-17)
k	Permeability
k_o	Coefficient of earth pressure at rest
L	Parameter in capped model (Figure 4-8)
L_r	Wave length of Rayleigh waves
n	Porosity
n_o, n_s	Optical indices in shocked and unshocked fluid in optical lever technique for measuring Hugoniot properties (Figure 2-53)
n_r	Parameter used in computing in situ Rayleigh wave velocity of a soil deposit
P	Pressure or mean normal stress (Equation 1-2, Figure 1-2)
P_a	Minimum pressure at which a phase change can occur in a rock (Equation 4-13)
P_f	Pressure level in a soil at which voids are assumed to have been eliminated or to be filled with water (Figure 4-3)
P_z	Empirical parameters in variable bulk modulus representation for a soil (Equation 4-17)
\bar{P}_o	Initial effective mean stress
\bar{P}_f	Effective mean stress at failure
P_{ff}	Contribution to total pressure from fluid equation of state (Equation 4-14)
P_K	Pressure at 0° Kelvin (Equation 4-2)
P_{sf}	Contribution to total pressure from solid equation of state (Equation 4-14)
P_m	Maximum pressure reached during loading of a rock (Equation 4-13)
\bar{P}	Effective mean normal stress (Figure 3-31) or effective consolidation pressure (Figure 3-4)
p	Pore fluid pressure
q	Ratio of major to minor semi-axis in capped model formulation (Equation 5-17)
Q	Square of minor semi-axis of elliptical cap in capped model formulation (Equation 5-6, Figure 5-6)
R	Strain hardening term in generalized stress/strain coefficients (Equation 4-39)
r	Ratio of specific heats at constant pressure and volume
S	Percent saturation (Figure 3-8)

s	Empirical coefficient relating energy required to meet a solid at normal density to that required at current density (Equation 4-10)
T	Temperature (Equation 4-3)
t	Time
U	Shock velocity (Equation 1-20, 1-23)
U_{rf}	Velocity of Rayleigh waves
u, v, w	Displacements in coordinate axes
x, y, z	Directions of coordinate axes
V	Current specific volume
V_0	Initial specific volume (Equation 1-22)
V_v	Specific volume of voids (Equation 3-1)
V_{sf}	Specific volume of solid particles (Equation 3-1)
W	Empirical coefficient in capped model (Equation 5-18)
X	Function of the derivatives of the yield criterion with respect to stress components (Equation 4-39)
Y	Fracture parameter (Equation 4-30)
α	Angle of internal friction (Equation 4-29)
β	Coefficient of volumetric thermal expansion per unit of specific internal energy (Equation 4-12)
β_0, β_1	Angles defining position of immersed foil in optical lever technique of measuring release adiabat properties (Figure 2-53)
γ	Grüneisen ratio (Equation 4-2)
Γ	Ratio of specific heat at constant pressure to specific heat at constant volume
δ_{ij}	Kronecker delta = 0 if $i \neq j$; = 1 if $i = j$
ϵ_{ij}	Components of strain tensor (Equations 1-7, 1-8)
$\epsilon_{xx}, \epsilon_{yy}, \epsilon_{zz}$	Direct strain components in x, y, z coordinate system (Figure 1-3)
$\epsilon_{xy}, \epsilon_{xz}, \epsilon_{yz}$	Shear strain components in x, y, z coordinate system (Figure 1-3)
$\epsilon_1, \epsilon_2, \epsilon_3$	Principal strain components
ϵ'_{ij}	Deviatoric strain tensor (Equation 1-8)
ϵ^P_{ij}	Plastic strain tensor (with dot signifies plastic strain rate tensor) (Equation 4-25)
η	Relative density; ratio of current to initial or reference densities

κ	Strain hardening parameter in capped model (Equation 5-10)
Λ	Scaler quantity in plastic potential flow rule (Equation 4-39)
λ	Lame's parameter; $= K - \frac{2}{3} G$
μ	Excess compression
μ^*, μ_G^*	Empirical coefficients in variable shear modulus representation (Equations 4-12, 4-18)
μ_m	Maximum value of excess compression experienced by an element of material
μ_p	Excess compression at which all voids in a rock are closed (Equation 4-13)
μ_{pp}	Maximum irreversible excess compression resulting from a phase change (Equation 4-13)
μ_z	Value of permanent excess compression corresponding to current μ_m
ν	Poisson's ratio (Equation 1-14)
ρ	Mass density
ρ_0	Reference or initial mass density
σ_{ij}	Stress tensor
$\sigma_{xx}, \sigma_{yy}, \sigma_{zz}$	Direct strain components in x, y, z coordinate system (Figure 1-1)
$\sigma_{xy}, \sigma_{xz}, \sigma_{yz}$	Shear strain components in x, y, z coordinate system (Figure 1-1)
$\sigma_1, \sigma_2, \sigma_3$	Principal stress components
σ_{ij}^i	Deviatoric stress tensor (Equation 1-3)
σ_c	Confining pressure in a triaxial compression test
τ	Shear stress
τ_{oct}	Octahedral shear stresses (Figure 1-2)
τ_f	Maximum shear strength, equal to $(\sigma_1 - \sigma_2)/2$
ω	Frequency of harmonic motion
ψ	Coefficient of internal friction
χ	Parameter in capped model (Figure 4-11)
τ_{max}	Maximum shear stress on a joint plane (Equation 2-1)
σ_n	Normal stress acting on a joint plane (Equation 2-1)
ϕ	Angle of internal friction on a joint plane (Equation 2-1)
θ	Angle defining preferred directions in a sample of rock or soil

Subscripts and Superscripts

C	Confining pressure
c	Stress or strain state after consolidation
d	Property measured under dynamic loading conditions. Distinction may be made between field (df) and laboratory (dl) conditions
f	Stress state at failure or maximum combined stress
i, j, k	Subscripts used in tensor notation for stress (σ) and strain (ϵ)
K	Temperature Kelvin
1, 2, 3	Principal components of stress or strain
max, min	Maximum, minimum values of a property, such as void ratio
o	Initial value of a property or initial (at rest) state
m, n	Dummy indices used in tensor notation for functions of stress or strain
oct	Referring to or acting on octahedral planes
N	Constant entropy
S, R	Shock loading and unloading conditions or states
rl	Parameter associated with Rayleigh wave
r	Relative to reference state
r, θ , z	Coordinates in a cylindrical system
s	Property measured under static conditions
T	Constant temperature
sl, fl	Solid and fluid states
v	Referring to voids in a solid
x, y, z	Coordinates in a Cartesian system
prime (')	Deviatoric component of stress or strain
	Time rate of change

SECTION 1

MATHEMATICAL AIDS IN DEFINING MATERIAL PROPERTIES

This section introduces quantities which are needed in defining mechanical properties of materials. These include stress, strain, moduli which relate stress to strain, specific internal energy, and wave speed. This section is intended to define these terms as they are used to describe the results of material property tests. For a complete discussion of these and other state variables, the reader should consult standard works (References 1-1 through 1-3).

STRESS

Stress is defined as the force per unit area as the area tends to zero. Stress components are defined on planes parallel to the coordinate axes. There are nine components, as illustrated in Figure 1-1(a). The components may be arranged in matrix form as follows:

$$\begin{bmatrix} \sigma_{xx} & \sigma_{xy} & \sigma_{xz} \\ \sigma_{yx} & \sigma_{yy} & \sigma_{yz} \\ \sigma_{zx} & \sigma_{zy} & \sigma_{zz} \end{bmatrix}$$

The individual components are written σ_{ij} in tensor notation. The σ_{xx} , σ_{yy} , σ_{zz} components are called direct or normal stresses. The others are shear stresses. The stress tensor is symmetrical such that $\sigma_{xy} = \sigma_{yx}$, $\sigma_{xz} = \sigma_{zx}$, $\sigma_{yz} = \sigma_{zy}$. Hence, only six of the nine components are independent.

The magnitude of the individual stress components depends on the coordinate system in which they are evaluated. For example, if stress components acting on coordinate planes are evaluated in the $x'-y'-z'$ system in Figure 1-1(b), $\sigma_{x'y'}$ will not, except for a special choice of axis rotation, be equal to σ_{xy} . Since the materials discussed below are assumed to be isotropic, whereby their properties are independent of coordinate axes, it is useful to define stress quantities which are also independent of coordinate directions. Such quantities are known as stress

invariants, because they are invariant with respect to coordinate transformation. The most commonly used invariant quantities are principal stresses, which are the maximum direct stresses and which act on planes of zero shear stress. They are illustrated in Figure 1-1(c).

Two other invariant quantities have important physical meanings. The so-called "first stress invariant," usually denoted by J_1 , is equal to the sum of the three direct stresses.

$$J_1 = \sigma_{xx} + \sigma_{yy} + \sigma_{zz} \quad (1-1)$$

$$= \sigma_{ii} \text{ in tensor notation}$$

It is proportional to the mean stress, sometimes called the pressure or isotropic or hydrostatic component of stress.

$$p = \frac{J_1}{3} \quad (1-2)$$

This quantity is often used as a measure of the confining stress acting on an element of material.

If the mean stress is subtracted from each direct component, the remainder is known as the deviatoric component of stress. This is illustrated in Figure 1-2(a). In matrix form, the deviatoric components are as follows:

$$\begin{bmatrix} \sigma_{xx} - p & \sigma_{xy} & \sigma_{xz} \\ \sigma_{yx} & \sigma_{yy} - p & \sigma_{yz} \\ \sigma_{zx} & \sigma_{zy} & \sigma_{zz} - p \end{bmatrix}$$

The tensor notation for individual deviatoric stress components is σ'_{ij} , which is related to the full stress tensor by

Mathematical Aids in Defining Material Properties

$$\sigma'_{ij} = \sigma_{ij} - \frac{1}{3} \sigma_{kk} \delta_{ij} \quad (1-3)$$

where

$$\delta_{ij} = 1 \text{ if } i = j; \delta_{ij} = 0 \text{ if } i \neq j$$

The second invariant of the stress deviator, usually denoted by J'_2 , is given by the following formula

$$J'_2 = \frac{1}{6} (\sigma_{xx} - \sigma_{yy})^2 + (\sigma_{yy} - \sigma_{zz})^2 + (\sigma_{zz} - \sigma_{xx})^2 + \sigma_{xy}^2 + \sigma_{yz}^2 + \sigma_{xz}^2 \quad (1-4)$$

J'_2 is proportional to shear stresses τ_{oct} acting on planes forming an octahedron in principal stress space, as illustrated in Figure 1-2(b). These are sometimes called octahedral shear stresses. J'_2 is often used as the effective or average shear stress on an element of material, just as J_1 is used as the average normal stress.

Other stress invariants which are sometimes used are the third stress invariant J_3 and the third invariant of the stress deviator J'_3 . The formulas for these quantities are as follows:

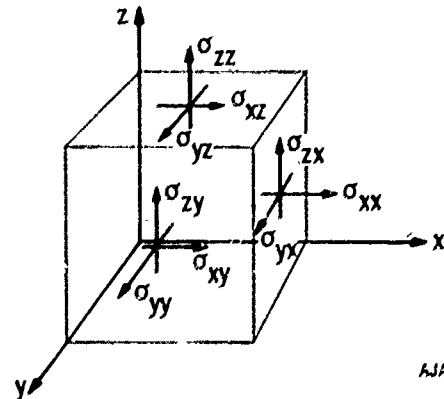
$$J'_3 = \sigma_{xx} \sigma_{yy} \sigma_{zz} - \sigma_{xx} \sigma_{yz}^2 - \sigma_{yy} \sigma_{xz}^2 - \sigma_{zz} \sigma_{xy}^2 + 2 \sigma_{xy} \sigma_{yz} \sigma_{xz}$$

$$J_3 = \sigma_{xx} \sigma_{yy} \sigma_{zz} + \left(\frac{J_1}{3}\right) (\sigma_{xy}^2 + \sigma_{yz}^2 + \sigma_{xz}^2) - \sigma_{zz} \sigma_{xy}^2 - \sigma_{xx} \sigma_{yz}^2 - \sigma_{yy} \sigma_{xz}^2 \quad (1-5)$$

$$- \left(\frac{J_1}{3}\right) (\sigma_{xx} \sigma_{zz} + \sigma_{yy} \sigma_{zz} + \sigma_{xx} \sigma_{yy}) + 2 \sigma_{xy} \sigma_{xz} \sigma_{yz} + \frac{2}{27} (J_1)^3 \quad (1-6)$$

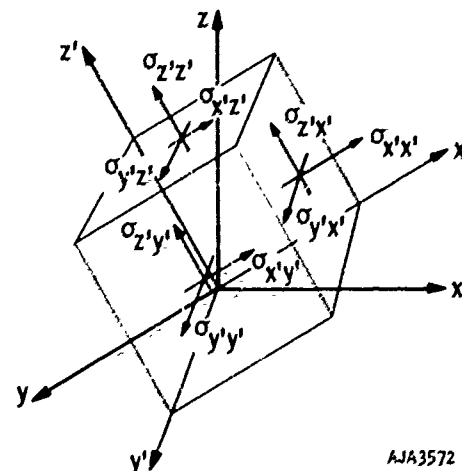
STRAIN

Strain is the change in distance between any two points of a body divided by the distance between them as that distance tends to zero. Strain components are defined in terms of the change in length of line segments or the change in an angle. If the strain is large, a distinction is made between the coordinates of points measured in the original configuration and those measured in the deformed configuration. The present discussion considers only infinitesimal strains,



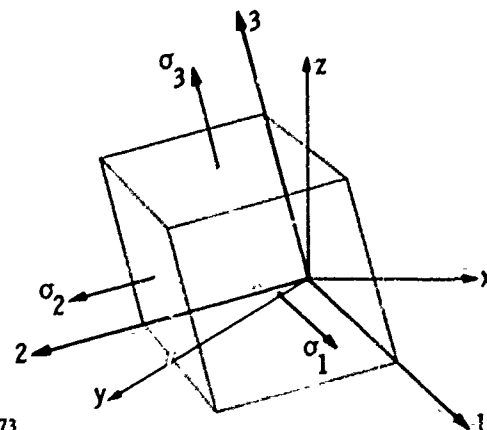
AJA3571

(a) STRESS COMPONENTS IN ARBITRARY CARTESIAN COORDINATES $x - y - z$



AJA3572

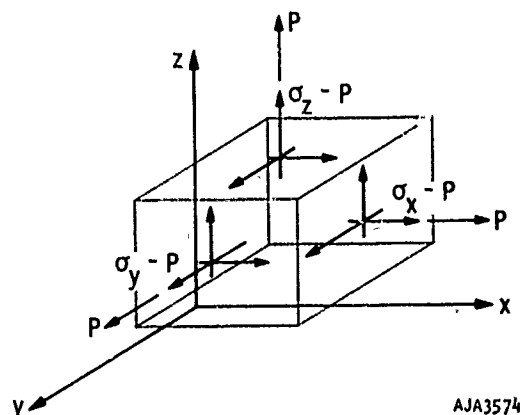
(b) STRESS COMPONENTS REFERRED TO OTHER ARBITRARY CARTESIAN COORDINATES $x' - y' - z'$



AJA3573

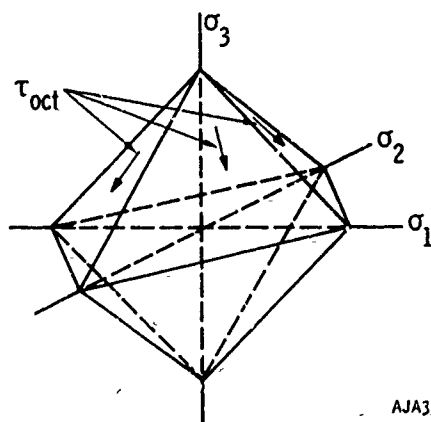
(c) PRINCIPAL STRESS COMPONENTS AND DIRECTIONS

FIGURE 1-1. STRESS COMPONENTS IN CARTESIAN COORDINATES



AJA3574

(a) HYDROSTATIC (P) AND DEVIATORIC (σ-P) COMPONENTS OF NORMAL STRESS IN ARBITRARY CARTESIAN COORDINATES X-Y-Z



AJA3575

(b) PLANES OF OCTAHEDRAL SHEAR STRESS DEFINED WITH RESPECT TO PRINCIPAL STRESS AXES

FIGURE 1-2. HYDROSTATIC AND DEVIATORIC COMPONENTS OF STRESS

however, so it is unnecessary to make such a distinction. In practical problems of ground shock, it is necessary to consider large strains in the region close to the explosive source. The small strain approximation is adequate only at points distant from the source. As in the case of stresses, there are nine strain components. Some of the deformation gradients and their interpretation as infinitesimal strain components are illustrated in Figure 1-3. The strain components may be written in matrix form as follows:

$$\begin{bmatrix} \epsilon_{xx} & \epsilon_{xy} & \epsilon_{xz} \\ \epsilon_{yx} & \epsilon_{yy} & \epsilon_{yz} \\ \epsilon_{zx} & \epsilon_{zy} & \epsilon_{zz} \end{bmatrix}$$

The individual components are written ϵ_{ij} in tensor notation. The ϵ_{xx} , ϵ_{yy} , ϵ_{zz} are called direct strains or extensions, and they represent the deformation gradient along one of the coordinate axes. The others are shear strains which represent the change in an angle which was a right angle in the undeformed configuration. The following discussion uses a symmetrical strain tensor in which $\epsilon_{xy} = \epsilon_{yx}$, $\epsilon_{xz} = \epsilon_{zx}$, $\epsilon_{yz} = \epsilon_{zy}$.

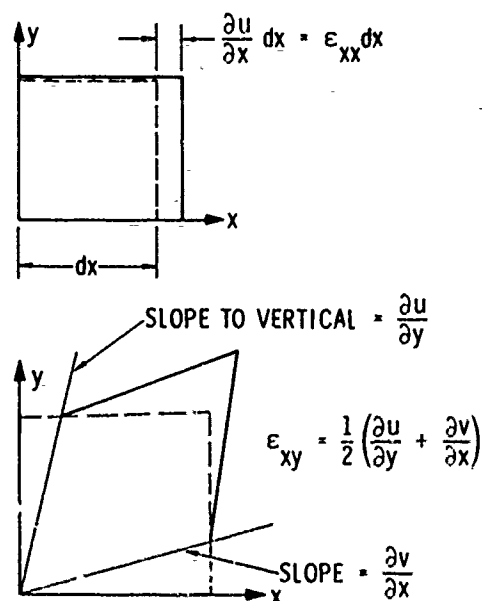
As in the case of stress components, strain components expressed in one coordinate system will not, in general, be equal to those expressed in a different system. This prompts the use of invariants. The principal strains ϵ_1 , ϵ_2 , ϵ_3 are the maximum extensional strains. The shear strains are zero in planes which contain the axes parallel to the principal strains.

Two other invariant quantities are frequently used. The first strain invariant, I_1 , is equal to the sum of the three extensional strains

$$I_1 = \epsilon_{xx} + \epsilon_{yy} + \epsilon_{zz} \quad (1-7)$$

$$= \epsilon_{ii}$$

I_1 is equal to the volumetric strain for small strain situations.



u, v ARE DISPLACEMENTS IN x, y DIRECTIONS RESPECTIVELY

AJA3576

FIGURE 1-3. STRAIN COMPONENTS IN CARTESIAN COORDINATES

Mathematical Aids in Defining Material Properties

By subtracting the volumetric strain from each extensional strain component, the deviatoric component of strain is obtained. The matrix form is

$$\begin{bmatrix} \epsilon_{xx} - I_1/3 & \epsilon_{xy} & \epsilon_{xz} \\ \epsilon_{yx} & \epsilon_{yy} - I_1/3 & \epsilon_{yz} \\ \epsilon_{yz} & \epsilon_{zy} & \epsilon_{zz} - I_1/3 \end{bmatrix}$$

Individual deviatoric strain components are given by

$$\epsilon'_{ij} = \epsilon_{ij} - \epsilon_{kk} \delta_{ij} \quad (1-8)$$

The second invariant of the strain deviator, I'_2 , is given by

$$I'_2 = \frac{1}{6} \left[(\epsilon_{xx} - \epsilon_{yy})^2 + (\epsilon_{yy} - \epsilon_{zz})^2 + (\epsilon_{zz} - \epsilon_{xx})^2 \right] + \frac{3}{2} (\epsilon_{xy}^2 + \epsilon_{yz}^2 + \epsilon_{xz}^2) \quad (1-9)$$

In analogy to the octahedral shear stress, I'_2 is proportional to the change in angle between octahedral planes. Hence, it is a measure of the pure distortional strain in a body just as I_1 is a measure of the pure volumetric strain.

The third invariant of the strain tensor is given by

$$I_3 = \epsilon_{xx}\epsilon_{yy}\epsilon_{zz} - \frac{1}{4} \epsilon_{xx}\epsilon_{yz}^2 + \epsilon_{yy}\epsilon_{xz}^2 + \epsilon_{zz}\epsilon_{xy}^2 - \epsilon_{xy}\epsilon_{xz}\epsilon_{yz} \quad (1-10)$$

I_3 and the third invariant of the strain deviator tensor are rarely, if ever, used as state variables in defining properties of earth materials.

ELASTIC MODULI

Up to this point, stress and strain components and invariants of stress and strain have been defined. The next step is to establish relationships between stress and strain on the basis of experimental data. The simplest relationships are for isotropic, linearly elastic materials whose temperature is constant. In such a material, the mean stress is uniquely related to the volumetric strain by the bulk modulus and the deviatoric stress is uniquely related to the deviatoric strain by the shear modulus as follows:

$$\sigma_{kk} = 3K\epsilon_{kk} \quad (1-11)$$

$$\sigma'_{ij} = 2G\epsilon'_{ij} \quad (1-12)$$

where K and G are the bulk and shear moduli, respectively. Equations 1-11 and 1-12 express Hooke's law in arbitrary coordinates. An isotropic elastic material is completely characterized by two independent constants such as K and G . Other constants can be defined in terms of these two. Young's modulus E relates the stress in a prism, which is free from stress on its lateral surface, to the strain in the direction of the stress.

$$E = \frac{9KG}{3K + G} \quad (1-13)$$

The prism also undergoes a lateral expansion which is a constant fraction of the axial compression (assuming the axial stress is compressive). The fraction is Poisson's ratio ν

$$\nu = \frac{3K - 2G}{2(3K + G)} \quad (1-14)$$

The constrained modulus B relates the stress in a prism, whose lateral surfaces are restrained against deformation, to the strain in the direction of the stress

$$B = K + \frac{4}{3}G \quad (1-15)$$

The ratio r of the lateral stress which is required to restrain lateral deformation to the axial stress is

$$k_o = \frac{3K - 2G}{3K + 4G} \quad (1-16)$$

A complete tabulation of such relationships for an elastic, isotropic material is given in Table 1-1.

In following sections, nonlinear relationships are found between mean stress and volumetric strain, and between deviatoric stress and strain. In general, K and G are expressed as functions of stress, strain, and previous history of loading. They are specified as tangent moduli, and represent the local slopes of their respective stress/strain relations at the appropriate level of stress or strain.

WAVE PROPAGATION

Although the basic properties of materials are usually specified in terms of stress, strain, and specific internal energy, it is sometimes necessary to define the response of a material under conditions of wave propagation. It is convenient to divide the discussion into the situation where changes of specific internal energy can be safely neglected, and those

TABLE 1-1. RELATIONSHIP AMONG ELASTIC MODULI

	Shear Modulus, G	Young's Modulus, E	Constrained Modulus, B	Bulk Modulus, K	Lame's Parameter, λ	Poisson's Ratio, ν	Stress Ratio in Uniaxial Strain, k_o
G, E	G	E	$\frac{G(4G - E)}{3G - E}$	$\frac{GE}{9G - 3K}$	$\frac{G(E - 2G)}{3G - E}$	$\frac{E - 2G}{2G}$	$\frac{E - 2G}{4G - E}$
G, B	G	$\frac{G(3B - 4G)}{B - G}$	B	$B - \frac{4}{3}G$	$B - 2G$	$\frac{B - 2G}{2(B - G)}$	$\frac{B - 2G}{2B}$
G, K	G	$\frac{9GK}{3K + G}$	$K + \frac{4}{3}G$	K	$K - \frac{2G}{3}$	$\frac{3K - 2G}{2(3K + G)}$	$\frac{3K - 2G}{3K + 4G}$
G, λ	G	$\frac{G(3\lambda + 2G)}{\lambda + G}$	$\lambda + 2G$	$\lambda + \frac{2G}{3}$	λ	$\frac{\lambda}{2(\lambda + G)}$	$\frac{\lambda}{\lambda + 2G}$
G, ν	G	$2G(1 + \nu)$	$\frac{2G(1 - \nu)}{1 - 2\nu}$	$\frac{2G(1 + \nu)}{3(1 - 2\nu)}$	$\frac{2G\nu}{1 - 2\nu}$	ν	$\frac{\nu}{1 - \nu}$
G, k_o	G	$\frac{2G(1 + 2k_o)}{1 + k_o}$	$\frac{2G}{1 - k_o}$	$\frac{2G(1 + 2k_o)}{3(1 - k_o)}$	$\frac{2Gk_o}{1 - k_o}$	$\frac{k_o}{1 + k_o}$	k_o
E, B	$\frac{3B + E - C}{6}$	E	B	$\frac{3B - E + C}{6}$	$\frac{B - E + C}{4}$	$\frac{B - E + C}{5B - E + C}$	$\frac{B - E + C}{4B}$
E, K	$\frac{3KE}{9K - E}$	E	$\frac{K(9K + 3E)}{9K - E}$	K	$\frac{K(9K - 3E)}{9K - E}$	$\frac{3K - E}{6K}$	$\frac{3K - E}{3K + E}$
E, λ	$\frac{E - 3\lambda + \pi}{4}$	E	$\frac{E - \lambda + \pi}{2}$	$\frac{E + 3\lambda + \pi}{6}$	λ	$\frac{-\lambda - E + \pi}{4\lambda}$	$\frac{2\lambda}{E - \lambda + \pi}$
E, ν	$\frac{E}{2(1 + \nu)}$	E	$\frac{E(1 - \nu)}{(1 + \nu)(1 - 2\nu)}$	$\frac{E}{3(1 - 2\nu)}$	$\frac{E\nu}{(1 + \nu)(1 - 2\nu)}$	ν	$\frac{\nu}{1 - \nu}$
E, k_o	$\frac{E(1 + k_o)}{2(1 + 2k_o)}$	E	$\frac{E(1 + k_o)}{(1 + 2k_o)(1 - k_o)}$	$\frac{E(1 + k_o)}{3(1 - k_o)}$	$\frac{Ek_o(1 + k_o)}{(1 + 2k_o)(1 - k_o)}$	$\frac{k_o}{1 + k_o}$	k_o
B, K	$\frac{3(B - K)}{4}$	$\frac{9K(B - K)}{3K + B}$	B	K	$\frac{3K - B}{2}$	$\frac{3K - B}{3K + B}$	$\frac{3K - B}{2B}$
B, λ	$\frac{B - \lambda}{2}$	$\frac{(B - \lambda)(B + 2\lambda)}{B + \lambda}$	B	$\frac{B + 2\lambda}{3}$	λ	$\frac{\lambda}{B + \lambda}$	$\frac{\lambda}{B}$
B, ν	$\frac{B(1 - 2\nu)}{2(1 - \nu)}$	$\frac{B(1 + \nu)(1 - 2\nu)}{1 - \nu}$	B	$\frac{B(1 + \nu)}{3(1 - \nu)}$	$\frac{B\nu}{1 - \nu}$	ν	$\frac{\nu}{1 - \nu}$
B, k_o	$\frac{B(1 - k_o)}{2}$	$\frac{B(1 + 2k_o)(1 - k_o)}{1 + k_o}$	B	$\frac{B(1 + 2k_o)}{3}$	Bk_o	$\frac{k_o}{1 + k_o}$	k_o
K, λ	$\frac{3(K - \lambda)}{2}$	$\frac{9K(K - \lambda)}{3K - \lambda}$	$3K - 2\lambda$	K	λ	$\frac{k_o}{3K - k_o}$	$\frac{\lambda}{3K - 2\lambda}$
K, ν	$\frac{3K(1 - 2\nu)}{2(1 + \nu)}$	$3K(1 - 2\nu)$	$\frac{3K(1 - \nu)}{1 + \nu}$	K	$\frac{3K\nu}{1 + \nu}$	ν	$\frac{\nu}{1 - \nu}$
K, k_o	$\frac{3K(1 - k_o)}{2(1 + 2k_o)}$	$\frac{3K(1 - k_o)}{1 + k_o}$	$\frac{3K}{1 + 2k_o}$	K	$\frac{3Kk_o}{1 + 2k_o}$	$\frac{k_o}{1 + k_o}$	k_o
λ, ν	$\lambda \frac{(1 - 2\nu)}{2\nu}$	$\lambda \frac{(1 + \nu)(1 - 2\nu)}{\nu}$	$\lambda \frac{(1 + \nu)}{\nu}$	$\frac{\lambda(1 + \nu)}{3\nu}$	λ	ν	$\frac{\nu}{1 - \nu}$
λ, k_o	$\lambda \frac{(1 - k_o)}{2k_o}$	$\lambda \frac{(1 + 2k_o)(1 - k_o)}{k_o(1 + k_o)}$	$\frac{\lambda}{k_o}$	$\frac{\lambda(1 + 2k_o)}{3k_o}$	λ	$\frac{k_o}{1 + k_o}$	k_o

NOTE: $\epsilon = \pm \sqrt{9\mu^2 + E^2 - 10EB}$

if $\sigma > 0$ $\epsilon, \pi > 0$

$\pi = \pm \sqrt{9\lambda^2 + E^2 + 2E\lambda}$

if $\sigma < 0$ $\epsilon, \pi < 0$

AJA3904

Mathematical Aids in Defining Material Properties

where such changes must be considered. Two types of waves are important in studying material properties. In a dilatational or irrotational wave, the particle velocity is parallel to the direction of the wave propagation. In a shear or equivoluminal wave, the particle velocity is transverse to the direction of the wave propagation. These two waves propagate at different speeds partly because they depend on different material properties, and hence, they can be used to measure two independent properties.

WAVE PROPAGATION (NEGLECTING INTERNAL ENERGY CHANGES)

An introduction to wave propagation in isotropic elastic media is given by Kolsky, Reference 1-5. It is shown that the velocity of dilatation waves in an infinite medium is

$$c_p = \left(\frac{K + \frac{4}{3}G}{\rho} \right)^{\frac{1}{2}} \quad (1-17)$$

where

K = Bulk modulus

G = Shear modulus

ρ = Mass density

This equation illustrates the point that the speed of wave propagation depends on the stiffness of the material in the direction of the particle motion. Equation 1-14 applies to an infinite medium or to a constrained rod. The dilatation wave speed in an unconstrained rod, in contrast, is

$$c_b = \left(\frac{E}{\rho} \right)^{\frac{1}{2}} \quad (1-18)$$

where

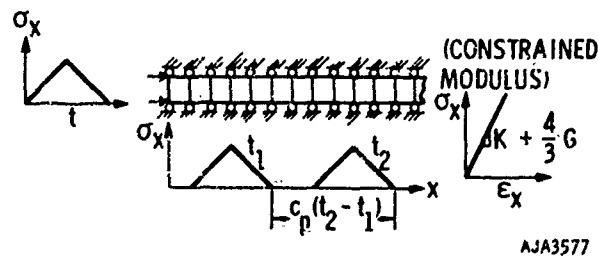
E = Young's modulus

The velocity of shear waves is

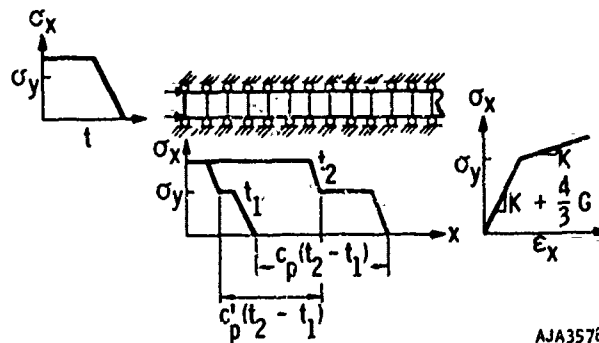
$$c_s = \left(\frac{G}{\rho} \right)^{\frac{1}{2}} \quad (1-19)$$

Most wave propagation experiments which are carried out for the purpose of studying material properties involve one-dimensional, plane wave propagation because it is simpler to interpret the results than in cylindrical or spherical flow. In one-dimensional, elastic plane wave propagation,

the shape of the input pulse is preserved as illustrated in Figure 1-4. Any change in shape can be attributed to nonlinear material properties. An example of how nonlinear material properties alter the shape of the pulse in constrained, plane wave propagation, is shown in Figure 1-4. The stiffness of the rod in one-dimensional strain is sometimes called the constrained modulus. For an elastic, perfectly plastic material, there are two moduli—one above and one below the yield point. Stresses below the yield point propagate with a velocity appropriate to a stiffness equal to $K + (4G/3)$.



(a) DILATATION WAVE IN AN ELASTIC ROD



(b) DILATATION WAVE IN AN ELASTIC, PERFECTLY PLASTIC ROD (MISES YIELD CRITERION)

FIGURE 1-4. LONGITUDINAL WAVE PROPAGATION IN A Laterally CONSTRAINED ROD

WAVE PROPAGATION (INCLUDING INTERNAL ENERGY CHANGES)

Aspects of shock wave propagation relevant to the present discussion are given in References 1-3 and 1-6. An idealized material is assumed to have the following properties:

- Compressibility decreases with increasing pressure
- Adding heat at constant volume produces an increase in pressure
- Density increases with pressure under adiabatic conditions

Wave Propagation (Including Internal Energy Changes)

A compressive shock is induced in the material which is constrained against expansion transverse to the direction of propagation. A compressive shock transition is a boundary between shocked and unshocked states which propagates supersonically; that is, at a speed which is faster than an infinitesimal amplitude wave. Accompanying the shock compression, which is defined by the stress component in the direction of propagation, is a particle velocity which is also in the direction of propagation. Assuming conservation of mass, momentum, and energy, the shock transition leads to relationships among the stress (σ), density (ρ), particle velocity (\dot{u}), shock velocity (U), and specific internal energy (e).

$$\rho_o U = \rho_s (U - \dot{u}_s) \quad (1-20)$$

$$\sigma_s - \sigma_o = \rho_o U \dot{u}_s \quad (1-21)$$

$$e_s - e_o = \frac{1}{2}(\sigma_s + \sigma_o)(V_o - V_s) \quad (1-22)$$

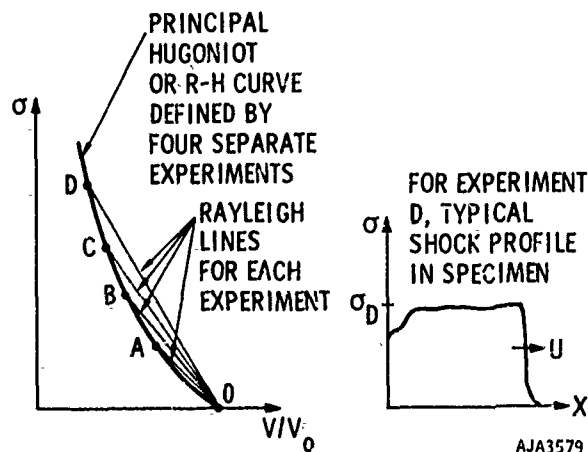
where subscripts o and s refer to equilibrium states before and following a shock front, respectively. When used with the equation of state of a particular material, Equation 1-22 is a unique expression of the state of a material. The projection of this Rankine-Hugoniot (R-H) curve into a P - V plane for a material having the properties described in a, b, and c above and being subjected to a plane shock wave is shown in Figure 1-5.

The velocity of propagation of the shock front is related to the slope of the chord drawn between A and B . From Equations 1-20 and 1-21,

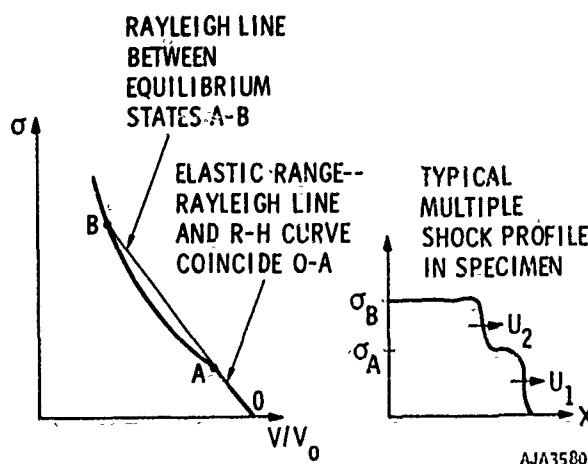
$$U = V_o \left[\frac{\sigma_s - \sigma_o}{V_o - V_s} \right]^{1/2} \quad (1-23)$$

In a material with a concave upward R-H curve, as shown in Figure 1-5, the shock velocity increases with stress level.

Establishing the R-H curve is the first step in defining the properties of a material in states where internal energy changes are significant. Under shock loading, the pressure above which internal energy changes must be considered varies with the material. However, above 20-30 kbars for a porous material and above 60-80 kbars for a nonporous material, internal energy changes are usually considered. A second step is to define the properties on unloading from the shocked state. Figure 1-6 illustrates a shock wave with a trailing rarefaction. The speed of the rarefaction U_R is greater than that of the



(a) SHOCK RESPONSE OF A SINGLE PHASE MATERIAL



(b) SHOCK RESPONSE OF A MATERIAL EXHIBITING A LINEAR ELASTIC RANGE

FIGURE 1-5. PRINCIPAL HUGONIOT DEFINED BY SHOCK WAVE EXPERIMENTS

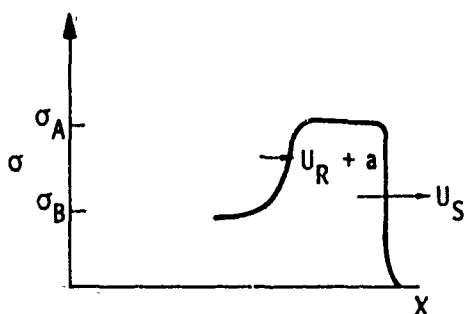
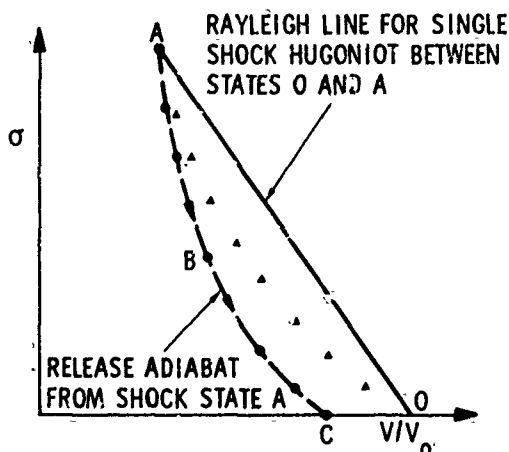
shock front U_s because the tangent to the R-H curve is steeper than the Rayleigh line. A further contribution to the rarefaction velocity relative to the shock front is that the rarefaction is carried along at a speed equal to the particle velocity. The states of pressure, specific internal energy, and relative density through which the material goes during unloading are assumed to be reached under conditions of adiabatic pressure release.

The basic measurements along an adiabatic stress release path are in terms of pressure P and particle velocity \dot{u} . In order to employ the data in formulating an equation of state, they are transformed to the P - V plane by means of the Riemann integral

Mathematical Aids in Defining Material Properties

AREA BETWEEN O-A RAYLEIGH LINE AND A-B RELEASE ADIABAT REPRESENTS PERMANENT ABSORPTION OF INTERNAL ENERGY OR "WASTE HEAT"

- ▲ STATES ON THE PRINCIPAL HUGONIOT MEASURED IN PREVIOUS EXPERIMENTS
- STATES ON THE RELEASE ADIABAT FROM A



AJA3581

FIGURE 1-6. RELATION BETWEEN HUGONIOT AND RELEASE ADIABAT

$$V_1 = V_0 + \int_{u_0}^{u_1} \left(\frac{\partial u}{\partial P} \right)_{N=\text{const}} du \quad (1-24)$$

The path may then be superposed on the principal hugoniot as shown in Figure 1-6. Implications of assuming that total net entropy remains constant during the adiabatic release process are described in Reference 1-7.

SUMMARY

The purpose of this section is to introduce the reader to ideas in mechanics of materials which are needed in the following sections. For a complete discussion of stress, strain, specific internal energy, and other thermomechanical variables, the reader should consult works such as References 1-1 through 1-3.

REFERENCES

- 1-1. Love, A. E. H., A Treatise on the Mathematical Theory of Elasticity, Fourth Edition, Dover Publications, New York, 1944.
- 1-2. Fung, Y. C., Foundations of Solid Mechanics, Prentice Hall, Englewood Cliffs, New Jersey, 1965.
- 1-3. Courant, R., and K. O. Fredricks, Supersonic Flow and Shock Waves, Interscience, Inc., New York, 1948.
- 1-4. U. S. Department of Defense publication.
- 1-5. Kolsky, H., Stress Waves in Solids, Dover Publications, New York, 1963.
- 1-6. Duvall, G. E., "Concepts of Shock Wave Propagation," Bull. Seismological Soc. of America, Vol. 52, No. 4, October 1962, pp. 869-893.
- 1-7. Rosenberg, J. T., et al., Dynamic Properties of Rocks, Stanford Research Institute, DASA 2112, July 1968.

SECTION 2

MECHANICAL PROPERTIES OF ROCK

INTRODUCTION

This section discusses the mechanical properties of rocks that are used to compute ground shock and rock/structure interaction effects. A classification of rocks derived below is based on the parameters directly influencing such mechanical properties as volumetric and shear stiffness, shear strength, and mass density. These parameters include adhesion, grain strength, grain ductility, grain size, and porosity. Within this framework, the constitutive behavior of competent rock over the complete range of stress levels, strain rates, and temperatures of interest is discussed in relation to yield stress and ductility, ultimate stress, postfailure behavior and the brittle-ductile transition. Deformation characteristics and failure mechanisms of a variety of rock types are discussed. High-pressure equation-of-state data are presented for rocks of interest. Static and dynamic experimental techniques for determining these properties are reviewed.

A major distinction is made between the behavior of homogeneous rocks and those containing major discontinuities such as joints. Laboratory scale experiments primarily reveal the properties of homogeneous rocks, although there has been some laboratory testing of discontinuous specimens. In situ experiments are performed primarily to study the properties of discontinuous rock masses. The main unsolved problem in representing the behavior of rock masses is to use homogeneous properties for rock between the major joints while at the same time accounting for the action of the joints.

The mechanical properties of in situ rock masses containing inherent structural heterogeneities are discussed. Techniques are presented for determining both deformational and frictional properties of in situ rocks.

The relationships between data derived from both laboratory and field experiments under (1) different stress states, (2) stress levels, and (3) different strain rates are discussed in terms of spanning the gap between sets of data derived under these different conditions. Some suggestions are given on the appli-

cability scaling data obtained from competent laboratory samples to mechanical properties and constitutive behavior of in situ rock masses.

MECHANICAL CLASSIFICATION OF ROCKS

Rocks can be considered as composites of mineral grains. These grains are held together either by a matrix substance or by physical or chemical bonds between the grains themselves. Minerals in rocks generally occur as crystalline materials, and most mineral grains are single crystals. Rock classifications are based upon the mineral composition, texture, and inferred origin of the rock. There is no direct relationship between the rock name and its mechanical properties. This section briefly discusses the geologic classification of rocks. Then, the list of rocks is reorganized into a system of mechanical classes, which are groups of rocks having similar mechanical behaviors under similar environmental conditions.

In addition to the mineralogy of the rock, its texture must be considered. Texture refers to the way in which the mineral grains fit together and to the type of intergranular bonding. Texture also refers to the size, size distribution, and shape of the mineral grains. On the basis of texture, rocks are grouped into broad categories: (1) "clastic" rocks, which are aggregates of mineral grains held together with a cement of some sort of material different than the mineral grains themselves, and (2) crystalline rocks, in which the mineral grains are held together by a physical chemical adhesion between the grains themselves. The crystalline rocks are very similar in some respects to metals.

In a mechanical classification, the problem of scale must also be considered. The classification of rocks is usually based upon small laboratory size samples of a few cubic inches. Ultimately, however, problems of the in situ rock mass must be considered.

There are two groups of factors that control the mechanical behavior of rock. The first group is the intrinsic material parameters, which include: (1) the adhesion of mineral grains (the strength of the matrix in the clastics, the binding strength between the mineral

Mechanical Properties of Rock

grains in the crystalline rocks), (2) grain strength, (3) grain ductility, (4) rock porosity, (5) rock permeability, and (6) grain size. The second group of factors is the environmental parameters: (1) confining pressure, (2) temperature, (3) pore pressure of fluids within the porosity of the rock, and (4) strain rate or rate of deformation to which the rock is subjected. Thus, the material parameters concern the texture and mineralogy of the rock, whereas the environmental parameters have to do with the local geologic conditions and induced factors of pressure, temperature, etc. The first part of this chapter deals primarily with the classification of rocks according to their material parameters. The last part, on constitutive relations, concerns the effect of environmental parameters upon the mechanical behavior of rock.

Common Rock-Forming Minerals

Table 2-1 lists the common rock-forming minerals and describes their mechanical properties. Most of the common rock-forming minerals are silicates, that is, minerals containing silicon and oxygen, one of the strongest chemical bonds. As a result of this strong bond, the silicate minerals tend to have a large grain strength and a low grain ductility, and thus they tend to be brittle. The exceptions are the "platy" silicates, which are very strongly anisotropic; these are the micas, muscovite and biotite, and the clay minerals represented here by kaolinite. These also tend to be the weakest of the silicate minerals, largely due to a very pronounced plane of weakness. The most common nonsilicate rock-forming minerals are the carbonates, calcite and dolomite, and the iron oxides represented by the hematites. These minerals tend to have intermediate strengths and ductilities. The calcite is the most ductile because it has the property of being able to deform by twinning of the crystal lattice. Dolomite lacks this property and is therefore more brittle.

Within the silicate minerals, the chemical composition has a strong effect on the density and the melting temperature. Those silicates which contain significant amounts of iron and magnesium--the "mafic" silicates tend to be more dense and have higher melting temperatures than those silicates which are high in silica and aluminum--the "silaic" silicates.

Geologic Classification of Rocks

There are three basic types of rocks, which are sedimentary, igneous, and metamorphic. The sedimentary rocks are formed by the deposition of erosion products which come largely from the destruction of preexisting rocks. After deposition and burial, these sedimentary or detrital grains are cemented together either by a foreign material or by a mineral cement

TABLE 2-1. COMMON ROCK-FORMING MINERALS

	Density	Strength	Ductility	Cleavage
SILICATES				
Quartz	2.7	⊕	⊖	
Feldspars				
Orthoclase	2.6	⊕	⊖	⊕
Plagioclase	2.7	⊕	⊖	⊕
Micas				
Muscovite	2.8	⊖ - ⊕	⊕	⊕
Biotite	3.0	⊖ - ⊕	⊕	⊕
Clays				
Kaolinite	2.6	⊖	⊕	⊕
Amphiboles				
Hornblende	3.05	⊕	⊖	⊕
Pyroxenes				
Augite	3.05	⊕	⊖	⊕
Olivine	3.5	⊕	⊖	⊖
NONSILICATES				
Calcite	2.7	⊕	⊕	⊕
Dolomite	2.8	⊕	⊖	⊕
Hematite	5.0	⊕	⊕	

Unconfined compressive strength at 24°C - $\leq 1 \text{ kb} \leq 10 \text{ kb} \leq +$

Ductility $\ominus \leq 2\% \leq \oplus \leq 10\% \leq \oplus$

AA4812

derived from partial solution and deposition of the minerals within the sediment itself. The "clastic" mechanical classification of rocks is mostly represented by the detrital sedimentary rocks; crystalline sedimentary rocks also occur either as limestones or as evaporites (Table 2-2(a)).

The igneous rocks are those formed by the crystallization from a molten rock mass ("magma"). The igneous rocks (Table 2-2(b)) are divided into two classes, depending upon whether crystallization took place at depth in the earth's crust to form the intrusive igneous rocks or on the earth's surface to form the extrusive igneous rocks. Intrusive igneous rocks tend to have a coarser grain size, and the grains are tightly interlocked. The extrusive igneous rocks tend to be finer grained and may contain large amounts of uncrystallized glass. Extrusive igneous rocks are often quite porous (for example, tuffs).

The third category contains the metamorphic rocks. In these, an original rock (igneous or sedimentary) has been subjected to high pressures and

Mechanical Classification of Rocks

high temperature, which cause it to recrystallize without actually melting. The metamorphic rocks are all crystalline (Table 2-2(c)).

The earth's crust is made up predominately of igneous rocks, about 5 percent sedimentary rocks, and a very small proportion of metamorphic rocks. However, the rocks most commonly encountered within a couple of kilometers of the earth's surface are the sedimentary type.

Mechanical Reclassification of Rocks

As mentioned above, the terminology applied to rocks is primarily based upon factors other than their mechanical behavior. Therefore, it is useful to devise a mechanical classification for the present discussion. A "mechanical class" is defined as being that group of rock types which exhibit similar stiffnesses and strengths under similar environmental conditions of temperature, pressure, and strain rate.

TABLE 2-2(a). SEDIMENTARY ROCK CLASSIFICATION†

Method of Formation	Grain Size	Rock	Description	Major Mineral Constituents	Mechanical Classification*
Clastic	Coarse (>2.0mm)	Conglomerate	Large grain in fine grained matrix	Various	II or IIIa
		Sandstone	Rounded grains in calcite or clay matrix	Quartz, calcite	IIb--IIIa
	Medium (0.1--2.0mm)	Quartzite	Rounded grains in silica matrix	Quartz	IIIb
		Clay	Plastic texture	Kaolinite, quartz, mica	Ia
	Fine (<0.1mm)	Shale	Laminated	Kaolinite, quartz, mica	Ib
Crystalline		Limestone	Coarse to fine grained	Calcite	VIa or b
		Dolomite		Dolomite, calcite	VI
		Coal		Coal	V
		Salt, gypsum		Halite, gypsum	V

†Tables 2-2a, b, and c are adapted from Farmer, 1968

*See Table 2-3

AA4817

Mechanical Properties of Rock

TABLE 2-2(b). IGNEOUS ROCK CLASSIFICATION[†]

Property	Sialic <66% Silica	Intermediate 52-66%		Basic 52%	Mechanical Classification*
Plutonic Texture (coarse grained)	Granite	Syenite	Diorite	Gabbro	VIIIb
Volcanic Texture (fine grained to glassy)	Rhyolite, tuff, obsidian	Trachyte	Andesite	Basalt	VIIa
Major Mineral Constituents	Quartz, orthoclase (mica)	Orthoclase, plagioclase (mica)	Plagioclase, hornblende	Plagioclase, pyroxene, olivine	

[†]Tables 2.2a, b, and c are adapted from Farmer, 1968

*See Table 2.3

AA4815

TABLE 2-2(c). METAMORPHIC ROCK CLASSIFICATION[†]

Texture	Rock	Description	Major Mineral Constituents	Mechanical Classification*
Massive	Hornfels	Micro-fine grained	Quartz	VIIIa
	Quartzite	Fine grained	Quartz	IIIb
	Marble	Fine to coarse grained	Calcite or dolomite	Va, b
Foliated	Slate	Micro-fine grained, laminated	Kaolinite, mica	Ib
	Phyllite	Soft, laminated	Mica, kaolinite	VIa
	Schist	Altered hypabyssal rocks, coarse grained	Feldspar, quartz, mica	VIb
	Gneiss	Altered granite, banded	Hornblende, quartz, feldspar	VIIIb

[†]Tables 2.2a, b, and c are adapted from Farmer, 1968

*See Table 2.3

AA4816

Mechanical Classification of Rocks

In this classification are the rock characteristics which appear to be most relevant to mechanical behavior. These parameters fall into two groups: mineralogical and textural. The mineralogical parameters determine how the mineral grains in the rock behave. The most important mineralogical parameters are the strength and ductility, (see Table 2-1). The most relevant textural parameter appears to be the adhesion, or the strength of bonding between the grains, which is a measure of the strength of the cement of clastic rocks or of the chemical bonding between the grain boundaries of crystalline rocks. Another factor involved in adhesion in unconsolidated clastics of Class 1a and 1b, is the effect of friction between the grain boundaries. Other textural parameters are the grain size, the "porosity" or open space within the rock, and the "permeability," or ease with which fluid can move between the pore spaces in the rock.

Of course, the various mineralogical and textural parameters are not completely independent of each other. For example, there is an obvious relation between the grain strength and the adhesion in the crystalline rocks, although the adhesion is usually much weaker than the grain strength. There is also a relationship between the porosity and the permeability of the rock. However, this relationship is not as obvious as it might first seem. There are a number of massive crystalline rocks, such as granites, whose porosity is primarily due to fracturing of the rock by tectonic forces. The fracturing is responsible for a low to intermediate porosity, but because the pore spaces are connected along the fractures, the permeability may be very high. Conversely, the shales have a high porosity but a very low permeability because of their very small grain size. So for the purposes of classification, these various parameters may be

TABLE 2-3. MECHANICAL CLASSIFICATION OF ROCK

	Class	Adhesion	Grain Strength	Grain Ductility	Grain Size	Porosity	Permeability	Anisotropy
Clastic Rocks:	1a	⊖	⊖	⊕	⊖	⊕	⊕ - ⊖	I
	b	⊕	⊖	⊕ - ⊕	⊖	⊕	⊖	A
	IIa	-	⊕ - ⊕	⊖	⊕ - ⊖	⊕	⊕	I
	b	⊕	⊕	⊖	⊕ - ⊕	⊕	⊕	I
	IIIa	⊕ <	⊕	⊖ / ⊕	⊕ - ⊕	⊕ - ⊖	⊕ - ⊕	I
	b	⊕ =	⊕	⊖ / ⊕	⊕	⊕ - ⊖	⊕	I
Crystalline Rocks:	IV	⊕ - ⊖	⊕	⊕ - ⊖	⊕ - ⊖	⊕ - ⊕	⊕ - ⊖	I
	V	⊖	⊖	+	⊕ - ⊖	⊕ - ⊖	⊕ - ⊕	I or A
	VIa	⊕ - ⊖	⊕ / ⊖	⊕ / ⊕	⊕ - ⊕	⊕ - ⊕	⊕	I
	b	⊕	⊕ / ⊖	⊕ / ⊕	⊖	⊕ - ⊖	⊕ - ⊖	I or A
	VIIa	⊕	⊕ - ⊖	⊕ / ⊕	⊖	⊖	⊕ - ⊖	A
	b	⊕	⊕ - ⊕	⊕ / ⊕	⊕ - ⊖	⊖	⊕ - ⊖	A
	VIIIa	⊕	⊕ / ⊕	⊖ / ⊕	⊖	⊖	⊕ - ⊖	I
	b	⊕	⊕ / ⊕	⊖ / ⊕	⊕ - ⊕	⊖	⊕ - ⊖	I

⊕ High, ⊕ intermediate, ⊖ low. (For numerical limits, see Table 2.4)

Anisotropy I - isotropic A - anisotropic Rock contains planes or directions of weakness.

/ Separates properties at low temperature and pressure (left) and those properties at high temperature and pressure (right)

+ < Adhesion strong, but less than grain strength.

+ = Adhesion equal to grain strength.

Adhesion Ultimate strength of cement or, coefficient of interval friction.

AA4820

Mechanical Properties of Rock

considered independent. One other obvious parameter, density, is not included. The reason is that density is dependent primarily upon the composition of the rock and within a mechanical class, the rocks may have a wide range of densities.

This mechanical classification presented in Table 2-3 was developed by R. C. Wilson for this sourcebook, as explained in the Preface. It is neither standard nor generally accepted by the majority of researchers in rock mechanics. It is used here in order to help clarify the present discussion.

The mechanical classification chart, Table 2-3, lists mechanical classes of rocks and the ranges of the various textural parameters upon which this classification is based. The definition and numerical ranges of the parameters which correspond with the symbols on the classification chart are listed in Table 2-4. Table 2-5 lists examples of common rocks in each of the mechanical classes. In using Tables 2-3 and 2-4 it must be kept in mind that the mechanical behavior of the different classes of rock depends on the environmental parameters--pressure, temperature, and strain rate.

In the clastic categories, Classes I through III, the rocks with the lowest stiffnesses and strengths are those in Class I and Ia, such as clay and altered tuffs. These are rocks with very high porosity, low to intermediate permeability, high compressibility, high ductility, and low-yield strength. In contrast, Class IIIa rocks are very strong clastics, in which the adhesion is slightly less than grain strength. Class IIIb comprises clastics in which the adhesion is equal to the grain strength. The quartzites (IIIb) are some of the strongest of all rocks and certainly the strongest of the clastics.

The crystalline rocks represent a broader range of mechanical properties, from the weak rocks of Class IV to the strong, stiff rocks of Class VII. Class IV is altered crystallines, where the adhesion is weakened by chemical weathering, and which, therefore, tend to behave like the clastic rocks in Class I. That is, the stiffness is relatively low, and the ductility is relatively high. The strongest crystalline rocks are those in Class VIIa, which are the dense, massive extrusives such as the andesites (VIIa), and massive igneous and metamorphic rocks of VIIb. The Class III rocks tend to be very stiff and have a high strength and a relatively low ductility. The mechanical behavior of these classes of rocks and the effects of environmental parameters of pressure, temperature and strain rate on strength are discussed in more detail below.

It must be noted that this rock classification is based on small laboratory samples of a few cubic inches in volume. In applying the mechanical classes of Table 2-3 to the larger rock mass in the crust of the earth, certain modifications must be made. The

TABLE 2-4. NUMERICAL RANGES OF MECHANICAL CLASSIFICATION PARAMETERS

1. Adhesion--ultimate compressive strength of intergranular bonding.
 $\ominus \leq 1000 \text{ bars} \leq \oplus \leq 10,000 \text{ bars}$
2. Grain strength--ultimate compressive strength.
 $\ominus \leq 1000 \text{ bars} \leq \oplus \leq 10,000 \text{ bars}$
3. Grain ductility--% strain before fracture.
 $\ominus \leq 1\% \leq \oplus \leq 10\%$
4. Grain size--mean diameter.
 $\ominus \leq 0.1 \text{ mm} \leq \oplus \leq 5 \text{ mm} \leq \oplus$
5. Porosity--% Pore volume/total volume.
 $\ominus \leq 1\% \leq \oplus \leq 10\% \leq \oplus$
6. Permeability--in millidarcies (1 millidarcy = 10^{-11} CM^2).
 $\ominus \leq 10^{-2} \text{ md.} \leq \oplus \leq 5.0 \leq \oplus$

AA4814

TABLE 2-5. EXAMPLES OF ROCK TYPES IN THE MECHANICAL CLASSES

Class	Typical Rock Types
Ia	Unconsolidated clays, altered tuffs
Ib	Shale, mudstone
IIa	Unconsolidated sands, gravels, volcanic ash
IIb	Weakly cemented sandstones
IIIa	Strongly cemented sandstones, welded tuffs
IIIb	Quartzite
IV	"Weathered" igneous and metamorphic rocks (adhesion weakened by chemical weathering and/or hydrothermal alterations)
V	Salt, gypsum, anhydrite
VIa	Coarse, porous limestones and marbles
VIb	Fine, compact limestones and marbles
VIIa	Phyllite, slate
VIIb	Schist, gneiss
VIIIa	Basalt, rhyolite, welded tuff, etc.
VIIIb	Granite, diorite, etc.

AA4819

scale factor is the most important. The stiffnesses and strengths of a rock mass appear to decrease as the sample volume increases. There are various reasons for this scale effect. For instances, volumes of rock involve large-scale structures of the rock, such as joints, irregularities, and rock interfaces. Also, in very large volumes of rock, body forces within the rock becomes important. Finally, as the temperature and pressure rise with increasing depth, the ductility increases and the stiffness decreases. The effect of large-scale structures on the mechanical behavior of the rock mass appears in the following discussion of constitutive relations and in situ rock mechanics.

MECHANICAL ROCK PROPERTIES AT HYDROSTATIC PRESSURE BELOW 10 KB AND STRAIN RATES BELOW 10^2 SEC^{-1}

The mechanical properties of rock most needed in ground shock calculations include rock stiffnesses, under both hydrostatic and deviatoric loading, ductility, strength, and postfailure behavior. Each of these properties depends on the texture and composition of the rock and also on the orientation, spatial distribution, areal extent, and mechanical properties of "weakness planes" in the rock mass, such as bedding planes and joints or faults. Furthermore, the mechanical properties of rock masses are functions of stress state, stress magnitude, loading path, interstitial fluid pressure, loading rate, and temperature.

The following is a summary of the pertinent mechanical properties of rock or rock masses which are known to affect ground shock calculations. The mechanical behavior of rock masses is assumed to fall into one of two broad categories:

- a. A rock mass can be treated as a continuum which is isotropic (and homogeneous) if it does not contain distinct weaknesses such as bedding planes, clay seams, joints or faults, etc. The rock mass continuum is assumed to be anisotropic in the presence of such weakness planes. In either case, the hypothesis is made that the mechanical behavior of the rock mass is controlled by average or effective mechanical properties, which might be evaluated by combining suitable experiments with field observations.
- b. The rock is a discontinuous mass whose behavior can be described in terms of the mechanical properties of blocks of competent rock and of the mechanical properties of discontinuities such as joints separating the blocks.

To perform ground shock calculations, it is assumed that a rock mass falls into the first or second category, depending primarily on whether the wave lengths of the induced stress waves are of the same order of magnitude or considerably greater than the spacings and the areal extent of the discontinuities. Although the above functional classification of rock masses considerably oversimplifies the actual problem, it is nevertheless useful for the sake of clarity in a condensed review. More detailed and probably more realistic structural classifications of rock masses may be found in the literature (Reference 2-2).

ROCK MASS CONTINUA

In the following summary of mechanical properties of several representative elastic and crystalline rock types, attention is given to rock behavior in compression, which is of primary interest in ground shock calculations. Most of the information presented pertains to the mechanical properties of competent rock. The effect of primary and secondary anisotropy is treated separately at the end of this section.

Constitutive Behavior of Competent Rock

Relatively few experiments are reported where the relationship between all the independent components of the stress and strain tensors is systematically explored. Instead, most tests only measure the principal stresses and the strain parallel to the numerically greatest principal stress. The resulting experimental data are most useful to evaluate rock ductility, yield, and failure conditions, but they are inadequate to develop constitutive laws and flow rules. The majority of tests are also limited to two stress states, where the intermediate principal stress equals the greatest or smallest principal stress, called "triaxial compression" and "triaxial extension," respectively (Reference 2-3). Almost no data exist which describes the influence of the intermediate principal stress on the stress-strain behavior of rock.

Most constitutive theories are formulated by relating stress to the volumetric and shear components of strain through the volumetric and shear stiffnesses of rock, respectively. These stiffnesses are defined as the effective bulk and shear moduli, and are determined from appropriate representations of experimental data. Bulk moduli are usually obtained from plots of mean stress versus mean strain or volumetric strain while shear moduli are obtained by comparing the maximum shear stress $1/2(\sigma_1 - \sigma_3)$ with the maximum shear strain $(\epsilon_1 - \epsilon_3)$ or by comparing the second invariant of the stress deviator tensor, J_2' , with the second invariant of the strain deviator tensor, I_2' . Both comparisons yield identical shear

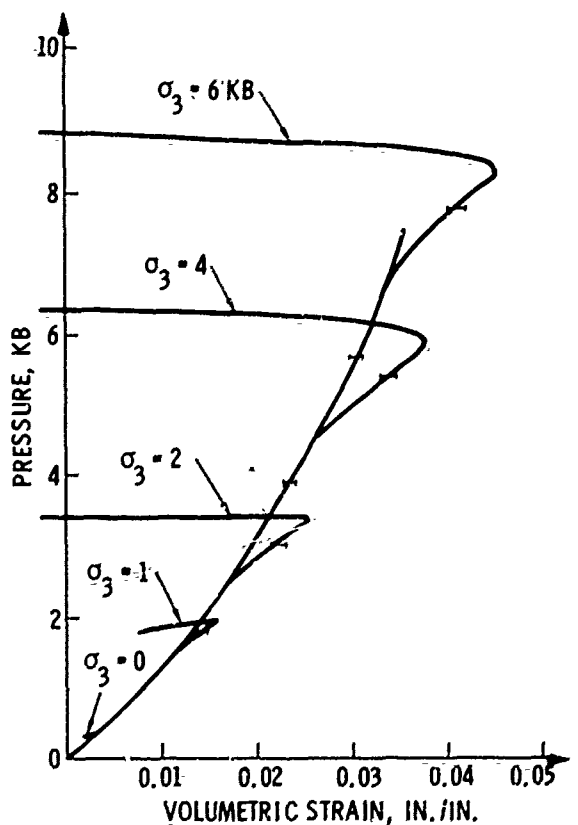
Mechanical Properties of Rock

modulus if the rock behavior is nearly linearly elastic. However, because most rocks exhibit complex nonlinear stress-strain behavior, the effective shear moduli which are determined by either method is correct only if the modulus is either independent of the magnitude of the intermediate principal stress or if the effect of the intermediate principal stress is the same as the influence of the greatest and smallest principal stresses.

Figures 2-1 through 2-7 show typical data for clastic rock (Coconino sandstone (Reference 2-4)), shale (Reference 2-5), and Nugget sandstone (Reference 2-6), limestone (Reference 2-7), marble (Reference 2-6), and granite (Reference 2-5). Generally, the stress/strain behavior is highly nonlinear. Comparison between the pressure/volumetric strain behavior under hydrostatic with that under deviatoric loading indicates strong coupling between volumetric deformation and shear stress. Dilatancy is prevalent throughout and begins at one-third to two-thirds of the maximum principal stress difference. Dilatancy is observed in brittle rocks in uniaxial compression and

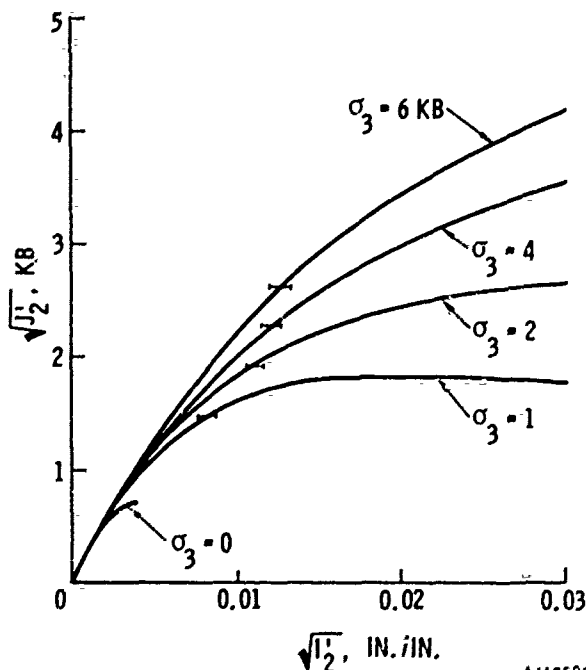
in triaxial compression at high confining pressure up to 8 kb (Reference 2-8). In some rocks having intermediate to high porosity and high grain boundary adhesion, dilatancy is preceded by distinct volumetric compaction (some shales (Reference 2-4), Solenhofen limestone (Reference 2-7)). Dilatancy is more dramatic close to maximum stress. The maximum amount of volumetric expansion is 0.2 to 2 times the volume decrease that would be observed if the rock behaved elastically (Reference 2-8). High-resolution measurements show that rock becomes rapidly stiffer as hydrostatic pressure increases due to the closing of preexisting cracks and/or collapse of pores. For stiffness at low hydrostatic pressure and a very rapid increase in stiffness with hydrostatic pressure is typical of weakly consolidated and altered rock with high initial porosity. This is illustrated in Figure 2-8, which shows the hydrostats for a dense granite (Reference 2-8) and a highly porous rhyolite (Reference 2-9). The large amount of hysteresis in rhyolite is mainly due to the breakdown of pores and permanent compaction.

Figures 2-1 to 2-6 clearly indicate that the shear stress/strain behavior of rock depends on mean stress. Rapid changes of the effective shear moduli (proportional to the slopes of the curves $(\sigma_1 - \sigma_3)/2$ versus $\epsilon_1 - \epsilon_3$ or $\sqrt{J_2}$ versus $\sqrt{I_2}$) both at low and high shear stress are typical of weakly consolidated and altered rock types.



(a) PRESSURE/VOLUMETRIC-STRAIN RELATION FOR GREEN RIVER SHALE

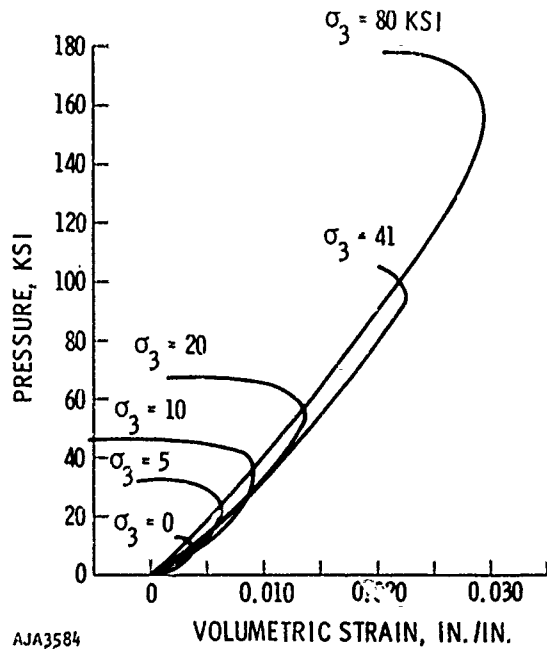
AJA3582



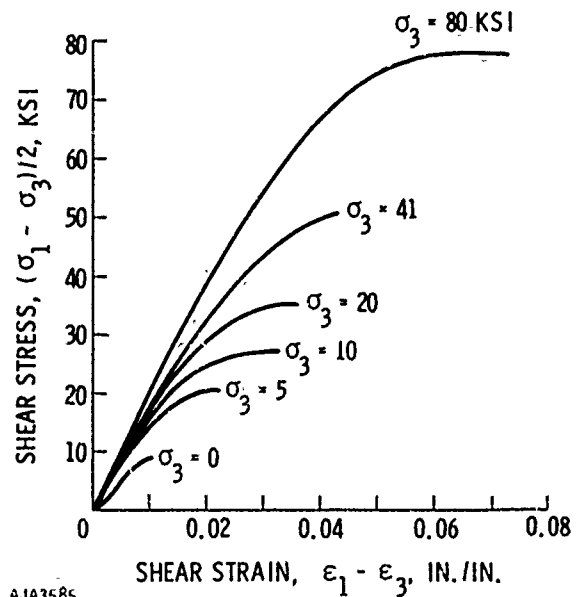
(b) DEVIATORIC STRESS/STRAIN RELATION FOR GREEN RIVER SHALE

AJA3583

FIGURE 2-1. STRESS/STRAIN RELATION FOR A SHALE (REFERENCE 2-5)



(a) PRESSURE/VOLUMETRIC-STRAIN RELATION FOR NUGGET SANDSTONE



(b) SHEAR STRESS/STRAIN RELATION FOR NUGGET SANDSTONE

FIGURE 2-2. STRESS/STRAIN RELATION FOR NUGGET SANDSTONE (REFERENCE 2-6)

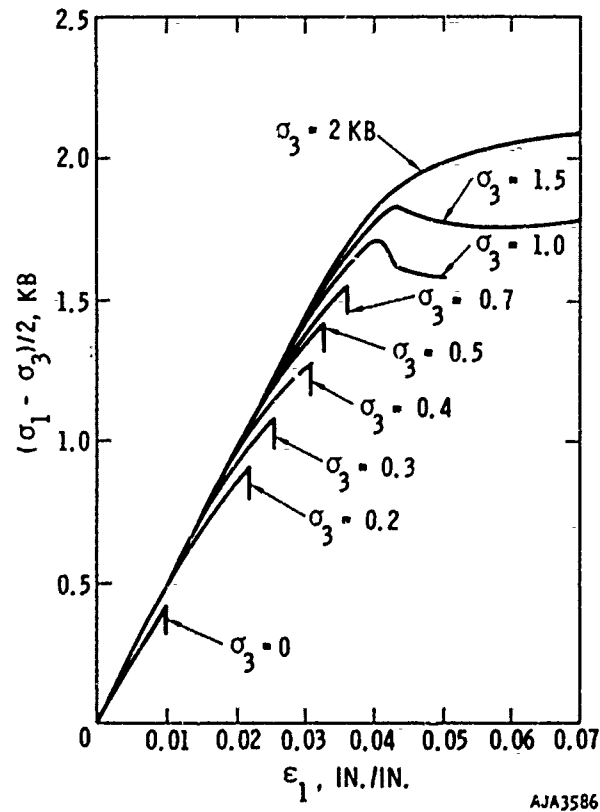
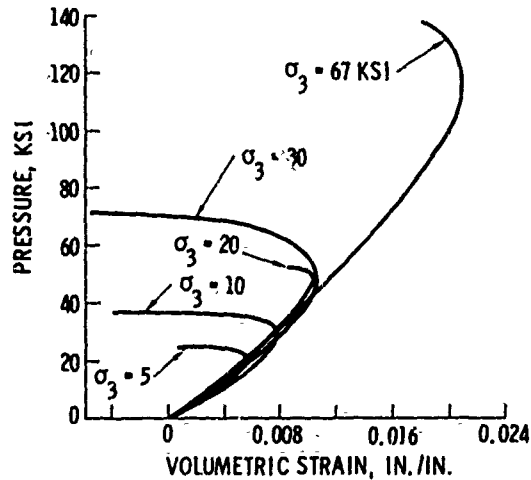
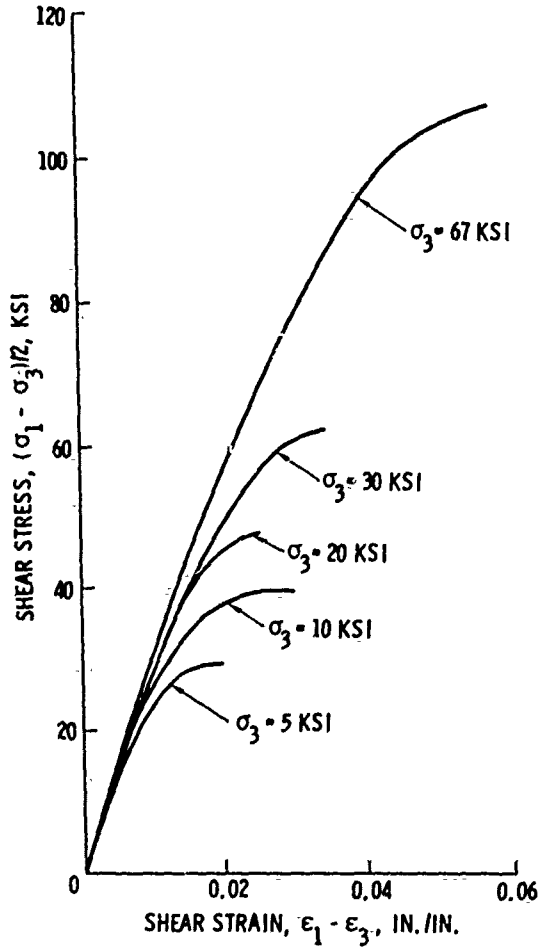


FIGURE 2-3. SHEAR STRESS/AXIAL STRAIN RELATION FOR COCONINO SANDSTONE (REFERENCE 2-4)

Mechanical Properties of Rock

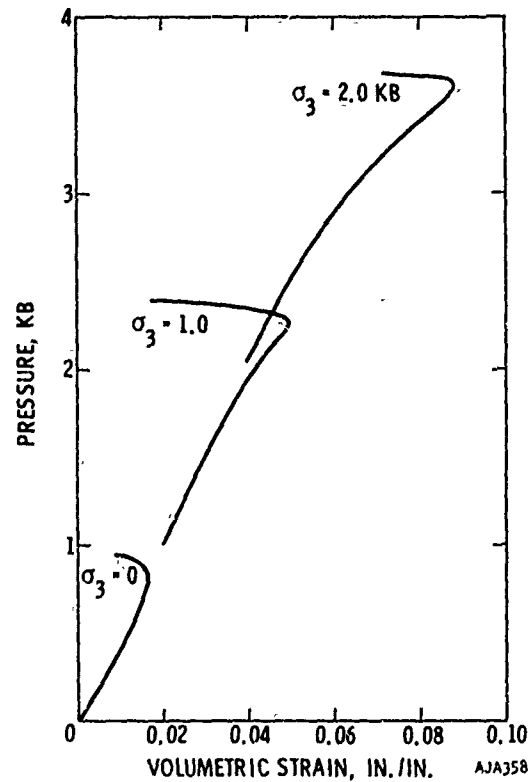


(a) PRESSURE/VOLUMETRIC-STRAIN RELATION FOR CEDAR CITY GRANITE

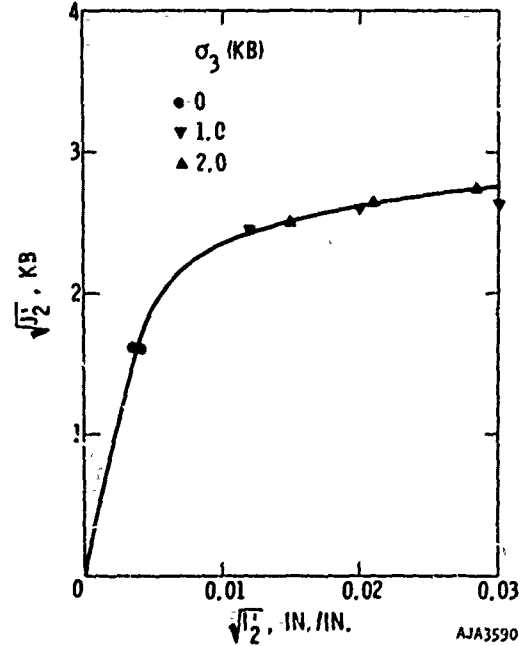


(b) SHEAR STRESS/STRAIN RELATION FOR CEDAR CITY GRANITE (REFERENCE 2-6)

FIGURE 2-4. STRESS/STRAIN RELATION FOR CEDAR CITY GRANITE (REFERENCE 2-6)

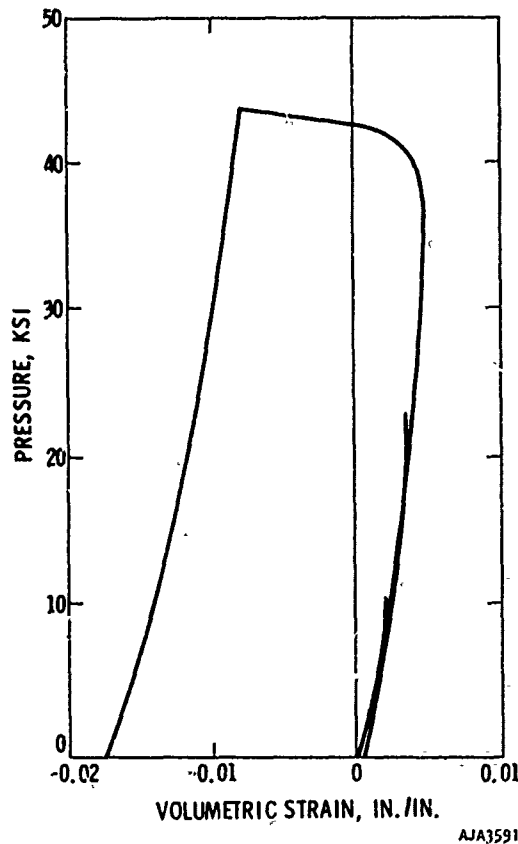


(a) PRESSURE/VOLUMETRIC-STRAIN RELATION FOR SOLENHOFEN LIMESTONE

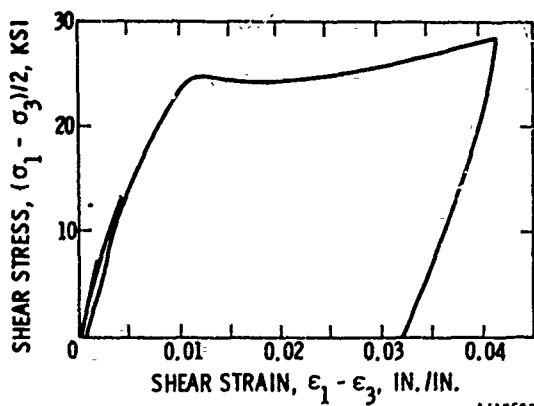


(b) DEVIATORIC STRESS/STRAIN RELATION FOR SOLENHOFEN LIMESTONE

FIGURE 2-5. STRESS/STRAIN RELATION FOR SOLENHOFEN LIMESTONE (REFERENCE 2-7)

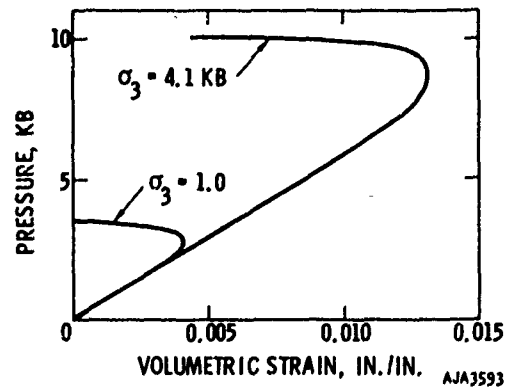


(a) PRESSURE/VOLUMETRIC-STRAIN RELATION FOR MARBLE

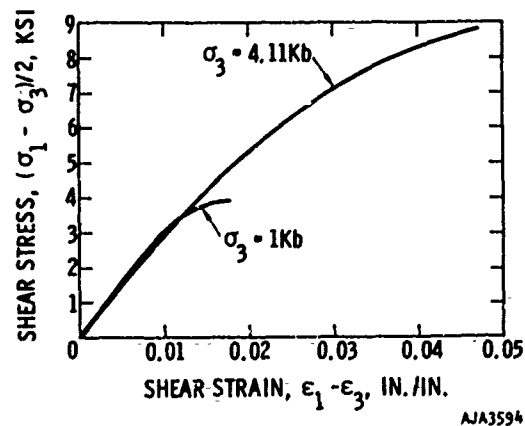


(b) SHEAR STRESS/STRAIN RELATION FOR MARBLE

FIGURE 2-6. STRESS/STRAIN RELATION FOR MARBLE SUBJECTED TO PROPORTIONAL LOADING ($\sigma_3/\sigma_1 = 0.338$) (REFERENCE 2-6)



(a) PRESSURE/VOLUMETRIC-STRAIN RELATION FOR GRANITE



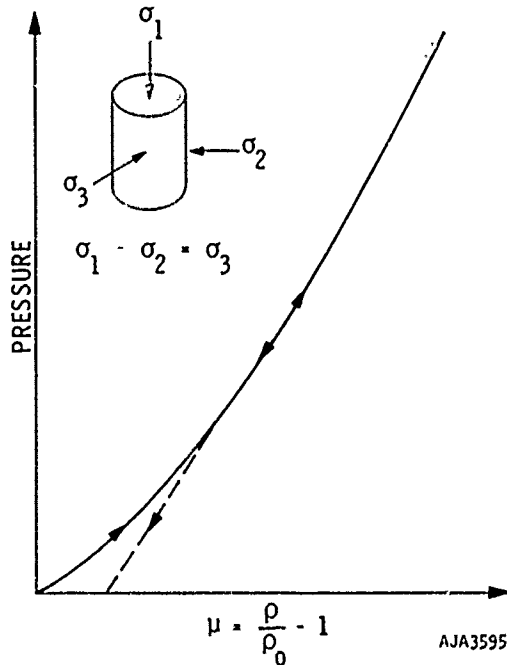
(b) SHEAR STRESS/STRAIN RELATION FOR GRANITE

FIGURE 2-7. STRESS/STRAIN RELATION FOR GRANITE (REFERENCE 2-8)

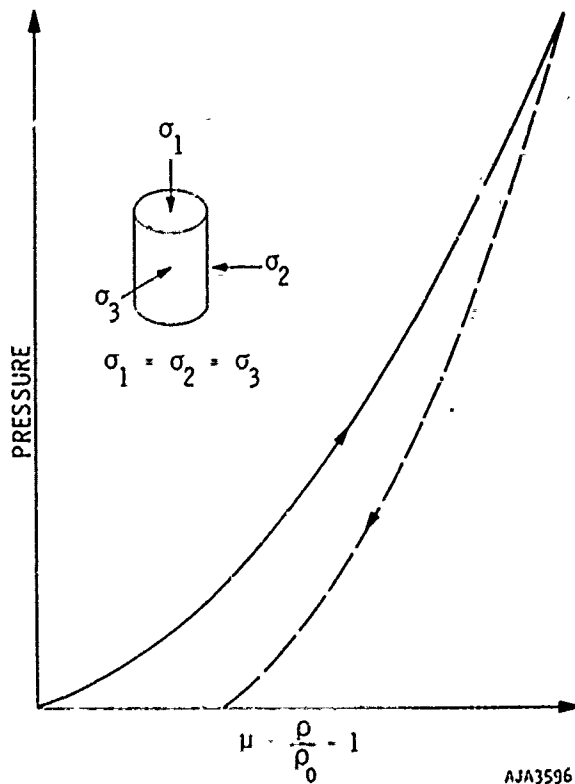
Several biaxial and multiaxial compression experiments suggest that the intermediate principal stress affects behavior less than does the smallest principal stress (References 2-10 to 2-15). The effect of the intermediate principal stress is demonstrated in Figures 2-9 and 2-10, which show data for Westerly granite (Reference 2-10, 2-15) and Dunham dolomite (Reference 2-11) subjected to biaxial and multiaxial compression, respectively. Increasing the intermediate principal stress appears to considerably lower the dilatancy and the shear strain at failure.

Little is known about the relationship between stress/strain behavior, loading history, and loading path. At high stress levels, loading history is probably important because of deformation-induced anisotropy (Reference 2-16). Loading history also determines the stress/strain behavior of rock during unloading. Stress path appears to have little influence

Mechanical Properties of Rock



(a) WESTERLY GRANITE (REFERENCE 2-7)



(b) JORUM RHYOLITE (REFERENCE 2-8)

FIGURE 2-8. HYDROSTATIC LOADING AND UNLOADING FOR TWO ROCKS

- (a) $\sigma_2 = \sigma_3 = 29$ KSI
 - (b) $\sigma_1 / \sigma_2 = 2$; $\sigma_3 = 0$
 - (c) $\sigma_2 = \sigma_3 = 5.08$ KSI
 - (d) $\sigma_2 = \sigma_3 = 0$
 - (e) 6.06, KSI
 - (f) 4, KSI
 - (g) 2, KSI
 - (h) 0.7, KSI
 - (i) 0, KSI
- } = σ_2 ; $\sigma_3 = 0$

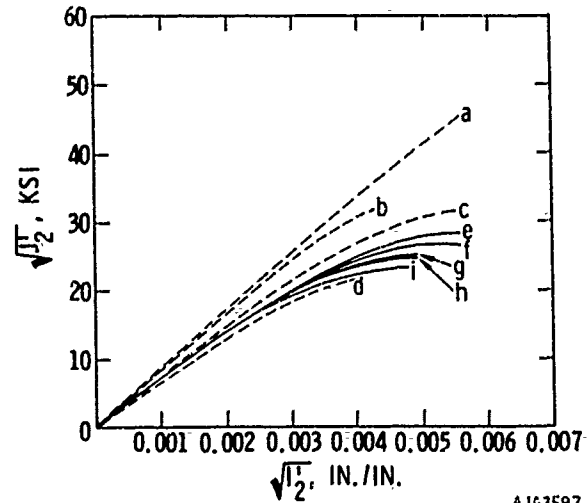


FIGURE 2-9. BIAxIAL STRESS/STRAIN RELATION FOR WESTERLY GRANITE (REFERENCE 2-15)

DUNHAM DOLOMITE: $\sigma_1 > \sigma_2 > \sigma_3 (=1.25 \text{ KB})$

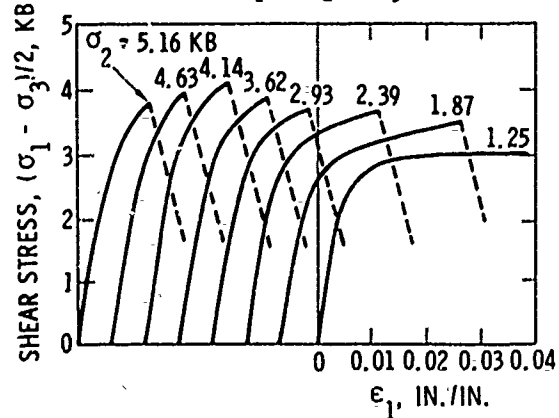


FIGURE 2-10. STRESS/STRAIN RELATION FOR DUNHAM DOLOMITE UNDER CONSTANT $\sigma_3 (=1.25 \text{ KB})$ AND σ_2 (REFERENCE 2-11)

on the constitutive behavior in triaxial compression ($\sigma_1 > \sigma_2 = \sigma_3$) but may be significant in multiaxial compression ($\sigma_1 \neq \sigma_2 \neq \sigma_3$) (Reference 2-17).

The constitutive behavior of all rocks tested to date depends on interstitial pore pressure, temperature, and strain rate, as shown in Figures 2-11 to 2-13 (References 2-19 to 2-24, 2-17). At low strain rate, an increase in pore pressure reduces the effective confining pressure. Except for chemical changes which are often negligible, this behavior can usually be completely reconciled with that of dry specimens if stress is described in terms of effective stress, which is the externally applied stress minus the pore pressure (Reference 2-19). The effective stress prevails throughout the solid framework of the rock. At higher strain rates ($>10^{-6}$ to 10^{-4} sec^{-1}) the mean stress in any grain exceeds the effective mean stress due to dilatancy hardening (Reference 2-19).

At elevated temperatures the behavior of rock is more nonlinear and the effective bulk and shear moduli are lower at all stress levels (References 2-20 to 2-22). The influence of strain rate on the constitutive behavior of rock is as yet poorly understood. However, measurements on granite at strain rates up to 10^2 sec^{-1} and up to 1 kb hydrostatic pressure indicate that effective moduli and the strains at fracture increase by no more than approximately 10 to 20 percent compared with quasistatically determined values (Reference 2-17).

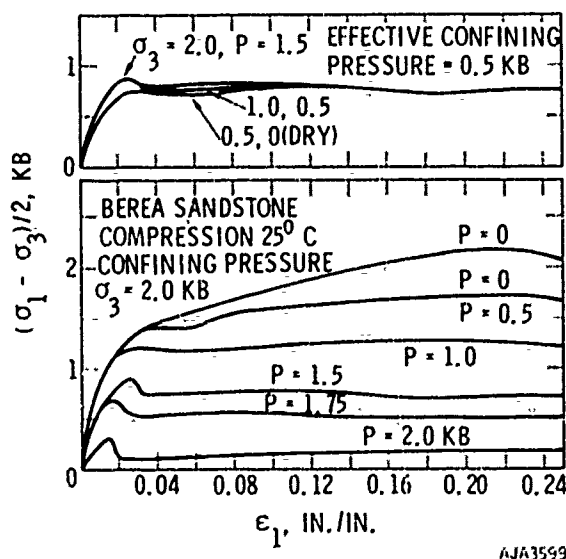


FIGURE 2-11. SHEAR STRESS/AXIAL STRAIN RELATION FOR BEREA SANDSTONE AT DIFFERENT LEVELS OF TOTAL CONFINING PRESSURE AND PORE FLUID PRESSURE (REFERENCE 2-18)

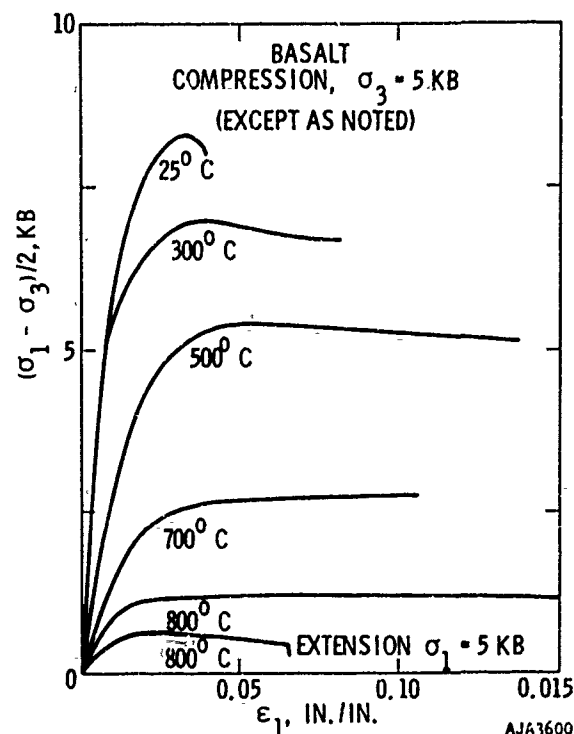


FIGURE 2-12. STRESS/STRAIN RELATION FOR A BASALT AT DIFFERENT TEMPERATURES (REFERENCE 2-20)

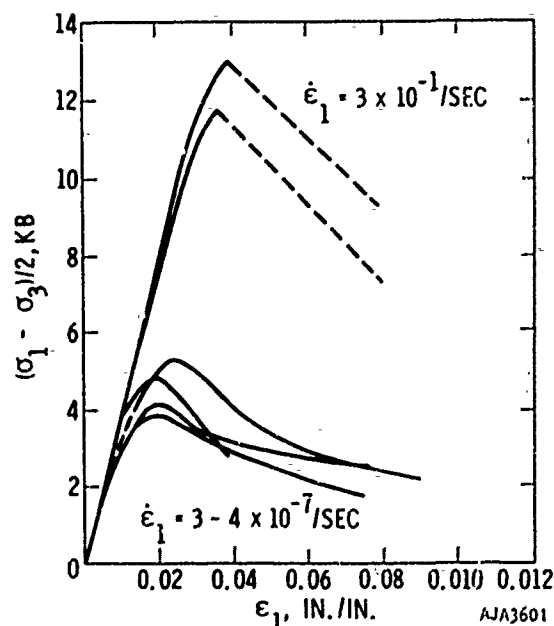


FIGURE 2-13. STRESS/STRAIN RELATION FOR EUREKA QUARTZITE UNDER CONFINEMENT OF $\sigma_3 = 5 \text{ KB}$ AT 500°C AND SUBJECTED TO DIFFERENT STRAIN RATES (REFERENCE 2-21)

Mechanical Properties of Rock

Yield Stress and Ductility

Yield strength is commonly defined as the stress or stress difference at which plots of σ_1 or $\sigma_1 - \sigma_3$ versus ϵ_1 depart significantly from linearity (Figures 2-1 and 2-6). Sometimes yielding is defined as the stress which produces a predetermined amount of strain, say 2 to 5 percent (References 2-11, 2-25). The latter definition of yield strength is ambiguous unless it is normalized, for example, with respect to an elastic modulus of the rock. There appear to be several alternatives to specifying yielding of rock. Yield stress might describe the onset of dilatancy or that stress at which a prescribed amount of energy is dissipated which is measured by hysteresis in stress/strain relations. The possibility of multiple definitions of yield stress indicates that yield stress is difficult to ascertain reliably. The definition of yield stress which is related to percent permanent strain upon load removal is not useful here. Because of a peculiar, highly nonlinear unloading behavior of most rocks, permanent strain is often a poor measure of the maximum deformation that is reached prior to unloading. Similar difficulties arise in defining ductility (Reference 2-11, 2-25). The term is almost always used in a qualitative sense to indicate the strain prior to failure. Figure 2-14 shows "ductility" data for a variety of rock types (Reference 2-16). Yield strength and ductility generally increase rapidly with increasing hydrostatic pressure. Above a certain threshold value of hydrostatic confinement, the yield stress of some rocks appears to depend much less on confinement. From what is now known, however, such behavior is more an exception rather than a rule.

The relationship between yield strength and ductility on one hand and magnitude of the intermediate principal stress on the other has only recently been explored (Reference 2-11). The experimental evidence indicates that ductility is substantially lowered with increasing magnitude of the intermediate principal stress. Both yield stress and rock ductility depend strongly on temperature and strain rate (References 2-21, 2-24); yield stress decreases and ductility increases at elevated temperature and/or at low strain rate.

Ultimate Strength

Ultimate strength is used here to denote the maximum stress difference or deviatoric stress which rock can sustain (Reference 2-25). Ultimate strength of several types of rocks are shown in Figure 2-15 (Reference 2-26). Clearly, the strength of rock increases rapidly with increasing hydrostatic pressure. It is important to recognize that the actual relationship between strength and confining pressure (Reference 2-27) is generally not the same as the relationship between yield stress and pressure. Figure 2-15 should

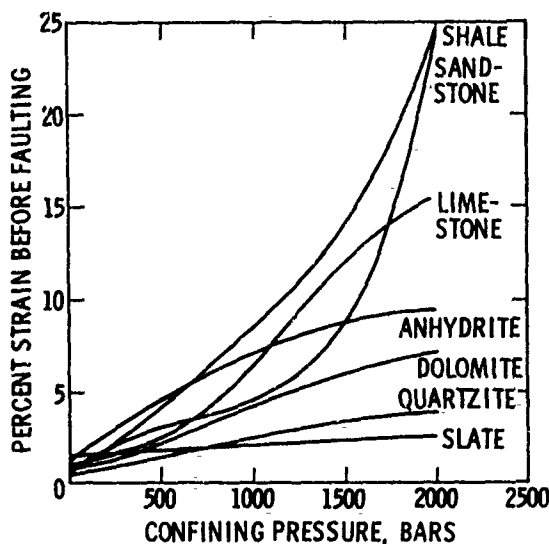


FIGURE 2-14. DUCTILITY OF SEVERAL COMMON ROCKS VARIES WITH CONFINING PRESSURE (REFERENCE 2-16)

- TYPE OF ROCK
- 1 POROUS SILICATE ROCKS
 - 2 NONPOROUS GRANITE
 - 3 NONPOROUS PERIDOTITE
 - 4 QUARTZITE
 - 5 MARBLE
 - 6 LIMESTONE
 - 7 DOLOMITE

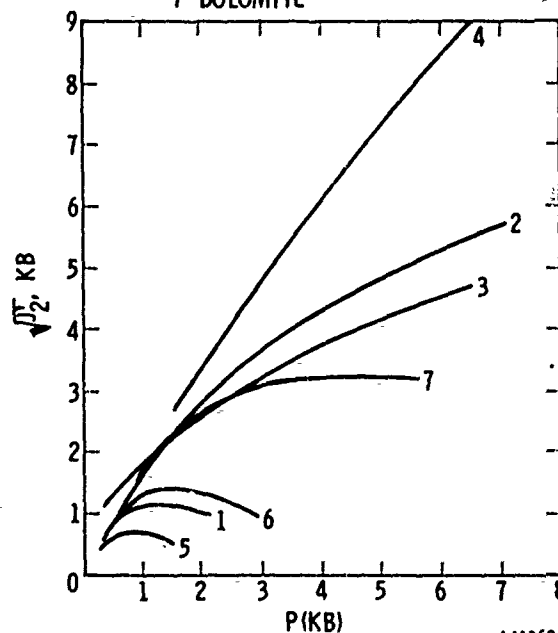


FIGURE 2-15. AVERAGE STRENGTH-PRESSURE CURVES OF DIFFERENT ROCK TYPES (REFERENCE 2-26)

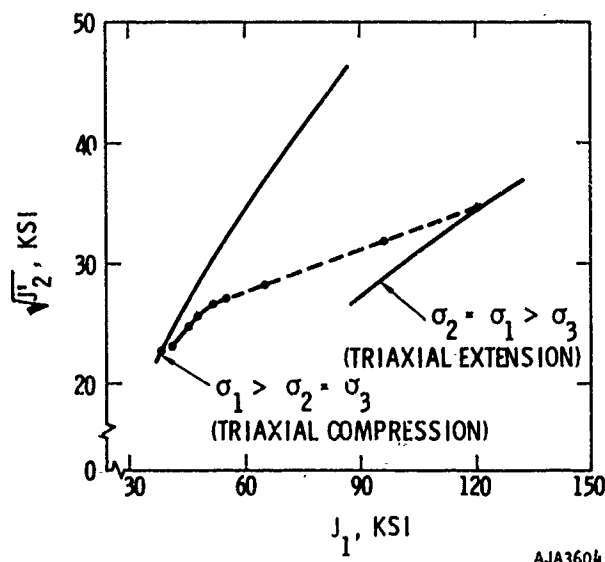


FIGURE 2-16. STRENGTH OF WESTERLY GRANITE UNDER TRIAXIAL COMPRESSION, TRIAXIAL EXTENSION AND INTERMEDIATE STRESS STATES (REFERENCES 2-7, -10, -15)

not be interpreted to indicate that the strength of rock is solely a function of hydrostatic pressure. Several studies indicate that strength also depends on the intermediate principal stress, σ_2 , as shown in Figures 2-10, 2-16, and 2-17 (References 2-10 to 2-15). Comparison of the strengths of granite in biaxial compression and in triaxial compression and extension ($\sigma_1 > \sigma_2, \sigma_3 = 0$; $\sigma_1 > \sigma_2 = \sigma_3$; $\sigma_1 = \sigma_2 > \sigma_3$) show that the strength of rock subjected to constant σ_3 increases with the magnitude of the intermediate principal stress. A recent analysis suggests that this increase is most pronounced in biaxial compression (Reference 2-17). If the influence of the intermediate principal stress is neglected, that is, if strength is expressed only as a function of hydrostatic component of stress, then the predicted strength will always be less than the actual strength. It is noteworthy that increasing the intermediate principal stress makes rock more brittle in that it increases the strength and decreases rock ductility (Reference 2-11).

The effect of loading history on the strength of rock depends primarily on the extent of previous deformation-induced anisotropy. It may sometimes be considerable as is shown in the discussion of anisotropy. The influence of stress path on the strength of virgin, isotropic samples was recently found to be negligible (Reference 2-28). This important result is demonstrated by the data in Figure 2-18 which define the failure locus of a granite for three different stress paths.

Figures 2-11, 2-19, 2-20, and 2-21 provide evidence for the influence of interstitial fluid pressure, strain rate and temperature on the ultimate stress (References 2-17, 2-19 to 2-24, and 2-29). At low strain rates the strength is completely characterized by effective stresses. At strain rates greater than approximately 10^{-6} to 10^{-4} sec^{-1} the strength increases due to dilatancy hardening (Figure 2-20) (Reference 2-19). In dry rocks, moderate strain rates (less than 10^2 sec^{-1}) produce a relatively small increase in strength (Figure 2-21) (Reference 2-17). At moderate strain rates, strength is most influenced by temperature. For example, the strength of basalt in Figure 2-12 decreased by more than one order of magnitude as the temperature was raised from 20° to 800°C (Reference 2-20).

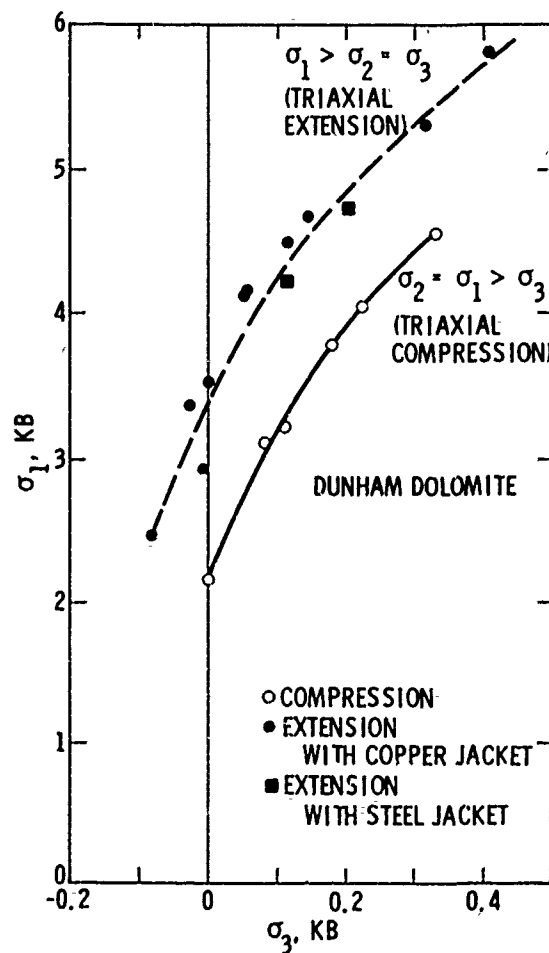


FIGURE 2-17. STRENGTH OF DUNHAM DOLOMITE UNDER TRIAXIAL COMPRESSION AND TRIAXIAL EXTENSION STRESS STATES (REFERENCE 2-10)

Mechanical Properties of Rock

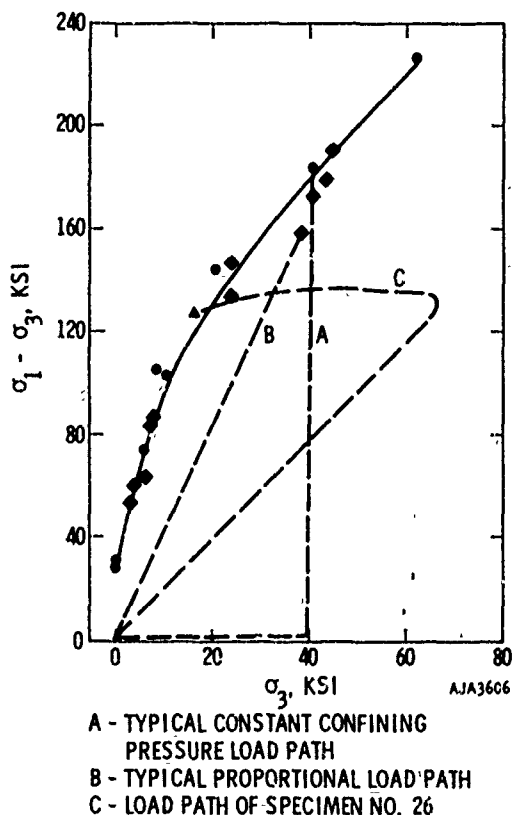


FIGURE 2-18. STRENGTH OF WESTERLY GRANITE UNDER DIFFERENT LOADING PATHS (REFERENCE 2-28)

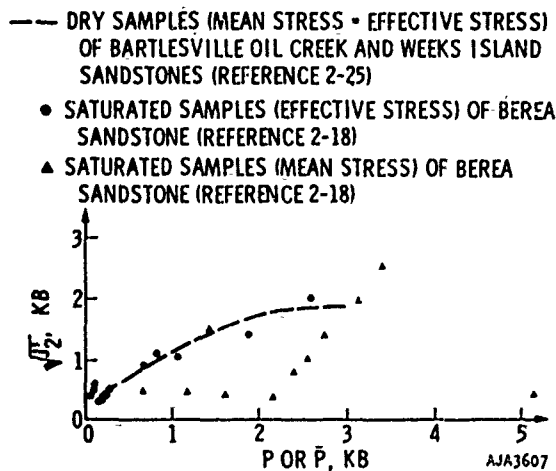


FIGURE 2-19. EFFECT OF PORE PRESSURE ON STATES OF STRESS AT FRACTURE, EFFECTIVE CONFINING STRESS APPEARS TO GOVERN STRENGTH OF SANDSTONE

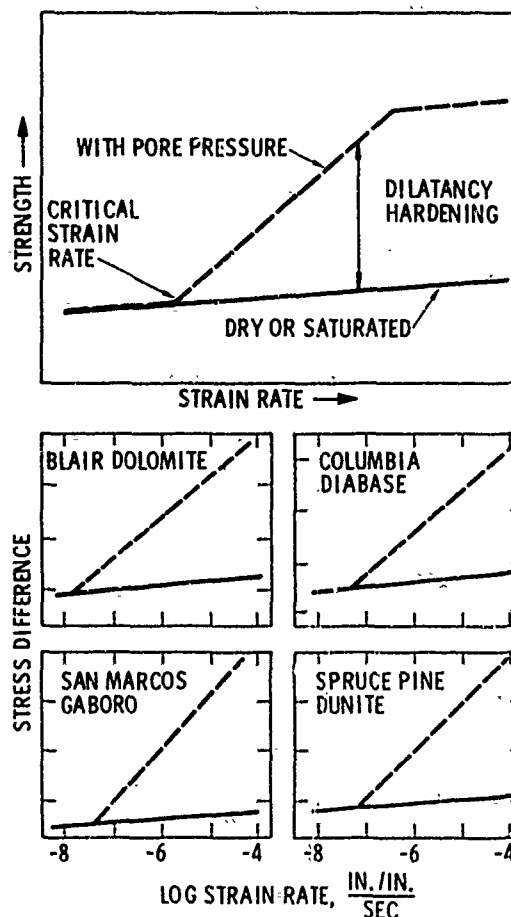


FIGURE 2-20. DILATANCY HARDENING FOR A TYPICAL ROCK AND FOR SPECIFIC ROCKS (REFERENCE 2-20)

Postfailure Behavior and Brittle-Ductile Transition

The postfailure behavior of rock characterizes the relationship between rock strength and strain once the ultimate stress is exceeded. Postfailure measurements have been made recently at fixed values of hydrostatic pressure. These tests suggest that the behavior of rocks past the peak load-bearing ability may be divided into two classes (Reference 2-30, 2-31). Class I designates a stable kind of behavior in the sense that external work must be done on the rock by the testing machine to reduce its load-bearing ability. The stress/strain relations in the postfailure region have a negative slope (Figure 2-22) (References 2-30, 2-32). In turn, Class II behavior is unstable in the sense that the elastic strain energy stored in the rock at the ultimate stress is greater than the energy stored in the rock, and the ultimate stress is greater than the energy needed to reduce its load-bearing capacity to zero (uniaxial and biaxial compression) or

- (a) 250, QUARTZITE, 8 KB, 900°
- (b) 5, MARBLE, 5 KB
- (c) 18, SOLENHOFEN, 1%
- (d) 15, SANDSTONE, 0.7 KB
- (e) 42, MARBLE, 5 KB, 500°
- (f) 10, WESTERLY GRANITE, 1.5 KB
- (g) 11, DIABASE, 1.5 KB
- (h) 18, DIORITE, 0.7 KB
- (i) 18, TUFF
- (j) 5, SOLENHOFEN, 0.7 KB
- (k) 14, GRANITE
- (l) 13, BASALT
- (m) 17, WESTERLY GRANITE
- (n) 15, TONALITE

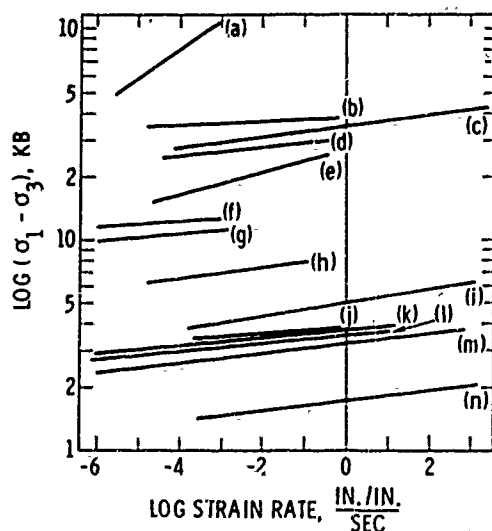


FIGURE 2-21. VARIATION OF STRENGTH WITH STRAIN RATE AT ROOM TEMPERATURE AND PRESSURE EXCEPT WHERE NOTED. NUMBERS AT THE LEFT OF EACH LINE INDICATE THE SLOPE OF THAT LINE (REFERENCE 2-29)

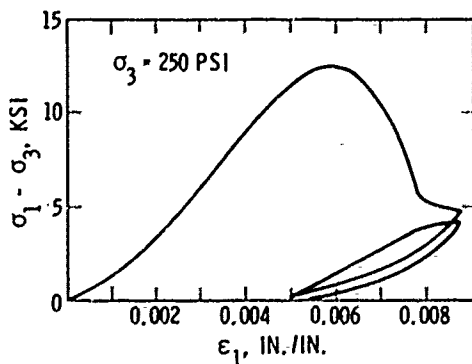


FIGURE 2-22. DIFFERENTIAL-STRESS/AXIAL-STRAIN RELATION FOR SANDSTONE. POSTFRACTURE BEHAVIOR (REFERENCE 2-32)

to some residual strength value (triaxial and multi-axial compression) which appears to be determined by the frictional resistance along fracture planes. Class II postfailure behavior is characterized by a postfailure curve of positive slope (Figure 2-23). Unstable (Class II) rock failure is associated with the release of elastic energy which may trigger failure in surrounding, yet unbroken, regions of a rock mass.

These two possible classes of failure modes are distinguishable only if special testing techniques are used. In most cases, postfailure events are observed as stick-slip, which is unstable motion along fracture surfaces in the stress regime between the ultimate strength and the residual strength (Figure 2-24) (References 2-3, 2-33 to 2-35). Some studies suggest that the first slip cycle may include the formation of faults as well as subsequent motion along fresh fracture planes (Reference 2-31). The magnitude of the unstable displacement along fracture surfaces during stick-slip and also the apparent residual strength depend on the amount of elastic strain energy which is released by the rock and on the amount of elastic strain energy which is released by the testing machine.

Postfailure and stick-slip behavior of rock depend on the coefficient of friction along the fracture surfaces, pore pressure, and temperature. Stick-slip vanishes once the frictional resistance along incipient fracture planes equals or exceeds the strength of the intact rock.

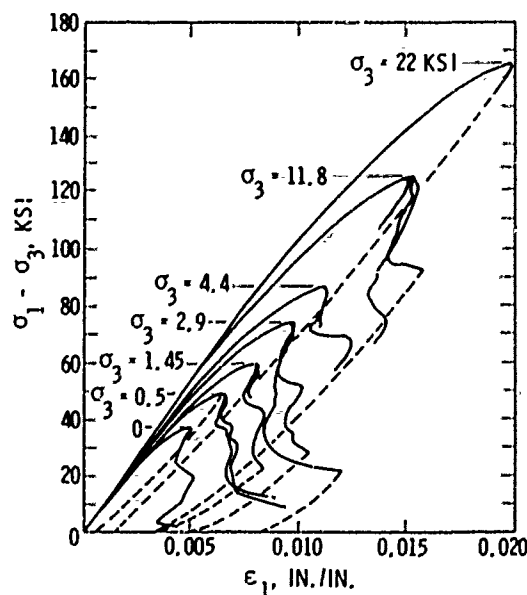


FIGURE 2-23. STRESS/STRAIN RELATION FOR WESTERLY GRANITE, INCLUDING POSTFAILURE RANGE (REFERENCE 2-31)

Mechanical Properties of Rock

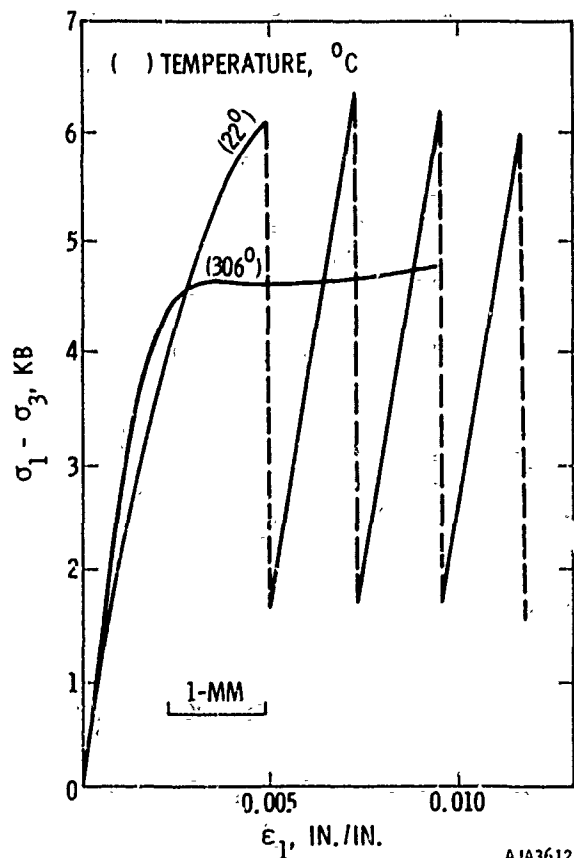


FIGURE 2-24. SLIDING ON SAWCUTS IN GRANITE, AT A CONFINING PRESSURE OF 2.1 KB. DOTTED PARTS OF THE CURVE AT 22° ARE SUDDEN STRESS DROPS. ACTUAL DISPLACEMENT ALONG THE SAWCUT DURING SLIDING IS INDICATED BY THE 1-MM BAR LINE (REFERENCE 2-37)

When the frictional resistance just equals the strength, the rock is said to have reached the brittle-ductile transition (Reference 2-36) and "failure" no longer causes stress to drop (Figure 2-25). Frictional resistance on fracture surfaces in rock is controlled by the coefficient of friction, stress state, pore pressure, and temperature. Presently, the coefficient of friction appears to be primarily a function of surface roughness and fault gouge. The effects of rock texture and mineralogy are currently explored in several investigations. Typical values for the coefficient of friction range from 0.5 to 0.85. By and large the friction coefficient decreases with increasing displacement because the sliding surfaces become smoother and fault gouge develops. When the friction coefficient is approximately independent of rock mineralogy, frictional resistance is determined mainly by the stress state and does not vary greatly with rock type

provided that the surface roughnesses considered are equivalent (Reference 2-35). In such cases, therefore, the brittle-ductile transition is governed by the variation of the ultimate strength with the magnitude of the hydrostatic pressure and intermediate principal stress. The brittle-ductile transition occurs at high stress if the ultimate stress increases rapidly with hydrostatic pressure (Figure 2-15).

If pore pressure is present at low strain rates, the brittle-ductile transition appears to be governed by the magnitudes of the effective stresses. At high values of pore pressure, stick-slip behavior apparently becomes more stable (Reference 2-19). Stick-slip becomes also more stable or vanishes at elevated temperatures (Reference 2-37). An example of this effect is given in Figure 2-24 for Westerly granite subjected to triaxial compression. This behavior is consistent with the known influence of temperature on the strength. Precise analyses of this phenomenon will require measurements of the frictional properties of rock surfaces at different temperatures.

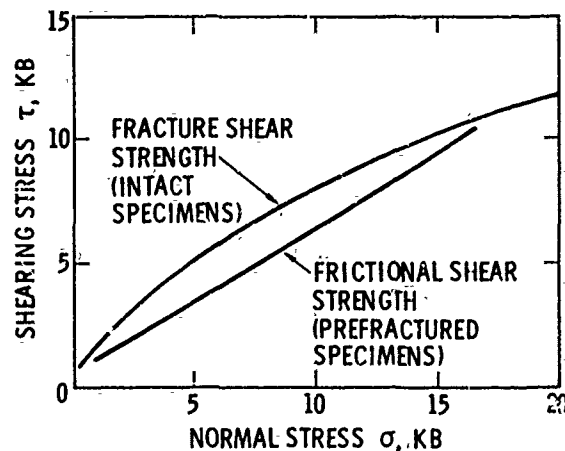


FIGURE 2-25. THE EFFECT OF NORMAL STRESS ON THE SHEAR STRESS AT FRACTURE AND ON THE FRICTIONAL SHEAR STRENGTH OF WESTERLY GRANITE (REFERENCE 2-34)

Deformation and Failure Mechanism

Observations of the mechanisms of rock deformation and failure have materially aided the interpretation and generalization of experimentally determined rock properties (Reference 2-38). Rock deformation and failure in compression are principally controlled by (1) closing of preexisting cracks, (2) deformation and collapse of pore spaces, (3) sliding along preexisting crack surfaces and growth of preexisting cracks,

(4) deformation, flow and failure along grain boundaries, (5) deformation, flow and failure of grain, and (6) recrystallization at high temperature.

Here flow denotes deformation which does not produce volume changes, and occurs by intragranular twin and translation gliding. "Failure" along grain boundaries and through grains refers to the local formation of cracks varying between one-half and five-grain diameters in length.

Deformation and failure mechanisms have been determined directly in microscopic studies or indirectly from measurements of hysteresis (References 2-6, 2-8), microseismic activity (Reference 2-39), resistivity (Reference 2-40), and dilatational and shear velocities (Reference 2-41). The number of mechanisms which may be active throughout the loading history of a particular rock depends on the rock type. Crack closure and pore collapse are mainly responsible for the sensitivity of bulk and shear moduli to hydrostatic pressure in porous and weakly consolidated materials. Intergranular and transgranular cracks appear to be typical in almost all rock types tested to date and are responsible for the observed volume increase (dilatancy) of rock subjected to deviatoric loading. Inter- and intragranular crack development seem to occur along preferred orientations. Below approximately 0.5 kb hydrostatic pressure cracks are generally aligned parallel to the greatest compressive stress. At high hydrostatic pressure cracks tend to be oriented at angles between 20 and 40 deg with respect to the maximum compression. Inter- and intragranular failure produces microseismic activity and changes in resistivity. Figure 2-26 illustrates the correlation between crack formation, microseismic activity and resistivity (References 2-40, 2-41). The development of cracks also explains the phenomenon of dilatancy hardening at elevated pore pressure and strain rates greater than approximately 10^{-6} to 10^{-4} sec^{-1} (Reference 2-19). Unless the rock permeability is high, voids are created at a rate which exceeds the flow-rate of the interstitial fluid. Consequently, the "average" pore pressure decreases with increasing dilatancy and the mean stress in the solid framework of the rock becomes greater. Therefore, the actual hydrostatic pressure increases, and the ultimate strength is raised.

Crack closure, pore collapse, crack formation and preferred crack orientation can also be inferred from measurements of the dilatational and shear wave velocities, particularly in dry rock (Reference 2-41). Because cracks and pores constitute obstacles in the path of a stress wave, both dilatational and shear wave velocities increase as they are removed by increasing hydrostatic pressure. On the other hand, the wave velocities decrease if cracks and pores develop during deviatoric loading. The influence of cracks and pores on the wave velocities in rock is illustrated in Figures 2-27 to 2-29 as a function of hydrostatic pressure and

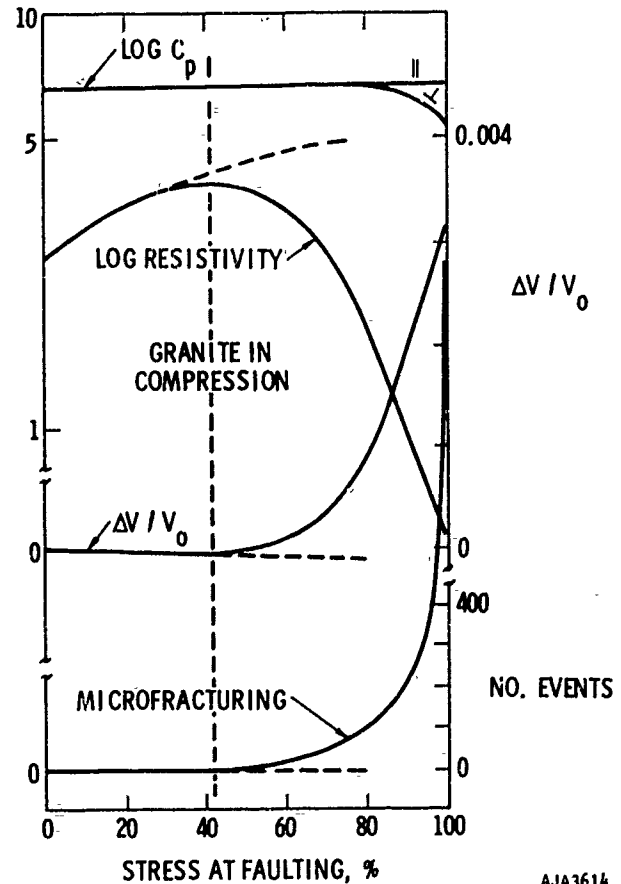


FIGURE 2-26. RELATION AMONG STRESS LEVEL, MICROFRACTURING ACTIVITY, RESISTIVITY, VOLUMETRIC STRAIN, AND DILATATIONAL WAVE SPEED (REFERENCES 2-8, -39, -40)

orientation relative to the direction of greatest compression. The latter is the direction in which cracks are most effectively closed.

If the stress/strain relation has a distinct peak, macroscopic rock failure usually takes place by conjugate faulting (References 2-25, 2-42). In most cases the fault angles are inclined at approximately 30 deg to the direction of greatest compression. In some rocks, particularly in marbles, close to the brittle-ductile transition, fault angles appear to be closer to 40 deg. Fracture by faulting occurs approximately in the plane of the greatest and least compression. Effects of the intermediate principal stress have been reported (Reference 2-10). Rock fracture tends to occur in a cleavage mode in triaxial extension ($\sigma_1 = \sigma_2 > \sigma_3$) when the smallest principal stress is close to zero or tensile (Reference 2-42). Cleavage fractures are nearly parallel to the plane of the greatest and intermediate principal (compressive) stresses.

Mechanical Properties of Rock

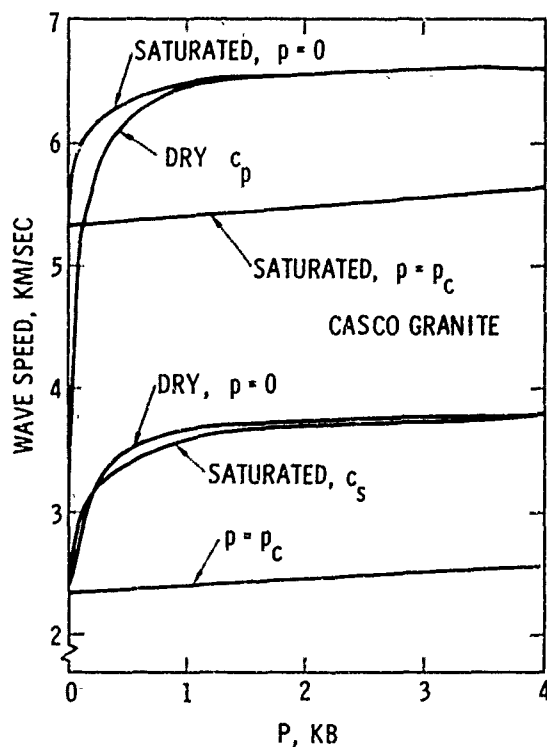


FIGURE 2-27. EFFECT OF FLUID PORE PRESSURE ON WAVE SPEEDS

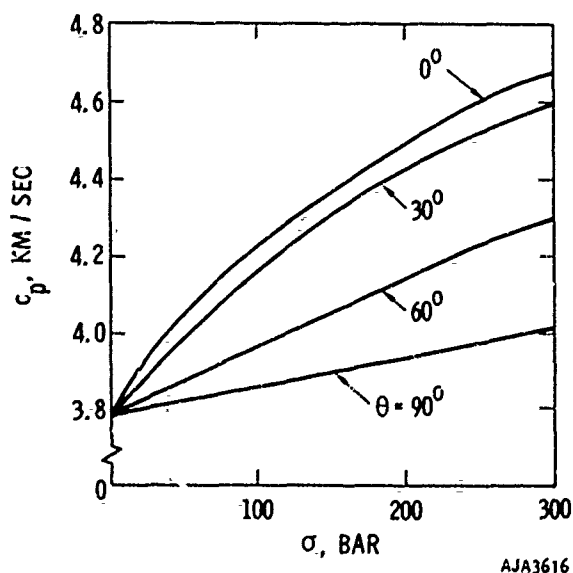


FIGURE 2-28. VELOCITY OF DILATATIONAL WAVES DEPEND ON DIRECTION OF PROPAGATION RELATIVE TO DIRECTION OF JOINTS AND STRESS ACROSS JOINTS (REFERENCE 2-41)

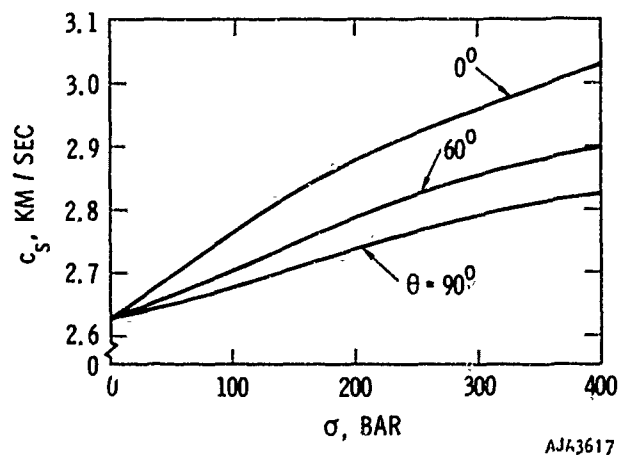


FIGURE 2-29. VELOCITY OF SHEAR WAVES DEPENDS ON DIRECTION OF PROPAGATION RELATIVE TO DIRECTION OF JOINTS AND STRESS ACROSS JOINTS (REFERENCE 2-41)

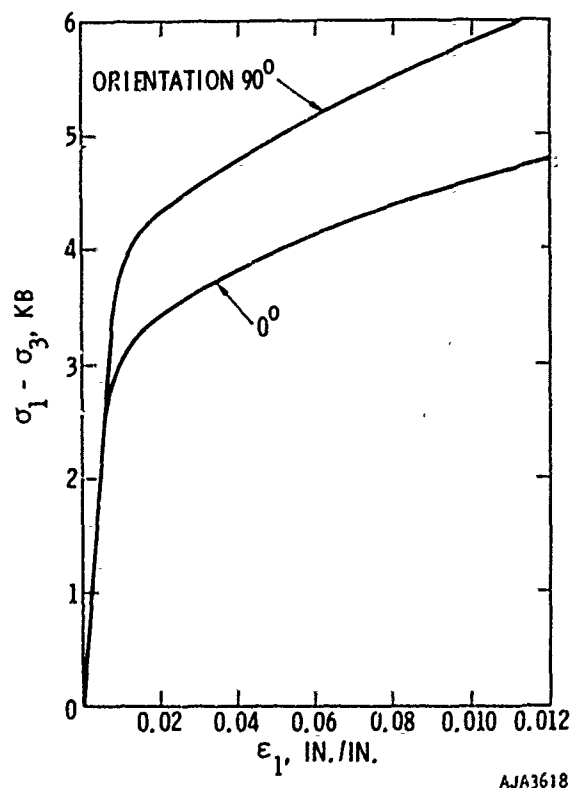


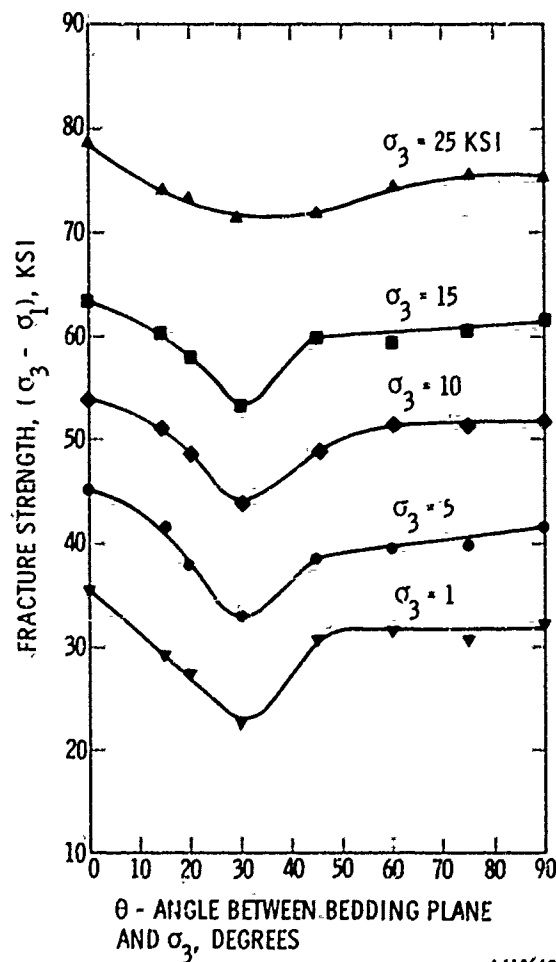
FIGURE 2-30. STRENGTH OF BELDENS MARBLE UNDER 2 KB CONFINING STRESS DEPENDS ON ORIENTATION OF CLEAVAGE PLANES RELATIVE TO MAJOR PRINCIPAL STRESS (REFERENCE 2-16)

Effects of Anisotropy

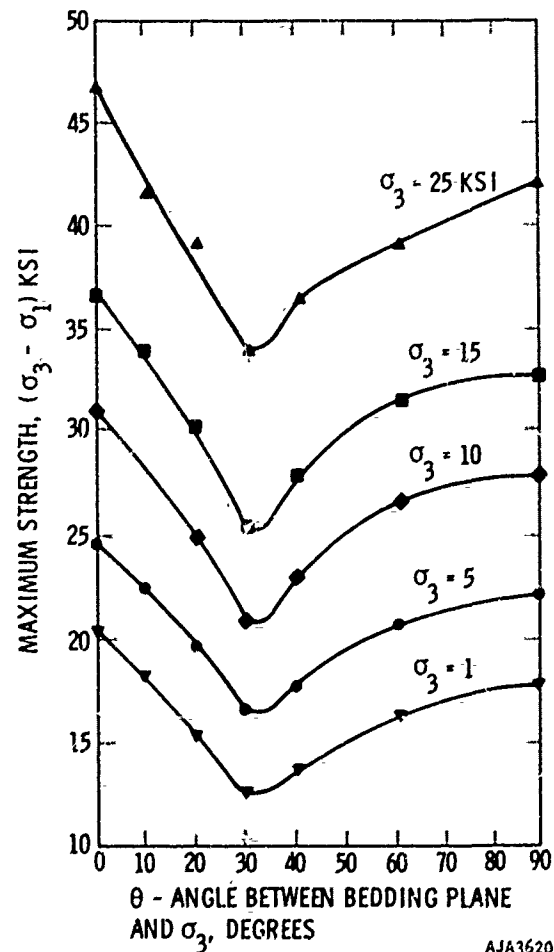
Rock may exhibit primary and secondary anisotropy. Primary anisotropy is determined by textural features such as bedding or layering of clay minerals. Secondary anisotropy is the result of tectonic loading which may have induced preferred crack patterns, preferred grain orientation or failure along joints and faults, etc. Rock masses in situ generally contain features of secondary anisotropy.

Anisotropy of any kind makes all mechanical rock properties directionally dependent (Reference 2-43 to 2-46). The effects of primary anisotropy are clearly demonstrated in Figures 2-30 to 2-32 in which directional stress/strain behavior, elastic constants and ultimate stress of two rock types are compared. The consequences of secondary anisotropy due to joint

and fault systems are generally severe at low hydrostatic stress and apparently small at high hydrostatic pressure. Figures 2-33 and 2-34 give some indication of the influence of "joints" which was studied in biaxial and triaxial compression on model materials. Clearly the strength and the stress/strain behavior strongly depend on the joint orientation and on the difference between joint strengths and the strengths of the solid parts of the model materials. At high confining pressure the effect of secondary anisotropy appears to be less pronounced. This fact is indicated by a comparison of the ultimate stresses of competent and artificially fractured sandstone (Figure 2-35) (Reference 2-17). The observed differences in strength may in fact disappear completely at very high hydrostatic pressure (>6 kb) if enough frictional resistance can be mobilized to reach the brittle-ductile transition.



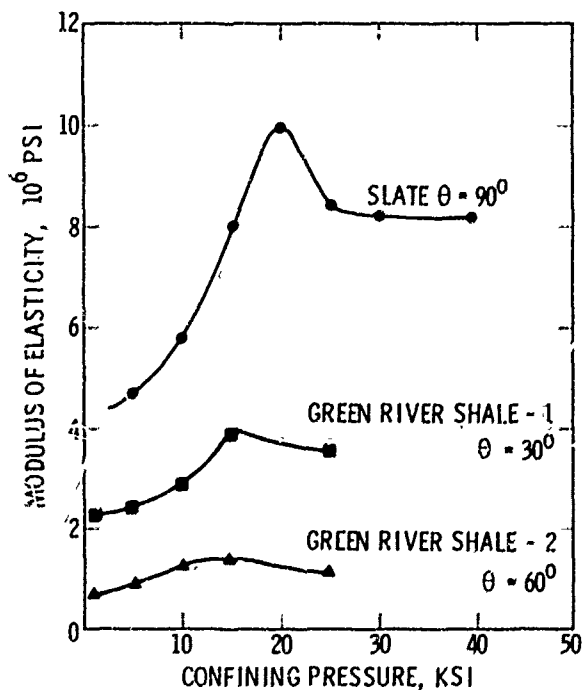
(a) GREEN RIVER SHALE-1, FRACTURE STRENGTH DATA



(b) GREEN RIVER SHALE-2, MAXIMUM STRENGTH DATA

FIGURE 2-31. ANISOTROPY IN STRENGTH OF SHALE (REFERENCE 2-43)

Mechanical Properties of Rock



AJA3621

FIGURE 2-32. VARIATION OF THE MODULUS OF ELASTICITY WITH RESPECT TO CONFINING PRESSURES (REFERENCE 2-43)

However, this suggestion need not always hold. For example, if the fractures of the sandstone in Figure 2-35 contained argillaceous gouge, then the strength of the fractured rock might well be controlled by the yield stress of the gouge material at stresses far below the ultimate strength shown.

Discontinuous Rock Masses

To predict the response of discontinuous rock masses in states where fracture is in the brittle mode, the properties of the discontinuities, or weakness planes, must be determined. To date the mechanical behavior of discontinuities is much less well-known than that of competent rocks. Hence little data exists which could be used to calculate the stiffnesses of discontinuities under hydrostatic and shear loading. Instead most investigations have concentrated on determining the strength of discontinuities. For the sake of brevity, any kind of discontinuity will be called "joint" from hereon. It should be recognized that this term is used loosely and does not agree with the geological definition of joints.

The relationship between shear stress and displacement, as well as the variation of shear strength of joints with relative displacement of joint surfaces, depends principally on joint geometry (Reference 2-46)

(including joint roughness, waviness, joint continuity and joint width), normal stress acting across the joint plane, interstitial fluid pressure, and on the type and thickness of joint fillings (References 2-46 to 2-52). The geometry of joints in turn is determined by the mode of formation of the joint, the size and the sense of displacements which have previously occurred and the normal stresses at which they occurred. Both the shear-stress/displacement relation and the shear strength appear to be very sensitive to temperature.

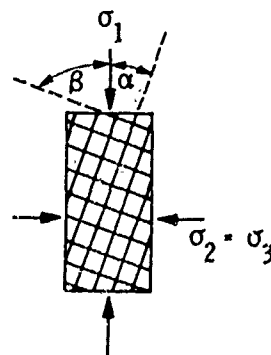
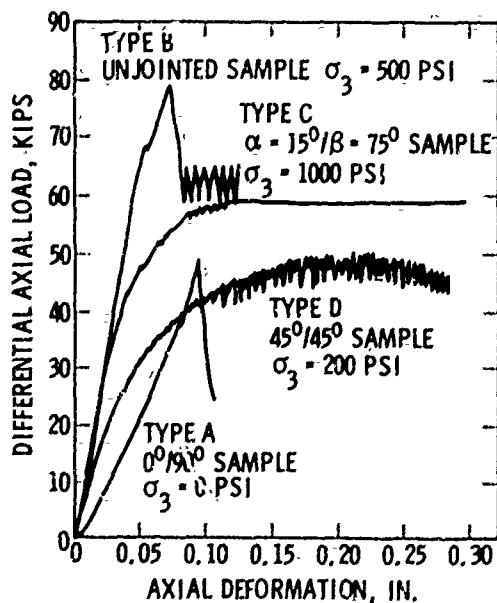


FIGURE 2-33. GEOMETRY OF BLOCK-JOINTED PLASTER OF PARIS TEST SPECIMEN



AJA3622

FIGURE 2-34. TYPICAL DIFFERENTIAL AXIAL LOAD-AXIAL DEFORMATION CURVES FOR COMPETENT AND BLOCK-JOINTED PLASTER OF PARIS (REFERENCE 2-45)

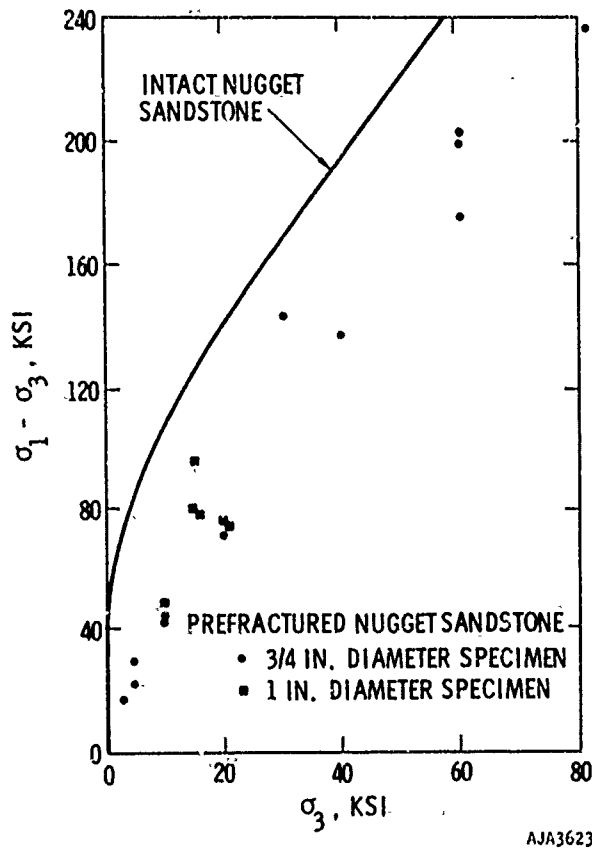


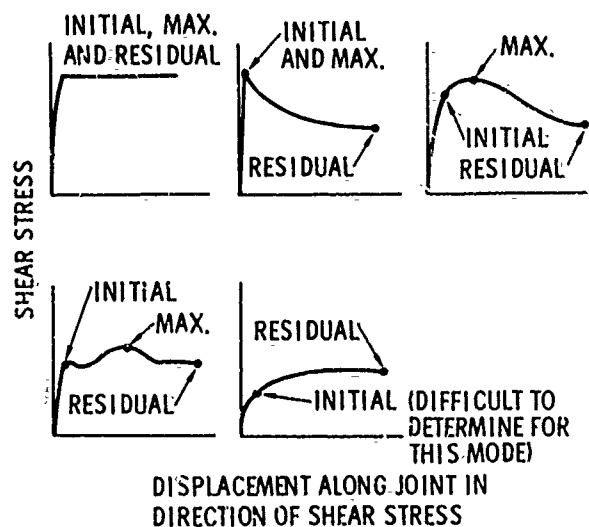
FIGURE 2-35. STRENGTH OF PREFRACTURED NUGGET SANDSTONE COMPARED WITH STRENGTH OF INTACT SPECIMENS (REFERENCE 2-15)

The effects of rock mineralogy and water content are distinct but appear to be small compared with the influence of other parameters. Figure 2-36 shows a typical set of records of shear stress versus displacement parallel to the joint surfaces (References 2-49 to 2-51). At low shear stress the deformation behavior is to approximately linearly elastic (Reference 2-51). This linearly elastic region is followed by nonlinear behavior until the shear stress becomes equal to the initial shear strength, which is defined by a local maximum in the shear-stress displacement diagram (Reference 2-50). In the absence of such a relative maximum, the initial shear strength is defined as that stress at which the change of the slope of the shear stress displacement curve becomes greatest prior to reaching the highest observed shear stress (maximum shear stress in Figure 2-36). Once the initial shear stress has been reached, the strength of joints varies in one of the following ways:

- a. The shear strength remains constant.

- b. The shear strength decreases monotonically to the residual shear strength (Figure 2-36). In this case, the initial shear strength equals the maximum shear strength.
- c. The shear strength increases to a maximum value called the maximum shear strength and then decreases to the residual shear strength.
- d. The shear strength drops to a local minimum called the minimum shear strength, increases again and subsequently drops to the residual shear strength.
- e. The shear strength increases, approaching the residual shear strength asymptotically. In this case the maximum shear strength equals the residual shear strength. The strength behavior of types 2 and 3 appear to be by far the most common regardless of the magnitude of the normal stress (References 2-49, 2-50).

The displacement required to reach the residual strength is mainly a function of surface roughness, normal stress across the joint plane and joint filling but typically varies between very small fractions of an inch and two inches (References 2-49 and 2-51).



NOTE: INITIAL STRENGTH DETERMINED BY POINT OF MAXIMUM CURVATURE

AJA3624

FIGURE 2-36. FOUR TYPICAL MODES OF JOINT STRENGTH AND DISPLACEMENT (PERCENTAGES BASED ON 121 DIRECT SHEAR TESTS OF NX CORES FROM AUBURN AND GRAND COULEE PROJECTS) (REFERENCES 2-49, -50, -51)

Mechanical Properties of Rock

Generally, the displacement decreases with increasing normal stress. Extremely small displacements are often associated with stick-slip. To avoid confusion it must be emphasized that the stick-slip phenomenon which was discussed earlier in the context of the post-failure behavior of competent rock is somewhat different in that it was observed under conditions where both the shear stress and the normal stress on the joint plane were varied. The shear-stress/displacement relation of joints appears to be insensitive to the rate at which the shear stress is applied (Reference 2-49).

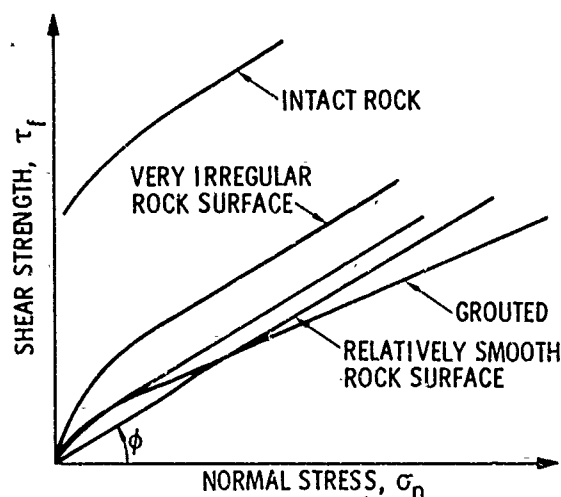
Figure 2-37 shows several schematic plots which define the maximum shear strength, τ_{max} , as a function of normal stress (σ_n), joint roughness and joint grouting for joints in a particular rock type (References 2-49, 2-52). For comparison Figure 2-37 also includes the failure envelope of the intact material. The observed variation of τ_{max} is considerable and is likely to be even more pronounced if the effect of temperature were considered. It should be noted that the grouted (filled) joint has a higher strength at zero normal stress but becomes progressively weaker than ungrouted joints as the normal stress is raised. The variation of shear strength of joints is generally related to the magnitude of the frictional resistance which can be mobilized. Consequently, shear strength is most commonly described by equations of the form

$$\tau_{max} = A_0 + A_1 \sigma_n = A_0 + \sigma_n (\tan \phi) \quad (2-1)$$

A_0 denotes the joint cohesion at zero normal stress. A_1 and ϕ are the coefficient of friction and the friction angle. For most rock A_1 and ϕ are remarkably constant and vary in the narrow range between 0.4 to 0.7 or between 22° and 35° , respectively (References 2-36, 2-49). At present the influence of interstitial water pressure is taken into account by subtracting the pore pressure from A_0 and σ_n , i.e., by defining effective cohesion and effective normal stress. The influence of pore pressure on A_1 and ϕ is virtually unknown.

Considerable progress has been made in predicting friction coefficients and maximum shear strength for unfilled joints (Reference 2-52). The scheme used is largely based on the observation of two basic types of failure behavior which consist of riding over asperities at low normal stress and of shearing through them at high normal stress. To what extent this scheme may be useful for ground shock calculations, however, is not clear.

Discontinuities in rock masses can present great difficulties in developing a mathematical model of the site. For example, if joints are extensive and sufficiently well lubricated, sliding may occur without appreciable inelastic deformation of the rock. In this



AJA3625

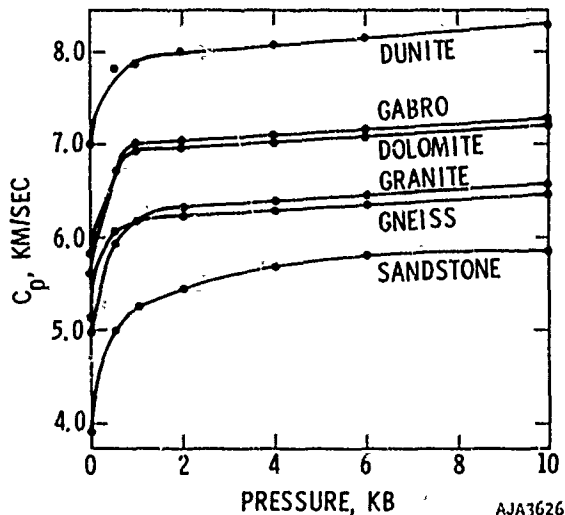
FIGURE 2-37. FAILURE ENVELOPES EXPECTED FOR ROCK MASSES (REFERENCES 2-49, -52)

case, energy dissipation is not averageable over large distances, and sparse sampling and laboratory testing are completely inadequate to define the properties of the site. The only presently available method of certifying a site model in such an instance is to perform a large scale field test, such as Project Piledriver, and to achieve favorable agreement between field data and computations which use a candidate model of the site.

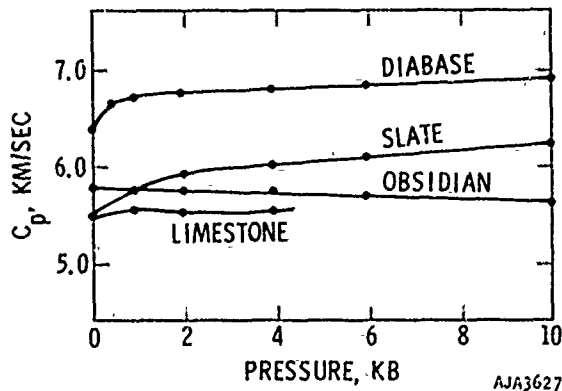
MECHANICAL PROPERTIES OF ROCKS AT STRAIN RATES ABOVE 10^2 SEC^{-1}

Since the main purpose of measuring material properties is to assist in the calculation of shock wave propagation, laboratory techniques have been developed to measure the response of small samples to dynamic loadings. These dynamic measurements range from the very low stress levels where sonic techniques are used to intensities ranging from several kilobars to megabars using shock-loading techniques like the gas gun and split Hopkinson Bar.

Tangent bulk and shear moduli can be calculated from dilatational and shear wave velocities. Since the tangent moduli may depend strongly on the level and state of stress, on the temperature, and on moisture content, the speed of small amplitude waves also depends on these factors (Reference 2-53). In some dry rocks, the compressional wave speed increases with increasing confining pressure due to the closure of cracks and other void spaces. This effect is illustrated in Figure 2-38(a). In other rocks which have a smaller volume of initial pore space, the compressional velocity depends much less on



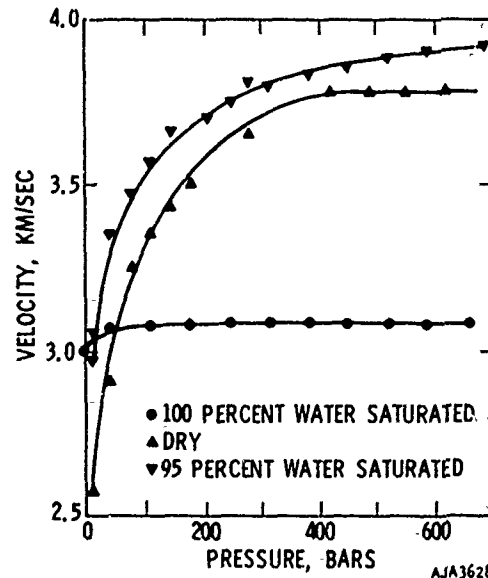
(a) ROCKS SHOWING A LARGE INCREASE IN SEISMIC VELOCITY AT LOW PRESSURE



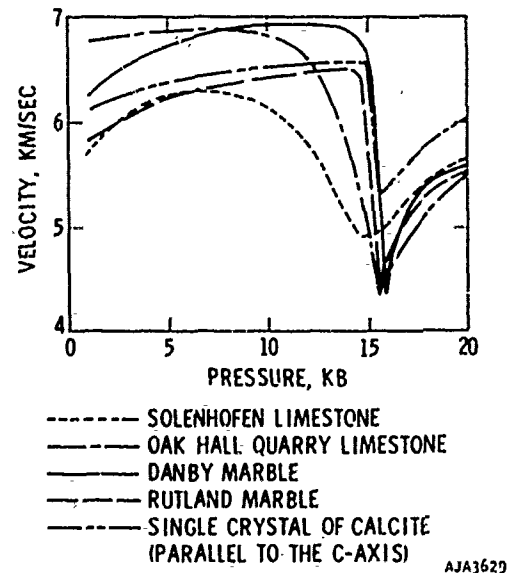
(b) ROCKS SHOWING A SMALL INCREASE IN SEISMIC VELOCITY AT LOW PRESSURE

FIGURE 2-38. VELOCITIES OF LOW AMPLITUDE (SEISMIC) DILATATIONAL WAVES AS FUNCTIONS OF PRESSURE (REFERENCE 2-54)

confinement, as is shown in Figure 2-38(b). If interstitial pore pressure is present, closure of voids may be resisted. In Figure 2-39, the effective confining pressure in the 95 percent saturated sample appears to differ little from the external pressure, and the velocity increases with external pressure. In the 100 percent saturated sample, however, the interstitial water apparently is under high pressure, and the effective confinement is apparently small and depends weakly, if at all, on the external pressure and there is little change in velocity. Phase changes are clearly reflected in the wave speed. The phase transition or transitions in calcite in the range 15 to 18 kb cause



(a) SEISMIC COMPRESSIONAL WAVE VELOCITY (KM/SEC) VERSUS PRESSURE (BARS) FOR DIFFERENT WATER CONTENT. THE GREAT DIFFERENCE IN VELOCITY FOR 95 PERCENT AND 100 PERCENT SATURATED SPECIMEN IS DUE TO THE DIFFERENCE IN THE CONDITIONS OF EFFECTIVE PRESSURE (REFERENCE 2-55)



(b) SEISMIC COMPRESSIONAL WAVE VELOCITY VERSUS PRESSURE IN CALCIUM CARBONATE ROCKS SHOWING EFFECT OF PHASE TRANSITION AT ABOUT 16 KB (REFERENCE 2-56)

FIGURE 2-39. SEISMIC COMPRESSIONAL WAVE VELOCITIES AS FUNCTION OF PRESSURE

Mechanical Properties of Rock

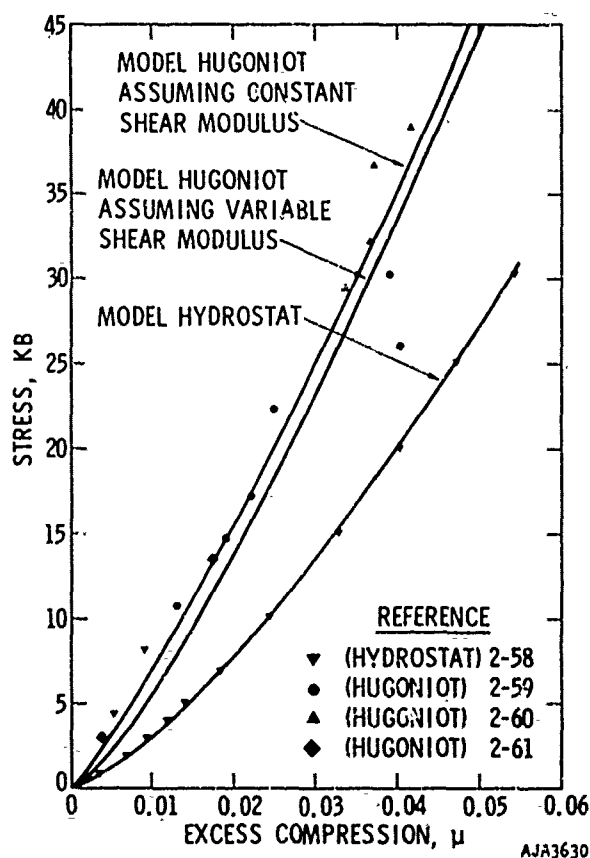
an abrupt decrease in the velocity as shown in Figure 2-39. This results from a net volume change due to a calcite-calcite transition.

At pressures exceeding about 50 kb, one-dimensional shock wave experiments provide most of the information on material properties. These experiments measure either stress or particle velocity in the direction of wave propagation and the wave velocity at the shock front. Rankine-Hugoniot equations for conservation of mass, momentum, and energy are used to transform the data into various forms, including stress versus specific volume as shown in Figure 2-40 for NTS granite. Also shown is the pressure/volumetric strain relation measured in hydrostatic compression in a separate experiment. In the pressure range of Figure 2-40, there is little difference in internal energy between the hydrostat and hugoniot. The stress difference between the two curves may then be related to the shear stiffness and strength of the rock. The hugoniot for granite, up to about 1 megabar, is shown in Figure 2-40(b). The hugoniot for NTS Tuff, Figure 2-41(a), reflects a considerably greater amount of compaction at low stress levels

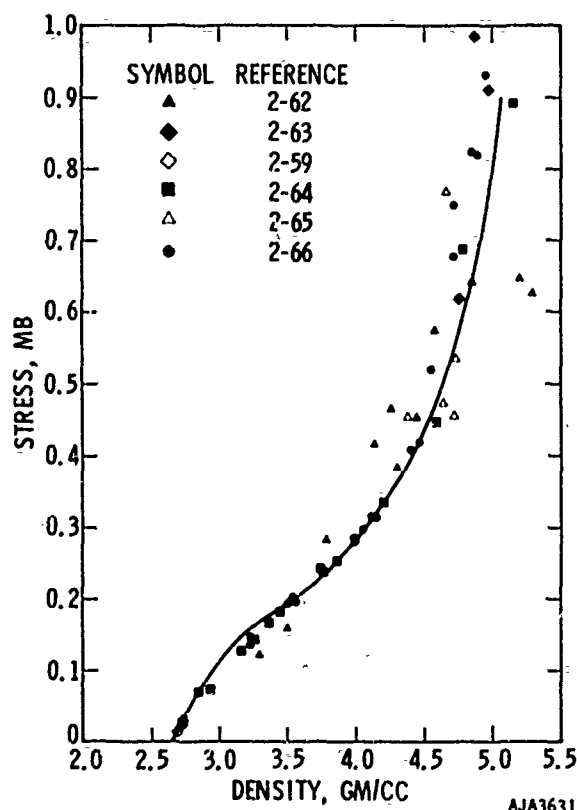
than for the granite. This is largely due to the higher initial porosity of the tuff. Adiabatic unloading from four different peak shock pressures, Figure 2-41(b), illustrate that the amount of permanent compaction increases with peak pressure. When some rocks are subjected to very high shock pressures, the opposite effect, a volumetric expansion upon complete unloading, is observed (Reference 2-72). The explanation for this is that the shock compression may increase the specific internal energy of the rock to the point where vaporization occurs. Thus, the rock may expand as a vapor whose specific volume at atmospheric pressure may be greater than its initial volume.

Laboratory Experiments

Laboratory experiments are conducted on samples from one cubic inch to several cubic feet in size. The cylinder is by far the most common sample shape. Cylinder diameters typically vary between 3/4 in. and 2 in. The length-to-diameter ratio ought to be at least 2:1. Table 2-6 lists the prevailing test methods and the mechanical properties which are monitored in each of these experiments.



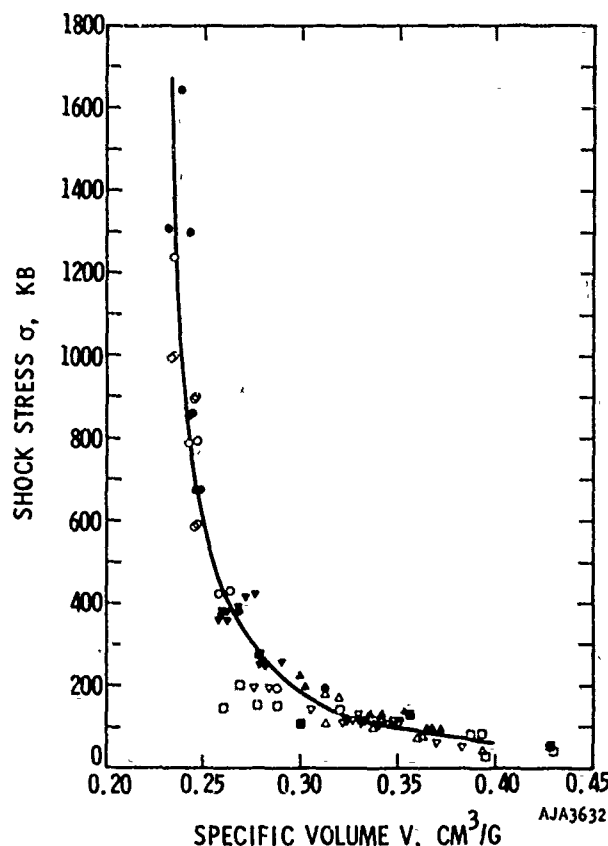
(a) HUGONIOT AND HYDROSTAT FOR NTS GRANITE AT LOW AND MODERATE PRESSURES



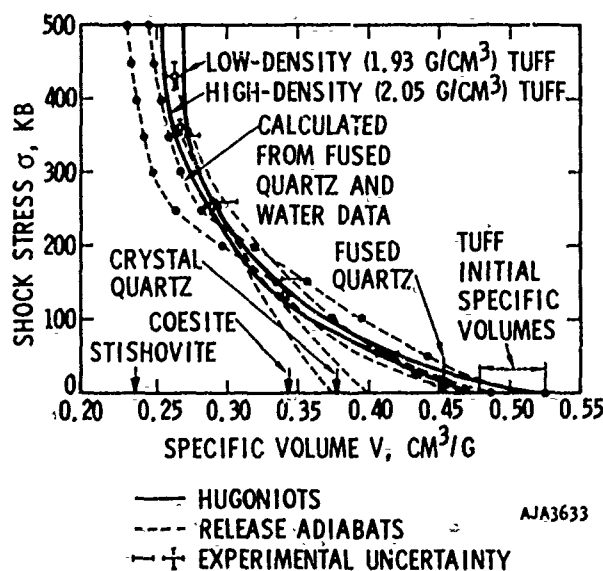
(b) HUGONIOT FOR NTS GRANITE. COMPLETE RANGE OF AVAILABLE DATA

FIGURE 2-40. HUGONIOT AND HYDROSTAT FOR NTS GRANITE

Properties of Rocks at Strain Rates Above 10^2 sec^{-1}



(a) HUGONIOTS FOR WET AND DRY NTS TUFF (REFERENCE 2-67)



(b) RELEASE ADIABAT DATA FOR SATURATED TUFF (REFERENCE 2-67)

FIGURE 2-41. HUGONIOTS AND RELEASE ADIABATS FOR DRY AND WET NTS TUFF

- ▼ REFERENCE 2-67, WET, $\rho_0 = 1.90$ TO 2.10 G/CM^3
POROSITY = 20 TO 35 PERCENT
- BASS, ET AL. 2-69, DRY, $\rho_0 = 1.46 \text{ G/CM}^3$
POROSITY = 27 PERCENT
- BASS, ET AL. 2-69, WET, $\rho_0 = 1.72$ TO 1.75 G/CM^3
POROSITY = 27 PERCENT
- △ LOMBARD 2-70, DRY, $\rho_0 = 1.60$ TO 1.70 G/CM^3
- ▲ LOMBARD 2-70, WET, $\rho_0 = 1.86$ TO 1.90 G/CM^3
- ISBELL 2-68, DRY, $\rho_0 = 1.75 \text{ G/CM}^3$
- ISBELL 2-68, WET, $\rho_0 = 1.97 \text{ G/CM}^3$
- ▽ WIEDERMANN AND CURTH 2-71, DRY,
 $\rho_0 = 1.61 \text{ G/CM}^3$

Quasi-Static Experiments

Experiments are said to be "static" or "quasi-static" if the externally imposed strain rate or the corresponding loading rate is less than approximately 10^{-2} sec^{-1} . The most basic facility in quasi-static experiments is the triaxial cell which applies hydrostatic pressure and axial loading independently. A section view of a typical triaxial compression chamber is shown in Figures 2-42 and 2-43 (References 2-6, 2-73). Triaxial cells are suitable to carry out triaxial compression and extension experiments and uniaxial strain tests. With modern servo-controlled apparatus a wide variety of stress and strain paths can be followed. Hydrostatic pressure is controlled by regulating the pressure in suitable fluids such as oil, kerosene, or gas (at high temperature and strain rate). Samples are sealed towards the hydrostatic pressure medium by jackets made of latex rubber, copper, graphite and copper, polyurethane, etc., (Figure 2-44) (Reference 2-6). Such jackets also permit the external pressure medium to be isolated from the pore pressure medium which is controlled independently (Figure 2-44). Triaxial cells are employed to conduct tests on competent as well as on fractured or discretely jointed samples including specimens which contain a single, artificially introduced, saw-cut discontinuity.

Biaxial stress states can be produced on thin-walled hollow cylinders subjected to internal or external pressure, or to axial loading and torsion (References 2-7, 2-12 to 2-14). Alternatively, biaxial stresses are generated in rectangular prism samples which are loaded by two pairs of pistons and specially designed, "lubricated" anvils (References 2-10, 2-15, 2-19). Multiaxial stress states are developed by subjecting rectangular prism samples to triaxial stress (Reference 2-11), by subjecting thin-walled cylinders to internal and external pressure and

Mechanical Properties of Rock

TABLE 2-6. ROCK AND SOIL MECHANICS EXPERIMENTS

Test Method	Stress State	Sample Geometry	Properties Measured
Uniaxial loading	$\sigma_1 > 0; \sigma_1 < 0^*$ $\sigma_2 = \sigma_3 = 0$	Cylinder, rectangular, prism, cube	Stress-strain behavior; ductility "yield" strength; ultimate stress under static and cyclic loading fatigue behavior; effects of temperature and strain rate deformation and fracture mechanisms.
Triaxial compression	$\sigma_1 > \sigma_2 = \sigma_3$	Cylinder, rectangular, prism, cube	Same as above; pore pressure effects, friction on joints
Triaxial extension	$\sigma_1 = \sigma_2 > \sigma_3$	Cylinder, cube	Same as above
Biaxial loading	$\sigma_1 > \sigma_2 = \sigma_3$	Hollow cylinder, rectangular, prism, cube	Same as above
Multiaxial loading	$\sigma_1 \neq \sigma_2 \neq \sigma_3$	Hollow cylinder, prism, cube	Same as above
Uniaxial strain	$\epsilon_1 > 0$ $\epsilon_2 = \epsilon_3 = 0$	Cylinder, cube	Same as above
Direct shear double shear	Multiaxial	Cylinder, rectangular, prism	Shear strength on prescribed planes including joints; pore pressure effect; friction on joints.

* $\sigma_1 > 0$ denotes compression

$\sigma_1 < 0$ denotes tension

AA4821

to axial stress (References 2-13, 2-14) or by compressing rectangular prism specimens between solid loading platens and flat jacks (Reference 2-3).

Triaxial compression experiments are most often used to determine the mechanical behavior of competent rock. However, in some cases triaxial compression tests are also employed to ascertain the mechanical properties of discontinuities, such as the friction coefficients of joints (Reference 2-72). Although the test permits high normal stresses to be developed across joints and pore pressure studies to be conducted easily, it has shortcomings as follows.

- It is difficult to vary the shear stress and

the normal stress acting on the joint plane independently.

- The stresses on the joint are accurately known only if the relative displacements of the joint surfaces are small.
- The areas of joints tested are necessarily small because of the size limitations of most triaxial cells.

As a result, laboratory joints may be poor models of joint surfaces in situ and the usefulness of experimentally observed friction coefficients might be questionable. Some of the disadvantages of the triaxial compression test on jointed rock can be overcome by

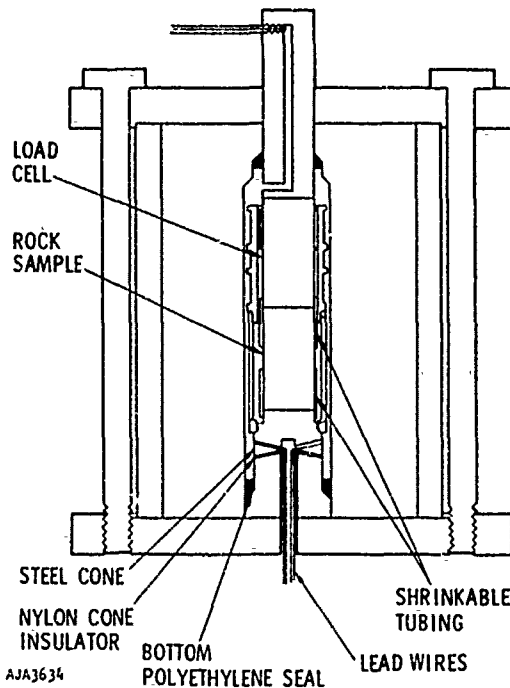


FIGURE 2-42. TEST CHAMBER (LOAD CELL INSIDE CHAMBER) FOR TRIAXIAL TESTING OF ROCK (REFERENCE 2-6)

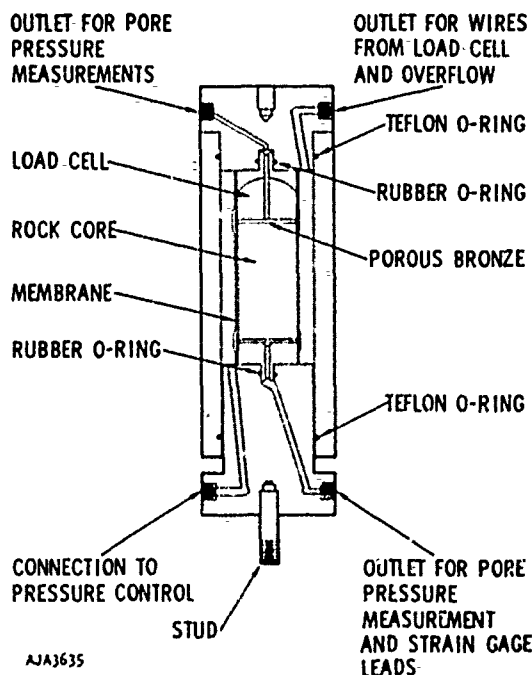


FIGURE 2-43. TEST CHAMBER FOR TRIAXIAL COMPRESSION OF ROCK WITH INTERSTITIAL PORE FLUID UNDER PRESSURE (REFERENCE 2-73)



(a) SPECIMENS FULLY INSTRUMENTED BUT NOT TESTED



(b) INTERNALLY GAGED, 50% SATURATED, HYDROSTATIC COMPRESSION, THEN 4 KB TRIAXIAL TEST TO FAILURE

FIGURE 2-44. INSTRUMENTATION OF ROCK SPECIMEN

carrying out so-called direct shear or double shear experiments (References 2-3, 2-49, 2-51, 2-52, 2-74). The principles of direct and double shear apparatus are illustrated in the schematics of Figure 2-45.

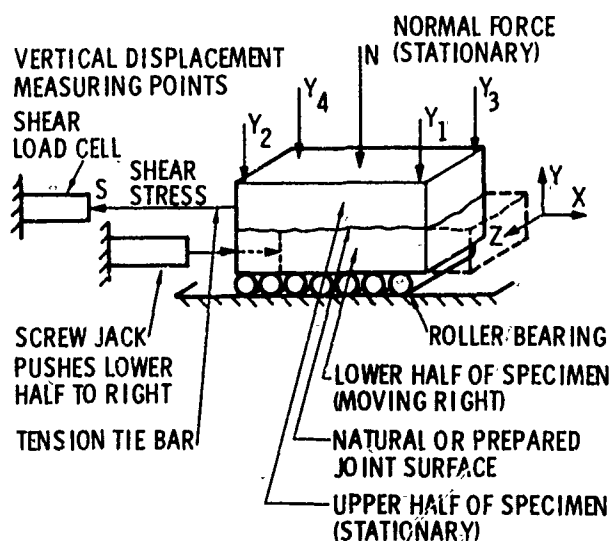
Load and pressure are measured by means of standard transducers, Figure 2-46. Strain is determined directly by means of strain gages or indirectly for measurements of the total sample deformations (References 2-6, 2-16, 2-31).

Dynamic Experiments

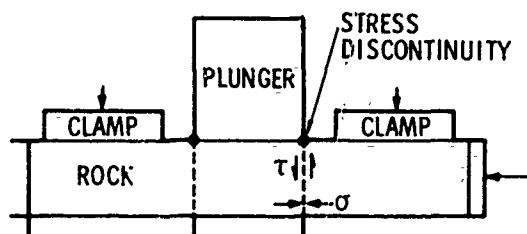
The term "dynamic test" is used here to describe experiments in which the dynamic material constant and strain rate effects are investigated up to strain rates of approximately 10^3 sec^{-1} .

The effect of strain rate up to about 10^{-1} sec^{-1} is evaluated by means of the same apparatus ordinarily used to conduct quasi-static experiments. Strain rate is varied by controlling the advance of the loading

Mechanical Properties of Rock



(a) DIRECT SHEAR APPARATUS (REFERENCE 2-49)



(b) DOUBLE SHEAR APPARATUS (REFERENCE 2-74)

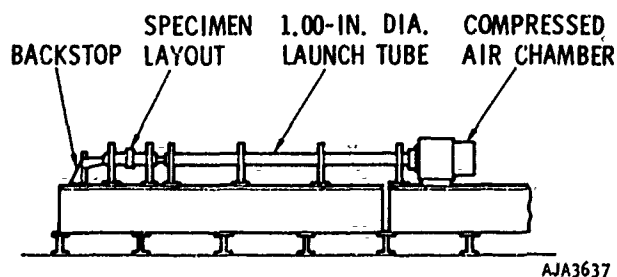
FIGURE 2-45. SCHEMATICS OF DIRECT AND DOUBLE SHEAR APPARATUS

piston. If the strain rate exceeds 10^{-1} sec^{-1} then a Hopkinson split bar apparatus is used, as shown in Figure 2-46 (Reference 2-75). In this apparatus a cylindrical specimen is placed between a weighbar and an anvil. Stress in the sample is determined from strain measurements on the weighbar and on the anvil which are subsequently converted to average stress throughout the sample. The strain in the rock is measured by means of strain gages which are bonded directly to the specimen surface. At very high strain rates the axial stress in the sample may vary as

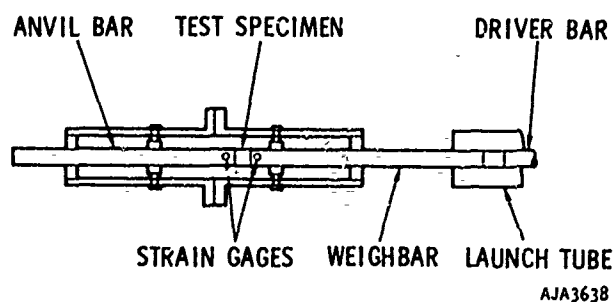
illustrated in Figure 2-47 (Reference 2-76). The maximum strain rate which can be obtained using the Hopkinson split bar test is approximately 10^3 sec^{-1} . At higher strain rates dispersion and other effects make it impossible to determine stress and strain accurately.

In several instances confined Hopkinson split bar experiments have been conducted at different levels of hydrostatic pressure (Reference 2-15). Hydrostatic pressure is generated by the application of lateral fluid pressure and an axial load through the weighbar. The dynamic phase of the test involves the application of a dynamic deviatoric stress through the weighbar.

Dilatational and shear wave velocities in rock are measured as illustrated in Figure 2-48 (Reference 2-77). Barium titanate (p-wave) or A-C cut quartz (s-wave) transducers are attached to end of a cylindrical sample. Then a voltage pulse which is applied to one transducer is connected to a mechanical pulse



(a) SCHEMATIC OF MODIFIED HOPKINSON BAR



(b) SPECIMEN LAYOUT

FIGURE 2-46. SPLIT-HOPKINSON BAR APPARATUS FOR MEASURING PROPERTIES AT VARIOUS STRAIN RATES (REFERENCE 2-75)

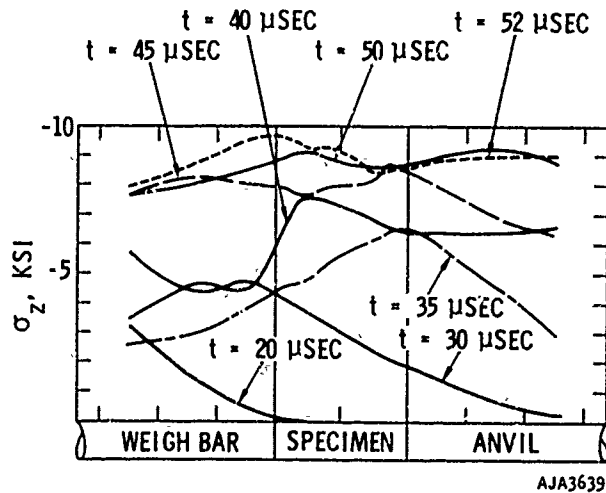


FIGURE 2-47. PROFILES OF AXIAL STRESS IN SPLIT-HOPKINSON BAR EXPERIMENT, SHOWING VARIATION IN STRESS DUE TO WAVE EFFECTS WHICH LIMIT RANGE OF INVESTIGATION BY THIS TECHNIQUE (REFERENCE 2-76)

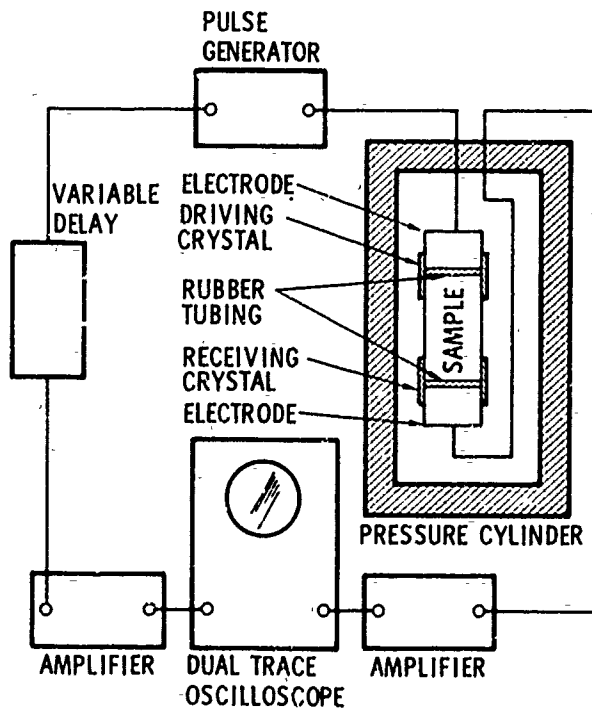


FIGURE 2-48. APPARATUS FOR MEASURING SONIC (LOW AMPLITUDE) DILATATION AND SHEAR WAVE VELOCITIES AT VARIOUS LEVELS OF CONFINING PRESSURES (REFERENCE 2-77)

which propagates through the specimen. When this pulse reaches the second transducer, it is converted back into an electrical signal. The wave speed is then computed by dividing the distance between the transducers by the travel time of the pulse. Modifications of this simple technique are suitable for the measurement of wave speeds under unconfined and confined conditions and on dry and wet specimens.

Shock Wave Experiments

Several laboratory techniques have been developed to measure the response of small samples to dynamic loading at strain rates greater than 10^3 sec^{-1} . One method, which covers the range of shock intensities from several kilobars to several megabars, uses a light gas gun to launch a flat projectile at a target. The impact creates a shock wave whose intensity and propagation velocity reflect the change between shocked and unshocked states. An alternative method, which is most useful above about 50 kb, uses chemical explosive lenses to launch the projectile. In addition to the shock-loading properties, the unloading properties are also useful in defining an equation of state. Shock unloading under adiabatic conditions is created by extending the shock-loading techniques and making measurements which lead to a definition of the shock unloading path. A third type of experiment uses a tamped chemical explosive charge in the center of a block of rock to generate a shock wave. The radial stress/time history is measured at various ranges from the source by pressure-sensitive wire gages. The structure and amplitude of the wave are interpreted with the aid of theory to obtain an indication of shear strength, wave speed, and other properties.

The light gas gun technique is illustrated in Figure 2-49, and the target and projectile are shown in Figure 2-50. The purpose of the shorting pins is to measure the times of arrival of the shock wave at various points in the target, from which the shock velocity may be determined. The velocity of the projectile just before impact is also measured, and by knowing this and the properties of the projectile material, the particle velocity in the target area can be determined. The shock velocity and particle velocity are converted to other quantities of interest by means of the Rankine-Hugoniot conservation equations as explained in Section 1. Typical measurements are shown in Figure 2-51.

The light gas gun can also be used to launch a projectile which generates a stress/time history in a pressure-resistive quartz crystal. In one of the techniques, illustrated in Figure 2-51(a), the rock to be tested is launched at the quartz crystal. In this

Mechanical Properties of Rock

experiment, the stress and particle velocity are converted into stress and relative density or other properties by means of the Rankine-Hugoniot equations. In the second technique illustrated in Figure 2-51(b), the quartz crystal measures stress amplitudes in a wave which has propagated through the specimen and has acquired a structure characteristic of an elastic material. The wave structure is interpreted by a trial-and-error procedure whereby candidate material properties are assumed and are used in numerical computations which simulate the experiment. Agreement between the experiment and the computations is considered to mean that the material properties were assumed correctly.

To produce shock unloading under adiabatic conditions, the backside of the specimen is placed against a material of different shock impedance. Wave reflection due to impedance mismatch at the interface is illustrated in Figure 2-52. The unloading properties of the rock are inferred by means of theory from the shock state of the buffer fluid, which is measured by optical means. The experimental setup, including explosive lens, is shown in Figure 2-53(a). The buffer fluid is shown in Figure 2-53(b). The method of interpreting the raw data is described in Reference 2-81.

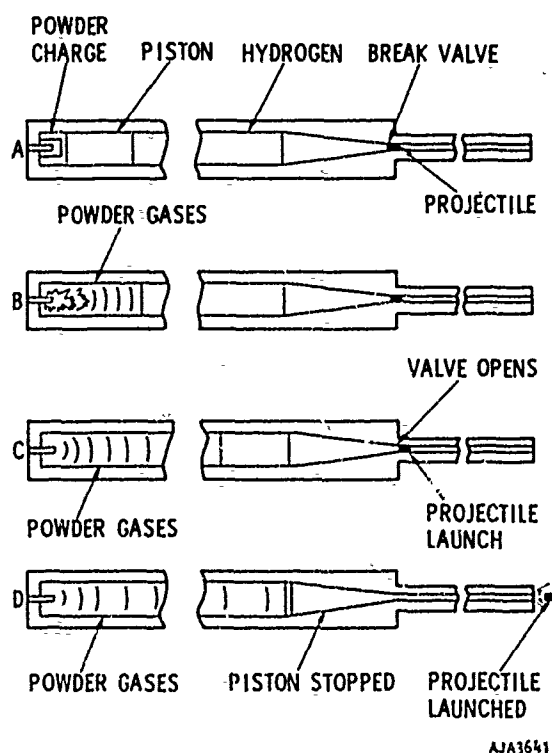
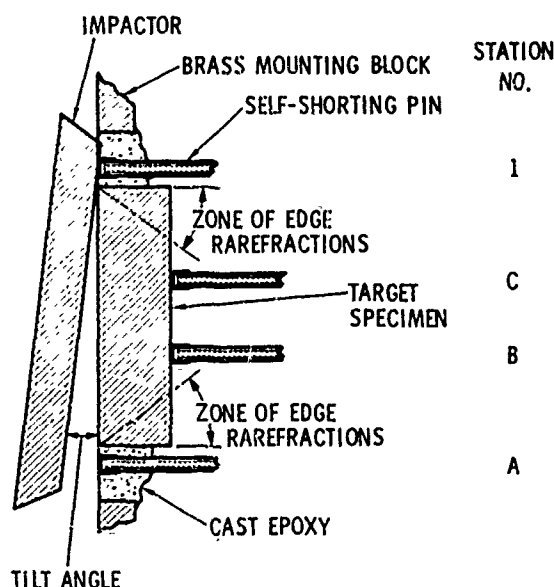
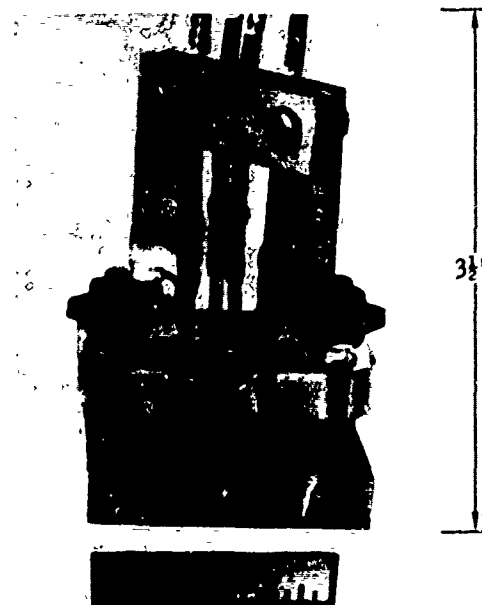


FIGURE 2-49. SEQUENCE OF EVENTS IN OPERATION OF A LIGHT GAS GUN (REFERENCE 2-78).

NOTE:
STATIONS A AND 1 INITIATE TIMING FOR SHOCK WAVE TRANSIT AND MEASURE TILT. STATIONS B AND C RECORD SHOCK WAVE ARRIVAL AT REAR SURFACE.

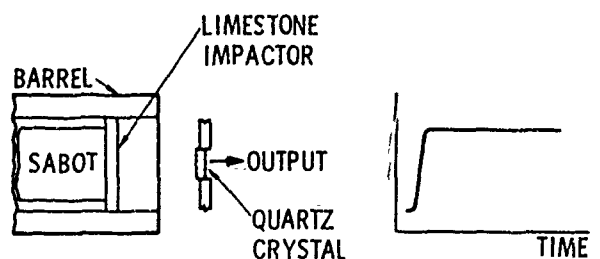


(a) TARGET FOR EQUATION OF STATE STUDIES (REFERENCE 2-79)

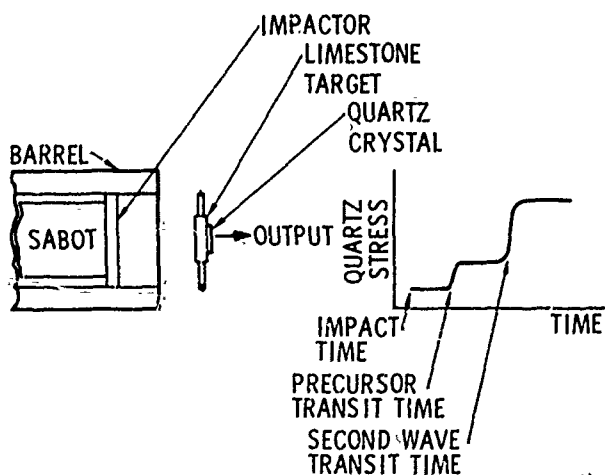


(b) EQUATION OF STATE STUDIES TARGET
FIGURE 2-50. TARGET CONFIGURATIONS FOR HIGH PRESSURE HUGONIOT TESTS (REFERENCE 2-79)

Properties of Rocks at Strain Rates Above 10^2 sec^{-1}

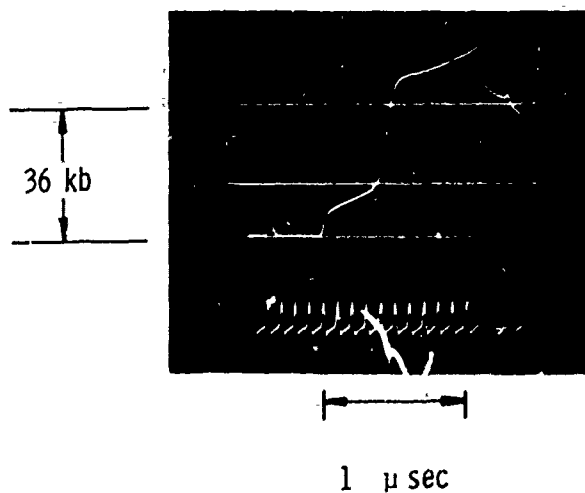


(a) DIRECT IMPACT TECHNIQUE



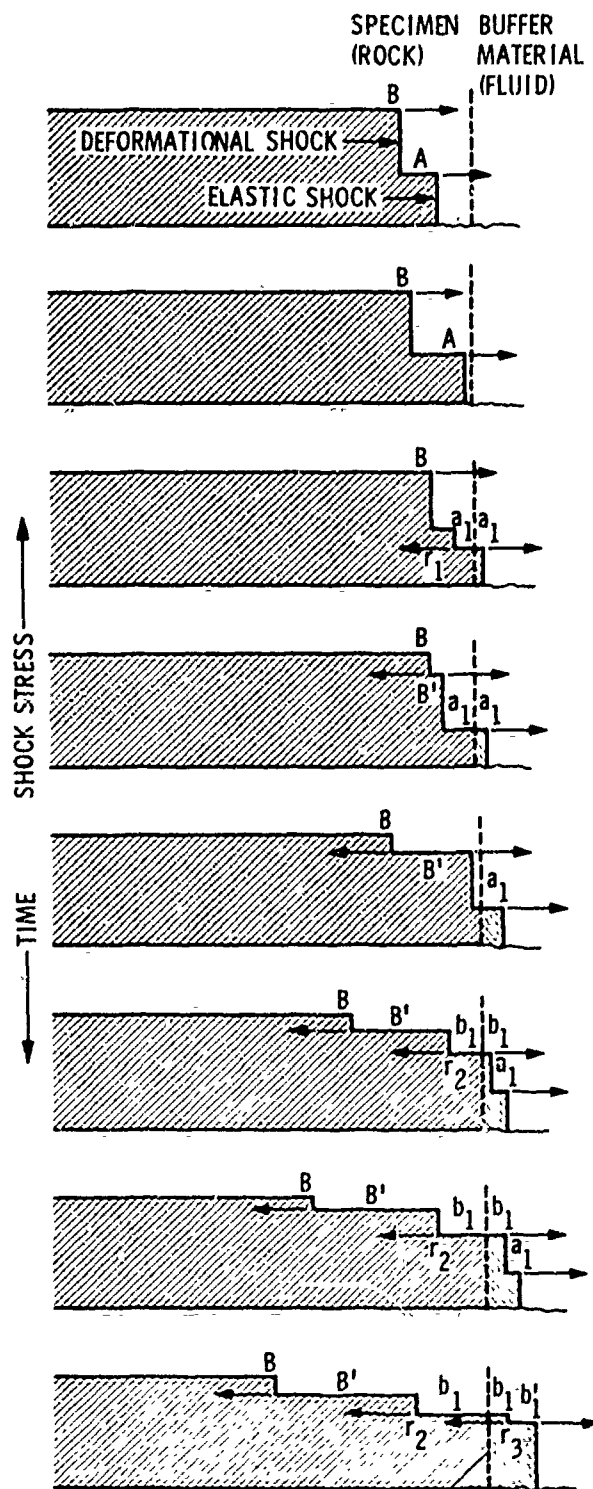
AJA3643

(b) WAVE PROFILE TECHNIQUE



(c) WAVE PROFILE RECORD FOR SOLENHOFEN LIMESTONE SPECIMEN

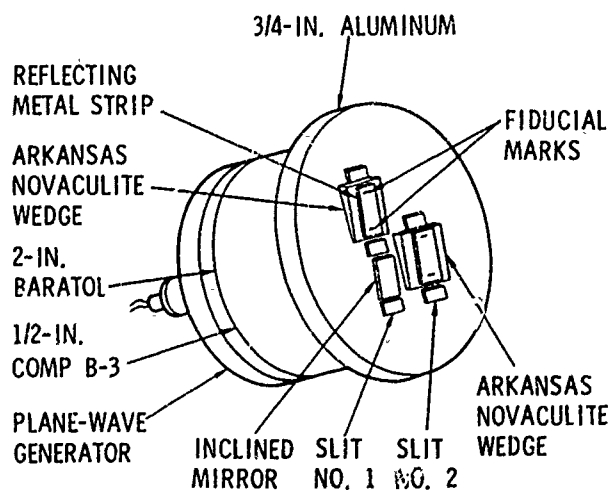
FIGURE 2-51. DYNAMIC PROPERTIES OF ROCKS MEASURED UNDER PLANE SHOCK WAVE CONDITIONS WITH QUARTZ TRANSDUCER TECHNIQUES (REFERENCE 2-80)



AJA3644

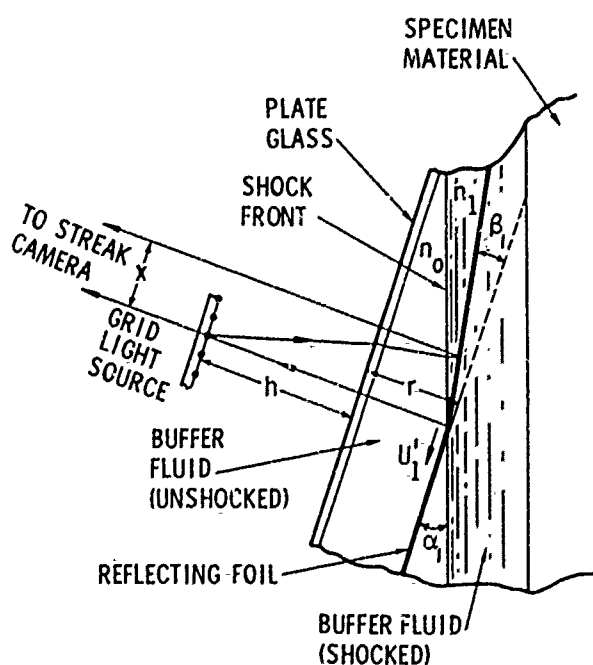
FIGURE 2-52. DIAGRAMMATIC SKETCH OF TWO SHOCK FRONTS IN ROCK INTERACTING WITH BUFFER MATERIAL (REFERENCE 2-81)

Mechanical Properties of Rock



AJA3645

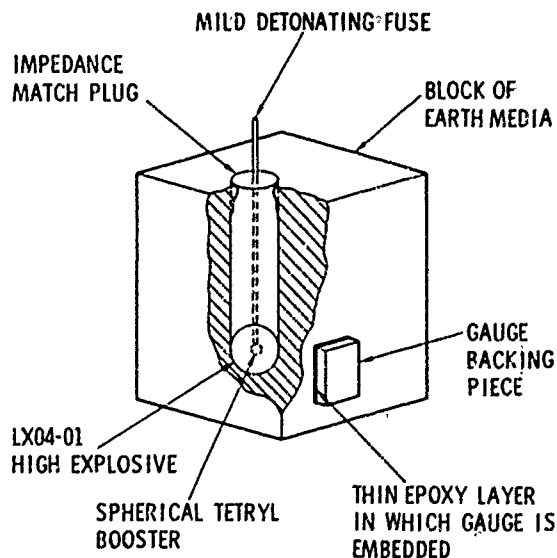
(a) GENERATION OF PLANE WAVES FOR MEASURING PROPERTIES BY THE OPTICAL LEVER TECHNIQUE



AJA3646

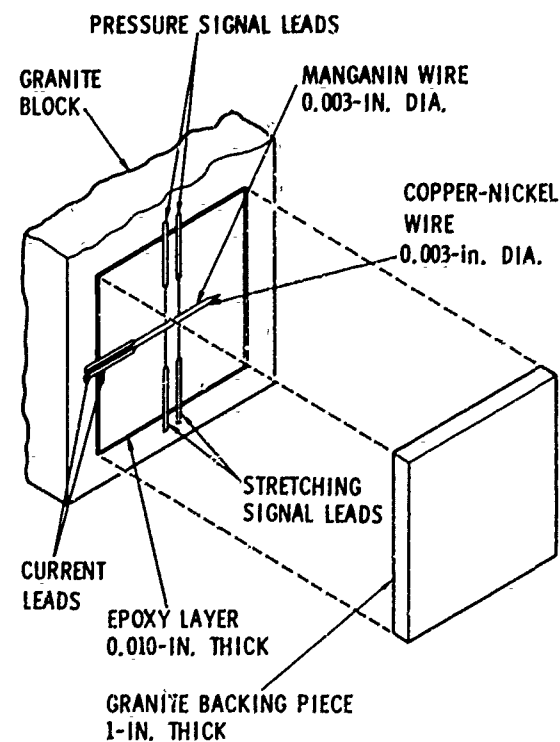
(b) OPTICAL LEVER TECHNIQUE REFLECTING FOIL IMMERSSED IN FLUID OF OPTICAL INDEX n_0 , AT ANGLE α , TO SHOCK; AFTER INTERACTION, FOIL ROTATED BY β_1 AND BUFFER FLUID HAS OPTICAL INDEX n_1

FIGURE 2-53. OPTICAL METHODS OF MEASURING PROPERTIES UNDER PLANE SHOCK WAVE CONDITIONS (REFERENCE 2-81)



AJA3647

(a) EXPLOSIVE GENERATION OF SPHERICAL WAVES IN 1 FOOT BLOCK OF ROCK



AJA3648

(b) SYSTEM FOR MEASURING RADIAL STRESS IN SPHERICAL WAVES WITH PRESSURE-SENSITIVE WIRES

FIGURE 2-54. PROPERTIES OF ROCKS MEASURED UNDER SPHERICAL SHOCK WAVE CONDITIONS WITH PRESSURE-SENSITIVE WIRES (REFERENCE 2-82)

A third type of shock wave experiment occupies a middle ground between laboratory and field experiments because the specimen is about 1 ft on a side and, hence, it may be large enough to contain heterogeneities typical of the in-situ rock mass even though the testing is done in a laboratory. The experiment is illustrated in Figure 2-54. Detonation of the explosive produces spherical waves whose intensity is measured at gages located between the parent block and a subsidiary block. This arrangement allows the shock wave to propagate past the gage as if it were in an infinite medium. The success of the technique depends on suitable instrumentation. Early work used manganin wire as a piezo-resistive gage material (Figure 2-54(b)). Later work used ytterbium wire as a piezo-resistive gage. Hence, the undesirable signal due to stretching of the gage, which is present in divergent wave propagation, is a much smaller percentage of the desired stress-induced signal. With the aid of a theory (Reference 2-87) based on conservation of mass, momentum and energy, the results of these experiments can be interpreted in terms of dynamic shear and mean normal stresses. Thus they provide a means of measuring shear strength under dynamic loading. These experiments are still in the developmental stage and are not presently used as a standard method of measuring properties.

Properties of the in Situ Rock Mass

The mechanical properties of the in situ mass may differ considerably from those of small laboratory samples because of the inherent structural heterogeneities found in rock masses. These structural features include joint sets, faults, bedding planes and cracks whose spacing may be large relative to the size of typical laboratory specimens, but small relative to the wave length of a ground shock pulse or the width of a structure. At this scale the measurement of the properties of the rock mass is less complete, less precise, and more qualitative than the measurement in the laboratory because of the difficulty in experimental techniques, high expense, and many variables inherent in the field environment.

Preliminary Investigation

The first type of investigation is usually a geological survey to determine rock type, joint spacing, bedding features, and depth of weathering. This is usually followed by a seismic refraction survey (Figure 2-55) to determine the dilatational and sometimes the shear wave velocities which indicate rock quality, thickness of soil overburden, or zone of weathering and depth to water table.

A drilling program in which extensive cores are taken usually follows the preliminary geologic and

geophysical survey. Preliminary tests of compressive strength are usually determined from the cores at the test site, but most of the core is sent to the laboratory for detailed analysis of the mechanical properties using sophisticated testing equipment. Prior to sending the core to the laboratory, a detailed log of the core is made as exemplified by the core log in Figure 2-56. In addition to a geologic description, the percent core recovery, joint frequency and depth to water table (if applicable) are usually recorded. A rock quality designation (RQD) (Reference 2-84) may also be obtained by measuring the percentage of core that comes in lengths of greater than 0.35 ft. The RQD has been correlated with several rock properties (Figures 2-57 and 2-58).

Experimental Methods (Dynamic)

Several different dynamic techniques have been used to determine material properties of a rock mass. These are

Geophysical techniques

Resistivity

Shock wave testing

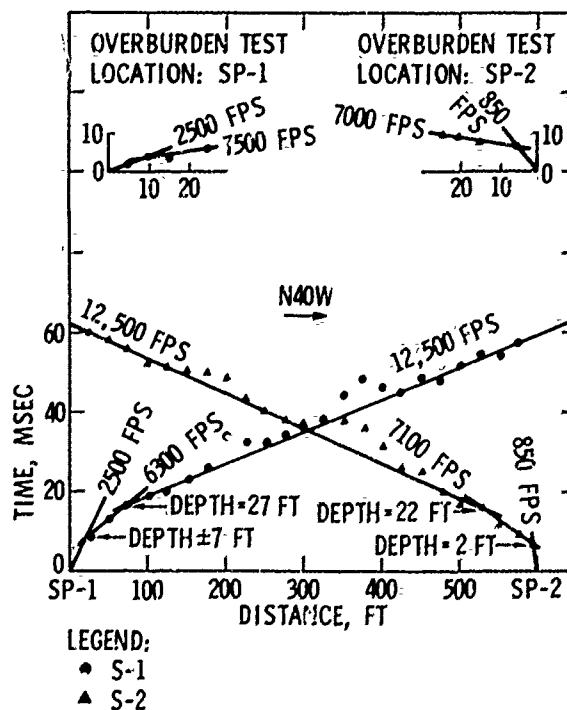


FIGURE 2-55. RELATION BETWEEN ARRIVAL TIME OF SEISMIC SIGNALS AND DISTANCE OF RECEIVER FROM SOURCE (SLOPES OF LINES BETWEEN POINTS ARE AVERAGE SONIC VELOCITIES (REFERENCE 2-83))

AJA3649

Mechanical Properties of Rock

LEGEND

CORE

- Log: Quartz diorite
 Darker colored segregations
 Lightly altered quartz diorite
 Core loss zone

Joints: Joint series (spacing between joints is less than 6 inches).

— 45° Stairred, filled, or tight joints or breaks with angle of dip. No angle of dip shown where joint is horizontal (15° or less).

... 45° Open and unstained joints or breaks with angle of dip. No angle of dip shown where joint is horizontal (15° or less).

--- 45° Postshot fracture with angle of dip. No angle of dip shown where joint is horizontal (15° or less).

DESCRIPTION

These abbreviations are found opposite appropriate joints along the left edge of the description column:

- l Tight, "hairline" joint
 cl Clay filled
 ls Limonite stained
 I Stained dark brown or black
 c Calcite filled

CORE RECOVERY

A percent based on the number of feet of core recovered versus the number of feet of core drilled.

BOREHOLE CAMERA JOINT DATA

Width and filling:

- 1/2-0 1/2 Inch joint, open
 1/4-f 1/4 Inch joint, completely filled
 1/16-pf 1/16 Inch joint, partially filled

JOINT FREQUENCY

Number of joints occurring within a 5-foot interval of core.

HARDNESS NUMBER

A relative measure of hardness found by averaging 3 readings from (A) the soil test rock classification hammer (steel base), (B) the Schmidt test hammer, Type L (steel base), or (C) the Schmidt test hammer, Type L (concrete base).

UNCONFINED COMPRESSIVE STRENGTH

Unconfined compressive strength test made on NX core (A) in laboratory or (B) in field.

AJA3651

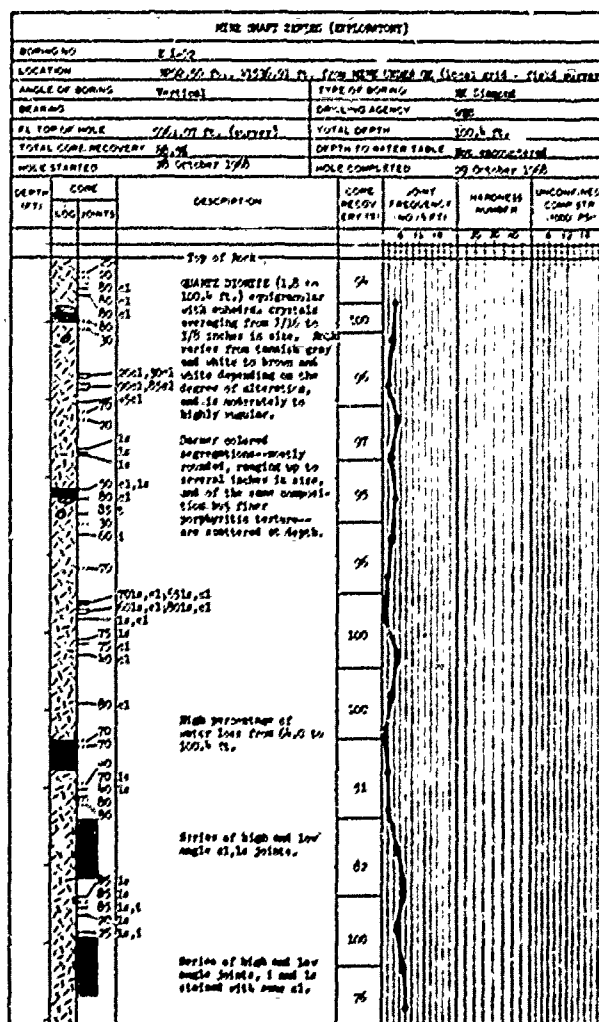
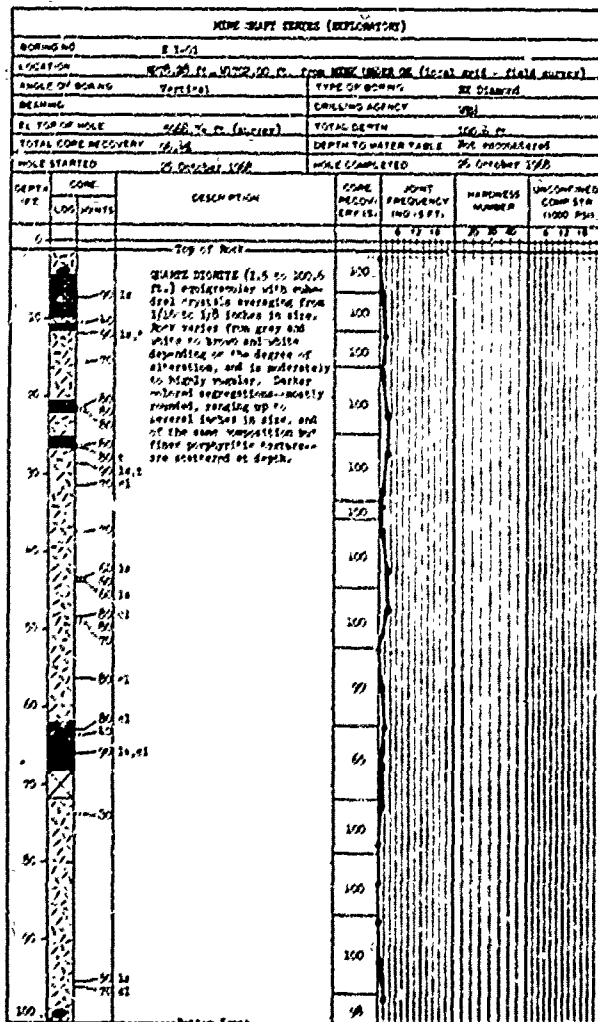


FIGURE 2-54. LOGS OF CORE BORINGS EL-01 AND EL-02 (REFERENCE 2-40)

AJA3650

- ▲ DWORSHAK DAM, GNEISS
- △ TWO FORKS DAM SITE, GNEISS AND SCHIST
- ◊ YELLOWTAIL DAM, LIMESTONE
- ◻ NEVADA TEST SITE, RHYOLITE AND DACITE
- NORTHWESTERN ILLINOIS, LIMESTONE
- ◊ GLEN CANYON DAM, SANDSTONE
- ◆ HAKENSACK GAS STORAGE FACILITY, SANDSTONE AND SILTSTONE
- MORROW POINT DAM, GNEISS AND SCHIST
- ▽ OLNEY MARYLAND, GNEISS
- TEHACHA PUMPING PLANT, GNEISS AND SANDSTONE
- ◆ WORLD TRADE CENTER, GNEISS AND SCHIST

C_f = 3D SONIC AND UPHOLE SEISMIC VELOCITIES

C_l = LABORATORY SONIC VELOCITY

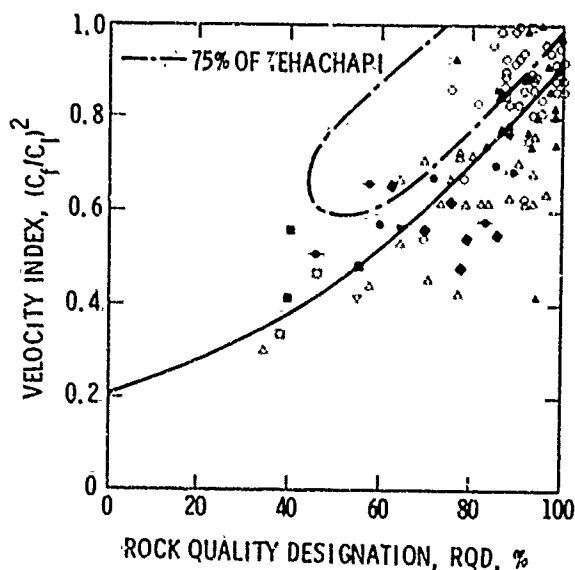


FIGURE 2-57. RELATIONSHIP BETWEEN ROCK QUALITY DESIGNATION AND VELOCITY INDEX (REFERENCE 2-84)

Geophysical Techniques. In addition to the surface seismic refraction survey mentioned previously, several borehole seismic techniques can be used to determine dynamic properties within the rock mass. These include

- a. Three-dimensional sonic log
- b. Cross-hole seismic survey
- c. Up-hole seismic survey (Figure 2-59)

- DWORSHAK DAM, GRANITE GNEISS, SURFACE GAGES
- ◊ DOWRSHAK DAM, GRANITE GNEISS, BURIED GAGES
- ◻ TWO FORKS DAMSITE, GNEISS
- YELLOWTAIL DAM, LIMESTONE
- ▲ GLEN CANYON DAM, SANDSTONE

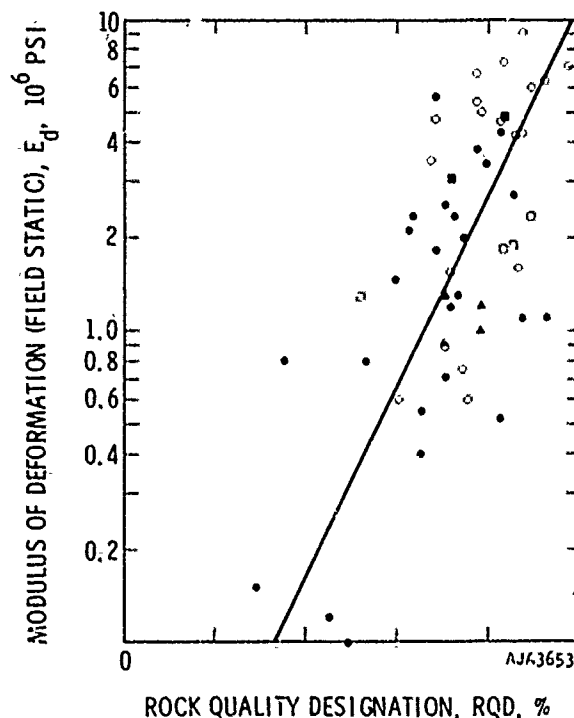


FIGURE 2-58. RELATION BETWEEN ROCK QUALITY DESIGNATION AND IN SITU STATIC MODULUS OF DEFORMATION (REFERENCE 2-85)

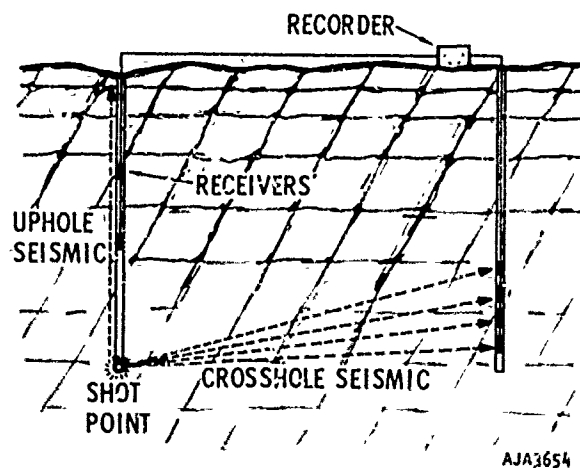


FIGURE 2-59. UP-HOLE AND CROSS-HOLE SEISMIC SURVEYS (REFERENCE 2-85)

Mechanical Properties of Rock

In all these techniques either (1) an electrical impulse or (2) a small charge is initiated in a borehole and the dilatational (c_p) and/or shear (c_s) wave arrivals are recorded by geophones or transponders located in boreholes. Using these and some other borehole logging techniques, density, porosity, and moduli can be determined. The moduli are usually determined from the data obtained from the 3-D velocity log, density log, and caliper log, and the following equations based on elasticity theory (Reference 2-84).

$$\nu = \frac{c_p^2 - 2c_s^2}{2(c_p^2 - c_s^2)}$$

$$G = \rho c_s^2$$

$$E = \rho c_p^2 \frac{(1 + \nu)(1 - 2\nu)}{(1 - \nu)}$$

$$K = \rho c_p^2 - 4G/3$$

ν = Poisson's ratio

c_p = P wave velocity

c_s = S wave velocity

G = Shear Modulus

ρ = Specific Gravity (density)

E = Young's Modulus

K = Bulk Modulus

Reference 2-57 contains typical computer printout of the calculations as a function of depth. Since these values are obtained at low stress levels, their apparent moduli are higher than would be measured at high stress levels. Also c_p measured in seismic surveys must differ from that measured in 3-D sonic logs (Figures 2-60, 2-61).

Resistivity. The electrical resistance of a unit cube of material is the reciprocal of the conductivity. Conductance in saturated rocks primarily takes place through the fluid in the void spaces so the resistivity is inversely proportional to the total porosity of a rock mass. In dry rocks, it is the resistivity of minerals and the amount of void space which are measured. Surveys are either conducted along a surface profile (analogous to a seismic refraction survey) or in a borehole (electrical logging). The

theory and experimental techniques are described in Reference 2-84. Resistivity has been correlated with rock quality and follows the same trends as seismic velocity. These are illustrated in Figure 2-62.

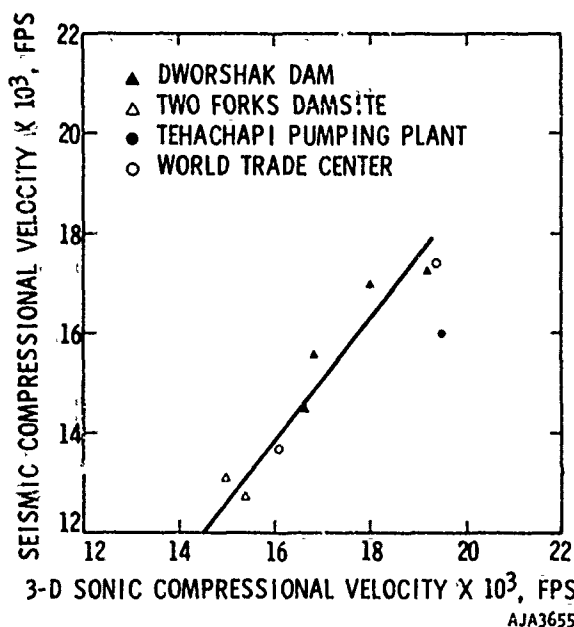


FIGURE 2-60. RELATIONSHIP BETWEEN 3-D SONIC AND SEISMIC COMPRESSIONAL WAVE VELOCITIES (CORRELATION BETWEEN TWO TYPES OF EXPERIMENTS) (REFERENCE 2-84)

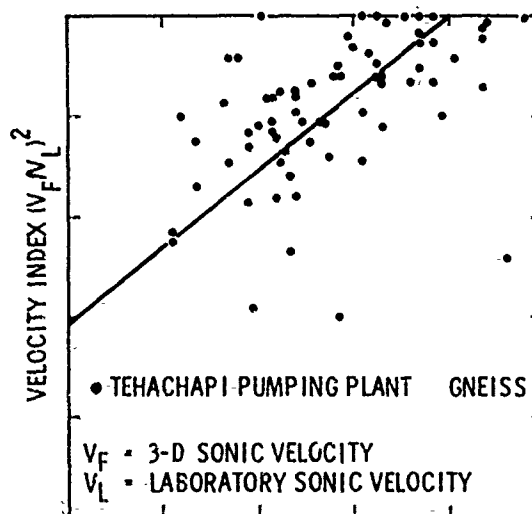
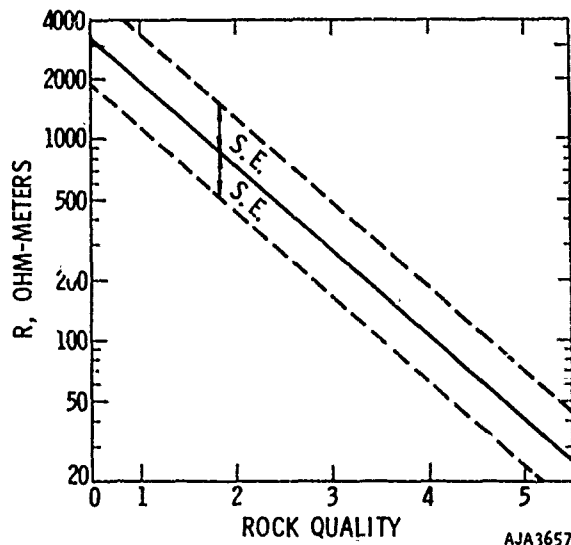
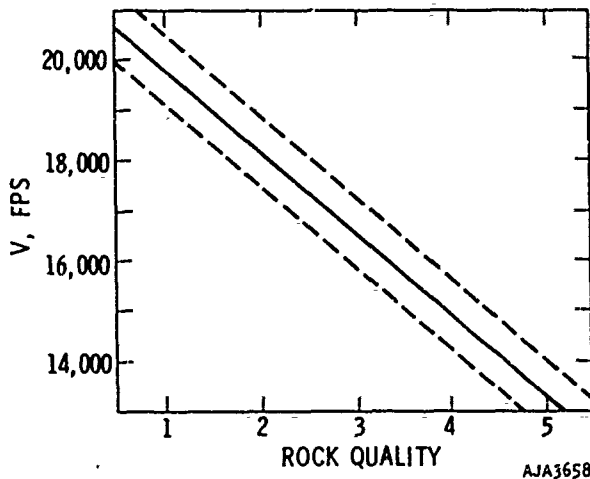


FIGURE 2-61. RELATIONSHIP BETWEEN RQD AND VELOCITY INDEX (REFERENCE 2-84)

Properties of Rocks at Strain Rates Above 10^2 sec^{-1}



(a) ELECTRICAL RESISTIVITY OF DEEP LAYER



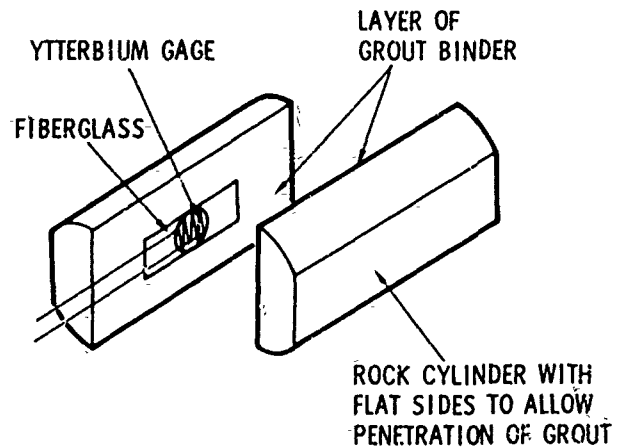
(b) SEISMIC VELOCITY OF DEEP LAYER

FIGURE 2-62. RELATIONSHIP BETWEEN ROCK QUALITY AND RESISTIVITY AND SEISMIC VELOCITY (REFERENCE 2-84)

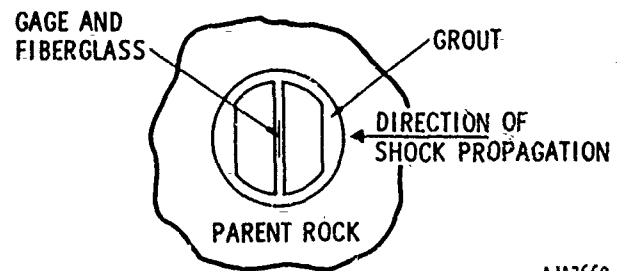
Shock Wave Testing. In situ measurements of stress in a diverging shock wave are made using a pressure-sensitive wire gage. The wire may be either manganin or ytterbium. The main problem in developing the gage has been the placement technique. The technique which is now adopted, shown in Figure 2-63, encases the gage in fiberglass to minimize stretching in the transverse directions. The gage and its fiberglass mount are then bonded with grout to the split core of Figure 2-63. The core is then replaced in a drill hole and bonded to the parent rock with more

grout. The end-on configuration to Figure 2-64 is preferred for some placement situations. A plot of stress attenuation versus distance for 1000-lb explosive charge is seen in Figure 2-65.

As is explained in Reference 2-87, small-scale shock wave tests are performed in situ as part of a material properties testing program. The purpose of these tests, such as Hudson Moon, is to supplement laboratory measurements by enlarging the volume of material tested. These small-scale in situ tests do not necessarily expose large-scale joint systems which may dominate the response of a site to a large yield explosion. In order to certify a site model for a large yield explosion, it is sometimes necessary to compare the results of such a field test with a computation based on the candidate model. Project Piledriver and the series of computations which followed the event illustrates an attempt to certify a model of the Piledriver site.



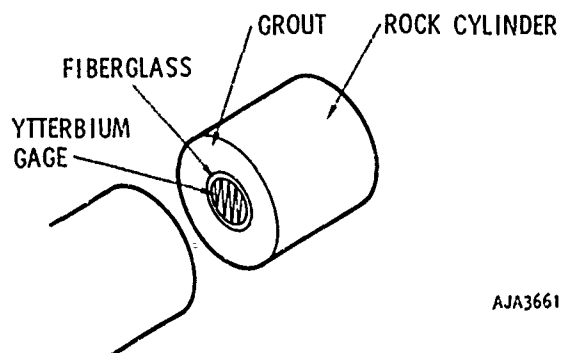
(a) EXPLODED VIEW OF SIDEWAYS MOUNTING



(b) SIDEWAYS MOUNTING IN PLACE

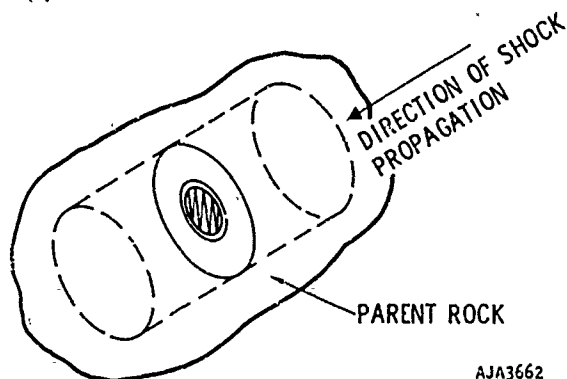
FIGURE 2-63. TECHNIQUE OF EMLACING STRESS GAGES IN-SITU (SIDEWAYS MOUNTING) (REFERENCE 2-87)

Mechanical Properties of Rock



AJA3661

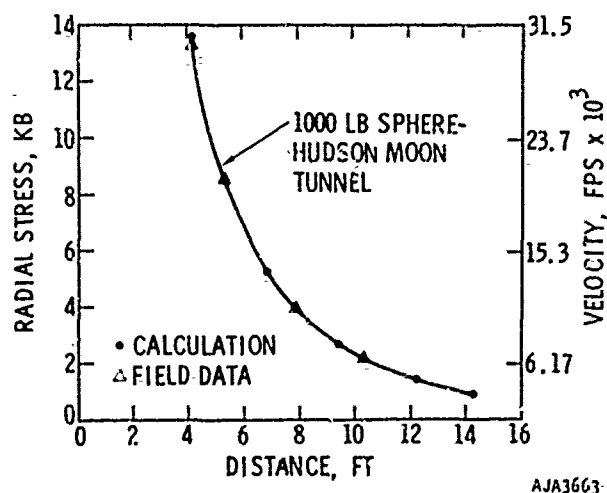
(a) EXPLODED VIEW OF END-ON MOUNTING



AJA3662

(b) END-ON MOUNTING OF GAGE IN SOFT ROCK

FIGURE 2-64. TECHNIQUE OF EMLACING STRESS GAGES IN SITU (END-ON MOUNTING) (REFERENCE 2-87)



AJA3663

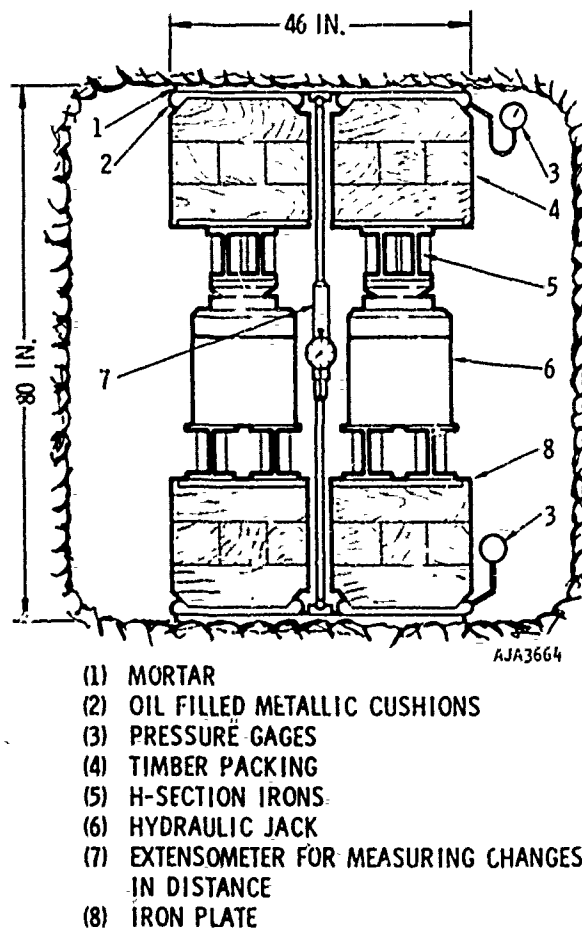
FIGURE 2-65. COMPARISON BETWEEN MEASUREMENTS AND A CALCULATION OF RADIAL STRESS IN A SPHERICAL SHOCK WAVE (REFERENCE 2-88)

Experimental Methods (Static)

There are several experimental methods for determining the in situ modulus of deformation and frictional properties of the rock mass. These methods differ considerably with regard to the volume of rock tested, expense, and assumptions made in obtaining the moduli. Among these are:

- Plate Jacking Test
- Uniaxial Jacking Test
- Pressure Chamber Test
- Radial Jacking Test
- Large Scale Uniaxial Compression Test
- Direct Shear Test

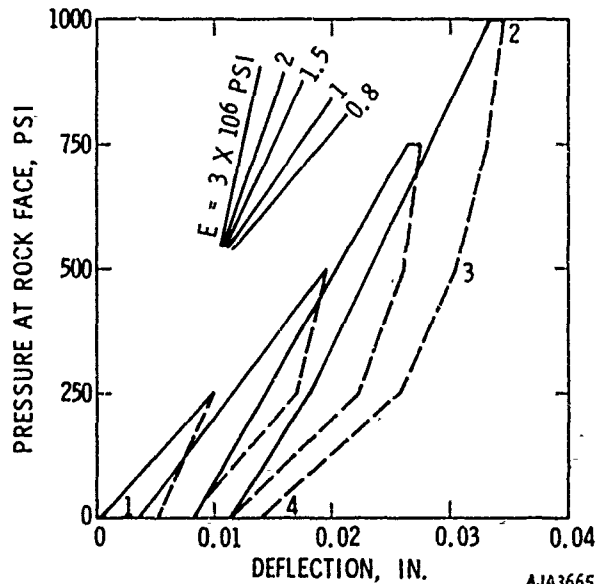
Plate Jacking. Plate jacking equipment which is designed to measure the effective modulus of a mass of rock is illustrated in Figure 2-66. The force exerted



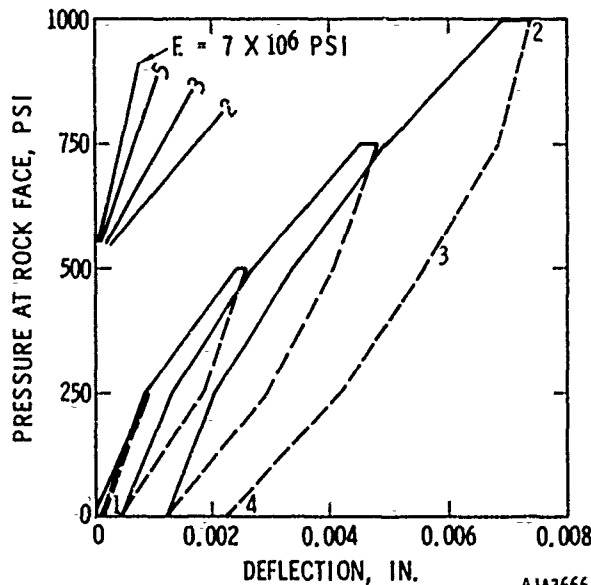
AJA3664

FIGURE 2-66. APPARATUS FOR PLATE JACK TESTS (REFERENCE 2-89)

by the hydraulic jacks is distributed by the timber packing and metallic cushions. The load is usually cycled over a period of a day or two at several different pressure levels. An extensometer which bears against the rock faces is used to determine deformation of the rock (Figure 2-67(b)). Other techniques may differ in detail but have the same basic elements.



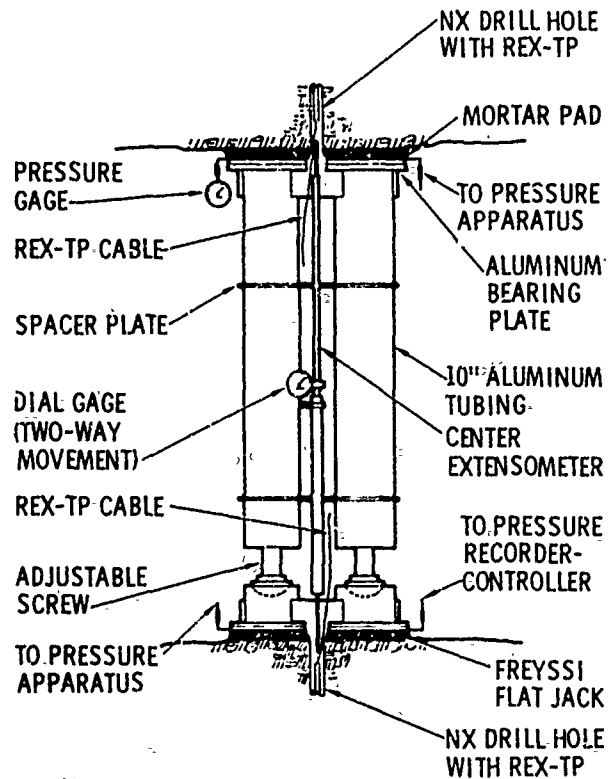
(a) CONCAVE UPWARD LOAD/DEFLECTION CURVE FROM A PLATE JACK TEST



(b) CONCAVE DOWNWARD LOAD/DEFLECTION CURVE FROM A PLATE JACK TEST

FIGURE 2-67. LOAD/DEFLECTION RELATIONS FROM PLATE JACK TESTS (REFERENCE 2-89)

Uniaxial Jacking Test. The uniaxial jacking test employs calibrated flat jacks to apply force and adjustable aluminum reaction columns (Figure 2-68). The resulting deformation is measured by a tunnel diameter gage and extensometers positioned in the tunnel wall (Reference 2-50). The orientation of the jacking system can be varied to suit geologic features. The load is typically cycled in much the same way as the plate jacking test.



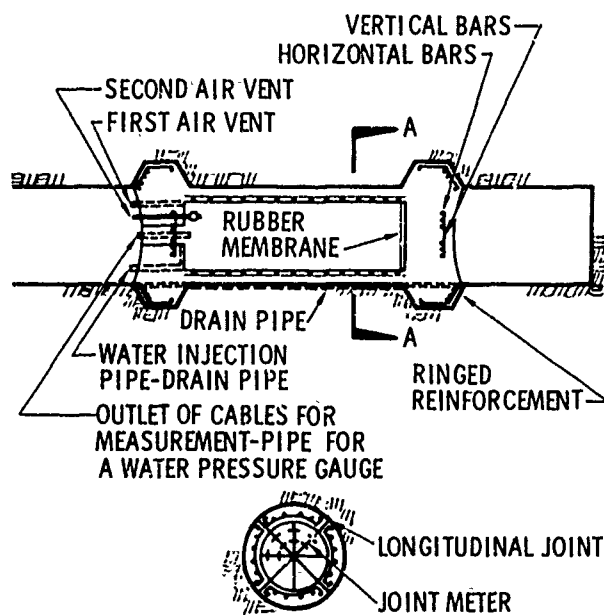
AJA3667

FIGURE 2-68. UNIAXIAL JACK FOR IN SITU MEASUREMENTS OF A DEFORMATION MODULUS (REFERENCE 2-90)

Pressure Chamber Test. The pressure chamber consists of installing and subsequently pressurizing an impermeable linear (bituminous material, lightly reinforced concrete, with or without an inner rubber membrane) in a test section of the tunnel (Figure 2-69). Deformations are measured using diametral or buried deformation gages. Analysis of the results is based on the elastic solution of a thick wall cylinder. A detailed discussion is presented in Reference 2-50.

Radial Jacking Test. The radial jacking test conducted by the U. S. Bureau of Reclamation is essentially a mechanical pressure chamber using several

Mechanical Properties of Rock



SECTION A-A

AJA3668

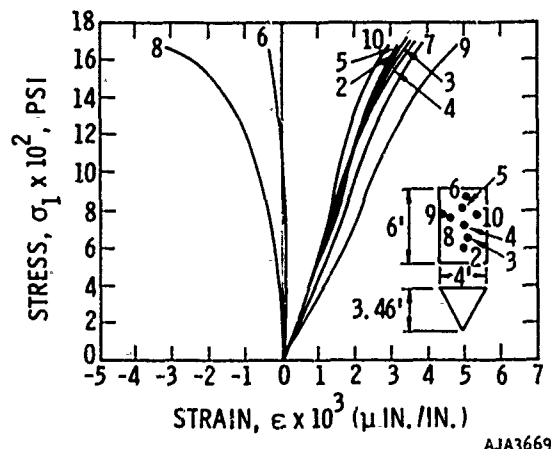
FIGURE 2-69. PRESSURE CHAMBER FOR IN SITU MEASUREMENT OF A DEFORMATION MODULUS (REFERENCE 2-84)

flat jacks set in structural rings installed and subsequently grouted in a test bore about 8.5 ft in diameter and 8 ft in length (Reference 2-50). The area loaded is about 32,000 in². Maximum pressures applied are on the order of 1000 psi, typical cyclic load sequence of 200 psi increments (0, 200, 0, 400, etc.) is held for a period of one to two days to account for creep. Deformation is measured primarily by multiple position extensometers and joint meters embedded in the tunnel walls. Linear deformation can be determined directly after the extensometer is calibrated.

In the plate, uniaxial and radial jacking tests, elasticity theory is used to calculate the modulus of deformation. Equations for normal deflections in the interior of a semiinfinite solid bounded by a plane surface are used in analyzing data from the plate and uniaxial jacking tests and a mathematical model using an infinitely long cylindrical hole in an infinite homogeneous mass is used for analyzing the radial jacking tests (Reference 2-50).

Large Scale Uniaxial Compression Tests. Large scale in situ uniaxial compression tests on prism-shaped specimens up to 6 x 9 ft have been conducted using a calibrated flat jack package to provide the axial load. Deformation of the sample is measured with DCDT's and large strain gages. Deformation

modulus (tangent modulus at 50 percent maximum stress) is derived directly from the stress-strain curves (Figure 2-70). The specimens and loading system are shown in Figure 2-71.



AJA3669

FIGURE 2-70. CEDAR CITY STRESS VERSUS STRAIN, IN SITU TEST NO. 6 (4 x 6 FT)



FIGURE 2-71. EXPERIMENTAL APPARATUS FOR IN SITU COMPRESSION TESTING OF LARGE ROCK SAMPLES

Properties of Rocks at Strain Rates Above 10^2 sec^{-1}

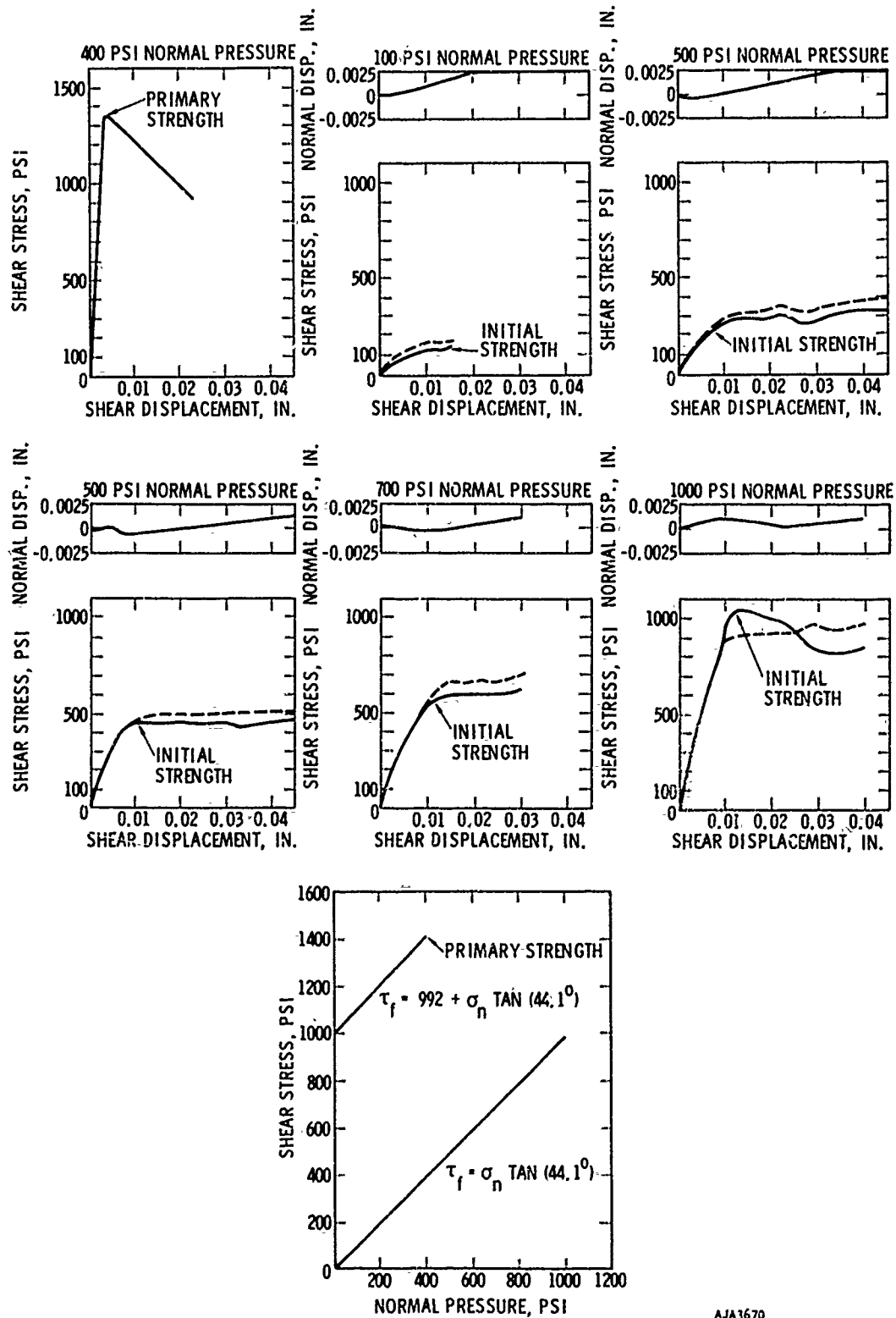


FIGURE 2-72. IN SITU SHEAR STRENGTH OF FOLIATED AMPHIBOLITE (REFERENCE 2-91)

Mechanical Properties of Rock

Direct Shear Tests. The frictional properties of joints play a role in the large displacements seen during nuclear and high explosive simulation experiments where joint blocks move relative to each other. Two types of in situ shear tests have been performed to measure these frictional properties. In the first test a normal load is applied by a hydraulic jack (either reacting against the roof or pulled by a cable) and the shear force by a second jack reacting against a side-wall. Typical results are shown in Figure 2-72. In the second test, single joints are tested using the technique discussed in the previous section where flat jacks are used to load a prism-shaped sample. Typical results are shown in Figure 2-73 for several different surface areas and angular relationships between the joint and axial loads. Both types of test indicate that frictional characteristics of joints are a function of (1) joint orientation, (2) joint filling material, and (3) joint surface roughness.

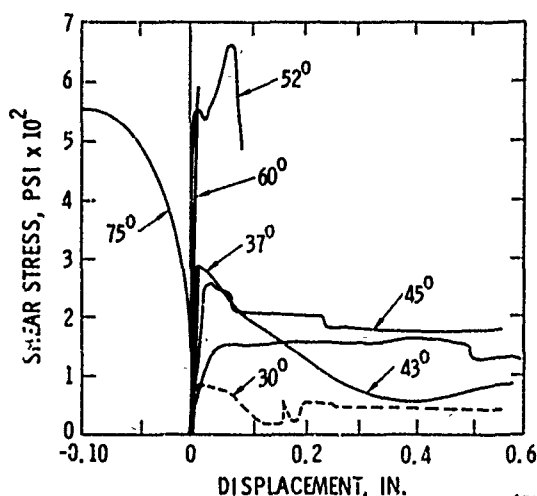


FIGURE 2-73. SHEAR STRESS VERSUS DISPLACEMENT FOR SPECIMENS WITH A SINGLE JOINT AT ANGLES FROM 30° TO 75° TO AXIS OF LOADING (REFERENCE 2-52)

TABLE 2-7. AVAILABLE EXPERIMENTAL DATA (REFERENCE 2-94)

Type of Property	Elastic	Unload	Yield	Yield/Crush	Strain Rate	Complex Shock Load/Unload	Two Dimensions
Type of Experiment	Static Ultrasonic Hugoniot	Static Release Isentrope	Static Hel	Static Indirect from impact unloading	Low- intermediate Decay of "Precursor" Direct impact	Designed load Variable release profile	Lab gun configurations Other
Initial Condition of Rock	Pressure Range Kbars						
Competent	0-8	Adequate	Adequate	Adequate	Little	Some	Some
	8-30	Some	Some	2-D	Indirect	Some	Some
	>30	Some	Some	2-D	Indirect	Some	Some
Cracked	0-8	Some	Some	Some	Little	None	None
	8-30	Some	Some	2-D	Indirect	None	None
	>30	None	None	2-D	Indirect	None	None
Saturated	0-8	Some	Some	None	None	None	None
	8-30	None	None	2-D	Indirect	None	None
	>30	None	None	2-D	Indirect	None	None

AA4822

SUMMARY

It is not presently possible to measure properties of rocks as they exist in situ over the complete pressure range (bars to megabars) of interest for ground motion calculations. Most data are derived from small laboratory samples rather than from in situ measurements. A composite picture of material behavior based on data from different types of experiments is difficult to develop because data are lacking in certain pressure ranges and because data are measured over a wide range of strain rates and stress states. For example, the relationship between the constitutive relations derived from static tests up to 8 kb and the equation-of-state data derived from pressure-volume-energy relations from dynamic shock wave experiments is not clear. The status of available data from laboratory tests in the different pressure regimes is summarized in Table 2-7 (Reference 2-94). Although the gaps in knowledge of laboratory properties of rocks may seem considerable, they are in fact small compared with the uncertainties involved in applying these data to in situ rock masses.

However, some of the gaps can be narrowed. For example, the variation of bulk modulus with hydrostatic pressure in laboratory samples appears to be similar to the behavior of large rock masses. In this respect, the mechanical behavior of rock may be considered qualitatively to be independent of scale. Thus, laboratory data may lead to accurate quantitative predictions of rock mass behavior to the extent that compositional, textural and structural features of the test rocks are representative of the in situ rock mass. The task of investigating in situ behavior in small-scale experiments will be easier if it turns out that the roles of homogeneous deformation and structural discontinuities such as joints or faults are mutually independent and can be tested independently. In wave propagation, homogeneous deformation might be the dominant effect when the spacing and areal extent of structural features is large compared with the length of the wave. Alternatively, if the spacing and areal extent of joints and faults is small compared with the length of the wave, then the rock mass is more likely to be dominated by discontinuities. Presently, the main problem is that the properties of rock masses are known from a few inadequate observations on model materials and from field tests for wave speed, resistivity and stiffness.

REFERENCES

- 2-1. Farmer, I. W., Engineering Properties of Rocks, Spon. London 1968.

- 2-2. Goodman, R. E., and J. M. Duncan, "The Role of Structure and Solid Mechanics in the Design of Surface and Underground Excavations in Rock," Structure Solid Mechanics and Engineering Design, Part 2, M. Te'eni, ed., Wiley-Interscience, 1971.
- 2-3. Jaeger, J. C., and N. G. W. Cook, Fundamentals of Rock Mechanics, Methuen, 1969.
- 2-4. Swolfs, H. S., Influence of Pore Fluid Chemistry and Temperature on Fracture of Sandstone Under Confining Pressure, Ph. D. Thesis, Texas, A & M University, 1971.
- 2-5. Green, S. J., R. J. Griffin and H. R. Pratt, Material Properties of a Shale for Shock Calculations--Obtained for El Paso Natural Gas Company, Technical Report TR 71-12, Terra Tek, Inc., 1971.
- 2-6. Swanson, S. R., Development of Constitutive Equations for Rocks, Ph. D. Thesis, University of Utah, 1969.
- 2-7. Green, S. J., et al., "Multiaxial Stress-Strain Behavior of Solenhofen Limestone and Westerly Granite at High Strain-Rates," Dynamic Rock Mechanics, G. B. Clark, ed., AIME, 1971.
- 2-8. Brace, W. F., B. W. Paulding and C. Scholz, "Dilatancy in the Fracture of Crystalline Rocks," J. Geophys. Res., Vol. 71, No. 16, 1966.
- 2-9. Stephens, D. R., Pressure-Volume Relationships for Tuffs and Rhyolites from the Nevada Test Site, UCRL 50578.
- 2-10. Mogi, K., "Effect of the Intermediate Principal Stress on Rock Failure," J. Geophys. Res., Vol. 72, No. 20, 1967.
- 2-11. Mogi, K., "Fracture and Flow of Rocks Under High Triaxial Compression," J. Geophys. Res., Vol. 76, No. 5, 1971.
- 2-12. Handin, J. C., H. C. Heard and J. N. Magourik, "Effects of the Intermediate Principal Stress on the Failure of Limestone, Dolomite, and Glass at Different Temperatures and Strain Rates," J. Geophys. Res., Vol. 72, No. 2, 1967.
- 2-13. Manzanti, B. B., and G. F. Sowers, Laboratory Testing of Rock Strength, ASTM Spec. Tech. Publ. No. 402, 1966.
- 2-14. Hoskins, E. R., "The Failure of Thick-Walled Hollow Cylinders of Isotropic Rock," Int. J. Rock Mech. Min. Sci., Vol. 6, 1969.

Mechanical Properties of Rock

- 2-15. Brown, W. S., S. R. Swanson and W. R. Wawersik, Influence of Dynamic Loading, Biaxial Loading and Prefracturing on the Stress-Strain and Fracture Characteristics of Rocks, Technical Report DASA-2713, 1971.
- 2-16. Donath, F. A., "Some Information Squeezed Out of Rocks," Am. Scientist, Vol. 58, No. 1, 1970.
- 2-17. Brown, W. S., and S. R. Swanson, Stress-Strain and Fracture Properties of Nugget Sandstone, Technical Report UTEC ME 71-058, University of Utah, 1971.
- 2-18. Handin, J., et al., "Experimental Deformation of Sedimentary Rocks Under Confining Pressure Tests," Bull. Am. Assoc. Petrol. Geol., Vol. 47, No. 5, 1963.
- 2-19. Brace, W. F., and R. J. Martin III, "A Test for the Law of Effective Stress for Crystalline Rocks of Low Porosity," Int. J. Rock Mech. Min. Sci., Vol. 5, 1968.
- 2-20. Griggs, D. T., F. J. Turner and H. C. Heard, "Deformation of Rocks at 500° - 800°C," Rock Deformation, Geol. Soc. America, Mem. 79, 1960.
- 2-21. Heard, H. C., "The Influence of Environment on the Brittle Failure of Rocks," Failure and Breakage of Rocks, C. Fairhurst, ed., AIME, 1967.
- 2-22. Handin, J., and R. V. Hayer, "Experimental Deformation of Sedimentary Rocks Under Confining Pressure Tests at High Temperature," Bull. Am. Assoc. Petrol. Geol., Vol. 42, No. 12, 1958.
- 2-23. Serdangecti, S., and G. D. Boozar, "The Effects of Strain Rate and Temperature on the Behavior of Rocks Subjected to Triaxial Compression," Min. Eng. Exp. Sta. Bull., Penn. State University, No. 76, 1961.
- 2-24. Heard, H. C., "The Effects of Large Changes of Strain Rate in the Experimental Deformation of Rock," J. Geol. Res., Vol. 71, No. 2, 1963.
- 2-25. Handin, J., "Strength and Ductility," Handbook of Physical Constants, S. P. Clark, Jr., ed., Geol. Soc. Am., Mem. 97, 1966.
- 2-26. Mogi, K., "Pressure Dependence of Rock Strength and Transition from Brittle Fracture to Ductile Flow," Bull. Earthquake Res. Inst., Tokyo University, Vol. 44, 1966.
- 2-27. Handin, J., and R. V. Hager, Jr., "Experimental Deformation of Sedimentary Rocks Under Confining Pressure Tests at Room Temperature on Dry Samples," Bull. Am. Assoc. Petrol. Geol., Vol. 41, 1957.
- 2-28. Swanson, S. R., and W. S. Brown, "An Observation of Loading Path Independence of Fracture of Rock," Int. J. Rock Mech. Min. Sci., Vol. 8, 1971.
- 2-29. Brace, W. F., and A. H. Jones, "Comparison of Uniaxial Deformation in Shock and Static Loading of Three Rocks," J. Geophys. Res., Vol. 76, 1971.
- 2-30. Wawersik, W. R., and C. Fairhurst, "A Study of Brittle Rock Failure in Laboratory Compression Experiments," Int. J. Rock Mech. Min. Sci., Vol. 7, No. 4, 1970.
- 2-31. Wawersik, W. R., and W. F. Brace, "Post-Failure Behavior of Granite and Diabase," Rock Mech., Vol. 3, No. 3, 1971.
- 2-32. Crouch, S. L., "Experimental Determination of Volumetric Strains in Failed Rock," Int. J. Rock Mech. Min. Sci., Vol. 7, No. 6, 1970.
- 2-33. Byerlee, J. D., and W. F. Brace, "Stick-Slip, Stable Sliding and Earthquakes--Effect of Rock Type, Pressure, Strain Rate, and Stiffness," J. Geophys. Res., Vol. 73, 1968.
- 2-34. Brace, W. F., and J. D. Byerlee, "Recent Experimental Studies of Brittle Fracture of Rocks," Failure and Breakage of Rock, C. Fairhurst, ed., AIME, 1967.
- 2-35. Byerlee, J. D., "Frictional Characteristics of Granite Under High Confining Pressure," J. Geophys. Res., Vol. 72, No. 14, 1967.
- 2-36. Byerlee, J. D., "Brittle-Ductile Transition in Rocks," J. Geophys. Res., Vol. 73, No. 14, 1968.
- 2-37. Brace, W. F., "California Earthquakes: Why Only Shallow Focus?," Science, Vol. 168, No. 3939, 1970.
- 2-38. Friedman, M., "Petrofabric Techniques for the Determination of Principal Stress Directions in Rocks," State of Stress in the Earth's Crust, W. R. Judd, ed., Am. Elsevier Publ. Co., 1964.
- 2-39. Scholz, C. H., "Microfracturing and the Inelastic Deformation of Rock in Compression," J. Geophys. Res., Vol. 73, No. 4, 1968.

References

- 2-40. Brace, W. F., and A. S. Orange, "Electrical Resistivity Change in Saturated Rock During Fracture and Frictional Sliding," J. Geophys. Res., Vol. 73, No. 4, 1968.
- 2-41. Nur, A. M., Effects of Stress and Fluid Inclusions on Wave Propagation in Rock, Ph. D. Thesis, M. I. T., 1969.
- 2-42. Brace, W. F., "Brittle Fracture of Rocks," State of Stress in Earth's Crust, W. R. Judd, ed., Elsevier Publ. Co., 1964.
- 2-43. Gray, K. E., "Some Rock Mechanics Aspects of Petroleum Engineering," Status of Practical Rock Mechanics, Grosvenor and Paulding, eds., AIME, 1968.
- 2-44. John, K., "Civil Engineering Approach to Evaluate Strength and Deformability of Regularly Jointed Rock," Rock Mechanics Theory and Practice, W. H. Somerton, ed., AIME, 1970.
- 2-45. Brown, E. T., and D. H. Trollope, "Strength of a Model of Jointed Rock," J. Soil-Mech. Found. Div., Proc. ASCE, 1970.
- 2-46. Piteau, D. R., "Geological Factors Significant to the Stability of Slopes Cut in Rock," Proc. Symp. Open Pit Mine Planning and Slope Stability, South Africa Inst. Mining and Metallurgy, Johannesburg, July 1970.
- 2-47. Hoskins, E. R., J. C. Jaeger and K. J. Rosengren, "A Medium Scale Direct Friction Experiment," Int. J. Rock Mech. Min. Sci., Vol. 5, 1968.
- 2-48. Jaeger, J. C., "The Behavior of Closely Jointed Rock," Rock Mechanics--Theory and Practice, W. H. Somerton, ed., AIME, 1970.
- 2-49. Coulson, J. H., The Effects of Surface Roughness on the Shear Strength of Joints in Rock, Technical Report MRD-2-70, Missouri River Division, Corps of Engineers, 1970.
- 2-50. Wallace, G. B., E. J. Slobir and F. A. Anderson, "Foundation Testing for Auburn Dam," Rock Mechanics--Theory and Practice, W. H. Somerton, ed., AIME, 1970.
- 2-51. Jaeger, J. C., and N. G. W. Cook, "Friction in Granular Materials," Structure, Solid Mechanics and Engineering Design, Part 1, M. Te'eni, ed., Wiley-Interscience, 1971.
- 2-52. Deere, D. U., et al., "Design of Surface and Near-Surface Construction in Rock," Failure and Breakage of Rock, C. Fairhurst, ed., AIME, 1967.
- 2-53. Rinehart, J. S., et al., Propagation Velocity of Longitudinal Waves in Rocks. Effect of State of Stress, Stress Level of the Wave, Water Content, Porosity, Temperature, Stratification, and Texture, Mining Engineering Series, Rock Mechanics.
- 2-54. Birch, F., "The Velocity of Compressional Waves in Rocks at 10 Kilobars--Part I," J. Geophys. Res., Vol. 65, No. 4, April 1960, pp. 1013-1102.
- 2-55. Wyllie, M. R., et al., "Elastic Wave Velocities in Heterogeneous and Porous Media," J. Geophys. Res., Vol. 21, No. 1, pp. 41-70.
- 2-56. Wang, C. - Y., "Velocity of Compressional Waves in Limestones, Marbles and a Single Crystal of Calcite to 20 Kilobars," J. Geophys. Res., Vol. 71, No. 14, July 15, 1966, pp. 3543-3547.
- 2-57. Schuster, S. H., and J. Isenberg, Free Field Ground Motion for Beneficial Facility Siting, Volume I--Equations of State for Geologic Media, SAMSO-TR-70-88, ATI-AJA-R-6819-776-2, June 30, 1970.
- 2-58. Private Communication from D. R. Stephens (Lawrence Radiation Laboratory), 1968.
- 2-59. Jones, A. H., and N. H. Froula, Uniaxial Strain Behavior of Four Geological Materials to 50 Kilobars, DASA-2209, March 1969.
- 2-60. Grine, D. R., Equations of State of Granite and Salt, UCRL-13004, Lawrence Radiation Laboratory, May 1961.
- 2-61. Ainsworth, D. L., and B. R. Sullivan, Shock Response of Rock at Pressures Below 30 Kilobars, WES TR 6-802, Army Engineer Waterways Experiment Station, November 1967.
- 2-62. Bass, R. C., et al., Hugoniot Data for Some Geological Materials, SC-4903(RR), Sandia Corporation, June 1963.
- 2-63. Shipman, F. H., et al., High Pressure Hugoniot Measurements for Several Nevada Test Site Rocks, DASA-2214, March 1969.
- 2-64. Lombard, D. B., The Hugoniot Equation of State of Rocks, UCRL-6311, Lawrence Radiation Laboratory, February 1961.
- 2-65. Bass, R. C., Additional Hugoniot Data for Geological Materials, SC-RR-66-548, Sandia Corporation, October 1966.

Mechanical Properties of Rock

- 2-66. McQueen, H. G., et al., "Hugoniot Equation of State of Twelve Rocks," J. Geophys. Res., Vol. 72, No. 20, 1967, p. 4999.
- 2-67. Rosenberg, J. T., et al., Dynamic Properties of Rocks, DASA-2112, Stanford Research Institute SRI PGU-6273, July 1968.
- 2-68. Isbell, W. M., Preliminary Data, General Motors Defense Research Laboratories.
- 2-69. Bass, R. C., et al., Hugoniot Data for Some Geologic Materials, SC-4903(RR), Sandia Corporation, June 1963.
- 2-70. Lombard, D. B., The Hugoniot Equation of State of Rocks, UCRL-6311, University of California, Lawrence Radiation Laboratory, February 1961.
- 2-71. Wiedermann, A. H., and O. E. Curth, Shock Unloading Characteristics of Crushable Rocks, Technical Documentary Report WL TDR-64-52, AFWL, Illinois Institute of Technology, August 1964.
- 2-72. Ahrens, T. J., et al., Dynamic Properties of Rocks, DASA-1868, Stanford Research Institute, September 1966.
- 2-73. Lane, K. S., and W. J. Heck, "Triaxial Testing for Strength of Rock Joints," Proc. Sixth Symp. on Rock Mech., University of Missouri, Rolla, 1964.
- 2-74. Maurer, W. C., "Shear Failure of Rock Under Compression," Soc. Petrol. Eng., Vol. 5, 1965.
- 2-75. Green, S. J., et al., Investigate the Effect of Material Strength on Wave Propagation in Rocks, Progress Report 8 to DASA, Washington, D. C., September 1967.
- 2-76. Isenberg, J., and F. S. Wong, Progress Report on Stress and Strain Distribution in Strain Rate Testing, R-7110-1787, Agabian-Jacobsen Associates, February 4, 1971.
- 2-77. Christensen, N. I., "Compressional Wave Velocities in Metamorphic Rock at Pressures to 10 Kilobars," J. Geophys. Res., Vol. 70, No. 24, December 15, 1965, p. 6147.
- 2-78. Isbell, W. M., et al., DASA Rock Study, Progress Report No. 7, General Motors Corporation, Manufacturing Development, February 3, 1967.
- 2-79. Shipman, F. H., W. M. Isbell and A. H. Jones, High Pressure Hugoniot Measurements for Several Nevada Test Site Rocks, Materials and Structures Laboratory, Manufacturing Development, General Motors Corporation, MSL-68-15, DASA-2214, March 1969.
- 2-80. Jones, A. H., and N. H. Froula, Uniaxial Strain Behavior of Four Geological Materials to 50 Kilobars, DASA-2209, General Motors Corporation, Manufacturing Development, March 1969.
- 2-81. Ahrens, T. J., Dynamic Properties of Rocks, Ground Shock Calculation Review Meeting, The Rand Corporation, Santa Monica, California, October 1965.
- 2-82. McKay, M. W., and C. S. Godfrey, Study of Spherically Diverging Waves in Earth Media, DASA-2223, Physics International Co., March 1969.
- 2-83. Kolb, C. R., et al., Geological Investigation of the Mine Shaft Sites, Cedar City, Utah, MS-2170, Army Waterways Experiment Station, Vicksburg, Mississippi, August 1970.
- 2-84. Deere, D. U., A. H. Merritt and R. F. Coon, Engineering Classification of In-Situ Rock, Report No. AFWL-TR-67-144, Air Force Weapons Laboratory, Kirtland AFB, New Mexico, 1971.
- 2-85. Deere, D. U., et al., "Design of Surface and Near Surface Construction in Rock Failure and Breakage of Rock," Proc. Eighth Symp. on Rock Mech., AIME, pp. 237-303.
- 2-86. Pratt, H. R., J. L. Bratton, and R. T. Zbur, Geology and Material Properties of the Estancia Valley Test Site, New Mexico, AFWL-TR-69-24, Air Force Weapons Laboratory, 1969.
- 2-87. Keough, D. D., et al., Constitutive Relations from In Situ Logranging Measurements of Stress and Particle Velocity, Interim Report, Phase 1, DASA 2685, Stanford Research Institute, 27 January 1971.
- 2-88. Robert Bjork, Personal Communication, 1971.
- 2-89. Shannon and Wilson, Inc., Report on In-Situ Tests, Dworshak Dam Site, for Army Engineer District, Walla Walls, Corps of Engineers, Seattle, 1964.
- 2-90. Wallace, G. B., E. J. Slebir, and F. A. Anderson, In-Situ Methods for Determining Deformation Modulus Used by the Bureau of Reclamation, ASTM Special Publ. 477, 1970, pp. 3-26.

List of General Sources

- 2-91. Wallace, G. B., E. J. Slebir, and F. A. Anderson, "Foundation Testing for Auburn Dam," Eleventh Symp. on Rock Mech., Berkeley 1969, p. 461-498.
- 2-92. Pratt, et al., In-Situ Rock Properties, Terra Tek Technical Reports 71-31 and 71-33, 1971.
- 2-93. Pratt, H. R., et al., In-Situ Rock Properties, Technical Report No. AFWL-TR-71-56, Air Force Weapons Laboratory, October 1971.
- 2-94. Sidney J. Green, Personal Communication, 1970.

LIST OF GENERAL SOURCES

Texts

- Stagg, K. G. and O. C. Zienkiewicz, ed., Rock Mechanics in Engineering Practice, John Wiley and Sons, New York, 1968.
- Obert, L. and W. I. Ouball, Rock Mechanics and the Design of Structures in Rock, John Wiley and Sons, New York, 1967.
- Jaeger, J. C. and N.G.W. Cook, Fundamentals of Rock Mechanics, Methuen and Co., Ltd., London, 1969.
- Farmer, I. W., Engineering Properties of Rocks. Spon. London 1968.
- Jaeger, J. C. Elasticity, Fracture, and Flow, Methuen and Co., Ltd., London, 1956.

References

- Clark, S. P. Jr., ed., Handbook of Physical Constants Geol. Soc. Am. Mem. 97
- ASTM STP 477, Determination of the In-Situ Modulus of Deformation of Rock, 1970
- ASTM STP 402, Testing Techniques for Rock Mechanics 1966
- ASTM STP 392, Instruments and Apparatus for Soil and Rock Mechanics, 1965
- ASTM STP 429, Determination of Stress in Rock, 1967
- Deere, D. U. and R. P. Miner, Engineering Classification and Index Properties for Intact Rock, Air Force Weapons Laboratory Tech. Rept. AFWL-TR-65-116, 1966
- Deere, D. U., A. H. Merritt, and R. R. Coon, Engineering Classification for In-Situ Rock, Air Force Weapons Laboratory, Tech. Rept. AFWL TR 67-144 1969

Journals and Abstracts

- Journal of Geophysical Research
- International Journal Rock Mechanics and Mining Science
- Rock Mechanics
- Tectonophysics
- Rock Mechanics Abstracts
- Geotechnical Abstracts
- Journal of the Soil Mechanics and Foundation Division, Proc. ASCE

SECTION 3

PROPERTIES OF SOILS

INTRODUCTION

This section discusses the properties of soils that govern its response to dynamic loading. As in the case of rocks, the basic governing properties are volumetric and shear stiffnesses, shear strength, and mass density. Major differences between the behavior of rocks and soils are due to differences in structure. Nevertheless, the same factors which affect basic properties of rocks also affect soils. The most important of these are stress intensity, stress state and loading history, porosity, interstitial pore fluids, and loading rate. To understand how these factors affect stress/strain and strength properties of soil, the relationship between the porosity, type of solid material, and stress history must be established.

Soil is the product of the chemical and physical weathering of rock. The particles may be transported by the forces of nature and deposited as sedimentary soils, or they may remain in place overlying the parent rock and forming residual soils. The weathering, transportation, and sedimentation develops soil deposits which may be broadly divided into coarse-grained soils and fine-grained soils. During deposition the behavior of coarse-grained soils is governed primarily by the forces of gravity, while the behavior of fine-grained soils is governed by interparticle forces of attraction and repulsion. Once soils have been formed, their behavior may be altered by stress changes due to glaciation or erosion, and changes in chemical environment such as the electrolyte concentration in the interstitial pore fluids.

Laboratory testing methods and the stress paths they impose are illustrated in Figure 3-1. Much of the behavior of soil is described below in terms of these methods.

The solid constituent of coarse-grained soil is made up of individual particles which are approximately equidimensional (References 3-2, 3-3) and have low specific surfaces (surface area per volume). The solid particles of coarse-grained soils, also called cohesionless soils, are classified as follows:

Gravel	2 in. to 6 in.
--------	----------------

Sand	0.06 in. to 2 in.
Silt	0.002 in. to 0.06 in.

The solid particles in coarse-grained soil thus may be as small as 0.002 in.

The degree of compactness is particularly important in the behavior of coarse-grained soils and depends primarily on the size, gradation, and particle shape of the solids. This is defined by the relative density, a measure of the relative compactness of the soil between its loosest state and its densest state. Relative density is defined as

$$D_r = \frac{e_{\max} - e_v}{e_{\max} - e_{\min}} (100\%) \quad (3-1)$$

where

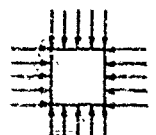
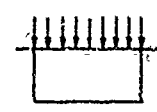
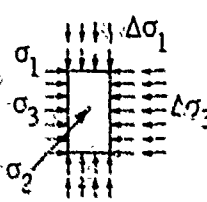
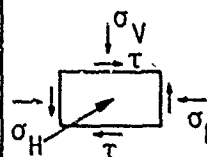
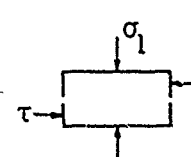
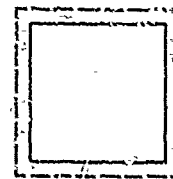
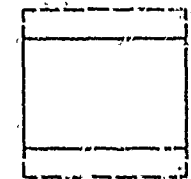
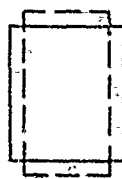
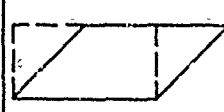

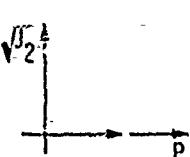
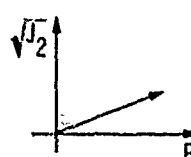
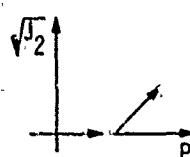
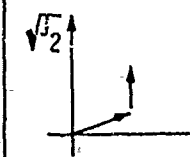
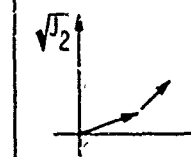
e_v	Void ratio of the soil	$\frac{V_v}{V_{sl}}$
V_v	Volume of void space/per unit volume (void space may be filled with gas and fluid space)	
V_{sl}	Volume of solids/per unit volume	
e_{\max}	Maximum void ratio for the soil	
e_{\min}	Minimum void ratio for the soil (Reference 3-4)	

Typical values of maximum and minimum void ratios, porosities, and unit weights are given in Table 3-1.

In general, the behavioral characteristics of coarse-grained soils are often categorized by the limiting states of relative density, e.g., loose and dense. Loose soil generally lies between 15 and 35 percent relative density, while dense soil is generally between 65 and 85 percent relative density. Loose coarse-grained soils tend to exhibit ductile stress/strain properties under a standard triaxial state of stress with a volume decrease during the application of shear stresses. Dense coarse-grained soils exhibit brittle stress/strain properties with a volume

Preceding page blank

Properties of Soils

TEST	ISOTROPIC COMPRESSION	UNIAXIAL COMPRESSION (OEDOMETER)	TRIAXIAL (COMPRESSION) (EXTENSION) (PLANE STRAIN)	SIMPLE SHEAR	DIRECT SHEAR
BASIC CONDITIONS	 $\sigma_1 = \sigma_2 = \sigma_3$		 $\Delta\sigma_1 \pm \text{OR} \Delta\sigma_3 \pm$		 $\sigma_1 \text{ CONSTANT AS } \tau \text{ APPLIED}$
TYPE OF DEFORMATION	VOLUMETRIC 	PRIMARILY VOLUMETRIC BUT SOME DISTORTION 	DISTORTION AND VOLUMETRIC 	DISTORTION 	PRIMARILY DISTORTION, BUT SOME VOLUMETRIC 
STRESS PATH			MOST COMMON $\sigma_c = \sigma_1 = \sigma_2 = \sigma_3$ $\sigma_c \text{ CONSTANT AS } +\Delta\sigma_1 \text{ IS APPLIED}$ 		
USES	FOR STUDY OF PURELY VOLUMETRIC STRAINS	VERY SIMPLE; APPROXIMATES CERTAIN FIELD CONDITIONS	STUDY STRESS/STRAIN AND STRENGTH PROPERTIES MANY VARIATIONS IN STRESS PATHS POSSIBLE	SHEAR STRESS/SHEAR STRAIN BEHAVIOR	SIMPLE TEST FOR MEASURING STRENGTH

AJA3672

FIGURE 3-1. STRESS/STRAIN TESTS ADOPTED IN PART (REFERENCE 3-1)

increase (dilatancy) during the application of shear (Figure 3-2).

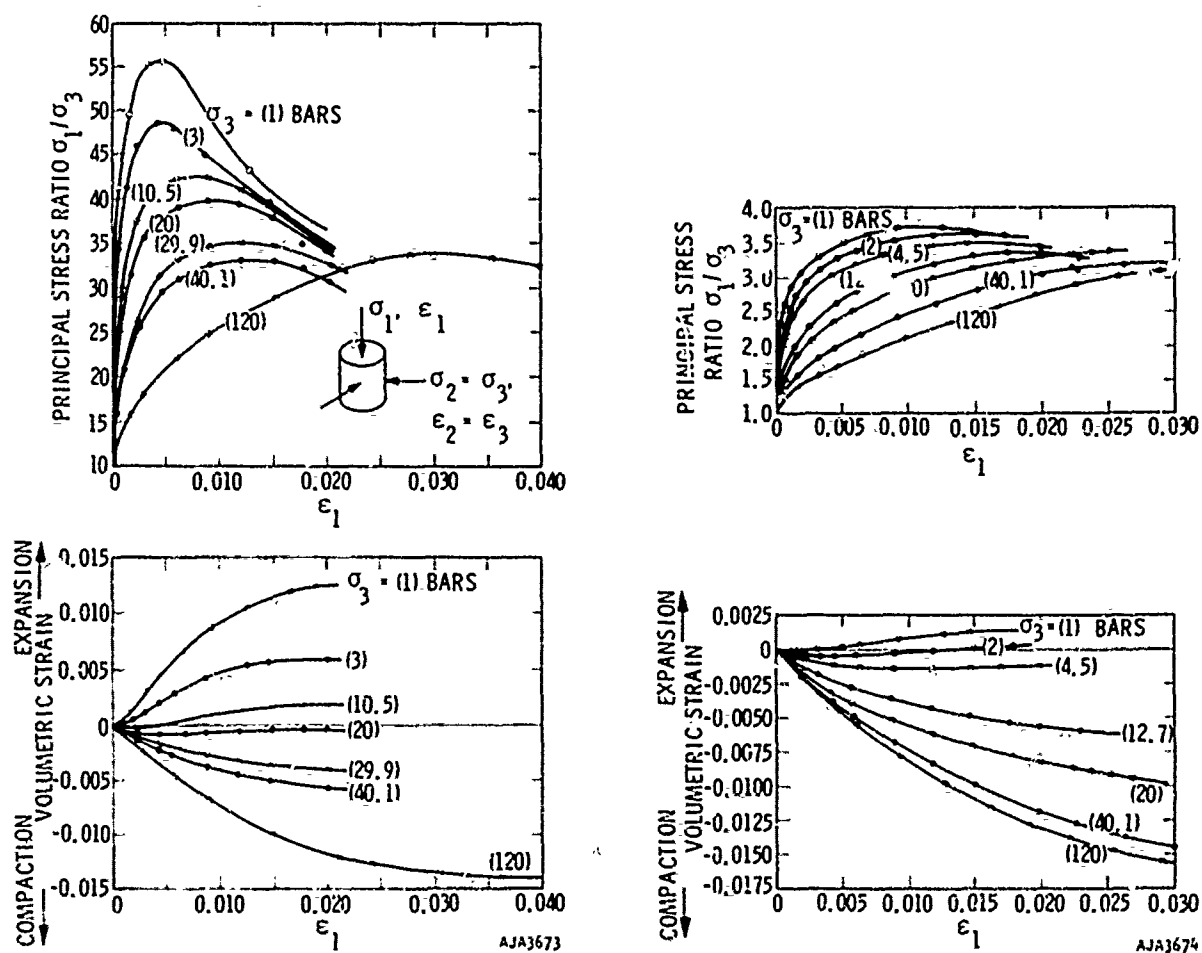
The boundary between these two states is defined by the void ratio at which shear deformation occurs without accompanying volume change. This is called the critical void ratio, and it varies inversely with mean normal stress (References 3-5, 3-6, and Figure 3-3). This difference in behavior between initially dense and initially loose dry sand seems to exist at pressures below 10 bars. At higher confining pressures, volume increase in dense sand is unlikely, and

the behavior is more readily characterized by a ductile type of stress-strain curve and a volume decrease as shown in Figure 3-2. Hence, the behavior in triaxial compression is highly dependent upon the confining pressure or mean normal stress.

Fine-grained soils are generally defined as those soils where the behavior and structure are heavily influenced by interparticle forces. They are called cohesive soils. The solid constituents of fine-grained soils are typically minerals formed by stacking sheets of Al and Si oxides into plate-like crystals. The

TABLE 3-1. MAXIMUM AND MINIMUM VOID RATIOS COARSE-GRAINED SOILS
(REFERENCE 3-80)

Description	Void Ratio		Porosity, %		Unit Weight Dry, PCF	
	Max	Min	Max	Min	Max	Min
Uniform spheres	0.92	0.35	47.6	26.0	--	--
Clean uniform sand	1.00	0.40	50	29	83	118
Silty sand	0.90	0.30	47	23	87	127
Fine to coarse sand	0.95	0.20	49	17	85	138
Silty sand and gravel	0.85	0.14	46	12	89	146

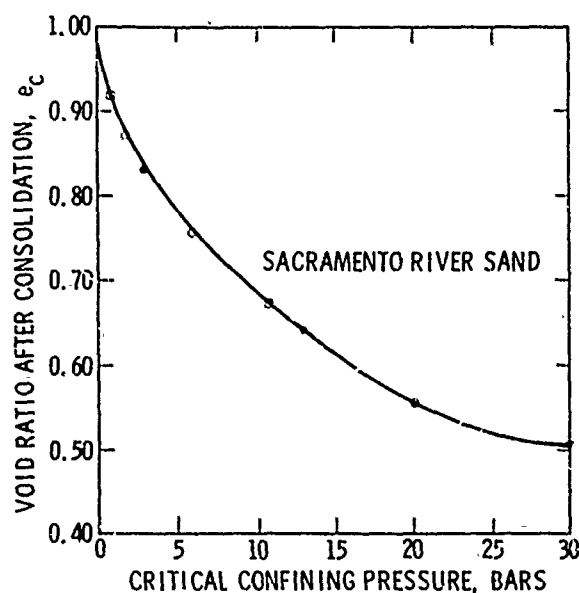


(a) DENSE SAND, INITIAL VOID RATIO 0.61

(b) LOOSE SAND, INITIAL VOID RATIO 0.87

FIGURE 3-2. RELATION BETWEEN CONFINING PRESSURE AND VOLUMETRIC STRAIN FOR SAND
AT TWO DIFFERENT INITIAL VOID RATIOS (REFERENCE 3-6)

Properties of Soils



AJA3675

FIGURE 3-3. THE CRITICAL VOID RATIO FOR COARSE-GRAINED SOIL, AT WHICH SHEAR DEFORMATION OCCURS AT CONSTANT VOLUME, IS UNIQUELY RELATED TO THE CONFINING PRESSURE (REFERENCE 3-6)

crystals have a net negative charge and a negative distribution charge over the surface (Reference 3-7).

The electrical charge depends on the particular characteristics of the mineral and the specific surface. The specific surface for the minerals of fine-grained soils may range from 300 to 30,000 times the specific surface of minerals found in coarse-grained soils. The average maximum dimension for clay particles is less than 0.002 in., and they extend down into the colloid sizes of 0.1 micron.

The clay platelets adsorb water (hydrate) and ions, which form a double layer and neutralize the electrical charge on the clay platelet. When clay platelets approach each other, i.e., double layers begin to overlap, they tend to repel one another due to the Coulombic electric forces between charges. A force of attraction also exists between platelets due to Van der Waal's forces. These forces depend on the spacing between particles and increase with decreased spacing (Reference 3-8). It is to be expected that water plays an important role in the behavior of fine-grained soils. Empirically defined limits of moisture content (weight of water divided by weight of solids per unit) are used to distinguish states of clay as solid, semisolid, plastic, or liquid. These moisture contents are defined by laboratory experiments and are called Atterberg Limits (Reference

3-9). A common index used to classify fine-grained soil is the plasticity index. This represents the moisture content range over which fine-grained soils behave plastically; that is, over which they can be molded without cracking and maintain shape. The plastic limit is the moisture content at which this plastic behavior begins and the liquid limit is the moisture content at which the soil behaves more like a liquid than a solid. The difference between these two moisture contents is the plasticity index.

The behavior of clay depends upon the moisture content and the orientation of the particles forming the mineral skeleton. Particles which are attached to each other will flocculate in a more or less edge-to-face orientation with particle-to-particle contact. Particles which tend to repel each other will disperse into a parallel array and there will be no particle-to-particle contact. Factors which reduce the thickness of the double layer such as increasing electrolyte concentration in the water will tend to cause clays to form in a flocculated state (salt water deposited clays).

The major component of volumetric strain in clay soils is due to changing of spacing between particles. Much of the strain which occurs in this way, especially in saturated clay from which water is expelled, is irrecoverable. Shear strains tend to align the particles in an orientation parallel to the slip surfaces; hence, flocculated clays tend to offer more resistance to shear deformation than dispersed clays (Reference 3-10).

Since deformation causing particle reorientation in clay is largely irrecoverable, the stress history has a significant influence on the stress/strain and strength behavior of clay soils. Typically, clay soils can be categorized by their past stress history as normally consolidated and overconsolidated. A normally consolidated clay in situ is under the maximum stress due to geostatic overburden which it has ever experienced. An overconsolidated state may result from the removal of a previous, larger stress. The soil is not completely consolidated or rebounded until the pore fluid stops flowing from the soil due to excess hydrostatic pore pressures. Clays consolidate upon settling out of suspension in water and can be overconsolidated by the removal of geostatic stress (erosion), addition of geostatic stress, and subsequent removal over long periods of time (glaciation) lowering and subsequent raising of the ground water table, etc.

The relationship between consolidation pressure and void ratio for a typical clay is shown in Figure 3-4 along with the corresponding triaxial stress/strain curves and shear strength versus effective confining pressure relationships. The influence of stress history on the undrained stiffness and strength of the clay is illustrated. The stress/strain behavior of dense sand resembles that of overconsolidated clay,

while the behavior of loose sand resembles that of normally consolidated clay.

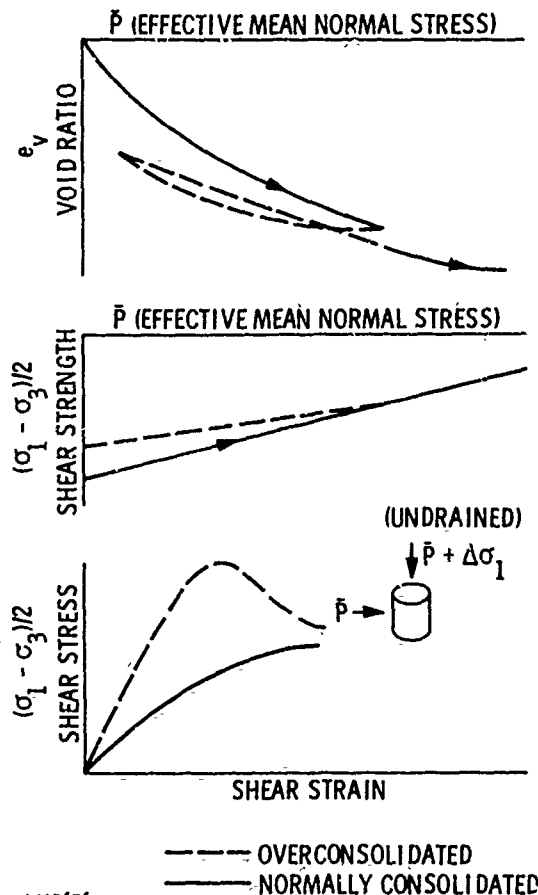


FIGURE 3-4. TYPICAL BEHAVIOR OF NORMALLY CONSOLIDATED AND OVERCONSOLIDATED CLAY

PROPERTIES OF SOILS

Effective Stresses in Soils

Both fine-grained and coarse-grained soils are affected by the percent saturation, or percent of void space filled with water. The behavior of soil varies greatly, depending on whether it is in the drained or undrained state during loading. The rate at which water can be expelled due to pore pressure gradients created by loading depends upon the size of the pore spaces and is characterized by the coefficient of permeability of the soil. Coarse-grained soils tend to have high permeabilities ($k = 10^{-1}$ cm/sec) while fine-grained soils tend to have low permeabilities

($k = 10^{-9}$ cm/sec). During shock loading, the rate of loading is generally faster than the rate at which pore fluid can be expelled. Since the fluid is generally much less compressible than the soil skeleton, pressure builds up in the pore fluid. In soils with less than 100 percent saturation, large volume changes can occur during dynamic loading by compressing the gas phase of the void space.

At all degrees of saturation, the behavior of soil depends on the effective confining stress (Reference 3-11). The effective stress is defined as the total stress minus the pore fluid pressure. In the case of fully saturated soils under slow or static loading, this principle is easy to apply since only the solid and liquid phase of the soil are involved and pore pressures can be evaluated (References 3-12, 3-13). Under shock loading conditions in a fluid-saturated solid, pore pressures develop in response to the propagation of the stress waves. Biot (Reference 3-14) found that two dilatational waves (compression waves under confined boundaries) develop, one in the fluid and one in the elastic structure of a porous elastic solid. Hardin (Reference 3-81) showed with the aid of Biot's theory that the dilatational velocity through the fluid of a saturated soil is higher than through the soil skeleton.

Structural coupling develops between the solid and fluid for dilatational waves but does not develop for shear waves. The velocity of propagation for shear waves and dilatational waves in the elastic structure will increase with confining pressure much faster than the velocity of propagation in the fluid. Although only qualitative conclusions can be drawn from this, it is likely that pore pressures due to shock loading differ from these due to equal static loads applied under undrained conditions. Rate-of-loading effects can be partially evaluated by comparing dynamic results with static results in the absence of pore fluid flow. In partially saturated soils, the effective stress depends upon the pore air and pore water pressures. These are more difficult to determine, and the effective stress principle is difficult to apply quantitatively to partially saturated soil. Qualitative application of effective stress principles (References 3-15, 3-16) is possible, however.

When soils are loaded, the stresses that develop within the soil mass are partitioned between the fluid phase and solid phase. This partitioning depends primarily on the relative compressibilities of the soil skeleton and pore fluid, which is influenced by soil structure, loading history, stress level, and degree of saturation. Strength and compressibility of the soil during loading depend primarily on the amount of applied stress transmitted to the solid skeleton. This is defined as the effective stress and is the total stress minus the pore pressure. The effective stress is transmitted within the soil framework by intergranular stresses at points of contact in coarse-grained soils and flocculated clays, and by interparticle electrical

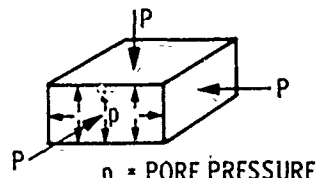
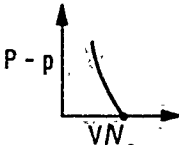
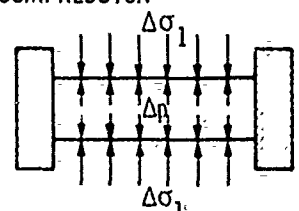

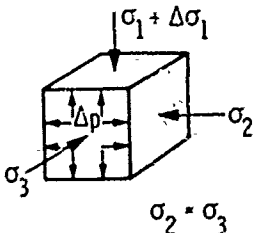
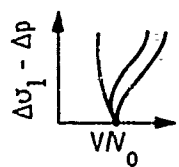
Properties of Soils

repulsion forces in dispersed clays. Due to the relatively small percent of total area in grain-to-grain contact, intergranular stresses may reach levels several thousand times higher than effective or total stresses. This can cause particle crushing in coarse-grained soils, but not usually in fine-grained soils.

If the void space is filled (saturated 100 percent) with a fluid which is incompressible relative to the soil skeleton, a large percentage of the total stress will be taken up by the pore fluid. Thus, experiments are often performed to determine how pore pressure develops as a soil is loaded. The result of an increase in pore pressure is a tendency for the pore fluid to flow toward zones of lower pore pressure, thus transferring the stress to the soil skeleton and relieving the pore pressures. However, even in soils of relatively high permeabilities, pore fluid does not migrate significantly during dynamic loading whose duration is less than about 100 milliseconds.

Pore pressures that develop in soil in response to an increase in total stress depend upon boundary conditions, amount of deformation, and degree of saturation. Typical pore pressure parameters are shown in Figure 3-5, which relate the pore pressures to total stress in uniaxial strain, hydrostatic compression, and triaxial compression experiments.

The influence of effective stresses on the behavior of soil appear in results obtained by Hendron, et al., (Reference 3-17), as shown in Figure 3-6. If the initial saturation is sufficiently high so that as the soil is compressed it reaches 100-percent saturation, then from that point on the increase in mean normal stress is practically all accounted for by an increase in pore-water pressure. If the effective confining stress is not increased, the strength of the soil cannot increase. Test Number 5 in Figure 3-6 never reaches 100-percent saturation; hence, the effective stress increases with the total stress and the soil strength increases. Test

	VOLUME CHANGE VS EFFECTIVE STRESS	PORE PRESSURE PARAMETER	
HYDROSTATIC COMPRESSION  <p>$p = \text{PORE PRESSURE}$</p>		$\bar{B} = \Delta p / \Delta p$	SATURATED SOIL $\bar{B} \approx 1$ INTACT ROCK $0.25 \leq B \leq 0.55$ BOULDER CLAY $S = 93\% \quad \bar{B} = 0.69$ $S = 87\% \quad \bar{B} = 0.33$ $S = 76\% \quad \bar{B} = 0.10$
ONE-DIMENSIONAL COMPRESSION 		$\bar{C} = \Delta p / \Delta \sigma_1$	SATURATED SOIL $\bar{C} \approx 1$ PARTIALLY SATURATED SOIL $0 < \bar{C} < 1$
TRIAXIAL COMPRESSION  <p>$\sigma_2 = \sigma_3$</p>		$\Delta p = \bar{B}[\Delta \sigma_3 + \bar{A}(\Delta \sigma_1 - \Delta \sigma_3)]$ $S = 100\%$ $\bar{A} = \frac{(\Delta p - \Delta \sigma_3)}{(\Delta \sigma_1 - \Delta \sigma_3)}$	$S = 100\%$ AT FAILURE VERY LOOSE FINE SAND $\bar{A} = 2 \text{ TO } 3$ SENSITIVE CLAY $\bar{A} = 1.5 \text{ TO } 2.5$ NORMALLY CONSOLIDATED CLAY $\bar{A} = 0.7 \text{ TO } 1.3$ LIGHTLY OVERCONSOLIDATED CLAY $\bar{A} = 0.3 \text{ TO } 0.7$ HEAVILY OVERCONSOLIDATED CLAY $\bar{A} = -0.5 \text{ TO } 0$ (REFERENCE 3-11 AND 3-8?)

AJA3677

FIGURE 3-5. PORE PRESSURE PARAMETERS

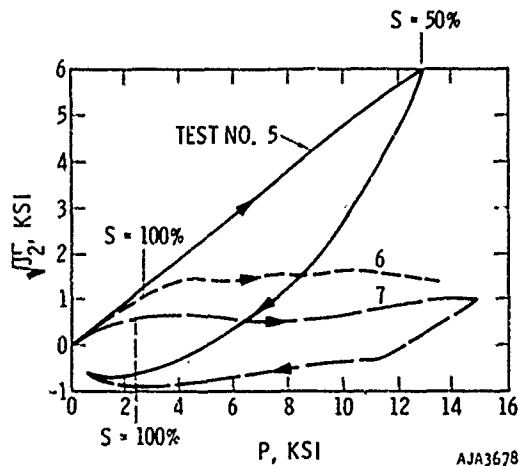


FIGURE 3-6. RELATIONSHIP BETWEEN P AND $\sqrt{J_2}$ FOR SOILS REACHING DIFFERENT DEGREES OF SATURATION DURING LOADING IN UNIAXIAL STRAIN (REFERENCE 3-17)

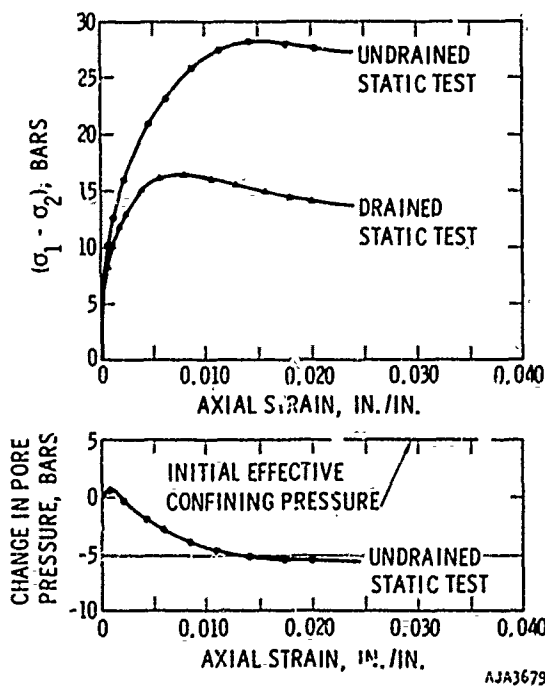


FIGURE 3-7. PRESSURE OF FLUID IN PORES AFFECTS SHEAR STIFFNESS AND STRENGTH. (IN THIS EXAMPLE, PORE PRESSURE DECREASES BELOW ATMOSPHERIC PRESSURE SO THAT THE EFFECTIVE CONFINEMENT EXCEEDS THE EXTERNALLY APPLIED CONFINEMENT.) (REFERENCE 3-18)

Number 7 reaches 100-percent saturation at a mean normal stress of 2240 psi, and no significant increase in strength occurs beyond this point. If the pore pressure becomes negative during undrained loading, an effective stress greater than the total stress results. This causes the soil to be stronger and stiffer than it is in the dry or drained state, as is illustrated in Figure 3-7. The drained strength of loose sand is greater than its undrained strength because loose sand tends to decrease in volume during shear, thus causing the pore pressures to increase as the load is applied.

In partially saturated soil, the effective stress is greater than the total stress since pore pressures are negative due to the surface tension of the water adhering to the soil particles. The surface tension lessens as the degree of saturation increases. The result is to decrease initial effective stress, thus causing an apparent lubricating effect in the stress/strain behavior. This behavior demonstrates the influence of effective stresses on compressibility, as shown in Figure 3-8.

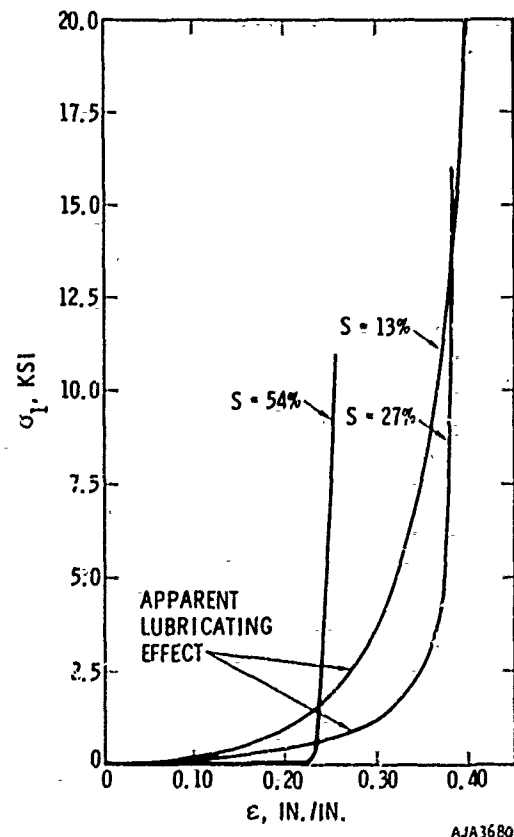


FIGURE 3-8. INFLUENCE OF DEGREE OF SATURATION ON STRESS/STRAIN RELATIONS UNDER UNIAXIAL STRAIN (REFERENCE 3-17)

Properties of Soils

The preceding discussion indicates that it would be preferable to consider the effective stress in the development of models to represent the strength and compressibility of soil up to a stress level where solid particle interaction controls the behavior of soil. However, in dynamic experiments it is usually not feasible to separate pore pressure from total stress. As a result, behavior of the soil and the models are most often defined in terms of total stress. At high stresses, where voids may be eliminated, plastic flow or melting of the solid constituent occurs. The particulate behavior of soils is less important, and the effective stress does not have the same meaning. Yield and deformation behavior might resemble characteristics shown in Figure 3-9, where the pore pressure depends on loading, history effects, temperature, compressibility of the soil skeleton, compressibility of the pore fluid, total stress path, state of stress including initial conditions, and void ratio.

Constitutive Behavior of Coarse-Grained Soils

Soil behavior depends on the type of minerals making up the solid phase, the void ratio, the degree of saturation and chemical composition of pore fluid, the stress history (overconsolidation ratio), the stress path, and the stress level. Theories of ideal particle

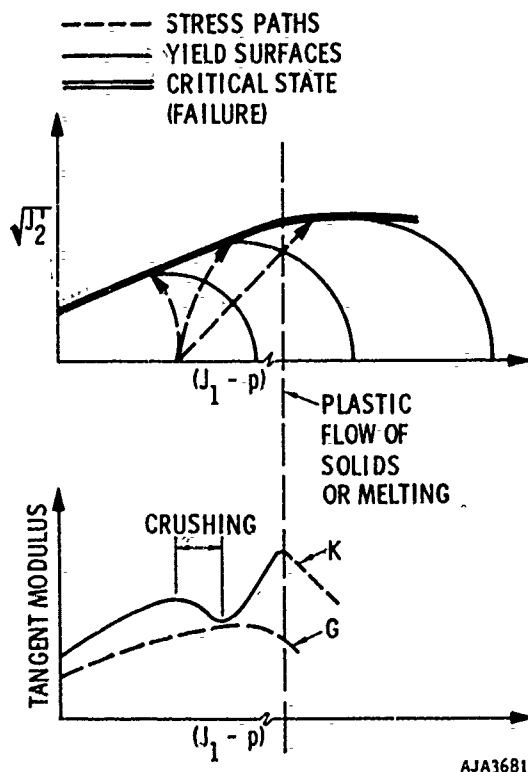


FIGURE 3-9. INFLUENCE OF EFFECTIVE STRESS

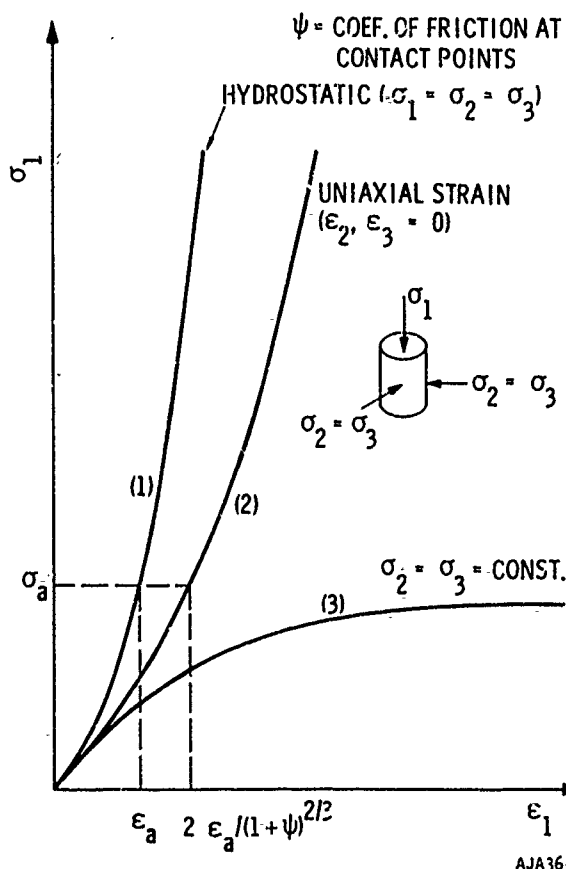


FIGURE 3-10. COMPRESSIVE STRESS/STRAIN RELATIONS FOR ELASTIC SPHERES SUBJECTED TO THREE TYPES OF LOADING ARE SIMILAR TO THOSE GENERALLY FOUND FOR COARSE-GRAINED SOILS

behavior (References 3-19 through 3-25) give some insight into the behavior of coarse-grained soil by analyzing the behavior of idealized packings of elastic spheres. These theories predict nonlinear behavior, as shown in Figure 3-10. The nonlinearity arises from the geometry of the surfaces in contact and not from the properties of the individual particles. In the hydrostatic and one-dimensional configuration, resistance to deformation is primarily a resistance to volume changes. The triaxial state of stress with constant radial stress represents resistance to deformation primarily from shearing resistance.

One theory (Reference 3-21) indicates that the mean stress is proportional to the $3/2$ power of the volumetric strain for a face-centered cubic array of elastic spheres subjected to hydrostatic compression. The constant of proportionality depends on Poisson's ratio and the shear modulus of the sphere material. This theory was extended by Hendron (Reference 3-22)

to one-dimensional compression, and similar stress/strain relationships were derived for loading and unloading. The stress/strain behavior is influenced by the coefficient of sliding friction between elastic spheres. The sliding motions give rise to irreversible movements, and the array of elastic spheres absorbs energy during a cycle of loading and unloading in one-dimensional compression. Theoretical considerations indicate that the percent of energy absorbed during loading and unloading in one-dimensional compression is a constant for a given material and depends only on the coefficient of friction at the contact points (Figure 3-11). Although the exact behavior of soil is not well defined by ideal packings of elastic spheres, many of the important behavioral characteristics are depicted by those theories. Work of Reference 3-24 shows the possibility of a negative rate of change of the tangent modulus associated with initial stress conditions and the transition from elastic shear distortions to gross sliding between particles.

The theoretical studies also demonstrate the relationship between the major and minor principal

stresses under uniaxial strain conditions. The stresses required to restrain the soil laterally are directly related to the coefficient of friction between solid particles. The restraining stresses become partially "locked in" and are the major principal stress where the soil is unloaded.

The study of ideal packings in triaxial compression (Reference 3-25) where the primary resistance to deformation is shearing resistance have resulted in relationships between principal stresses at failure such as

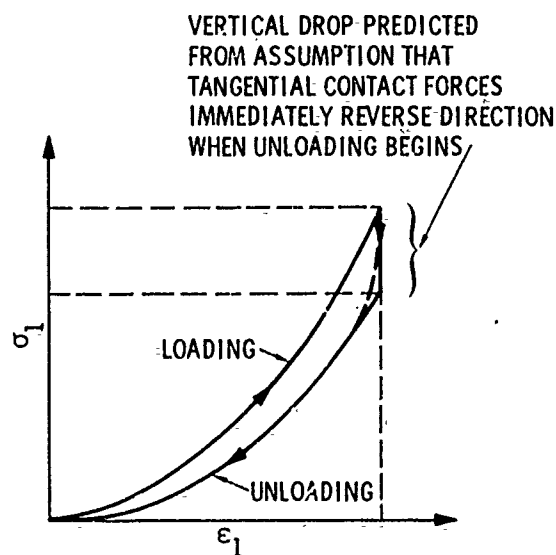
$$\frac{\sigma_1 - \sigma_3}{\sigma_3} = \frac{\sqrt{6} + 8\psi}{\sqrt{6} - 4\psi} \quad (3-2)$$

where ψ is the coefficient of friction at the contact points. The relationships developed indicate that the angle of internal friction is due to friction at particle contacts plus a component due to the structural arrangement of the particles.

The volume change and strength of an assembly of dry particles subjected to shearing stresses has been studied extensively (References 3-26, 3-27). The studies indicate that dilatancy and strength depend on the friction at contacts, the geometry of packing, and the energy loss in remolding.

Mean Normal Stress/Volumetric Strain. Experimental results on the behavior of dry coarse-grained soil under hydrostatic compression indicate three distinct phases in the mean normal stress/volumetric strain (P/μ) relationship. The first phase occurs at low stress levels (below 10 bars), where the soil behavior is significantly influenced by the initial void ratio and the initial state of stress (References 3-5, 3-28). The second phase occurs when intergranular stresses become sufficiently high to cause crushing of the soil grains. The third phase occurs after the influence of the initial void ratio and crushing have diminished.

Irreversible strains occur upon unloading in phase one and decrease nearly linearly with an increase in the relative density (Reference 3-29). At these stress levels the soil grains are relatively free to move around, and the irreversible nature of the P/μ relationship is attributed to unstable grains that move to more stable positions upon application of hydrostatic stresses. The soil generally reaches a stable arrangement after cyclic loading, and very limited hysteresis occurs beyond a few cycles of equal hydrostatic loading. The number of cycles required to reach this state increases with an increase in the void ratio of the soil. The actual P/μ relationship in phase one is not as stiff as the $3/2$ power relationship predicted by theory and described above. This results from the number of contacts between grains being increased continuously as the stress is increased.

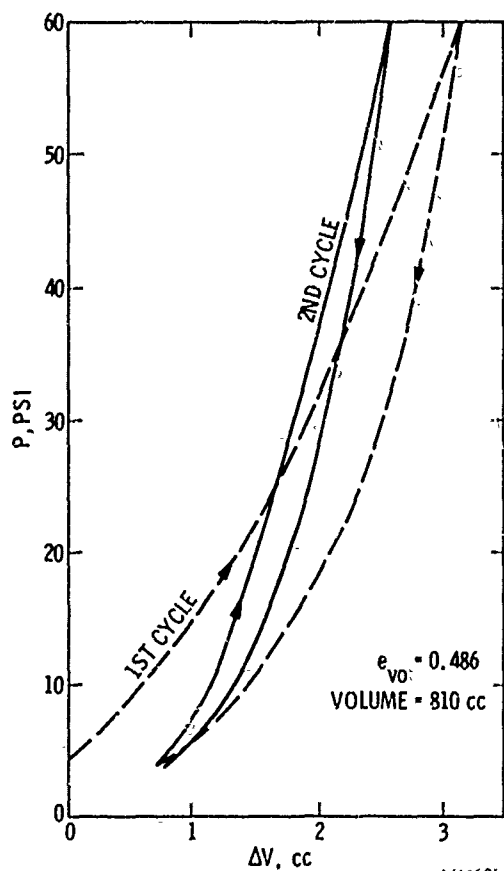


$\Delta e/e$ = PERCENT ENERGY ABSORBED DUE TO
LOADING AND UNLOADING
= $2\psi/(1 + \psi)$ FOR FACE CENTERED ARRAY

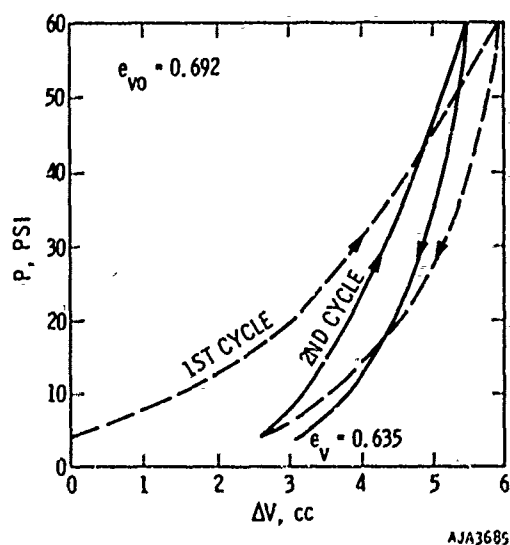
AJA3683

FIGURE 3-11. LOADING AND UNLOADING COMPRESSIVE-STRESS/STRAIN RELATION FOR ELASTIC SPHERES SUBJECTED TO UNIAXIAL STRAIN. THIS RELATION IS SIMILAR TO THAT GENERALLY FOUND FOR COARSE-GRAINED SOILS. (REFERENCE 3-22)

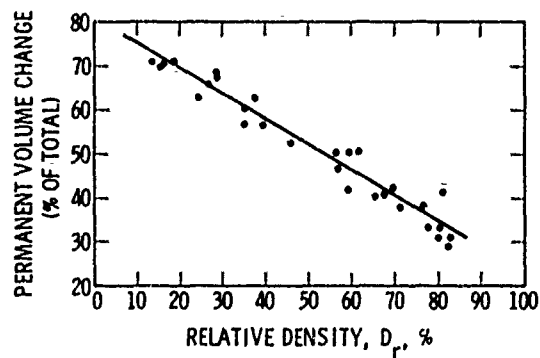
Properties of Soils



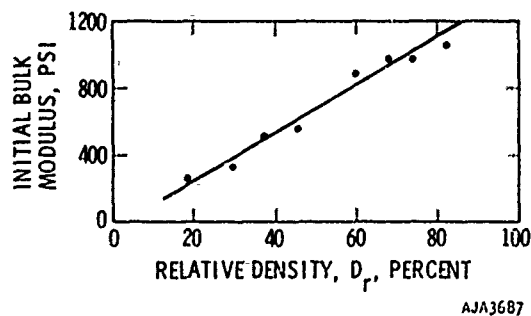
(a) HYDROSTATIC COMPRESSION OF DENSE SAND
(REFERENCE 3-28)



(b) HYDROSTATIC COMPRESSION OF LOOSE SAND
(REFERENCE 3-28)



(c) PERMANENT COMPACTION OF SAND
VARIES WITH RELATIVE DENSITY
(REFERENCE 3-29)



(d) INITIAL BULK MODULUS OF A SAND
INCREASES WITH RELATIVE DENSITY
(REFERENCE 3-29)

FIGURE 3-12. BULK PROPERTIES OF DRY SAND
UNDER HYDROSTATIC COMPRESSION
DEPENDS STRONGLY ON INITIAL
VOID RATIO OR RELATIVE DENSITY

Evidence on this behavior is shown in Figure 3-12.

Eventually, the hydrostatic stress becomes great enough to crush the individual particles, and the original structure of the soil is changed (Reference 3-5). Crushing is most intense during this second phase of hydrostatic loading up to a breakdown stress, which may occur around 100 bars. The breakdown stress usually defines the stress required to eliminate all the effects of the initial void ratio which involve size, shape, and distribution of grains. In this range the crushing, rearrangement of grains, and subsequent readjustment in contact stresses occurs with some time lag. Under dynamic loading and unloading at these stress levels, coarse-grained soils are stiffer than under static loading because there is insufficient time to permit readjustment of the internal framework. A transition zone in the P/μ relationship may exist above the breakdown stress, where some further

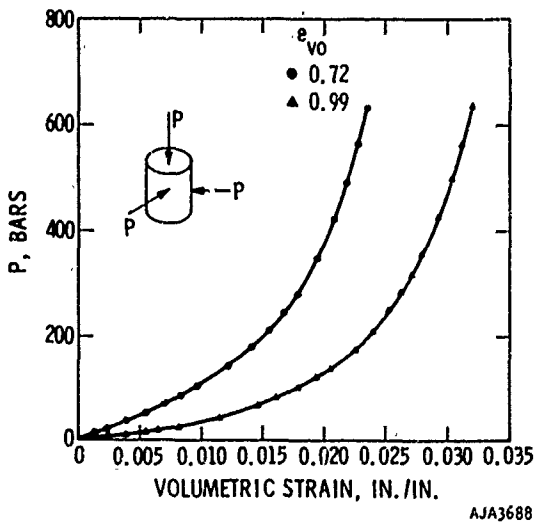


FIGURE 3-13. PRESSURE VERSUS VOLUMETRIC STRAIN RELATIONS FOR HYDROSTATIC LOADING OF A SAND AT TWO DIFFERENT INITIAL VOID RATIOS (REFERENCE 3-5)

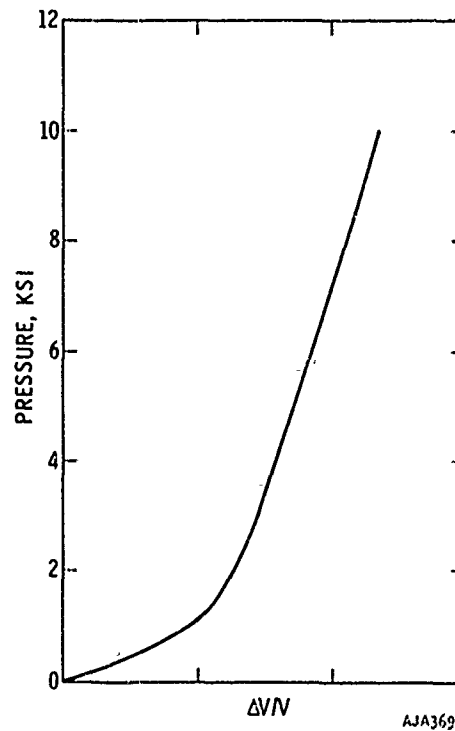


FIGURE 3-15. PRESSURE/VOLUMETRIC STRAIN RELATION FOR DRY OTTAWA SAND (REFERENCE 3-31)

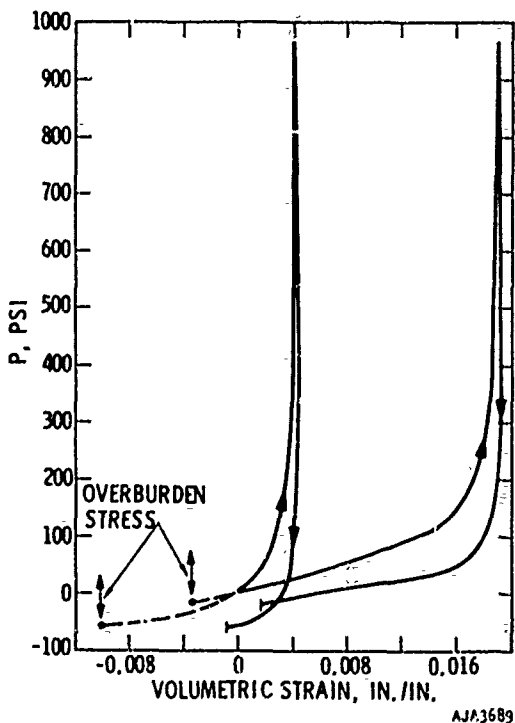


FIGURE 3-14. PRESSURE VERSUS VOLUMETRIC STRAIN RELATIONS FOR HYDROSTATIC LOADING AND UNLOADING OF SAND AT TWO DIFFERENT LOCATIONS (REFERENCE 3-62)

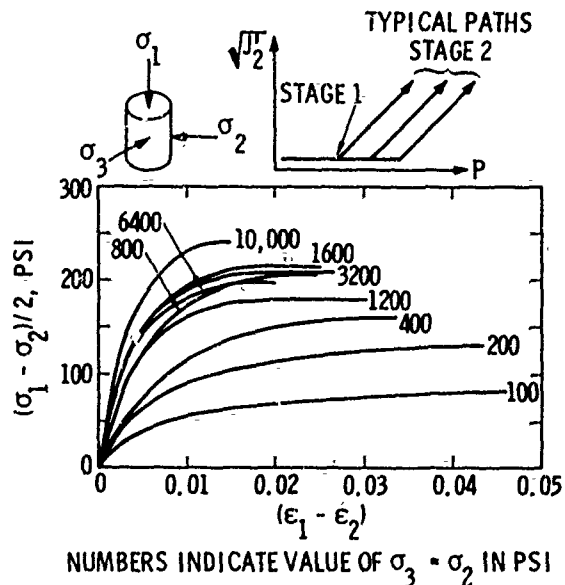
crushing and rearrangement occurs. However, crushing and readjustment of grains diminish rapidly as initially loose and dense soils approach the same void ratio. Above 200 bars the influence of the initial void ratio on the bulk tangent modulus seems to disappear for this soil, as indicated by the P/μ curves in Figure 3-13. Figure 3-14 shows evidence of appreciable hysteresis and residual strain due to hydrostatic compression. It is worthwhile noting, however, that most of the energy absorption occurs in the initial phase of the P/μ curve. At stresses above 10 bars, the soil unloads nearly along the loading path.

The third phase of the hydrostatic compression curve occurs above 200 bars, where the hydrostatic compression curve may become approximately linear as shown in Figure 3-15. Most of the strain above this level is expected to be recoverable upon loading.

The stress levels at which the various phases of behavior appear differ for different soils. The results in Figures 3-12 through 3-15 are intended to show typical behavior.

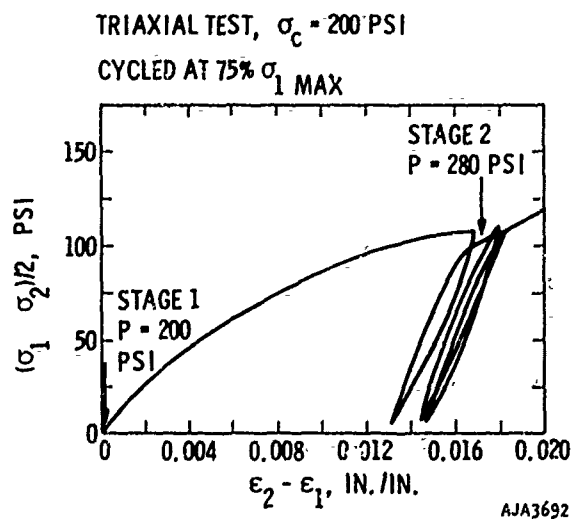
Deviatoric Stress/Strain Relations in Coarse-Grained Soils. The effect of mean normal stress on deviatoric stress/strain relations and the tendency for deviatoric stresses to contribute to volumetric

Properties of Soils



AJA3691

(a) TRIAXIAL COMPRESSION TESTS



AJA3692

(b) CYCLIC LOADING IN TRIAXIAL COMPRESSION

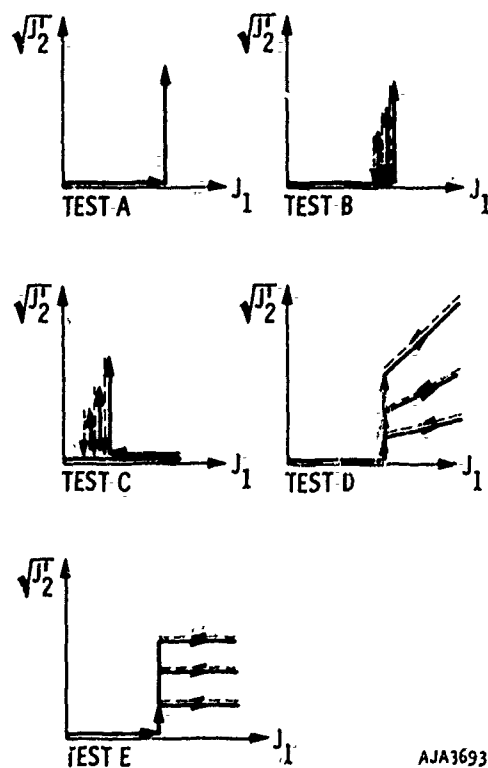
FIGURE 3-16. SHEAR STRESS/STRAIN RELATIONS FOR MCCORMICK RANCH SAND (REFERENCE 3-30)

strain are the main topics of this subsection. Typical shear stress/strain relations from standard triaxial compression tests are shown in Figure 3-16. The main features of these relations are as follows:

- The shear stress/strain relations are concave to the shear strain axis and irreversible shear strain occurs.

- The initial slope or initial shear modulus increases with the amount of initial effective confining pressure. (Stage 1)
- The maximum shear stress increases with effective confining pressure.
- If the previous maximum shear stress is not exceeded during several cycles of unloading and reloading, the unloading/reloading shear stress/strain relations are approximately linear.
- The mean normal stress is greater at Stage 2 than at Stage 1 in a standard triaxial test, and the shear modulus is influenced by both the level of shear stress and the mean normal stress.

Partly to overcome the difficulty mentioned in (e) above, a series of tests has been performed where the deviatoric stress can be varied independently of the mean normal stress (Reference 3-32). The stress paths investigated are shown in Figure 3-17. The results shown in Figure 3-18 confirm those of Figure 3-16(b). This behavior, which may be characterized



AJA3693

FIGURE 3-17. STRESS PATHS FOR INVESTIGATING DEFORMATION PATHS UNDER DEVIATORIC STRESS (REFERENCE 3-32)

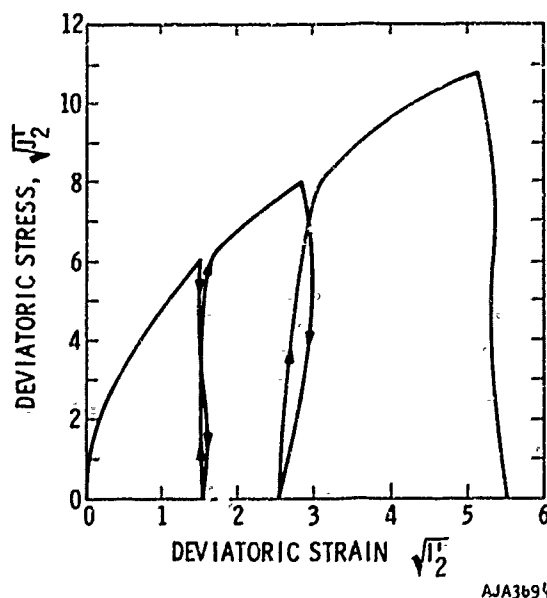


FIGURE 3-18. DEVIATORIC STRESS/STRAIN RELATIONS FOR A SAND IN A TEST WHERE THE MEAN NORMAL STRESS IS CONSTANT, TEST B, FIGURE 3-17 (REFERENCE 3-32)

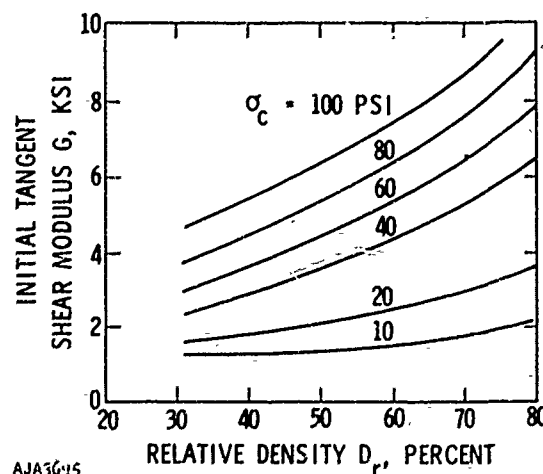
by a nonlinear virgin loading curve and an approximately linear unloading/reloading curve, is observed up to stress levels near failure or maximum stress. Near failure, however, the unloading/reloading curves become increasingly nonlinear.

As would be expected in materials which rely on intergranular friction for strength and stiffness, the tangent shear moduli for coarse-grained materials depend on relative density and confining pressure. Figure 3-19 shows how the initial shear modulus increases with relative density and confining pressure. The initial shear modulus affects such parameters as seismic shear wave velocity. Thus higher shear wave velocities are expected at increasing depths.

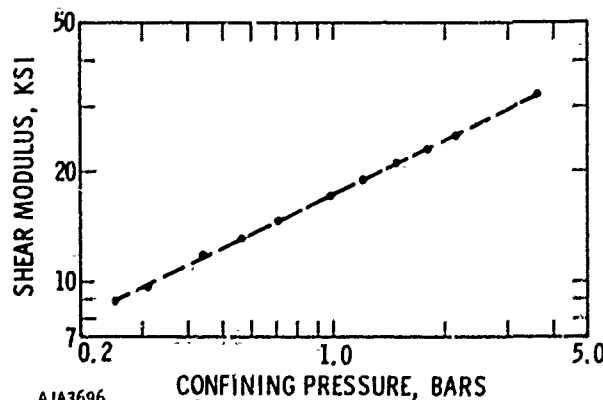
It has already been shown that deviatoric stresses induce volumetric strains in coarse-grained soils. (See Figures 3-2(a) and 3-2(b).) Tests on coarse-grained soil, which maintain constant mean normal stress during the application of deviatoric stresses, show a tendency for volumetric expansion near failure. The amount of volumetric increase depends on the void ratio and the effective pressure. For example, as the effective confining pressure increases, the tendency for volumetric expansion as deviatoric stresses are applied decreases; at pressures above some critical value, volume expansion does not occur.

The deviator-stress/volumetric-strain relation under constant mean normal stress is shown in Figure 3-20. The companion deviatoric stress versus deviatoric strain curve is shown in Figure 3-18.

If the mean normal stress is increased in a proportional loading test, the volume may increase or decrease because, in this type of test, deviatoric stresses increase concurrently with mean normal stress. The amount of compaction due to an increasing mean normal stress decreases as the difference among principal stresses increases (principal stress ratio increases). It is evident from Figure 3-21 that in a proportional loading test, volume expansion occurs if the principal stress ratio is high enough. For the case shown in Figure 3-21 the transition between compaction and expansion appears to be at a principal stress ratio of between 4 to 4.5.



(a) INITIAL TANGENT SHEAR MODULUS DEPENDS ON CONFINEMENT AND RELATIVE DENSITY (REFERENCE 3-29)



(b) INITIAL SHEAR MODULUS OF A DRY SAND INCREASES WITH CONFINING PRESSURE (REFERENCE 3-61)

FIGURE 3-19. SHEAR MODULUS OF SAND INCREASES WITH CONFINING PRESSURE

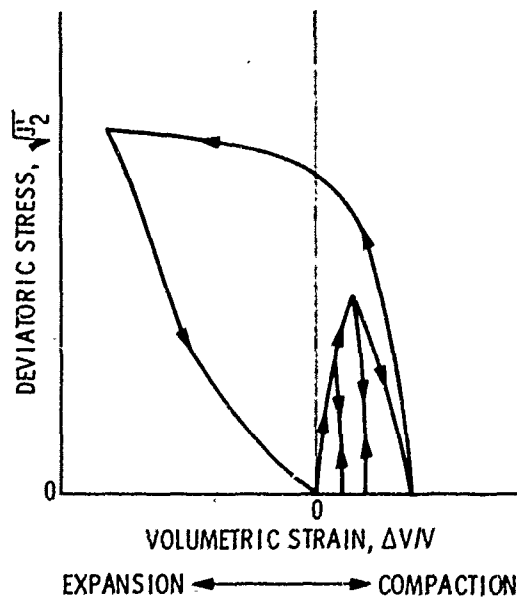


FIGURE 3-20. VOLUMETRIC STRAIN VERSUS DEVIATORIC STRESS FOR A COARSE-GRAINED SOIL SUBJECTED TO A CONSTANT MEAN NORMAL STRESS OF 15 PSI (REFERENCE 3-32) (REFERENCE 3-32)

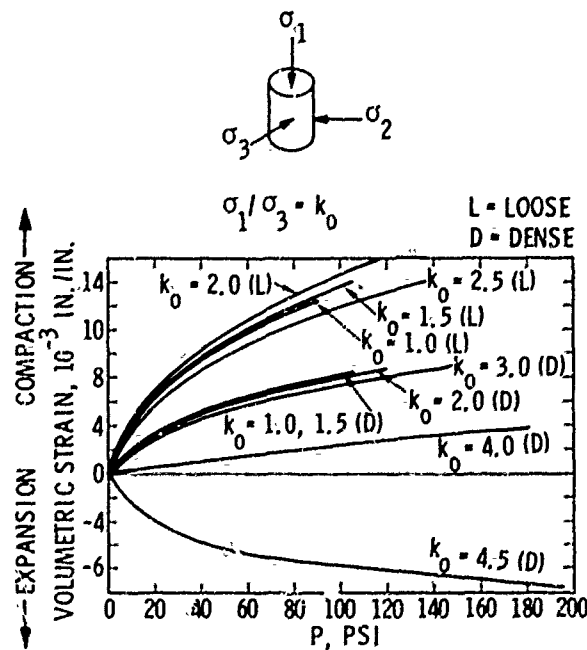


FIGURE 3-21. VOLUMETRIC STRAIN IN COARSE-GRAINED SOILS SUBJECTED TO PROPORTIONAL LOADING MAY INCREASE OR DECREASE DEPENDING ON PRINCIPAL STRESS RATIO (REFERENCE 3-33)

Test C in Figure 3-17 determines whether the subsequent pressure/volumetric strain relation for hydrostatic loading is influenced by previous cycles of loading and reloading in the deviatoric stress. The finding is that the subsequent pressure/volumetric strain relation is not appreciably affected unless the shear stress approaches failure. If failure in shear is approached, there is a tendency for plastic volumetric expansion, which makes the subsequent pressure/volumetric strain relation more compressible.

In addition to the concept of critical confining stress, described above, there is another important level of pressure, called the "breakdown" stress, which affects deviatoric stress/strain relations and shear strength. At pressures higher than the breakdown stress, grain crushing occurs, shear strength is unaffected by initial void ratio, and along with the

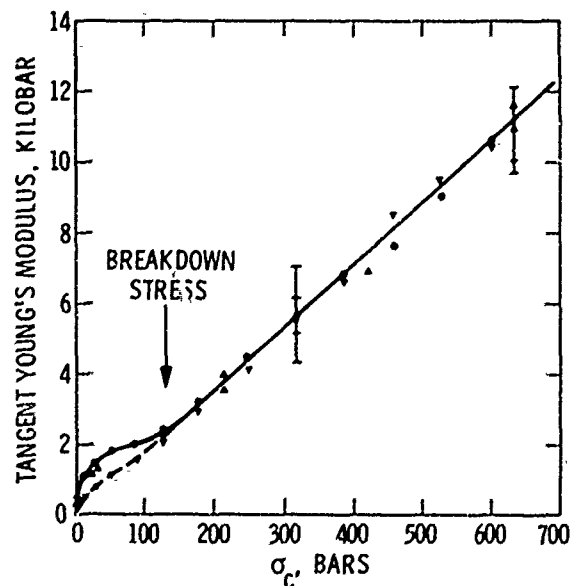
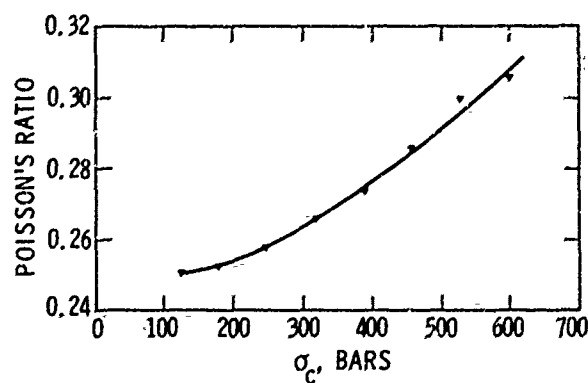
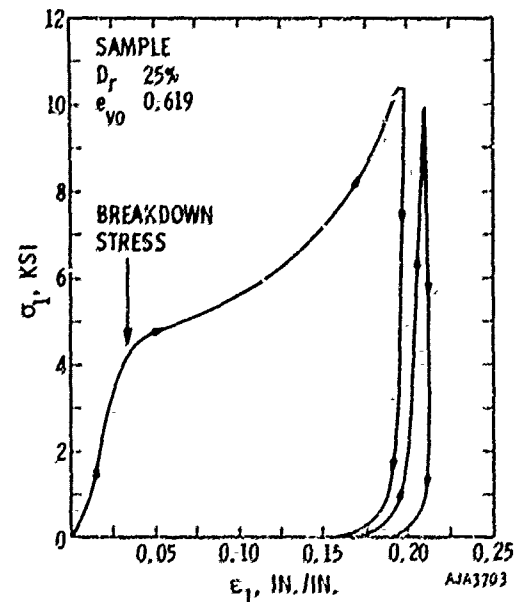


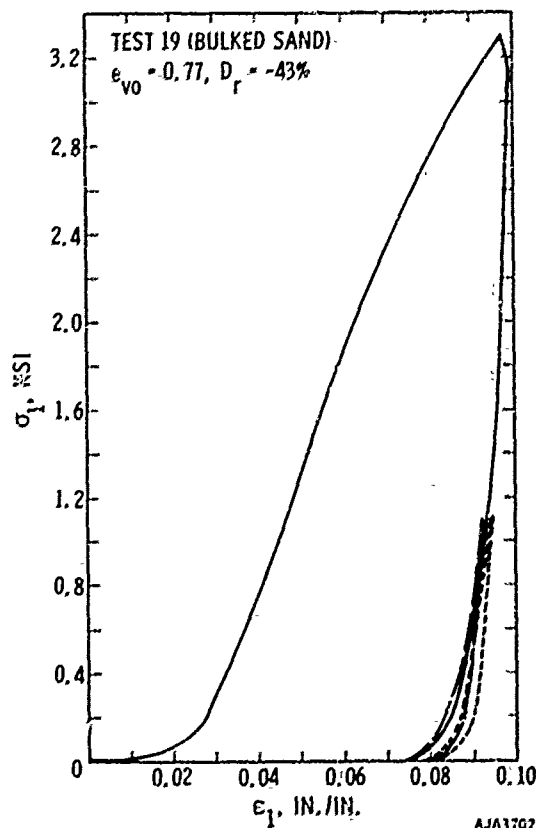
FIGURE 3-22. BREAKDOWN STRESS IS ASSOCIATED WITH AN INCREASE IN POISSON'S RATIO AND A LINEAR RELATION BETWEEN STIFFNESS AND CONFINING STRESS

tangent moduli, it increases linearly with increasing mean normal stress. At pressures below the breakdown stress, strength is affected by initial void ratio, and tangent moduli and strength vary as the $1/2$ to $1/3$ power of mean normal stress. Some of these effects are illustrated in Figure 3-22.

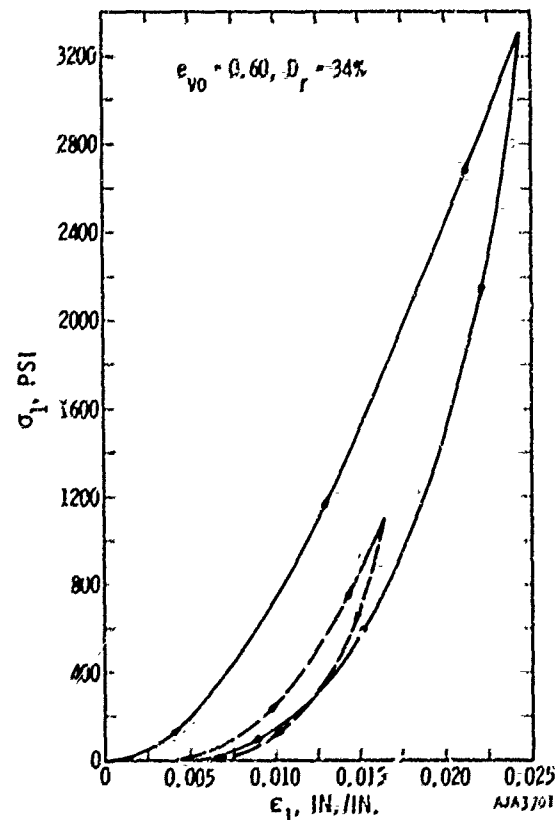
Factors such as the breakdown stress and influence of initial void ratio are reflected in the stress/strain relations in a state of uniaxial strain. This is a pertinent experiment to perform due to the simplicity of the boundary conditions and because the modulus in uniaxial strain (constrained modulus) is related to the speed of compressional wave propagation in an infinite medium (References 3-34, 3-35, 3-36, 3-37). Figure 3-23 shows stress/strain relations for Minnesota sand subjected to uniaxial strain. Comparison between Figures 3-23(a) and (b) shows that high initial void ratios (low relative density) contribute to low stiffness, a large amount of energy absorption, and large permanent strain. Figure 3-23(c) shows that the breakdown stress for Minnesota sand at $D_r = 0.25$ and $e_{vo} = 0.619$ is about 4300 psi. This is higher than the breakdown stress indicated in Figure 3-22 for Chattahoochee River sand. Such differences are discussed in Reference 3-34, where it is



(b) INITIALLY LOOSE SAND UNDER STATIC LOADING (REFERENCE 2-34)



(a) INITIALLY DENSE SAND UNDER STATIC LOADING (REFERENCE 3-34)



(c) INITIALLY DENSE SAND UNDER DYNAMIC LOADING, ILLUSTRATES BREAKDOWN STRESS (REFERENCE 3-35)

FIGURE 3-23. MINNESOTA SAND UNDER UNIAXIAL STRAIN (REFERENCE 3-34)

Properties of Soils

suggested that the breakdown stress is related to the initial relative density and to the grading. A loose sand has higher grain-to-grain contact stress than a dense sand at the same level of externally applied stress, and hence grain fracture occurs sooner. A well-graded sand provides more contact points per unit of volume, and hence the stress at each contact point is less than that in a sand having coarse grains of uniform size.

A stress/strain relation in uniaxial strain for a fine sand containing some silt and clay particles (McCormick Ranch sand) is shown in Figure 3-24. At low stress levels, stress/strain relations for undisturbed samples of this soil are concave to the strain axis in contrast to the reconstituted soil in Figure 3-23.

The relationship between the axial and lateral stresses for Minnesota sand subjected to uniaxial strain is shown in Figure 3-25. This information is used as a check on a candidate mathematical model. The curve is initially linear on loading and the slope is generally called the earth pressure at rest. The loading slope approaches 45 degrees as crushing or plastic flow occurs and flattens as the soil locks up again.

Effects of Loading Rate. The stiffness and strength of coarse-grained soils has been shown to depend on void ratio, shapes of particles, hydrostatic stress, and deviatoric stress. Crushing strength of

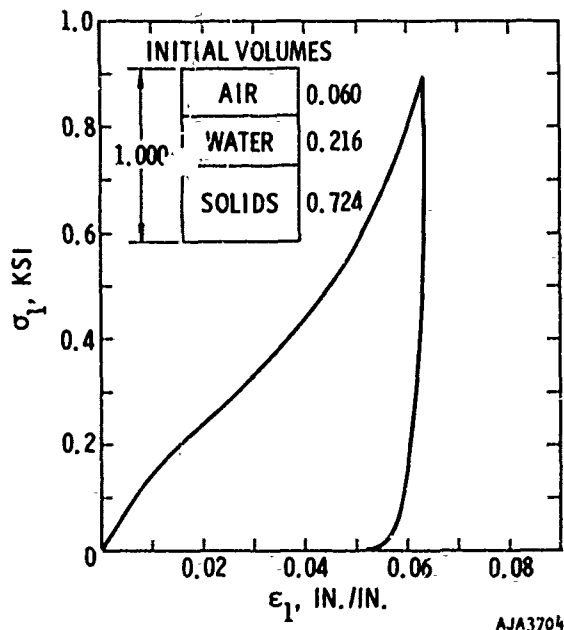


FIGURE 3-24. MCCORMICK RANCH SAND UNDER UNIAXIAL STRAIN (REFERENCE 3-85)

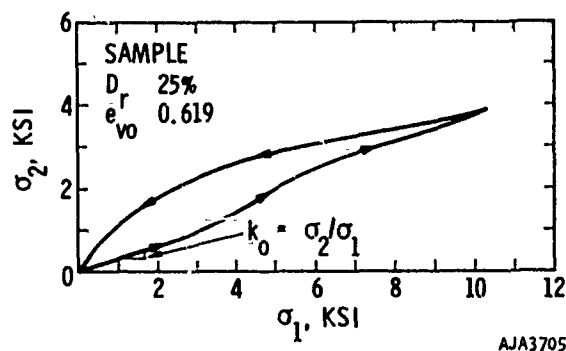


FIGURE 3-25. RELATIONSHIP BETWEEN LATERAL AND AXIAL (σ_1) STRESSES FOR MINNESOTA SAND UNDER DYNAMIC LOADING IN UNIAXIAL STRAIN (REFERENCE 3-35)

particles tends to influence the behavior at high stresses, while the influence of the initial void is diminished. The loading rate can affect the behavior of cohesionless soils due to:

- Rate dependence of grain sliding, interlocking, and rearrangement (dilatancy)
- Development of pore pressures under saturated conditions
- Rate dependence of grain crushing

Transient loading tests have been performed in a standard triaxial configuration (References 3-38, 3-39) and simple shear configuration (Reference 3-40) on dry cohesionless soils. At low confining pressures, the triaxial results indicate that an increase in strength, an increase in stiffness, and a decrease in strain at failure results when loading rates of about 5 msec to failure are compared with rates of 5 minutes to failure. The increase in strength is only about seven percent, indicating the strain rate dependence of sliding friction and dilatancy is small. The simple shear tests indicate that a threshold rate exists beyond which rate effects are unchanged. Dynamic strengths fifty percent larger than static strengths are reported (Reference 3-40) for dynamic simple shear tests. Sand degradation was noted in these tests at all overburden pressures ranging from 0.416 psi to 83.3 psi.

At confining pressures of 15 bars in the dynamic triaxial tests, an increase in the strain rate from 0.1 to 10,000 percent per minute produced about a 20-percent strength increase in dense sand (Reference 3-39).

If cohesionless soil is saturated, rapid or dynamic loading rates usually induce changes in the pore pressure, which in turn are reflected as changes in the effective confining pressure in the soil. Hence, the

behavior of a saturated sand tested statically in an undrained condition reflects somewhat its behavior under dynamic loads when there is no time for drainage to occur. Seed and Lundgren (Reference 3-41) report a strength increase of 40 percent in dynamic triaxial tests on saturated dense sand. Results obtained by Whitman and Healy (Reference 3-38) for dense saturated sand indicate a decrease in pore pressure until cavitation occurs; however, very little difference in behavior is observed between static undrained and dynamic undrained tests. From this, it appears that rate effects in this soil are primarily related to pore pressure. Results obtained on loose sand indicate a strain rate effect in the form of a tendency to dilate more under rapid loading than slow loading (Reference 3-38). This tendency to dilate causes the pore pressures to be less in dynamic tests than in static tests. However, the similarity in results between the undrained static and dynamic tests indicate that the influence of pore pressure changes on the behavior of cohesionless soils can be estimated at least qualitatively from static undrained tests. More insight into this behavior is given in Reference 3-42. The undrained strength of saturated cohesionless soils depends on the critical confining pressure, which is related to the void ratio of the soil. The initial pore pressure that exists in saturated sand can be reduced until the cavitation pressure is reached. If the initial pore pressure is high, it can be reduced upon shearing until the resulting effective confining pressure reaches the critical confining pressure (point at which shearing occurs without volume change). Hence, the influence of the rate of loading on the development of pore pressures in saturated cohesionless soils depends upon the initial void ratio, the initial pore pressure, and the critical confining pressure for the soil.

Vesic and Clough (Reference 3-5) have shown that deformation of sand under hydrostatic stresses greater than 42 bars depends on the duration of loading. They measured significant volume decrease under constant pressure between 10 and 1000 seconds of loading. This is attributed to grain crushing and subsequent rearrangement of particles, as are the rate effects in dense sand, reported in Reference 3-39. The marked difference in behavior of the dense sand at low and high pressure is associated mainly with the effect of strain rate on the energy required for particle crushing. Evidence of this is shown in the results of uniaxial strain tests on dry Pennsylvania sand reported by Davisson and Hendron (Reference 3-36) and shown in Figure 3-26. The loading rate effect is distinct above the stress level (2000 psi) where significant crushing occurs. This rate effect causes the dynamic stiffness at high stress levels to be significantly greater than for static loading.

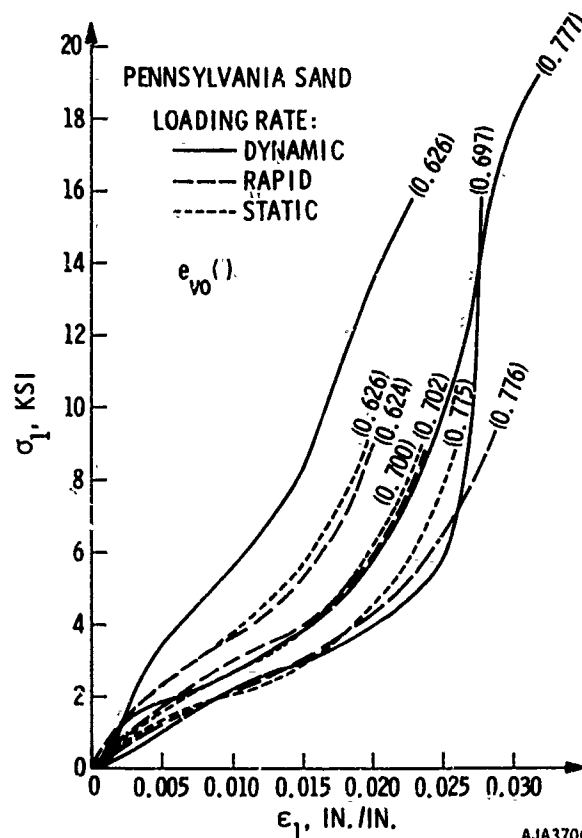


FIGURE 3-26. EFFECT OF LOADING RATE AND INITIAL VOID RATIO ON AXIAL STRESS/STRAIN RELATIONS OF A SAND SUBJECTED TO UNIAXIAL STRAIN (REFERENCE 3-36)

Elastic Wave Velocity. Elastic moduli can be related to the velocity of propagation of a stress pulse through an elastic material. Such relationships are used in soils to evaluate the tangent moduli of soil as a function of void ratio and confining pressure and to investigate layer thicknesses in soil profiles. The amplitude of the stress wave is very small; consequently, the moduli of soil under large stress excursions is generally much less than the instantaneous tangent modulus estimated from wave velocities. Methods of testing have been developed (References 3-43 through 3-48) to evaluate shear moduli, Young's moduli, and constrained moduli from wave velocity or resonant column techniques in the laboratory. Vibratory techniques and travel time evaluations (References 3-78 and 3-79) have been used to obtain wave velocities in the field.

Typical results for cohesionless soils are shown in Figure 3-27. The shear wave velocity (and hence, it is assumed, the shear modulus) depends primarily on the mean normal stress and the void ratio. The

Properties of Soils

relative density, degree of saturation, and deviatoric component of the initial state of stress have negligible influence on the tangent shear modulus obtained by applying low strain (2.5×10^{-5}) (Reference 3-45). The shear moduli decrease with increasing amplitude of shearing strain greater than 10^{-5} radians. Permanent changes develop in dry sand subjected to vibration at shearing strains around 10^{-4} radians. The low strain dynamic shear modulus is increased and the static compressibility of the soil is decreased due to an apparent cyclic restraining effect without a change in void ratio (Reference 3-46).

Although the shear and unconfined compressional wave velocities are essentially independent of moisture conditions, the dilatational wave velocity depends on the degree of saturation. At 100-percent saturation, the dilatational wave velocity is greater than that in water. It increases slightly as the effective confining stress is increased (Reference 3-44).

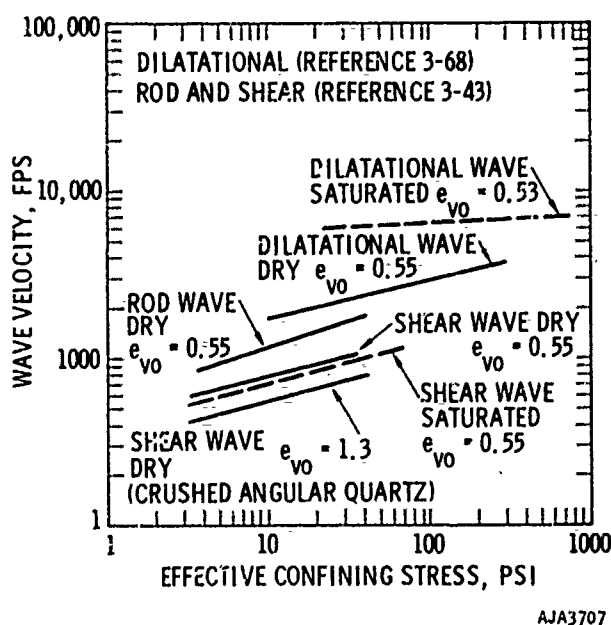


FIGURE 3-27. WAVE VELOCITIES IN OTTAWA SAND

Constitutive Behavior of Fine-Grained Soils

The behavior of fine-grained soil is significantly influenced by interparticle forces. The most obvious difference between fine-grained and coarse-grained soils is the cohesiveness in fine-grained soils at certain moisture contents that allows it to be molded into a well-defined shape. This is explained by physiochemical attractive forces which exist at the points of contact of the minerals. These attractive forces are independent of external loads and depend

primarily on the type of clay mineral making up the solid skeleton.

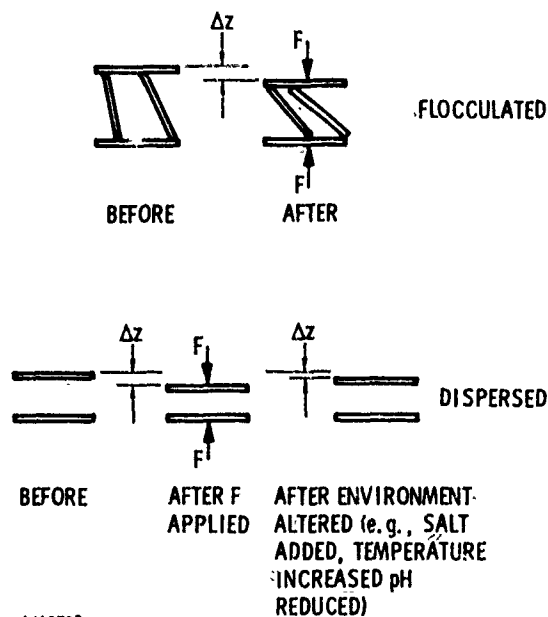
In addition to the attractive forces between clay platelets, repulsive forces also exist and provide a means (in addition to particle-to-particle contact) by which soils stresses are transmitted through the soil skeleton. The internal stress transmission through the soil skeleton depends on the soil structure which in turn depends on the moisture content, electrolyte concentration, clay mineral type, and other factors which influence the interparticle forces. Figure 3-28 indicates the strain mechanisms and interparticle forces which develop in the soil skeleton for somewhat idealized models. Although the internal mechanism of stress transmission through the soil skeleton is different in fine-grained soils and coarse-grained soils, the strength behavior of both types of soil is basically Coulombic.

Because of the nonlinear nature of the interparticle forces as a function of particle spacing and also because most fine-grained soils are mixed with coarser particles and deposited in a structure that is more flocculated than dispersed, the application of external stresses may alter the structure, creating irrecoverable deformations and imposing important stress history effects on the soil.

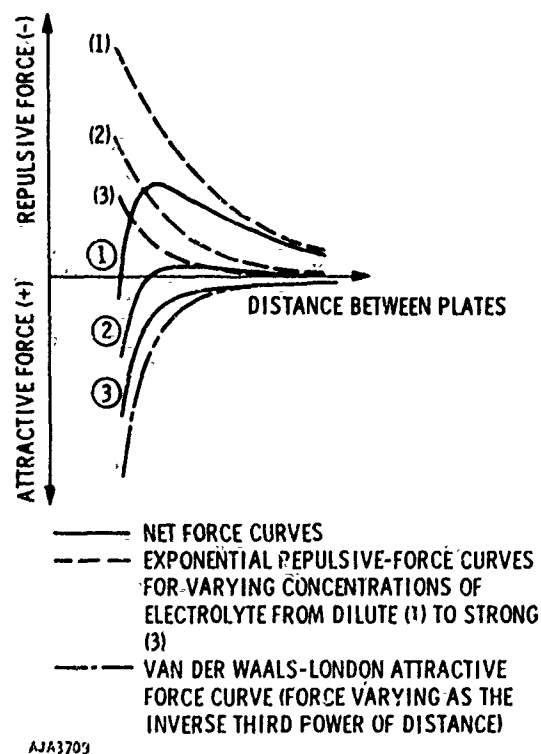
A distinction between the behavior of saturated and partially saturated fine-grained soils is necessary. In partially saturated soils, the water layers around the clay platelets are not as fully developed. Large volume changes occur in undrained loading of partially saturated soil due to the compressibility of the pore air space. Although the effective stress principle applies in both saturated and partially-saturated soil, it is difficult to determine pore pressures in partially saturated soil. The behavior of partially saturated soil is primarily influenced by the degree of saturation and moisture content.

In the compaction of fine-grained soil, the compactive effort and water content will determine the dry density of the soil. A typical compaction curve is shown in Figure 3-29. The moisture content which produces the maximum dry density is called the optimum water content. Compacted soils with less than optimum water content tend to have a flocculated structure and exhibit more strength than compacted soils with more than optimum water content. Soils wetter than optimum tend to form in a dispersed structure (Reference 3-83).

Saturated Fine-Grained Soil. The behavior of saturated clay depends largely on its past history and void ratio. The major features of the past history are the extent to which the clay has been consolidated and the amount of unloading that has occurred. As indicated in Figure 3-4, the hydrostatic loading and unloading of drained saturated clay soils results in substantial permanent deformation. This is due to

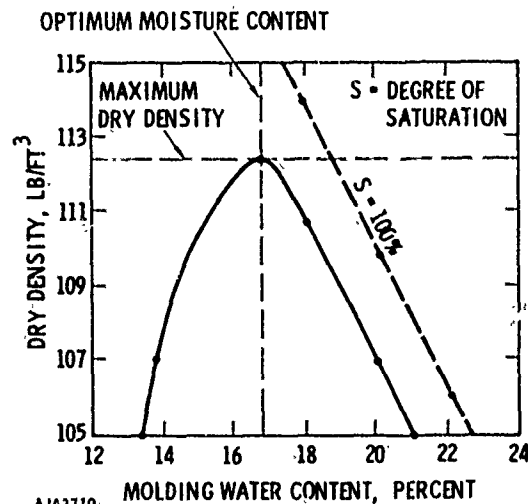


(a) STRAIN MECHANISMS

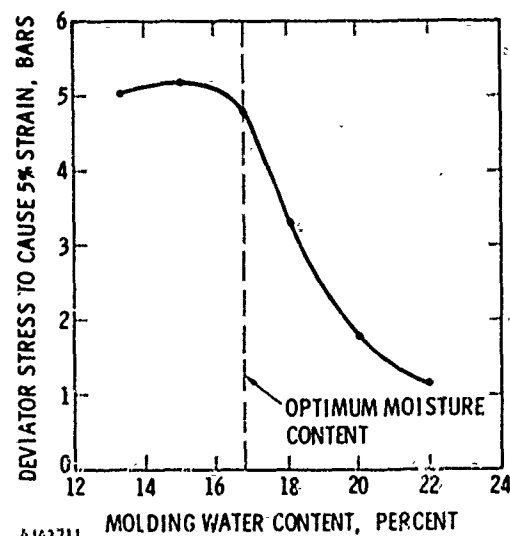


(b) NET FORCE BETWEEN TWO CLAY MINERAL SURFACES AS A FUNCTION OF SPACING

FIGURE 3-28. STRESS AND STRAIN MECHANISMS IN SOILS (REFERENCE 3-1)



(a) COMPACTION CURVE



(b) STRENGTH OF SOIL VARIES WITH WATER CONTENT

FIGURE 3-29. SHEAR STRENGTH/MOISTURE CONTENT RELATIONSHIP FOR COMPACTED PARTIALLY SATURATED SOIL (REFERENCE 3-83)

expulsion of pore water. The externally applied stresses are partitioned internally between the pore water and soil skeleton. In completely saturated clay soils, practically all the applied stress is taken up in the pore water because it is much stiffer than the soil skeleton. If under static loading there is a pore pressure gradient, water drains from the soil, thus decreasing the void ratio and moisture content and increasing the stress carried by the soil skeleton. Under these conditions, the pore pressure dissipates

Properties of Soils

and the effective confining pressure increases. During ground-shock loading, drainage is usually not possible because loading is too rapid. In this situation, the degree of prior consolidation must be considered.

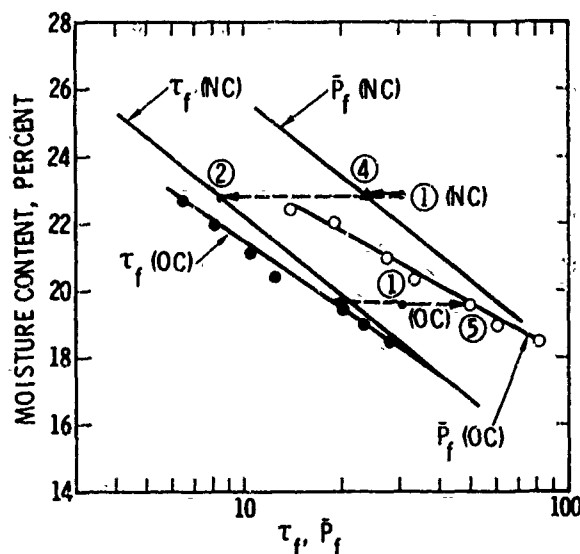
Figure 3-30(a) illustrates the behavior of a saturated clay which is first consolidated and then subjected to triaxial compression under undrained conditions, (constant moisture content). Figure 3-30(b) illustrates the path in the shear-stress/normal-stress plane which two different samples of the same clay would experience depending on prior consolidation. The total stress path (TSP) is defined by the externally applied stresses. The effective stress path (ESP) is defined by subtracting the pore pressure from the total stress. Both samples are first brought to an effective confining stress of 30 psi (State 1, NC). As deviator stresses are applied to the normally consolidated sample (NC), the pore pressure increases. This results in a net decrease in effective confinement (Path 1NC→4) and failure at a relatively low value of shear stress (Path 1NC→2). As deviator stresses are applied to the overconsolidated sample (initial condition, State 10C), the pore pressure changes very little, resulting in an increase in effective confinement (Path 10C→5) and failure at a relatively high value of shear stress (Path 10C→3). This behavior is accounted for in laboratory testing, where the effects of the consolidation pressure, overconsolidation ratio, aging, and stress paths representative of field conditions are considered.

Since the behavior of clay is controlled essentially by the effective stresses, the pore water pressures that develop during undrained loading of clay depend on the pore pressure parameters shown in Figure 3-5. In general, the change in pore pressure upon loading can be related to the change in the mean normal stress and the change in the octahedral shear stress by

$$\Delta p = \bar{B} \Delta \bar{p} + \bar{A} \Delta \sqrt{J'_2} \quad (3-3)$$

where \bar{B} and \bar{A} are the pore pressure parameters (Reference 3-84). \bar{B} depends on the relative compressibility of the soil skeleton and pore fluid, on the porosity of the soil, and the degree of saturation. As indicated in Figure 3-5, \bar{B} is nearly unity for most saturated soils. The parameter \bar{A} is similar to the pore pressure parameter determined by standard triaxial testing shown in Figure 3-5. For standard triaxial testing $\bar{A} = (\bar{A}_1 - 1/3)/\sqrt{2}$. In triaxial testing of a normally consolidated clay, \bar{A}_1 may decrease with the application of shear stresses and may approach negative values near -0.5 for heavily overconsolidated clay soils (OCR > 10). OCR is the overconsolidation ratio, and is defined as the ratio of the maximum posteffective overburden pressure to the effective vertical pressure presently existing on the soil or applied in a test.

τ_f = SHEAR STRENGTH (SHEAR STRESS PATH—)
 \bar{p}_f = EFFECTIVE MEAN NORMAL STRESS AT FAILURE (EFFECTIVE MEAN NORMAL STRESS PATH—)



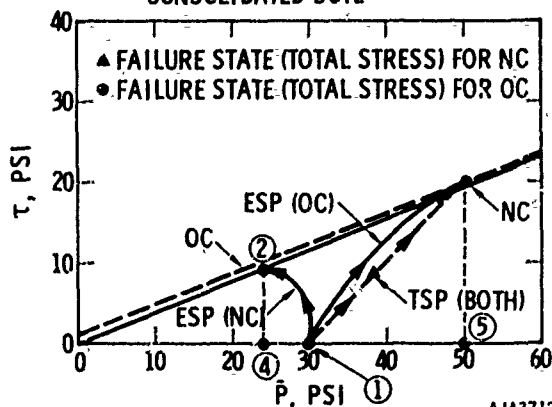
(a) MOISTURE CONTENT VERSUS EFFECTIVE CONFINEMENT AND SHEAR STRENGTH (REFERENCE 3-49)

ESP = EFFECTIVE STRESS PATH

TSP = TOTAL STRESS PATH

OC = FAILURE CRITERION FOR OVER CONSOLIDATED SOIL

NC = FAILURE CRITERION FOR NORMALLY CONSOLIDATED SOIL



(b) STRESS TRAJECTORIES

FIGURE 3-30. EFFECTIVE AND TOTAL STRESS PATHS FOR OVERCONSOLIDATED AND NORMALLY CONSOLIDATED UNDRAINED SOILS SUBJECTED TO TRIAXIAL COMPRESSION STRESS (REFERENCE 3-49)

Both the stiffness and the strength of clay are influenced by the effective mean normal stress and the overconsolidation ratio. Triaxial tests on saturated normally consolidated clay samples (Reference 3-50) indicate a nearly unique relationship among the octahedral shear stress, effective confining stress, and octahedral shear strain as shown in Figure 3-31. This nearly unique dependence of the stress/strain curves and maximum shear stress on the effective confining stress has long been recognized in triaxial tests on normally consolidated clay. The behavior is highly dependent upon the overconsolidation ratio as indicated by results of triaxial tests on normally consolidated and overconsolidated remoulded Boston Blue clay shown in Figure 3-32.

Using the ratio of the undrained shear strength to preshear effective confining pressure is a practical way of normalizing the shear strength behavior of saturated clays. This ratio lies between 0.25 and 0.35 for many clays which are first consolidated under hydrostatic compression and then tested in triaxial compression. Clays which increase in strength with time and clays which tend to expand during application of shear stresses in a triaxial test may have shear-strength/consolidation-pressure ratios that decrease from 0.7 at a plasticity index of less than 40 to values around 0.3 with a plasticity index greater than 160.

The overconsolidation ratio influences the undrained shear-strength/consolidation-pressure ratio. For clays of medium plasticity ($PI \approx 50\%$), the ratio may vary from 0.25 to greater than 1 as the overconsolidation ratio varies from 1 to 30. As

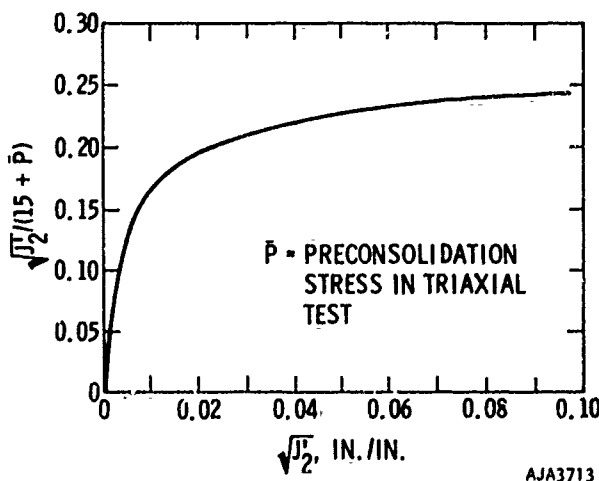


FIGURE 3-31. FOR A FINE-GRAINED SOIL, AN APPARENTLY UNIQUE RELATION EXISTS AMONG OCTAHEDRAL SHEAR STRESS, $\sqrt{J_2}$ OCTAHEDRAL SHEAR STRAIN AND EFFECTIVE PRECONSOLIDATION STRESS \bar{P}_0 (REFERENCE 3-50)

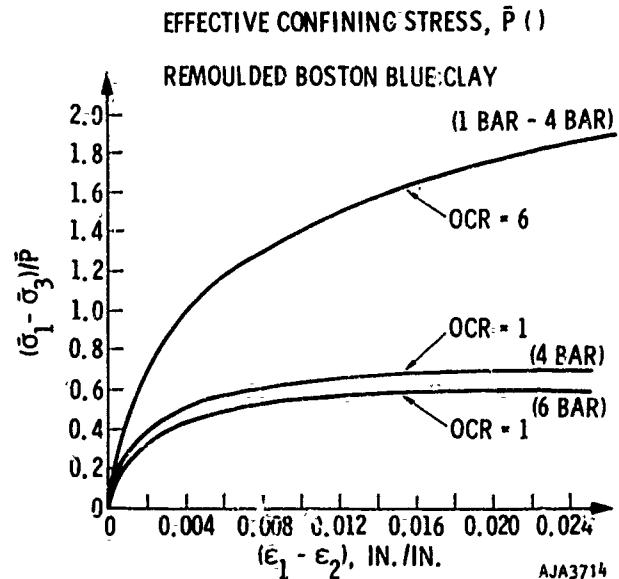


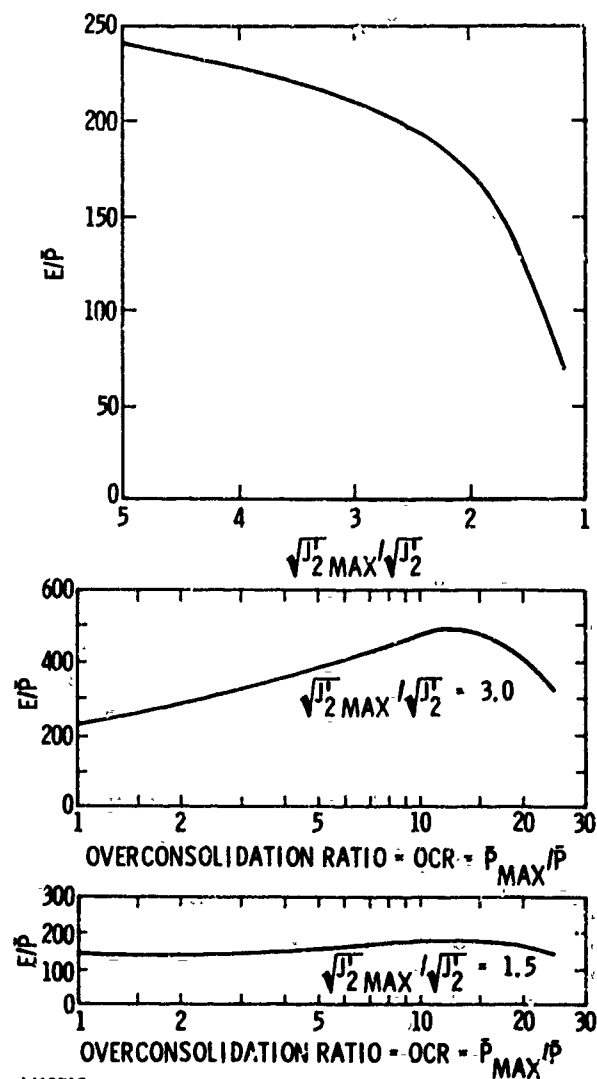
FIGURE 3-32. SHEAR STRESS (NORMALIZED TO EFFECTIVE CONFINING STRESS) VERSUS SHEAR STRAIN FOR A FINE-GRAINED SOIL DEPENDS ON THE PREVIOUS HISTORY OF LOADING, WHICH IS MEASURED IN THIS EXAMPLE BY THE OVERCONSOLIDATION RATIO (OCR) (REFERENCE 3-51)

the plasticity index of fine-grained soils decreases, the overconsolidation ratio has a more pronounced effect on undrained shear strength.

The undrained shear strength is significantly affected by the stress path, anisotropic consolidation, and rate of loading. The typical behavior cited above should be used only as a guide to the important parameters controlling undrained shear strength of saturated clay. When the states of stress developed in the field are similar to those imposed in laboratory testing, then these relationships allow the strength of a soil to be estimated from the plasticity index, preshear consolidation pressure and overconsolidation ratio.

Further insight into the stiffness of clay during undrained shear can be gained from results of secant modulus evaluations (Reference 3-51). The secant modulus is the principal stress difference divided by the major principal strain. Normalizing this modulus by dividing by the preshear consolidation pressure gives ratios ranging from 50 to 500. The modulus/consolidation pressure ratio is influenced by the ratio of shear strength to shear stress and the overconsolidation ratio. Typical results for Boston Blue clay are shown in Figure 3-33. This modulus is often normalized by dividing by the undrained shear strength of the clay. This ratio decreases rapidly with an

Properties of Soils



AJA3715

FIGURE 3-33. SECANT YOUNG'S MODULUS OF A CLAY AS A FUNCTION OF SHEAR STRESS (NORMALIZED TO SHEAR STRENGTH) AND OVERCONSOLIDATION RATIO (REFERENCE 3-51)

increase in the overconsolidation ratio. For normally consolidated clay the modulus/strength ratio may range from 600 to 1200, well below yield, and from 200 to 500 when the shear stresses are about two-thirds the yield stress. Results such as those in Figures 3-31, 3-32 and 3-33 indicate that overconsolidation ratio and stress level must be accounted for in prescribing stress/strain relations.

Drained uniaxial strain tests are often used to predict the long-term compressibility of saturated clays. These consolidation tests can be used to determine whether a soil sample is normally consolidated or overconsolidated. It is also possible to

estimate the overconsolidation ratio from these tests (Reference 3-52). As a clay soil is consolidated and then rebounds due to removal of stress, the in situ lateral effective stress in response to this one-dimensional stress history is dependent upon the overconsolidation ratio and the plasticity index of the soil. Evidence of this behavior was obtained from laboratory tests performed by Kane, et al. (Reference 3-53) on remolded samples of five clays. The results are shown in Figure 3-34. No evidence of grain crushing occurs at stresses below 20,000 psi.

In undrained uniaxial strain tests on saturated soil, the lateral stresses are nearly equal to the axial stresses in loading and unloading. The constrained tangent modulus increases rapidly toward the bulk modulus of the water and soil skeleton combined. The rate at which the constrained tangent modulus increases with increasing axial stress is somewhat dependent on the soil plasticity as shown in Figure 3-35.

Partially Saturated Fine-Grained Soils. The major difference in the behavior of partially saturated soil and completely saturated soil is due to the high compressibility of the remaining air. The degree of saturation is defined as the percent of the void space filled with water and is an indicator of the compressibility of partially saturated soils. Since the compressibility of the pore fluid greatly exceeds that of the soil skeleton, the pore pressures that develop due to changes in the total loading are insignificant. It follows that the change in the effective mean normal stress approximately equals the change in total mean normal stresses. This behavior has been observed up to about 85 percent saturation. At higher degrees of saturation, the pore pressure begins to increase rapidly with total stress.

Hydrostatic compression tests performed on partially saturated soils (Reference 3-30) indicate the hydrostatic stress is nearly linearly related to the volumetric strain until a threshold stress is reached. Beyond the threshold stress the pore pressure parameter increases rapidly with total stress and the degree of saturation approaches 100 percent. This causes a transition in the pressure/volumetric strain relationship as the tangent bulk modulus increases to the bulk modulus of water and the soil skeleton combined. The threshold stress depends upon the initial degree of saturation. For McCormick Ranch sandy clay under static loading, the transition in the stress/volumetric strain curve occurs at approximately 90 to 95 percent saturation for an initial saturation of about 80 percent. The transition zone in the Watching Hill clay under static loading, reported in Reference 3-30, occurs in the range of saturation between 75 and 80 percent for an initial degree of saturation of about 42 percent. The bulk modulus up to the threshold stress is approximately 16,000 psi for the McCormick Ranch sandy clay and approximately

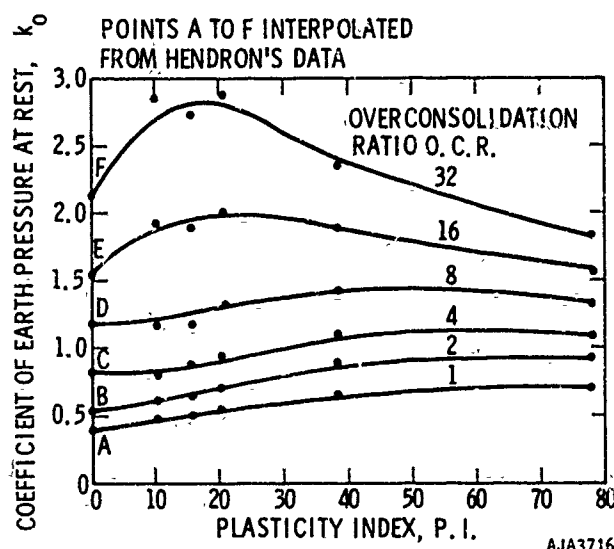


FIGURE 3-34. RATIO OF LATERAL STRESS TO AXIAL STRESS (k_0) WHICH DEVELOPS IN A FINE-GRAINED SOIL SUBJECTED TO UNIAXIAL STRAIN AS A FUNCTION OF OVERCONSOLIDATION RATIO AND PLASTICITY INDEX (REFERENCE 3-53)

200 psi for the Watching Hill clay. Both soils reach constant bulk moduli at approximately 800 to 1000 psi.

Partially saturated clay soils tend to develop irrecoverable volumetric strains. These are about 60 percent of the maximum volumetric strain for Watching Hill clay. The unloading stress/strain relation is approximately linear until the transition zone is reached, where significant hysteresis begins. Some significant features of this behavior are shown in Figure 3-36.

When shear stresses are applied to partially saturated soil after the application of hydrostatic pressures, the shear modulus and strength of the soil depend on the effective mean normal stress. As shown in Figure 3-37, the shear stress/strain relations for Watching Hill clay are influenced by the confining stress, until it exceeds the transition zone in the hydrostatic pressure/volumetric strain curve. Beyond the transition zone, the strength and shear modulus of the soil are influenced only slightly by further increases in external hydrostatic stress. This is because a large portion of the increase in the external hydrostatic stress is taken up by the pore fluid and does not contribute significantly to the effective confining stress. As has been frequently pointed out, the effective stress governs shear stiffness and strength of the soil which do not change once saturation has been achieved.

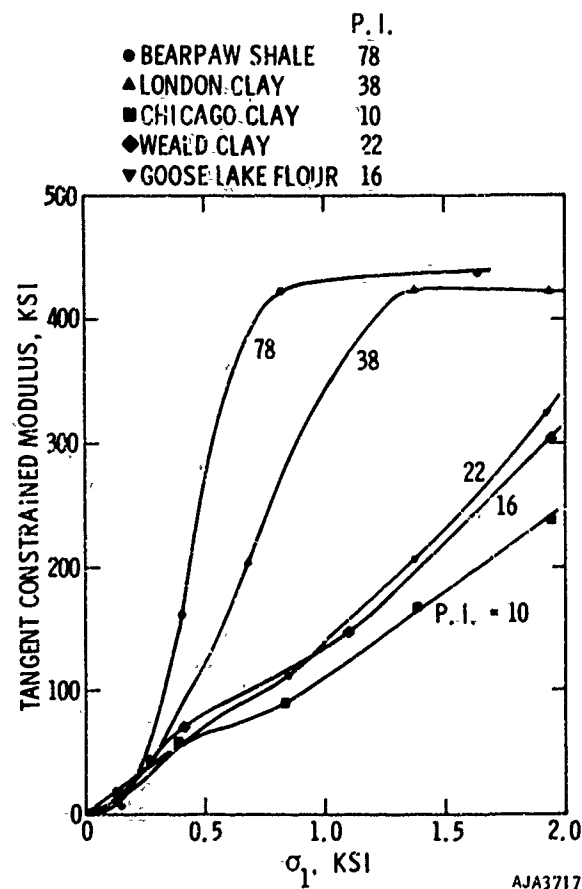


FIGURE 3-35. TANGENT CONSTRAINED MODULUS VERSUS AXIAL STRESS RELATION FOR FINE-GRAINED SOILS SUBJECTED TO UNIAXIAL STRAIN IS INFLUENCED BY THE PLASTICITY INDEX (REFERENCE 3-53)

As long as the increase in mean normal total stress causes an increase in the mean normal effective stress without a partition of stress between the soil skeleton and pore fluid, the shear strength increases nearly linearly with mean normal stress. The failure envelope is concave toward the mean normal stress axis as the pore fluid begins to pick up some of the normal stress and becomes nearly horizontal when 100 percent saturation is reached. As the plasticity of the soil increases, the shear strength is influenced less by the mean normal stress at complete saturation. Evidence of the behavior is shown in Figure 3-38, where the shear stress to cause failure is plotted against the mean normal total stress for silty clay and silty sand from the Watching Hill site. Data are shown for different degrees of initial saturation. At 50 percent saturation, the mean normal stress has considerable effect on the strength of silty sand but little effect on the strength of silty clay.

Properties of Soils

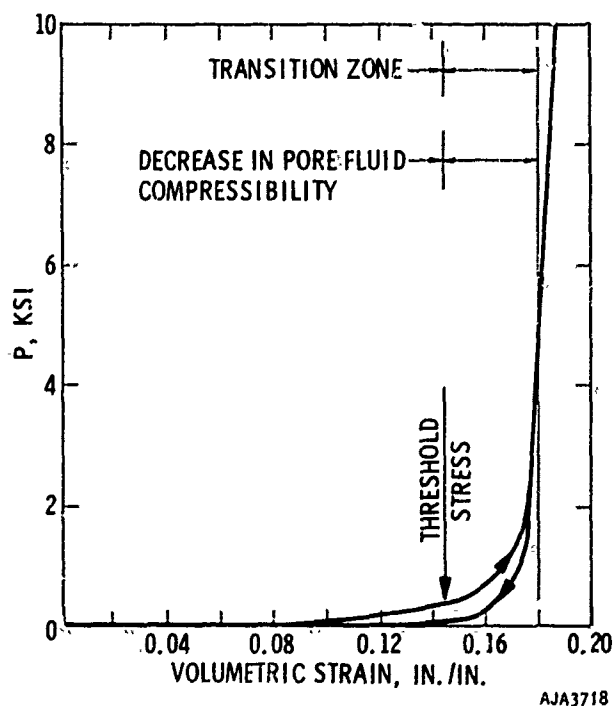


FIGURE 3-36. PRESSURE VERSUS VOLUMETRIC STRAIN FOR WATCHING HILLS CLAY SUBJECTED TO HYDROSTATIC COMPRESSION (REFERENCE 3-30)

Uniaxial strain tests on partially saturated soils illustrate important aspects of the stress/strain behavior. The axial stress/strain curves may exhibit a high initial stiffness, followed by yielding and then by locking, as shown in Figure 3-39. High initial stiffness usually results from high overburden stresses, heavy overconsolidation, rate of load application, or cementation. Once the influence of these factors is overcome by application of stresses, the soil may yield (concave toward the strain axis) and then lock as the void ratio is decreased and the degree of saturation is increased. Residual strains in confined, partially saturated cohesive soils are approximately 90 percent of the peak strains. Such soils have unloading/reloading stress/strain relations along nearly the same path. Beyond the point of previous maximum loading, the stress/strain relation is affected little by cycles of unloading/reloading at lower stress levels. This is shown in the results of uniaxial strain tests on partially saturated sandy clay from the HEST Test V Dakota, Figure 3-40.

The radial stresses required to maintain zero lateral strain are about proportional to the axial stress until the total stresses begin to be partitioned between the pore fluid and soil skeleton. The coefficient of proportionality between the effective radial stress and effective axial stress is the coefficient of

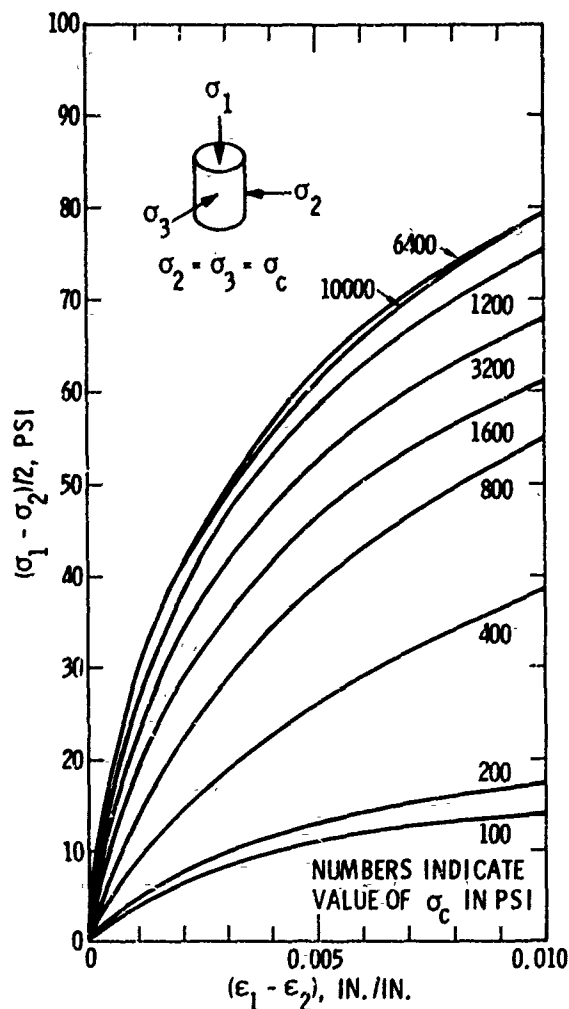
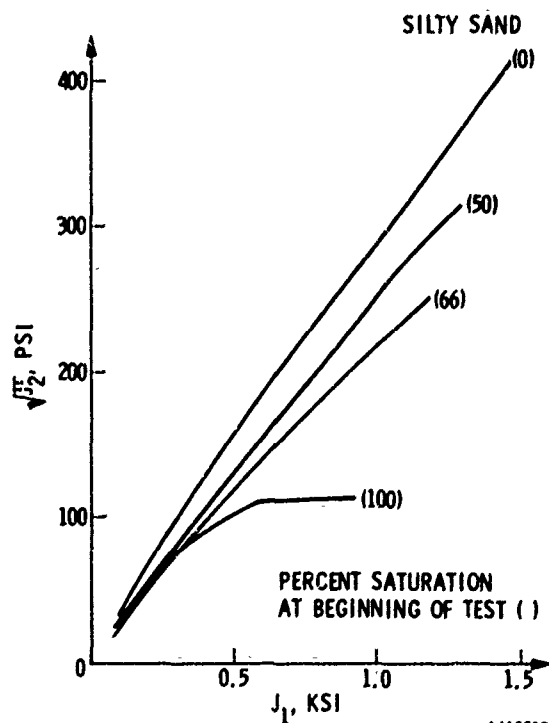
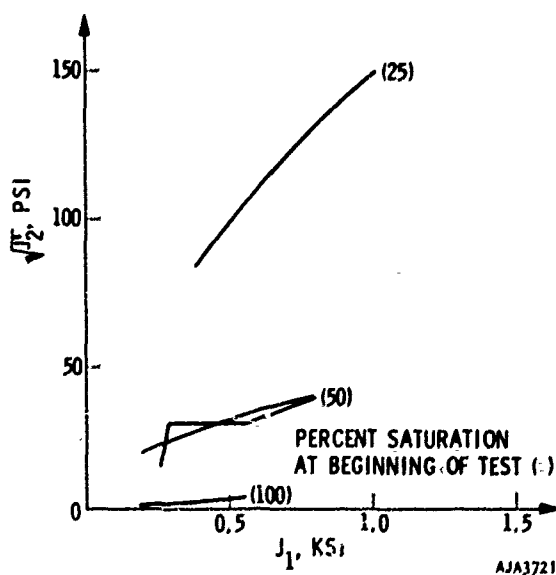


FIGURE 3-37. SHEAR-STRESS/STRAIN RELATIONS FOR WATCHING HILL CLAY (REFERENCE 3-30)

earth pressure at rest, k_0 . This coefficient is less than unity at stresses below plastic flow. The incremental axial stress tends to become equal to the incremental radial stress as 100-percent saturation is approached. The radial stress may become greater than the axial stress on unloading. This behavior is shown in Figure 3-41(a) for uniaxial data on HEST Test V samples. The principal stress difference versus the mean normal stress is shown for this data in Figure 3-41(b). Comparisons are made with the results of the Mohr strength envelope derived from triaxial tests and two idealized failure envelopes. The influence of the degree of saturation is shown in these data as the principal stress difference becomes independent of the mean total stress.



(a) SHEAR STRENGTH OF REMOLDED WATCHING HILLS GREY SILTY SAND AT DIFFERENT DEGREES OF SATURATION (REFERENCE 3-54)



(b) SHEAR STRENGTH OF REMOLDED WATCHING HILLS BROWN SILTY CLAY AT DIFFERENT DEGREES OF SATURATION (REFERENCE 3-54)

FIGURE 3-38. SHEAR STRENGTH DEPENDS ON CONFINING STRESS AND DEGREE OF SATURATION

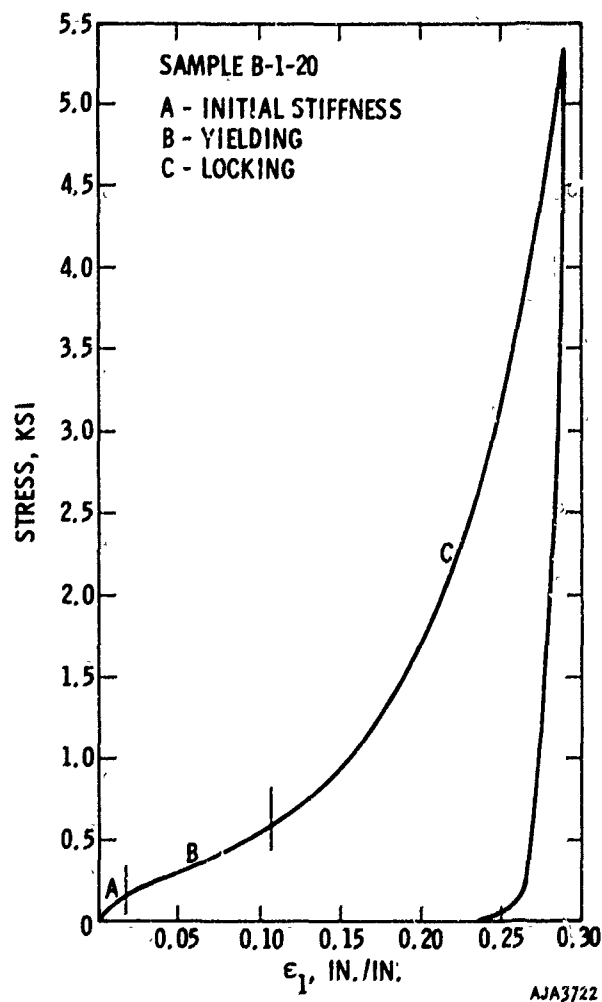


FIGURE 3-39. STRESS/STRAIN RELATION FOR PARTIALLY SATURATED FINE-GRAINED SOIL SUBJECTED TO UNIAXIAL STRAIN (REFERENCE 3-17)

The state of hydrostatic and deviatoric stresses affect the tangent bulk modulus and tangent shear modulus. This behavior can be evaluated qualitatively by comparing the results of pressure/volume and deviatoric stress/strain relationships derived from subjecting soil samples to different stress paths. Figure 3-42 shows the pressure/volume relationship resulting from hydrostatic loading, uniaxial compression, proportional loading ($\sigma_1/\sigma_3 = \text{constant}$) and triaxial loading ($\sigma_3 = \text{constant}$). Although the shear stresses in uniaxial compression are small due to lateral confinement, nonetheless the associated pressure/volume curve indicates that the soil is more compressible due to the introduction of small shear stresses. As shear stresses are increased with increasing mean normal stress in proportional loading,

Properties of Soils

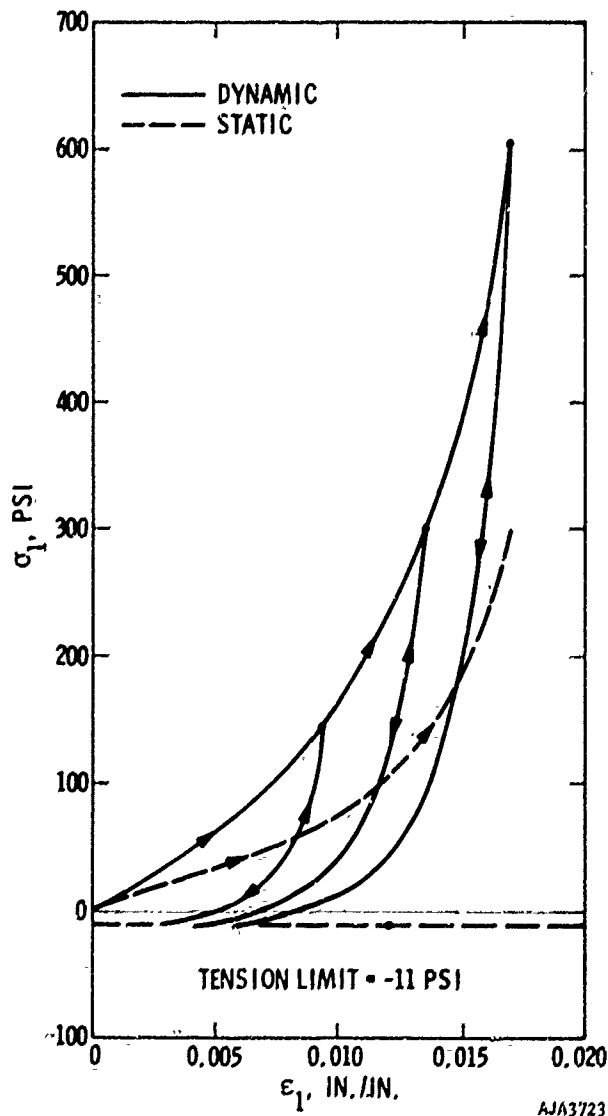
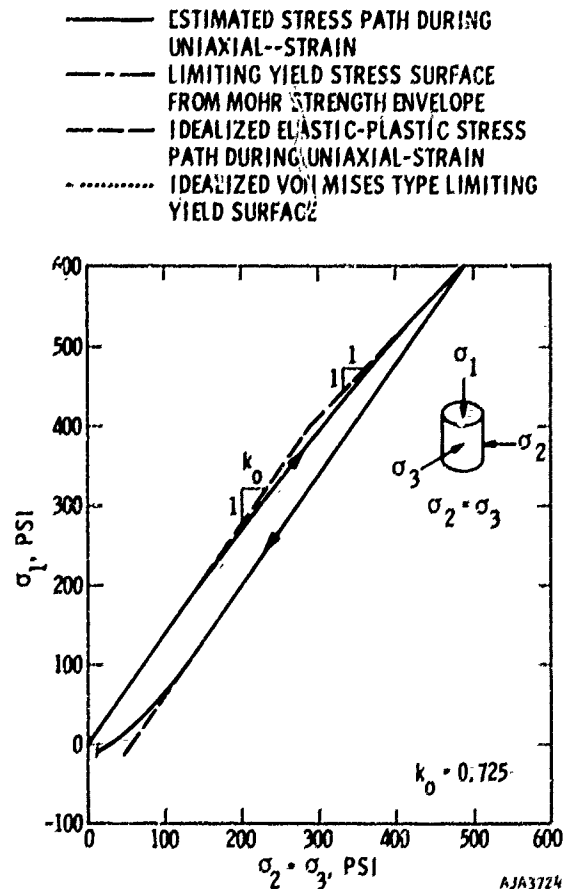


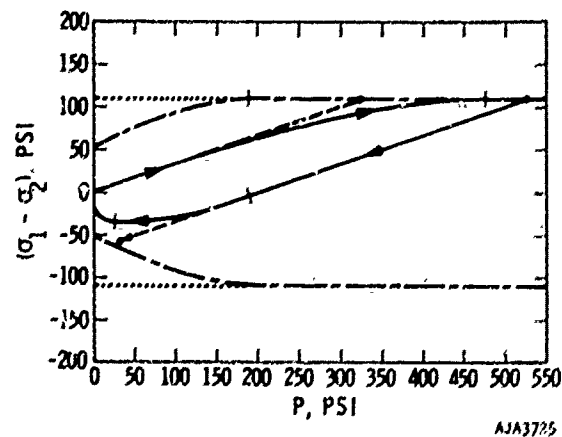
FIGURE 3-40. STRESS/STRAIN RELATIONS FOR SANDY CLAY SUBJECTED TO UNIAXIAL STRAIN (REFERENCE 3-85)

the tangent bulk modulus begins to decrease. In triaxial shear, where the shear stresses increase very rapidly with little change in mean normal stress, the tangent bulk modulus approaches zero, i.e., large volume decrease with little change in mean normal stress. Similar results occur at higher pressures except that, as the soil becomes saturated by decreasing the void ratio, the difference in the P/μ curves derived from uniaxial compression and hydrostatic compression vanishes.

At lower hydrostatic stress levels it is possible for the volume of the soil to increase upon application of shear stresses. This transition between increase

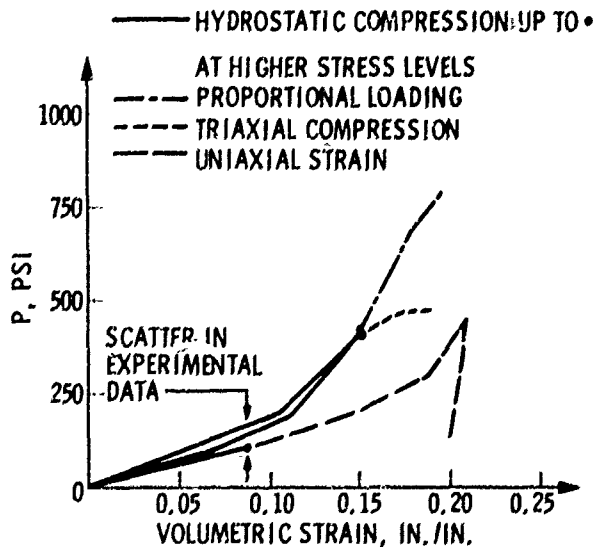


(a) MAJOR AND MINOR PRINCIPAL STRESSES DURING LOADING/UNLOADING IN UNIAXIAL STRAIN



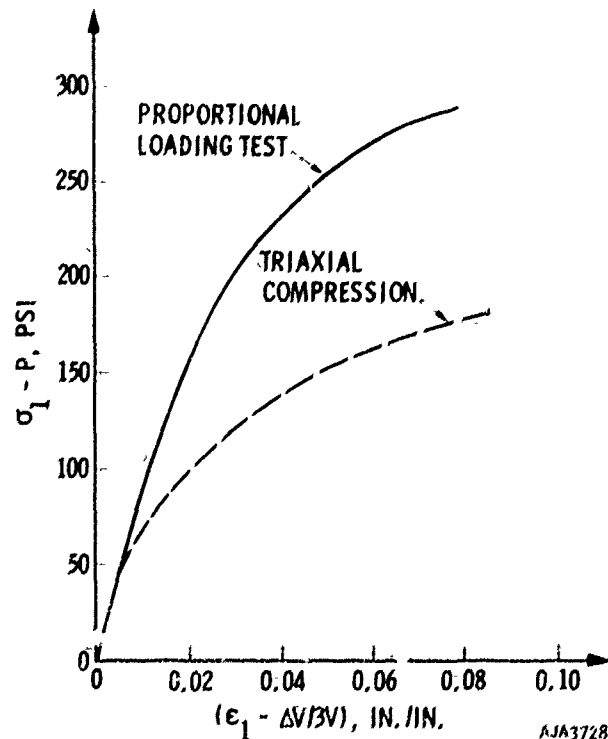
(b) STRESS DIFFERENCE VERSUS MEAN NORMAL STRESS DURING LOADING/UNLOADING IN UNIAXIAL STRAIN

FIGURE 3-41. STRESS PATHS DURING LOADING OF A CLAY IN UNIAXIAL STRAIN (REFERENCE 3-85)



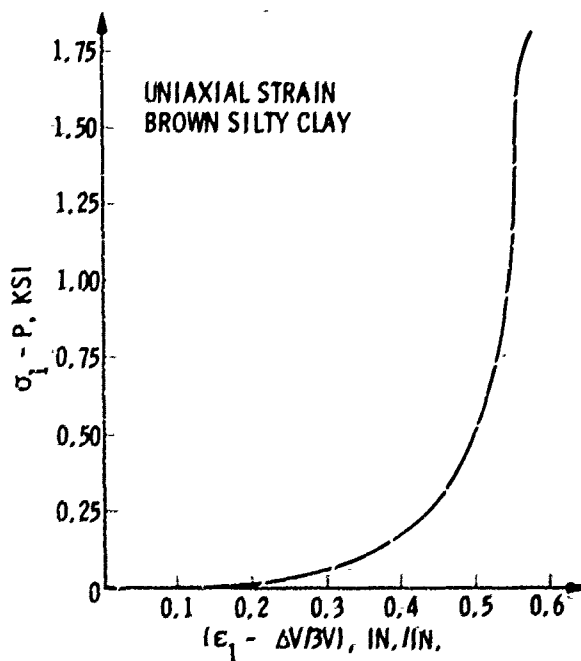
AJA3726

FIGURE 3-42. PRESSURE/VOLUME RELATIONSHIPS FOR WATCHING HILLS SANDY CLAY SUBJECTED TO DIFFERENT LOADING CONDITIONS (REFERENCE 3-30)



AJA3728

FIGURE 3-44. DEVIATORIC STRESS/STRAIN RELATIONS FOR WATCHING HILLS BROWN CLAY SUBJECTED TO DIFFERENT LOADING CONDITIONS (REFERENCE 3-30)



AJA3727

FIGURE 3-43. DEVIATORIC STRESS/STRAIN RELATION FOR WATCHING HILLS BROWN CLAY SUBJECTED TO UNIAXIAL STRAIN (REFERENCE 3-30)

in volume and decrease in volume is related to the critical void ratio and critical confining pressure of the soil discussed previously.

The deviatoric stress/strain relations are affected by the different stress paths which develop in uniaxial strain, proportional loading and triaxial compression, as shown in Figures 3-43 and 3-44. In uniaxial strain the tangent shear modulus increases with deviatoric stress under the influence of increasing effective mean normal stress. As the soil becomes saturated, there is a suggestion in Figure 3-43 that the shear stiffness begins to decrease. In proportional loading and triaxial compression, shear stiffness decreases monotonically, as shown in Figure 3-44.

Effects of Rate of Loading. The static stiffness and strength of saturated fine-grained soil is primarily influenced by stress history, void ratio, and structure. Loading rate affects the behavior of saturated fine-grained soil: primarily through its effect on pore pressures. Some dynamic direct shear tests (Reference 3-55) indicate that very little rate dependence is found in dry fine-grained soil. The dynamic behavior of dry clay is similar to dry sand

Properties of Soils

in that the rate sensitivity due to particle friction and rearrangement is small. Rate sensitivity due to crushing is practically nonexistent.

Tests on normally consolidated clay soils at strain rates from 0.01 (in./in.)/min to 0.00002 (in./in.)/min indicates that the rate sensitivity at small strains (<0.5 percent) is related to distortion, whereas the rate sensitivity at larger strains (>5 percent) is related to a volume change phenomenon (Reference 3-56). Deviator stresses and principal effective stress ratios were found to increase with an increase in strain rate at low strains without significant influence on the pore pressures. At the higher strains, the deviator stresses increase with rate, pore pressures decrease with rate, and the principal effective stress ratio is unaffected.

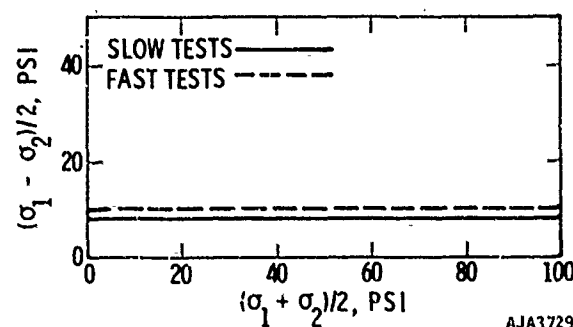
For saturated fine-grained soils, the shear strength is independent of the total mean normal stress. The shear strength under these conditions is often called the apparent cohesion of the soil and represents the undrained shear strength of saturated plastic clays. Direct dynamic shear tests on several clay soils indicate that the shear strength for normally consolidated saturated clays is increased by about a factor of two over static values when loads are applied in a few milliseconds.

As the degree of saturation decreases in fine-grained soils or as the plasticity decreases, the dynamic strength/static-strength ratio also tends to decrease, because the influence of moisture and pore pressure changes is diminished. Evidence of this behavior is shown in Figure 3-45. There is evidence that the dynamic-strength/static-strength ratio is higher in overconsolidated clays than in the same clay normally consolidated. For the same effective confining pressure the overconsolidated clay will have a lower void ratio.

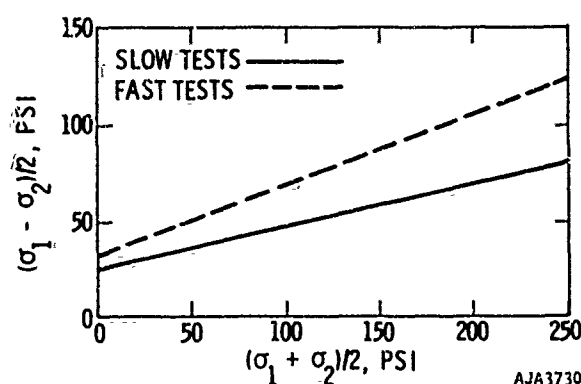
Dynamic triaxial tests on compacted clay (Reference 3-57) indicate that the secant modulus is highly dependent upon the rate of loading. Typical results for the secant modulus to one percent strain are shown in Figure 3-46. The secant modulus may vary by a factor of three due to loading rate effects. Comparing dynamic loading-rate results in the order of 6 msec to peak to conventional laboratory rates of a few minutes to peak shows that a factor of two exists between the secant moduli from ordinary tests and the secant moduli from dynamic tests.

In one-dimensional compression, the secant moduli from dynamic tests are generally twice those obtained from static tests even as the degree of saturation approaches 100 percent, as shown in Figure 3-40.

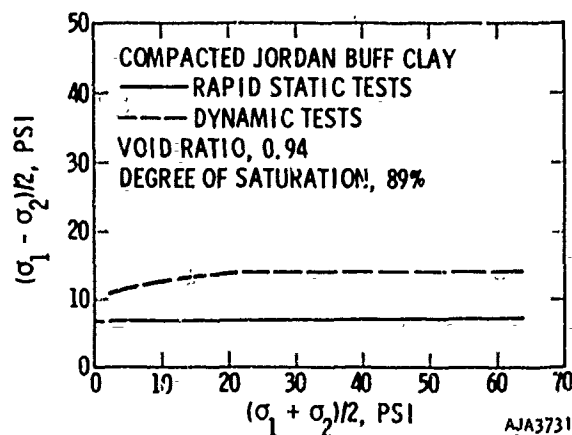
Elastic Wave Velocities. Limited data on the use of wave velocities to establish tangent moduli of soils is available on fine-grained soils. Results of wave velocity (ultrasonic) and resonant column tests



(a) SANDY SILT, WATCHING HILL
(REFERENCE 3-54)



(b) SANDY CLAY, WATCHING HILL
(REFERENCE 3-54)



(c) JORDAN BUFF CLAY (REFERENCE 3-55)

FIGURE 3-45. EFFECT OF LOADING RATE ON SHEAR STRENGTH OF COHESIVE SOILS

Experimental Techniques for Determining Soil Properties

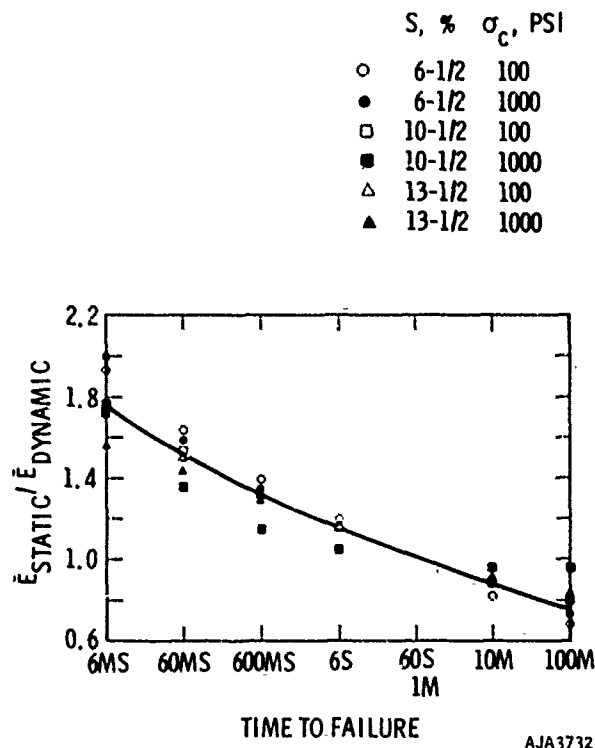


FIGURE 3-46. INFLUENCE OF TIME TO FAILURE ON THE NORMALIZED SECANT MODULI AT AN AXIAL STRAIN OF 1 PERCENT (REFERENCE 3-57)

(References 3-47, 3-48, 3-58, and 3-59) indicate that clays with low-surface activities (plasticity index/percent by weight of soil particles smaller than 2. microns) exhibit wave velocity characteristics similar to cohesionless soils. Their shear moduli decrease with increasing void ratio and varies approximately with the mean normal stress to the 0.5 power. Secondary effects due to time are pronounced in fine-grained soils. These secondary effects result in a buildup in stiffness not associated with changes in void ratio or confining pressure. They may be unimportant at stress levels of interest in nuclear weapons effects.

There is some indication that the shear modulus increases more rapidly with confining pressure than the 0.5 power as the surface activity of the clay minerals increases (Reference 3-58). The low amplitude shear wave velocity decreases as the moisture content increases because the soil density is greater and because the soil becomes less stiff. Beyond about 70-percent saturation, the water phase controls the velocity of dilatational waves.

Typical results showing the influence of void ratio and effective mean normal stress are shown in Figure 3-47.

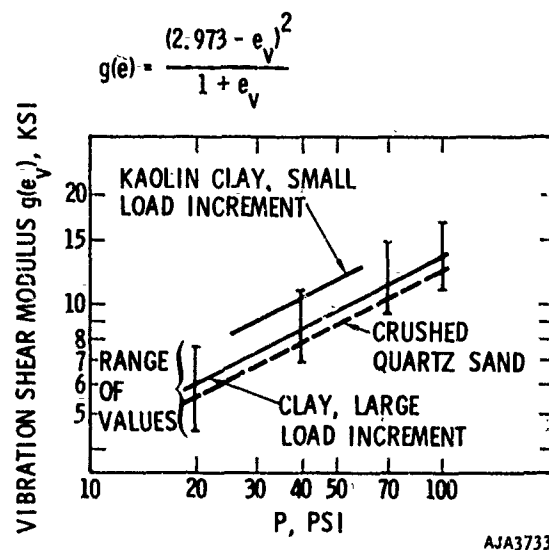


FIGURE 3-47. TANGENT SHEAR MODULUS OF FINE-GRAINED SOILS WITH INCREASING MEAN STRESS, DECREASES WITH INCREASING VOID RATIO (REFERENCE 3-58)

EXPERIMENTAL TECHNIQUES FOR DETERMINING SOIL PROPERTIES

As in the case of rock, the main goal of measuring soil properties is to aid in developing mathematical models for calculations of ground motion. Laboratory and field measurements are performed for different purposes. Laboratory experiments are capable of applying uniform static or dynamic stresses to small samples and of measuring complete stress and strain tensors. Field measurements supplement laboratory experiments by indicating geologic features such as layering and accounting for sample disturbance and effects of sample size.

This section describes techniques of performing laboratory and field experiments. Improvement in these techniques over the past 8 to 10 years is one of the major reasons for improvement of ground-motion calculations for soil sites.

Laboratory Testing

Both static and dynamic laboratory tests are commonly performed. Static tests are capable of investigating elaborate stress paths in which usually all components of stress and strain are measured. Dynamic tests include rapid loading, in which the load is applied within a few milliseconds but wave effects are absent, and wave propagation tests. In some dynamic tests, all components of stress and strain are not routinely measured.

Properties of Soils

Static Laboratory Testing. The static laboratory tests to be described below include those for applying triaxial compression and uniaxial strain. Direct shear and plane strain testing devices are also mentioned. The results of these tests can often be extrapolated to dynamic behavior by suitably modifying the static results.

A major consideration in design of the experimental apparatus is uniformity of stress and strain in the specimen. Nonuniform stress and strain, for example due to restraint by the metal end platens, can affect the apparent stress/strain properties of the specimen. Analysis by the finite element method is presently being used to aid in separating the effects

of end restraint from the fundamental stress/strain properties of laboratory specimens and to help evaluate a variety laboratory testing procedures (Reference 3-87). Since the analysis must first assume a model on the basis of experimental data which may be to some extent tainted by inhomogeneous stress and strain, the analysis does not give an absolutely correct stress and strain distribution in the specimen. However, the analysis can show the extent and approximate magnitude of these effects. The results of a finite element analysis of stress and strain in a sample of soil subjected to two different levels of axial stress in a triaxial compression test with constant confining stress of 400 psi is shown in Figure 3-48.

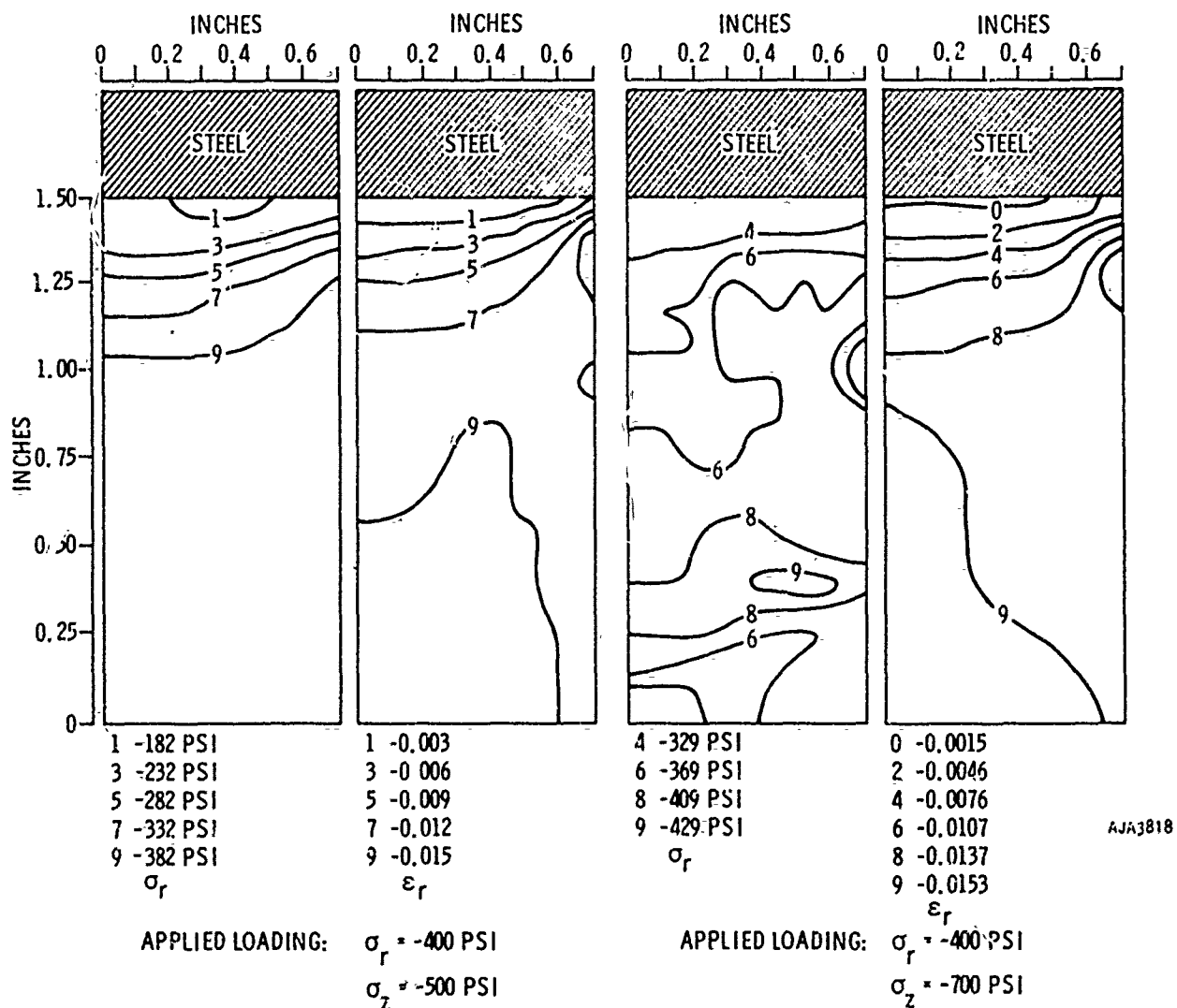


FIGURE 3-48. RADIAL STRESS AND STRAIN DISTRIBUTION IN A TRIAXIAL COMPRESSION EXPERIMENT AS INDICATED BY FINITE ELEMENT ANALYSIS (REFERENCE 3-87)

STATIC TRIAXIAL COMPRESSION

The triaxial compression test is the most common method of measuring strength and deformation properties. Cylindrical samples of having a height-to-diameter ratio of about 2.5 are subjected to stress paths as illustrated in Figure 3-1. A triaxial compression cell can be used (Reference 3-60) to subject samples to triaxial extension, triaxial compression, hydrostatic compression, and proportional loading. Devices are now available which enable lateral confining pressure to be applied up to 10,000 psi (Reference 3-30).

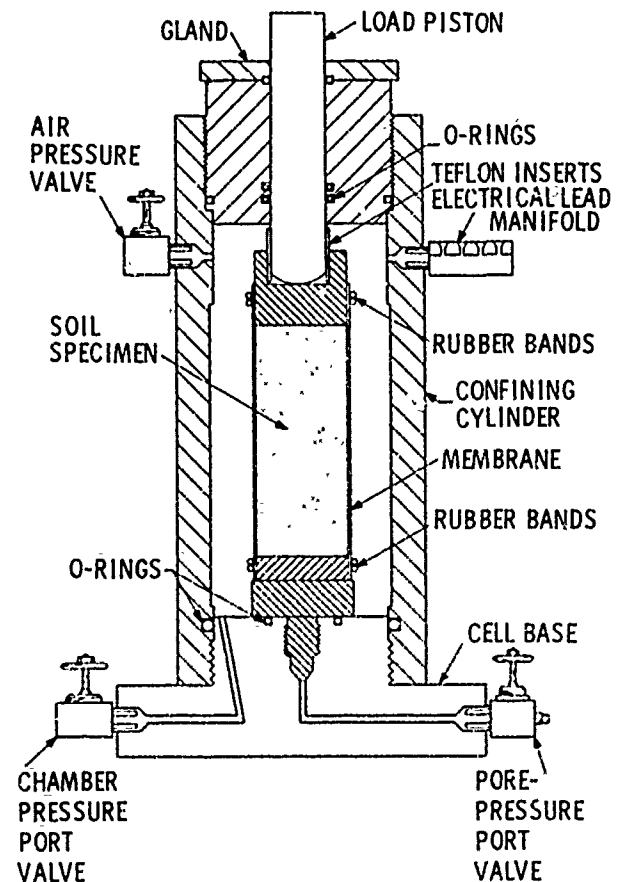
The soil sample is jacketed in a membrane and placed on a pedestal in a pressure chamber as shown in Figure 3-49. The total confining pressure on the sample is applied by increasing the cell pressure. The axial load is increased or decreased through a load piston. Measurements consist of axial load and deformation, confining pressure, radial deformation (Figure 3-50), and pore pressure or volume of fluid flow from the sample. The pore pressures are usually measured through porous stones in contact with the sample either by pressure-sensitive discs at the top and bottom or by needles placed into the sample. The pore pressure is usually measured with a mercury null indicator and manometer or by electrical transducers.

Various stress paths may be imposed on the sample as noted above, and the sample may be allowed to drain freely without buildup of excess pore pressures. In this case the total and effective stress paths are the same. Such tests are called drained or slow tests in contrast to undrained or quick tests where no pore fluid is allowed to drain from the sample. In the latter case the effective stress path and the total stress path differ by the amount of the pore pressure as is described in Figure 3-30. If the properties are to be used in ground-motion calculations, they are always measured under undrained conditions.

Triaxial compression devices have been developed to perform tests on rectangular samples where the three principal stresses can be independently controlled and the deformations in the directions of the principal stresses measured (References 3-64, 3-65), Figure 3-51. The device of Ko and Scott (Reference 3-65) uses a mechanical-hydraulic analog of an octahedral plane in principal stress space. The device is well suited to performing tests that maintain constant mean normal stress on the soil sample during shear.

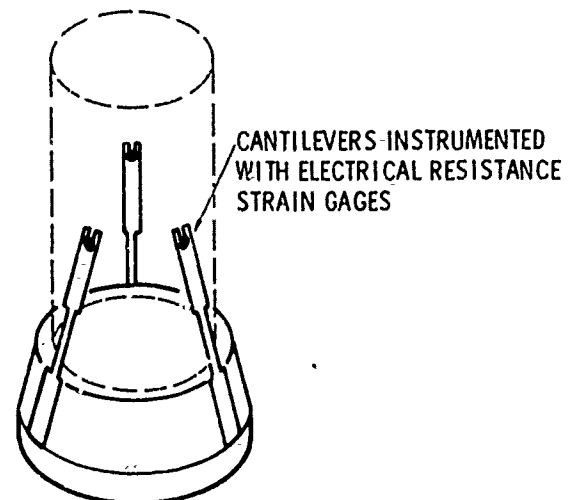
STATIC UNIAXIAL STRAIN

An oedometer test is conducted in uniaxial strain with the load applied to a cylindrical or a rectangular sample. The samples have a diameter (or breadth) of at least 2.5 times their thickness, which may range between 1.0 and 2.5 in. Figure 3-52, measurements of radial stress (Reference 3-63), axial stress, axial



AJA3734

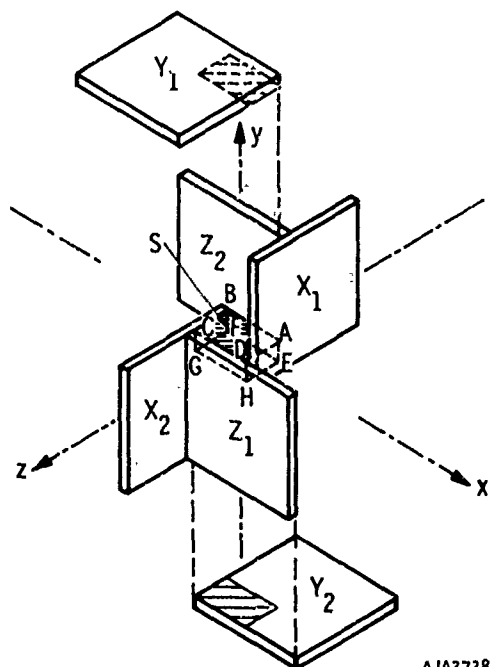
FIGURE 3-49. TRIAXIAL CELL (REFERENCE 3-30)



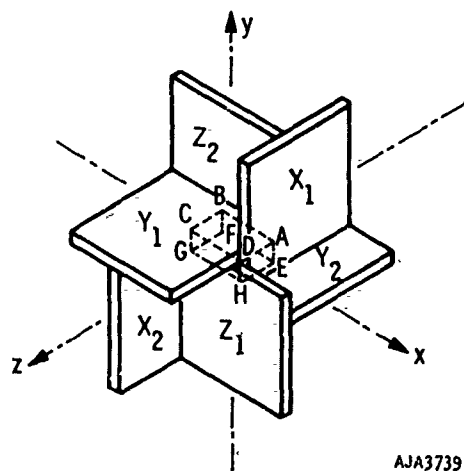
AJA3735

FIGURE 3-50. LATERAL DEFORMER (REFERENCE 3-30)

Properties of Soils



(a) PARTIALLY ASSEMBLED



(b) ASSEMBLED

FIGURE 3-51. SCHEMATIC DIAGRAM OF TRUE TRIAXIAL TEST APPARATUS (REFERENCE 3-64)

deformation, and pore pressure are made. The tests can be performed as either constant rate of strain. Static uniaxial strain tests have been performed with axial stresses in excess of 20,000 psi (References 3-17 and 3-35).

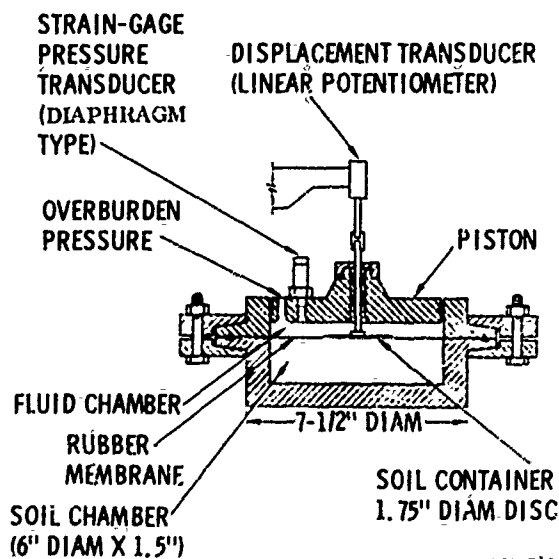
Uniaxial strain tests on saturated clay soils that allow drainage and pore-pressure dissipation are used to estimate primary consolidation (due to expulsion of

pore fluid) and secondary compression (creep deformation after pore pressures have dissipated). These consolidation tests are also used to estimate the maximum previous pressure on the soil and thus to judge whether it is normally consolidated or overconsolidated. For use in ground motion computations, however, properties are always measured under undrained conditions.

OTHER STATIC TESTS

Devices have been developed which subject soil samples to direct shear by forcing a sample to fail on a horizontal plane. This is accomplished by relative lateral movement of split solid rings as shown in Figure 3-1. The normal load (vertical) and deformation, and the lateral (horizontal) load and deformation are measured to establish approximate shear-stress/strain relations and volume-change/shear-strain relations and volume-change/shear-strain behavior. An improvement over this technique is the direct simple shear test, in which the soil sample is placed in a wire-reinforced rubber membrane rather than in the solid split rings and sheared horizontally (Reference 3-67). The shear strains are more nearly uniform within the sample and constant volume (undrained) conditions can be maintained by controlling the vertical normal stress.

Plane-strain testing devices have been developed (Reference 3-86) which allow measurement of all three principal stresses on rectangular soil samples. Deformations in the direction of major and minor principal stress are measured.



AJA3740

FIGURE 3-52. DYNAMIC OEDOMETER (REFERENCE 3-63)

Dynamic Direct Shear Testing

Dynamic Laboratory Testing. The dynamic laboratory tests to be described below include triaxial compression, uniaxial strain and direct shear tests. The advantage of dynamic testing over static testing for application to ground shock problems is that properties are measured more nearly under the same conditions that occur during shock loading. The disadvantage is that measurements of stress and strain are more difficult. New aspects of the experiments such as ensuring uniformity of stress and strain over a gage length and separating intrinsic rate effects from dynamic characteristics of the testing apparatus must also be considered.

Dynamic Triaxial Testing

Until recently, the dynamic stress paths that could be imposed in triaxial testing were limited to a static confining pressure with the application of a dynamic axial stress. Most of the equipment used in this type of testing was patterned after the M. I. T. hydraulic loader, (Reference 3-68) shown in Figure 3-53. Rise times as rapid as 3 milliseconds have been obtained with devices of this type by operating the press pneumatically (Reference 3-69). Pore pressure measurements are made during dynamic loading of coarse-grained soil using needle probes connected to dynamic pressure transducers. Pore pressure measurements have not been successful in fine-grained soils loaded at high rates due to the long time lag in the response of pore pressure probes.

The U. S. Army Waterways Experiment Station has developed a dynamic high pressure triaxial testing device which controls the dynamic application of confining pressure and axial load (References 3-66, 3-70). The device develops confining pressures up to 15,000 psi and measures axial load and deformation, confining pressure, and radial deformation during application of the dynamic stresses. Stress paths can be controlled with respect to the rise time, dwell time, and decay time of the radial and axial stresses.

DYNAMIC UNIAXIAL STRAIN

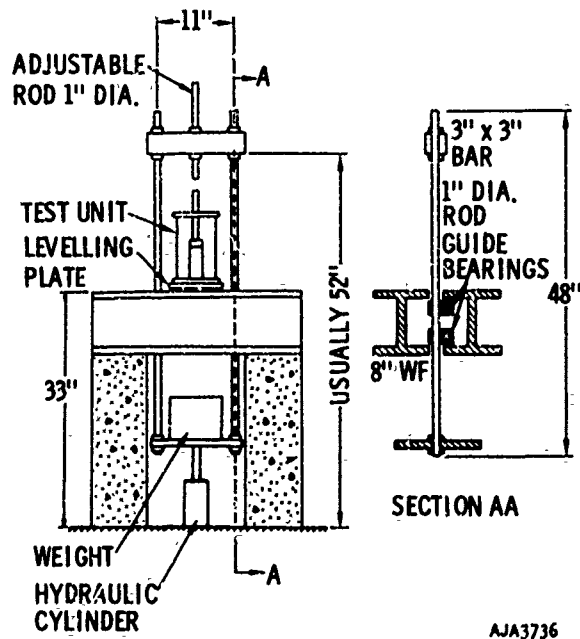
The major factors to consider in dynamic uniaxial strain experiments are radial rigidity and axial friction at the lateral boundary, the distribution of applied pressure, and the distribution of strain. In addition to minimizing boundary effects on the measurements and compensating for equipment deformation, it is also necessary to measure the lateral stresses that develop in one-dimensional tests to provide complete data on stress and strain tensors.

The one-dimensional compression device developed at the Waterways Experiment Station allows testing of large diameter samples to minimize size effects (Reference 3-71). The basic loading chamber is shown in Figure 3-54 and is similar in many respects

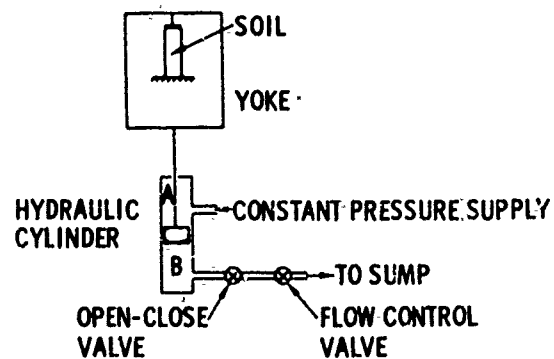
to most uniaxial strain devices. A particular advantage of the WES device is the ability to control the rise time (as short as 1 ms) dwell time and decay time (as short as 25 ms) of the loading pulse using a Dynapak piston-on-fluid stress transfer to the soil. Using fluid to transmit stress to the soil decreases the variation of stress across the sample.

DYNAMIC DIRECT SHEAR TESTING

Dynamic failure envelopes for soils have been obtained by using a pneumatic stress-controlled, direct shear apparatus (Reference 3-55). The device is



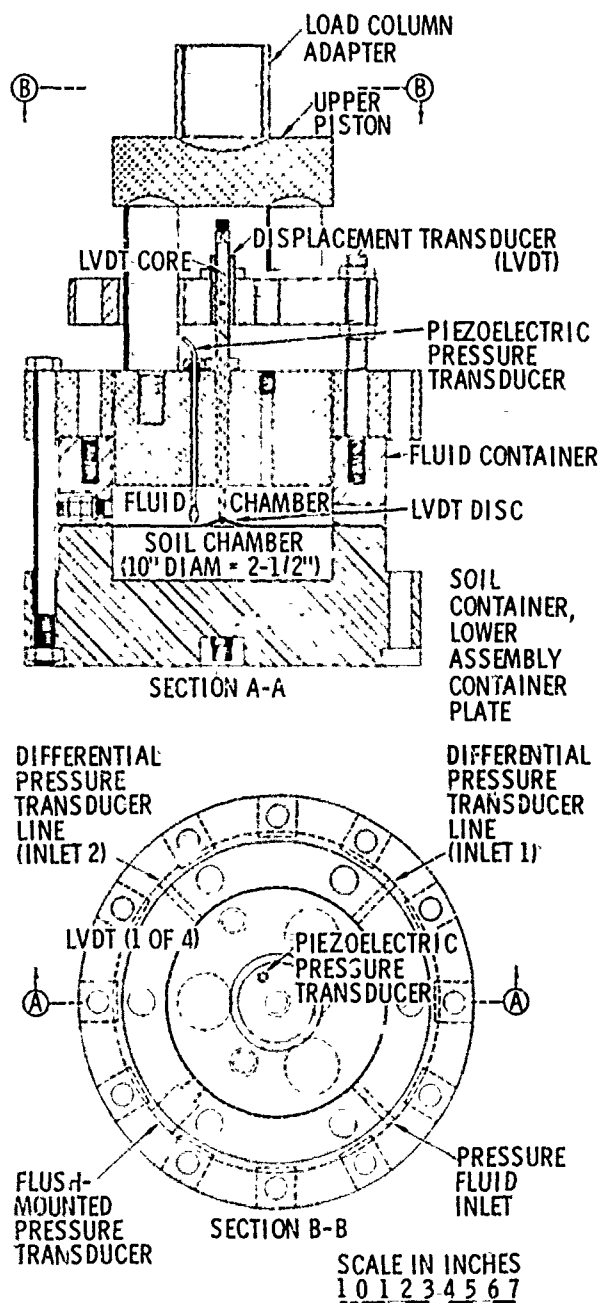
(a) LOADING YOKE AND FRAME



(b) HYDRAULIC CONTROL SYSTEM

FIGURE 3-53. MIT APPARATUS FOR RAPIDLY LOADED TRIAXIAL TESTS (REFERENCE 3-68)

Properties of Soils



NOTE: AN ADDITIONAL SOIL CONTAINER-LOWER ASSEMBLY CONTAINER PLATE, WITH THE SAME OVERALL DIMENSIONS AND WITH A 1-IN. THICK CHAMBER, IS AVAILABLE

WES 10-IN. -DIAM ONE-DIMENSIONAL COMPRESSION DEVICE

AJA3741

FIGURE 3-54. DRAWING OF BASIC ASSEMBLY, WES DYNAMIC OEDOMETER (REFERENCE 3-63)

similar in principle to static, direct shear tests. The dynamic transverse load can be applied with rise times of 1 to 5 ms and the normal force can be varied during shear and measured with a force transducer. Constant rate of deformation may be applied, and the transverse and normal deformations are recorded.

Laboratory Ultrasonic Techniques. Laboratory techniques are available to evaluate tangent module under a combination of static loading with small, dynamically applied excursions. The excursions occur either as a stress-wave or as small-amplitude, vibratory motion.

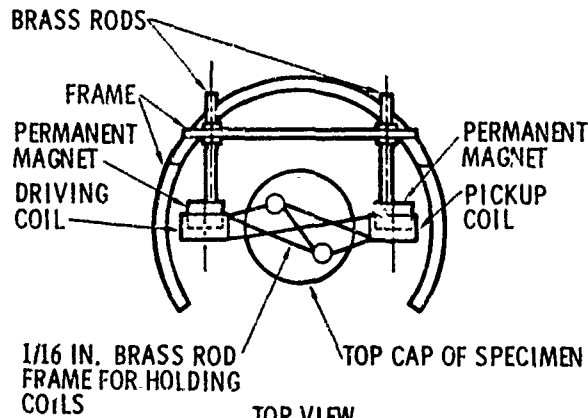
Figure 3-55 illustrates the resonant column technique (Reference 3-72). Longitudinal or torsional vibrations are produced in the soil rod through the base (fixed-free condition). Accelerometers are used at both ends of the rod to determine the frequency at which resonance occurs and the equivalent wave length. The results of this test are interpreted using resonant rod, elastic theory, and applying the proper boundary condition. Free-free boundary conditions have also been imposed on the sample, and vibrations can be introduced by using an oscillator-driven, vibrating membrane or driving coils and permanent magnets. Most of the devices apply strains of the order of 10^{-5} in./in. However, a resonant column apparatus has been developed to apply strain in excess of 10^{-4} in./in. (Reference 3-73).

Wave propagation techniques have been used to evaluate the soil moduli under small stress excursions (References 3-44, 3-47, 3-48). The technique employs piezoelectric crystals as the source of the stress wave and as the detector of arrival time as shown in Figure 3-56. The wave velocity is inversely proportional to the square root of the mass density of the soil and proportional to the square root of a tangent stiffness parameter or modulus. The relevant modulus depends upon the type of disturbance and the boundary conditions. A piezoelectric crystal that exerts a compressive pulse on a confined sample of soil generates a dilatational wave, whereas a crystal that exerts a torsional input generates a shear wave. Difficulties in interpreting the results of such tests include having the first arrival masked due to dispersion of the wave front.

In Situ Testing

The purposes of in situ testing include measurement of indices which can be correlated with such engineering properties as bearing capacity, direct measurement of strength and stiffness and detection of such geologic features as layering and location of a water table. As in the case of rocks, in situ experiments are less well-controlled and yield less precise information than laboratory experiments. Therefore, they are used more for qualitative than for quantitative data.

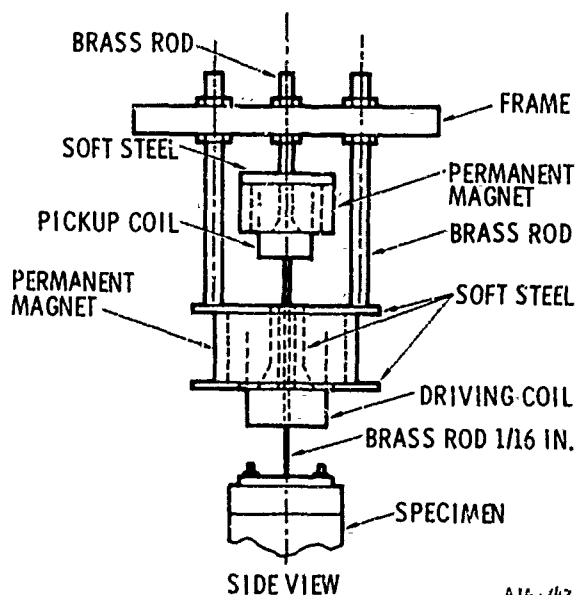
Dynamic Direct Shear Testing



TOP VIEW

(a) SHEAR MODULUS

AJA3742



SIDE VIEW

(b) YOUNG'S MODULUS

AJA3743

FIGURE 3-55. SOIL VIBRATION MECHANISMS FOR SHEAR WAVE APPARATUS (a) AND COMPRESSION WAVE APPARATUS (b) (REFERENCE 3-72)

In Situ Penetration Tests. Two common in situ tests which indicate properties indirectly are the standard penetration test and core penetration tests (Reference 3-74). The standard penetration test is conducted by driving a spoon sampler 12 in. into the soil. The results are correlated with the relative density of cohesionless soils and the slope of an expected Mohr-Coulomb failure envelope. Correlations exist generally for stress levels below 10 bars. No satisfactory correlations exist to indicate the behavior of cohesive soils except to distinguish between soft, medium, and hard strata.

The core penetrometer test exists in a variety of forms. The Dutch penetrometer is the most widely used, which consists of a 60-degree core with a 1.4-in. diameter which is pushed 20 in. into the soil at a rate of 0.4 in./sec. The force required for penetration has been related to Young's modulus for coarse-grained soils and the compression index $(1 + e_0)\sigma/0.435B$ for fine-grained soils.

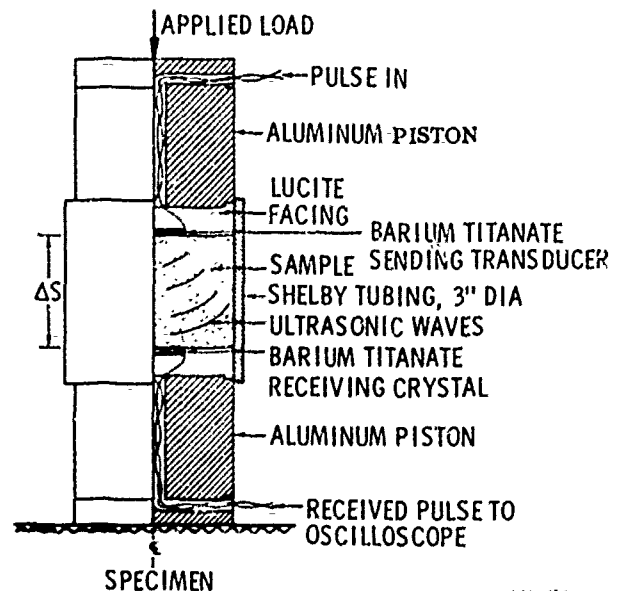
In Situ Plate Loading and Other Tests. In situ plate loading tests are used to estimate load/deformation relationships which may be extrapolated to larger areas using various empirical approaches or dimensional analysis. In some cases the expected load/deformation behavior is interpreted by means of an elastic theory to evaluate a secant modulus. A similar approach is used with a limiting plastic equilibrium theory to establish a value for shear strength. Only the soil within a zone approximately twice the width of the plate influences the measurements. Hence, extrapolation to very large areas is impossible with this method.

$M =$ MODULUS

$P =$ MASS DENSITY OF SOIL

$M = pc^2$

$c = \Delta t / \Delta L,$ VELOCITY OF TRAVEL ACROSS SAMPLE BETWEEN SENSORS



AJA3744

FIGURE 3-56. APPARATUS FOR ULTRASONIC WAVE PROPAGATION THROUGH SOIL (REFERENCE 3-68)

Properties of Soils

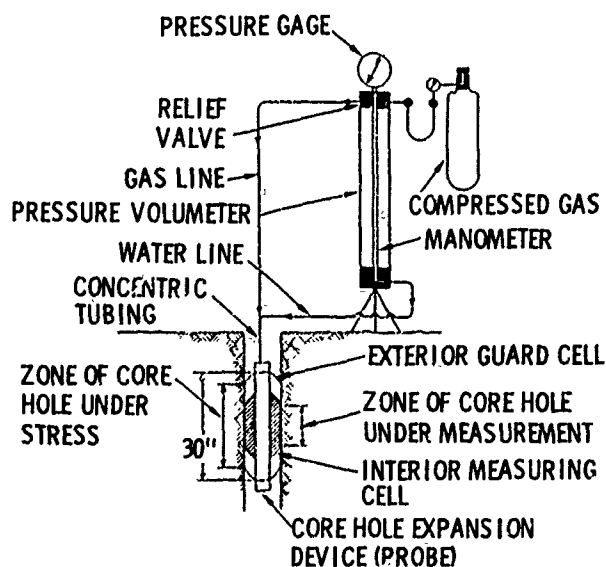
Other field tests such as the vane shear test, pressure meter test and bore hole direct shear test are intended to measure more fundamental quantities in the soil. The vane shear test is used primarily to evaluate the shear strength of soft clay soils. Interpretation of the results is difficult since the test drainage conditions and the state of stress in the soil are not well known, and the principal directions of stress and strain rotate during the test. The test provides a good indication of variations in strength of a soil profile.

The pressure meter (Reference 3-75) shown in Figure 3-57 applies a pressure to the side of a bore hole deforming the soil. The pressure and volume change measured over the central part of the cell are related to a secant modulus of the soil. This is found by assuming Young's modulus and the secant modulus to be equal and then using elasticity theory. Yielding is detected from the relation between pressure and volume change. The results represent drained conditions for coarse-grained soils and undrained conditions for fine-grained soils.

The bore hole direct shear device shown in Figure 3-58 is similar to a laboratory direct shear device (Reference 3-76). The shearing plates are forced against the side of the bore hole by applying normal pressure. Then the plates are pulled along the walls of the bore hole to determine the soil shear resistance. The shear strength is presented as a function of normal pressure. Shortcomings of this test are that the state of stress imposed on the soil is not known, and rotation of principal stresses occurs during testing.

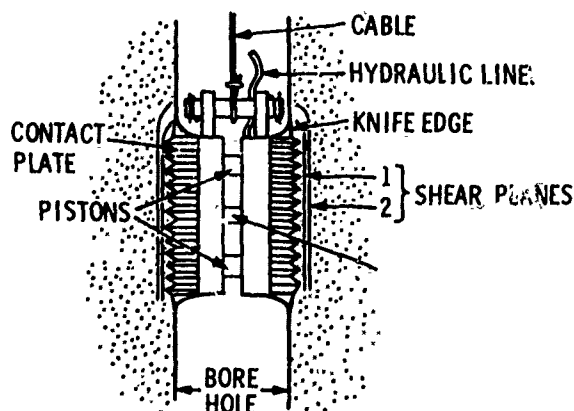
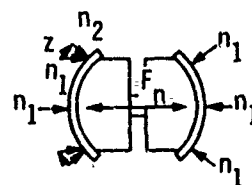
Block shear tests are sometimes performed to determine the shear strength of large soil samples carved out in situ. These tests are better than laboratory tests on small samples when the macrostructure of the soil deposit requires the use of large samples as in fissured clays (Reference 3-77).

Field Seismic Tests. Field seismic tests are used to estimate elastic properties of soil at small excursions from the overburden stress and to detect layering in a soil profile. Dilatational, Rayleigh, and shear waves can be reliably detected in soil. The dilatational (compressional) wave travels at the highest velocity in soil. Hence, its first arrival can be detected. Vertical disturbances on the surface of the ground couple most of the energy into Rayleigh surface waves whose slower velocity and concentration near the surface distinguishes them from dilatational waves. Shear waves have about the same velocity as Rayleigh waves but are distinguished from them by having particle motion transverse to the direction of propagation and by their ability to propagate at any depth.



AJA3745

FIGURE 3-57. SCHEMATIC DRAWING OF PRESSURE METER EQUIPMENT (REFERENCE 3-75)



NOTE: CIRCUMFERENTIAL SHEARING RESISTANCE z MUST BE MINIMIZED FOR UNIFORM DISTRIBUTION FOR CONTACT PRESSURE n_1 . KNIFE EDGES MINIMIZE END RESISTANCE.

AJA3746

FIGURE 3-58. SCHEMATIC OF BORE-HOLE SHEAR DEVICE (REFERENCE 3-76)

The first-arrival technique is used in refraction surveys (Reference 3-78) to locate underlying strata that transmit the compressional wave at a higher velocity than does the overlying layers. The average dilatational wave velocity can be detected for each layer by creating a disturbance at the ground surface and measuring the first arrival of the disturbance with transducers spaced along a line on the ground surface.

Change in slope of the arrival-time/distance relationship indicates that the first arrival of the disturbance has traveled through an underlying material with a velocity of propagation greater than the overlying material. Using the analysis of refraction of elastic waves, inclined and multiple layering can be located.

First-arrival measurements are also used to determine the average velocity of propagation by measuring travel times between bore holes. An explosive charge is triggered in one bore hole with a sensor located in another bore hole. The average velocity is found from the distance and transmit time between the charge and sensor. Differences in average vertical and horizontal properties or the influence of overburden stresses can be evaluated by measuring horizontal travel time (cross-hole shots) or vertical travel times (up-hole shots). Since the dilatational wave produces particle motion parallel to the direction of propagation and the shear wave produces particle motion perpendicular to the direction of propagation, sensors can be arranged to distinguish the two types of waves. The constrained modulus, B , and shear modulus, G , can be evaluated directly from the dilatational and shear wave velocities, respectively.

The velocity of the Rayleigh wave is very nearly equal to the velocity of the shear wave. Hence, Rayleigh wave measurements are sometimes used to evaluate the shear modulus of the soil. Rayleigh waves attenuate rapidly with depth and have nearly completely dissipated at a depth of one wave length. It is sometimes assumed that the Rayleigh wave properties approximate the average soil properties within a depth of one-half a wave length, (Reference 3-79). The Rayleigh wave velocity is measured using a source of harmonic vibration on the surface of the soil and measuring along the surface of the soil the points which are vibrating in phase with the source. This represents a multiple of wavelengths, and the Rayleigh wave velocity U_{Rf} is related to the frequency of harmonic motion, F , and the wavelength, L_r , by

$$U_{Rf} = FL_r$$

By reducing the frequency, soil properties at greater depths can be obtained. However, the size of the oscillator must then be increased to develop waves having sufficient energy that the motions may be clearly detected.

SUMMARY

This chapter summarizes the mechanical properties of soil and the testing procedures which are used in constitutive equations for ground motion calculations. The constitutive behavior of all soils is influenced by initial void ratio, degree of saturation, stress history, path, and rate of loading. The importance of relating strength and stiffness to effective stress is pointed out. It is also noted, however, that it is often possible and desirable to evaluate the behavior of saturated and partially saturated soil on the basis of total stress, and that this is the usual practice in measuring properties for ground shock effects. Evidence of extreme differences between saturated and partially saturated soils is cited. A distinction is made between fine-grained and coarse-grained soils due to different types of stress transfer between grains. In fine-grained soils, stress transfer is dominated by electrical forces, whereas in coarse-grained soils it is dominated by friction.

The task of measuring soil properties is easier than that of measuring rock properties in that soil tends to be more homogeneous and the mechanisms of energy dissipation are averageable over greater distances. As a consequence, energy absorption, stress/strain behavior, and strength of soil can be established on the basis of experiments performed in a laboratory on small samples. Static and dynamic laboratory testing procedures are described above in which, in the optimum tests, the complete stress and strain tensors can be measured. Shortcomings of these tests, besides possible distortions due to small sample size, include inhomogeneous stress and strain distribution due to edge and end constraints. Field testing is described as a supplement to laboratory testing wherein qualitative information on overall site features is obtained and used to modify properties based on laboratory measurements.

The major advances which have occurred in the last 8 to 10 years are in the area of applying soil dynamics to effects of explosions and in the area of improved sampling and laboratory testing techniques. The requirement for samples to reach the laboratory at their in situ void ratio and moisture content has been understood for many years and is now being accomplished routinely at some laboratories. These sampling and laboratory testing programs are being supplemented from time to time by large-scale explosive field tests, such as Operation Distant Plain and Middle Gust, where mathematical models, based on laboratory data, are used in calculations and compared with field measurements of motion and stress. Favorable agreement is considered to confirm the validity of soil sampling and testing, the mathematical modeling procedures, and the program of field measurements. Lack of agreement indicates that errors

Properties of Soils

were made in at least one of these areas. In cases where there is disagreement, it is extremely difficult to decide exactly where the errors are.

LIST OF GENERAL SOURCES

Texts

Lambe, T. W. and R. V. Whitman, (1969) Soil Mechanics John Wiley and Sons, New York

Richart, F. E., Jr., J. R. Hall, Jr., and R. D. Woods (1970) Vibrations of Soils and Foundations, Prentice-Hall Int. Series, Englewood Cliffs, N. J.

Leonards, G. A. (ed.) (1962), Foundation Engineering, McGraw-Hill Book Co., New York

Lambe, T. W. (1951), Soil Testing for Engineers, John Wiley and Sons, New York

Scott, R. F. (1963), Principles of Soil Mechanics, Addison-Wesley, Reading, Mass.

REFERENCES

ASTM Standards, 1967 Bituminous Materials; Soils; Skid Resistance Part II, Std. D-2049-64T

Design Manual, Soil Mechanics, Foundations and Earth Structures, NAVDOCKS DM-7, Dept. of the Navy Bureau of Yards and Docks, Washington

Proceedings, International Symposium on Wave Propagation and Dynamic Properties of Earth Materials, (1967), University of New Mexico Press, Albuquerque, New Mexico

Proceedings, of the Symposium on Soil-Structure Interaction, (1964) University of Arizona, Tucson, Arizona

Whitman, R. V., (1970), The Response of Soils to Dynamic Loadings Final Report, Army Waterways Experiment Station DASA Contract Report No. 3-26, Vicksburg, Miss.

Proceedings of the International Conference on Soil Mechanics and Foundation Engineering, Cambridge, Mass 1936, Rotterdam 1948, Zurich 1953, London 1957, Paris 1961, Montreal 1965, Mexico City 1969, Moscow 1973

REFERENCES

3-1. Lambe, T. W., and R. V. Whitman, Soil Mech., John Wiley and Sons, Inc., New York, 1969.

3-2. Koerner, R. M., "Effect of Particle Characteristics on Soil Strength," J. of the Soil Mech. and Foundation Div., ASCE Vol. 96, No. SM4, Paper 7393, July 1970, pp. 1221-1234.

3-3. Koerner, R. M., "Behavior of Single Mineral Soils in Triaxial Shear," J. of the Soil Mech. and Foundation Div., ASCE, Vol. 96, No. SM4, Proc. Paper 7432, July 1970, pp. 1373-1391.

3-4. ASTM/Standards, 1967, Bituminous Materials; Soils; Skid Resistance, Part II, STD. D-2049-64T, pp. 610-618.

3-5. Vesic, A. S., and Clough, W. G., "Behavior of Granular Materials Under High Stresses," J. of the Soil Mech. and Foundation Div., ASCE, Vol. 94, No. SM3 Proc. Paper 5954, May 1968, pp. 661-688.

3-6. Lee, K. L., and H. B. Seed, "Drained Strength Characteristics of Sand," J. of the Soil Mech. and Foundation Div., ASCE, Vol. 93, No. SM6, Proc. Paper 5561, November 1967, pp. 117-143.

3-7. Grim, R. E., Applied Clay Mineralogy, McGraw-Hill, 1962.

3-8. Rosenqvist, I. T., "Physico-Chemical Properties of Soils: Soil Water Systems," J. of the Soil Mech. and Foundation Div., ASCE, Vol. 85, No. SM2, April 1959, pp. 31-53.

3-9. Lambe, T. W., Soil Testing for Engineers, John Wiley and Sons, New York, 1951.

3-10. Lambe, T. W., "A Mechanistic Picture of Shear Strength in Clay," Proc. ASCE Research Conf. on Shear Strength of Cohesive Soils, Boulder, Colorado, 1960, pp. 555-580.

3-11. Skempton, A. W., "Effective Stress in Soils, Concrete, and Rocks," Pore Pressure and Suction in Soils, Butterworth, London, 1961, pp. 4-16.

3-12. Bishop, A. W., "The Measurements of Pore Pressure in the Triaxial Test," Pore Pressure and Suction in Soils, Butterworth, London, 1961, pp. 38-46.

3-13. Whitman, R. V., et al., "Time-Lags in Pore Pressure Measurements," Proc. Fifth Int. Conf. on Soil Mech. and Foundation Eng., 1961, Paris, Vol. 1, p. 407.

3-14. Biot, M. A., "The Theory of Propagation of Elastic Waves in a Fluid-Saturated Porous Solid," J. Acoust. Soc. of Am., Vol. 28, March 1956, pp. 168-191.

3-15. Bishop, A. W., et al., "Factors Controlling the Strength of Partly Saturated Cohesive Soils," Proc. ASCE Res. Conf. on Shear Strength of Cohesive Soils, 1960, pp. 503-532.

References

- 3-16. Croney, D., and J. D. Coleman, "Pore Pressure and Suction in Soil," Pore Pressure and Suction in Soils, Butterworth, London, 1961, pp. 31-38.
- 3-17. Hendron, A. J., et al., Effect of Degree of Saturation on Compressibility of Soils from the Defence Research Establishment Suffield, WES Contract Report S-69-3, April 1969.
- 3-18. Seed, H. B., and K. L. Lee, "Liquefaction of Saturated Sands During Cyclic Loading," J. of the Soil Mech. and Foundation Div., ASCE, Vol. 92, No. SM6, November 1966, pp. 81-104.
- 3-19. Mindlin, R. D., "Mechanics of Granular Media," Lecture, Second U. S. National Congress of Appl. Mech., Ann Arbor, Michigan, June 1954, pp. 13-20.
- 3-20. Deresiewicz, H., "Mechanics of Granular Matter," Adv. in Appl. Mech., Academic Press, Inc., New York, N. Y., Vol. V, pp. 233-306.
- 3-21. Duffy, J., and R. D. Mindlin, "Stress-Strain Relations and Vibrations of Granular Medium," J. Appl. Mech., Vol. 24, Trans. ASME, Vol. 79, 1957, pp. 585-593.
- 3-22. Hendron, A. J., Jr., et al., The Energy Absorption Capacity of Granular Materials in One-Dimensional Compression, Tech. Doc. Report No. AFSWL-TRD-62-91, AFSWC, Kirtland AFB, New Mexico, January 1963.
- 3-23. Miller, E. T., Stresses and Strains in a Planar Array of Elastic Spheres, Research Report R63-39, Dept. of Civil Eng., Mass Inst. of Technol., August 1963.
- 3-24. Whitman, R. V., et al., "Yielding and Locking of Confined Sand," J. of the Soil Mech. and Foundation Div., Vol. 90, No. SM4, Proc. ASCE, July 1964, pp. 57-85.
- 3-25. Thurston, C. W., and H. Deresiewicz, "Analysis of a Compression Test of a Face-Centered Cubic Array of Elastic Spheres," J. of Appl. Mech., Vol. 26, Trans. ASME, Vol. 81, 1959, pp. 251-255.
- 3-26. Rowe, P. W., "The Stress-Dilatancy Relation for Static Equilibrium of an Assembly of Particles in Contact," Proc. Roy. Soc., (London), Vol. 269, 1967, pp. 500-527.
- 3-27. King, J. W. G., and E. A. Dickinson, "Comparison of Stress-Dilatancy Theories," J. of the Soil Mech. and Foundation Div., Vol. 96, No. SM5, Proc. ASCE Paper No. 7516, September 1970, pp. 1697-1713.
- 3-28. Ko, H. K., and R. F. Scott, "Deformation of Sand in Hydrostatic Compression," J. of the Soil Mech. and Foundation Div., Vol. 93, No. SM3, Proc. ASCE, Proc. Paper No. 5245, May 1967, pp. 137-156.
- 3-29. Domaschuk, L., and N. H. Wade, "A Study of Bulk and Shear Moduli of a Sand," J. of the Soil Mech. and Foundation Div., Vol. 95, No. SM2, Proc. ASCE, Proc. Paper No. 6461, March 1969, pp. 561-581.
- 3-30. Mazanti, B. B., and C. N. Holland, Study of Soil Behavior Under High Pressure, Vols. 1, 2, 3, Contract Report 4-70-2, Army Waterways Experiment Station, Vicksburg, Miss., February 1970.
- 3-31. Paulding, B. W., et al., Behavior of Rocks and Soils Under High Pressure, AFWL-TR-65-51, Air Force Weapons Lab., Kirtland AFB, New Mexico, December 1965.
- 3-32. Ko, H. K., and R. F. Scott, "Deformation of Sand in Shear," J. of the Soil Mech. and Foundation Div., Vol. 93, No. SM5, Proc. ASCE, Proc. Paper 547, September 1967, pp. 283-311.
- 3-33. El-Shoby, M. A., "Deformation of Sands Under Constant Stress Ratios," Proc. Seventh Int. Conf. on Soil Mech. and Foundation Eng., Vol. 1, Mexico City, 1969, pp. 111-120.
- 3-34. Hendron, A. J., Jr., The Behavior of Sand in One-Dimensional Compression, Tech. Doc. Report No. RTD-TDR-63-3089, Air Force Weapons Laboratory, October 1963.
- 3-35. Davisson, M. T., et al., Static and Dynamic Behavior of Sands in One-Dimensional Compression, Technical Report No. AFWL-TR-65-29, Air Force Weapons Laboratory, December 1965.
- 3-36. Davisson, M. T., and A. J. Hendron, Jr., A Review of Dynamic One-Dimensional Stress-Strain Relationships for Soils, Aerospace Corporation, San Bernardino, California, February 1966.
- 3-37. Gardner, W. S., "Stress-Strain Behavior of Granular Soils in One-Dimensional Compression," presented at ASCE Structural Eng. Conf., Miami, Florida, 1966.
- 3-38. Whitman, R. V., and K. A. Healy, "Shear Strength of Sands During Rapid Loadings," J. of the Soil Mech. and Foundation Div., Vol. 88, No. SM2, Proc. ASCE, Proc. Paper 3102, April 1962, pp. 99-133.

Properties of Soils

- 3-39. Lee, K. L., et al., "Effect of Transient Loading on the Strength of Sand," Proc. Seventh Int. Conf. on Soil Mech. and Foundation Eng., Mexico City, 1969, pp. 239-248.
- 3-40. Atakol, K., and H. G. Larew, "Dynamic Shearing Resistance of Dry Ottawa Sand," J. of the Soil Mech. and Foundation Div., Vol. 96, No. SM2, Proc. ASCE, Proc. Paper No. 7186, March 1970, pp. 705-721.
- 3-41. Seed, H. B., and R. Lundgren, "Investigation of the Effect of Transient Loading on the Strength and Deformation Characteristics of Saturated Sands," Proceedings, ASTM, Vol. 54, 1954.
- 3-42. Seed, H. B., and K. L. Lee, "Undrained Strength Characteristics of Cohesionless Soils," J. of the Soil Mech. and Foundation Div., Vol. 93, No. SM6, Proc. ASCE, Proc. Paper 5618, November 1967, pp. 333-360.
- 3-43. Hardin, B. O., and F. E. Richart, Jr., "Elastic Wave Velocities in Granular Soils," J. of the Soil Mech. and Foundation Div., ASCE, Vol. 89, No. SM1, Proc. Paper 3407, February 1963, pp. 33-65.
- 3-44. Whitman, R. V., and F. V. Lawrence, Discussion on "Elastic Wave Velocities in Granular Soils," J. of the Soil Mech. and Foundation Div., ASCE, Vol. 89, No. SM5, September 1963, pp. 112-119.
- 3-45. Hardin, B. O., and W. L. Black, "Sand Stiffness Under Various Triaxial Stresses," J. of the Soil Mech. and Foundation Div., ASCE, Vol. 92, No. SM2, Proc. Paper 4712, March 1966, pp. 27-42.
- 3-46. Drnevich, V. P., and F. E. Richart, Jr., "Dynamic Prestraining of Dry Sand," J. of the Soil Mech. and Foundation Div., ASCE, Vol. 96, No. SM2, Proc. Paper 7180, March 1970, pp. 453-469.
- 3-47. Lawrence, F. V., Jr., "Ultrasonic Shear Wave Velocities in Sand and Clay," Response of Soils to Dynamic Loads, Report No. 23, M.I.T., Cambridge, Mass., January 1965.
- 3-48. Rao, H. A., Balakrishna, "Wave Velocities through Partially Saturated Sand-Clay Mixtures," Response of Soil of Dynamic Loadings, Report No. 24, M.I.T., Cambridge, Mass., March 1966.
- 3-49. Henkel, D. J., "The Effect of Overconsolidation on the Behavior of Clays during Shear," Geotechnique, Vol. VI, 1956, p. 139.
- 3-50. Yong, R. N., and E. McKyes, "Yield and Failure of Clay Under Triaxial Stresses," J. of the Soil Mech. and Foundation Div., ASCE, Vol. 97, No. SM1, Proc. Paper 7790, January 1971, pp. 159-176.
- 3-51. Ladd, C. C., "Stress-Strain Modulus of Clay in Undrained Shear," J. of the Soil Mech. and Foundation Div., ASCE, Vol. 90, No. SM5, September 1964, pp. 103-132.
- 3-52. Casagrande, A., "The Determination of the Preconsolidation Load and Its Practical Significance," Proc. First Int. Conf. on Soil Mech. and Foundation Eng., Cambridge, Mass, 1936, p. 60.
- 3-53. Kane, H., et al., A Study of the Behavior of Soil and Rock Subjected to High Stresses, Tech. Report No. AFWL-TR-64-157, AD 614-451, Air Force Weapons Laboratory, March 1965.
- 3-54. Jackson, J. G., and J. E. Windham, Preliminary Report, Operation Distant Plain, Event 6, Soil Property Investigation for Project 2.10, Soil Sampling and Testing, Army Waterways Experiment Station, Vicksburg, Miss., December 1967.
- 3-55. Schimming, B. B., et al., "Study of Dynamic and Static Failure Envelopes," J. of the Soil Mech. and Foundation Div., ASCE, Vol. 92, No. SM2, Proc. Paper 4736, March 1966, pp. 105-124.
- 3-56. Richardson, A. M., and R. V. Whitman, "Effect of Strain-Rate Upon Undrained Shear Resistance of a Saturated Remoulded Fat Clay," Geotechnique, Vol. 13, 1963.
- 3-57. Olsen, R. E., and J. F. Parola, "Dynamic Shearing Properties of Compacted Clay," Proc. Int. Symposium on Wave Propagation and Dynamic Properties of Earth Materials, Univ. of New Mex. Press, 1967.
- 3-58. Hardin, B. O., and W. L. Black, "Vibration Modulus of Normally Consolidated Clay," J. of the Soil Mech. and Foundation Div., ASCE, Vol. 94, No. SM2, Proc. Paper 5933, March 1968, pp. 353-369.
- 3-59. Humphries, W.K., and H. E. Wahls, "Stress History Effects on Dynamic Modulus of Clay," J. of the Solid Mech. and Foundation Div., ASCE, Vol. 94, No. SM2, Proc. Paper 5834, March 1968, pp. 371-389.
- 3-60. Bishop, A. W., and D. J. Henkel, The Triaxial Test, Edward Arnold Ltd., London, 1962.

References

- 3-61. Hardin, B. O., and J. Music, "Apparatus for Vibration of Soil Specimens During the Triaxial Test," Instruments and Apparatus for Soil and Rock Mechanics, ASTM STP 392, ASTM 1965, pp. 55-74.
- 3-62. Jackson, J. G., Factors That Influence the Development of Soil Constitutive Relations, Misc. Paper No. 4-980, Army Waterways Experiment Station, July 1968.
- 3-63. Schindler, L., Design and Evaluation of a Device for Determining the One-Dimensional Compression Characteristics of Soils Subjected to Impulse Type Loads, Army Engineer Waterways Experiment Station, November 1968.
- 3-64. Hambley, E. C., "A New Triaxial Apparatus," Geotechnique, June 1969, p. 307.
- 3-65. Ko, H. Y., and R. F. Scott, "A New Soil Testing Apparatus," Geotechnique, March 1967, p. 40.
- 3-66. Ehrigott, J. Q., and R. C. Sloan, "Development of a Dynamic High-Pressure Triaxial Test Device," Technical Report S-71-15, Waterways Experiment Station, Vicksburg, Nov. 1971.
- 3-67. Bjerrum, L., and A. Landva, "Direct Simple-Shear Tests on Norwegian Quick Clays," Geotechnique, Vol. 16, No. 1, 1966, pp. 1-20.
- 3-68. Whitman, R. V., The Response of Soils to Dynamic Loading, Final Report, Army Waterways Experiment Station, Contract Report No. 3-26, May 1970.
- 3-69. Olson, R. E., and H. Kane, "Dynamic Shearing Properties of Compacted Clays at High Pressures," Proc. Sixth Int. Conf. on Soil Mech. and Foundation Eng., Vol. 1, Montreal, 1965.
- 3-70. Ehrigott, J. Q., "Development of a Dynamic High Pressure Triaxial Test Device," preprint from Rock Mech. Conf., Univ. of Missouri, 1971.
- 3-71. Schindler, L., "An Improved Facility for Testing Soils in One-Dimensional Compression," Proc. Int. Sym. on Wave Prop. and Dyn. Properties of Earth Materials, Univ. of New Mexico, August 1967, p. 847.
- 3-72. Hall, J. R., Jr., and F. E. Richart, Jr., "Dissipation of Elastic Wave Energy in Granular Soil," J. Soil Mech. and Foundation Div., ASCE, Vol. 89, No. SM6, November 1963, pp. 27-56.
- 3-73. Drnevich, V. P., et al., "Effects of Amplitude of Vibration on the Shear Modulus of Sand," Proc. Int. Sym. on Wave Prop. and Dyn. Prop. of Earth Materials, Univ. of New Mexico, August 1967.
- 3-74. Hvorslev, M. J., "Subsurface Exploration and Sampling of Soils for Civil Engineering Purposes," Report of Committee on Sampling and Testing, Soil Mech. and Foundation Div., ASCE, 1948.
- 3-75. Gibson, R. E., and W. F. Anderson, "In Situ Measurement of Soil Properties with the Pressuremeter," Civ. Eng. and Public Works Review, London, May 1961.
- 3-76. Handy, R. L., and N. S. Fox, "A Soil Bore-Hole Direct-Shear Test Device," Highway Res. News, HRB, Spring 1967.
- 3-77. Shamon, W. L., S. D. Wilson, and R. H. Muse, "Field Problems: Field Measurements," Foundation Engineering, Chapter 13 McGraw Hill, New York, 1962, p. 1032.
- 3-78. Richart, F. E., Jr., et al., Vibrations of Soils and Foundations, Prentice-Hall, Inc., Englewood Cliffs, New Jersey, 1970.
- 3-79. Ballard, R. F., Jr., Determination of Soil Shear Moduli at Depths by In Situ Vibratory Techniques, Misc. Paper No. 4-691, Army Engineer Waterways Experiment Station.
- 3-80. Hough, B. K., Basic Soils Engineering, Ronald Press, N. Y., 1957.
- 3-81. Hardin, B. O., Study of Elastic Wave Propagation and Damping in Granular Materials, Ph. D. Dissertation, Univ. of Florida, August 1961.
- 3-82. Skempton, A. W., "The Pore Pressure Coefficients A and B," Geotechnique, Vol. 4, 1954.
- 3-83. Seed, H. B., et al., "The Strength of Compacted Cohesive Soils," ASCE Res. Conf. on Shear Strength of Cohesive Soils, Boulder, Colorado, 1960, pp. 877-964.
- 3-84. Henkel, D. J., "The Shear Strength of Saturated Remolded Clays," ASCE Res. Conf. on Shear Strength of Cohesive Soils, Boulder, Colorado, 1960, p. 533.
- 3-85. Jackson, J. G., and J. E. Windham, Soil Property Investigation for HEST Test V, Technical Report S-68-1, Army Waterways Experiment Station, May 1968.

Properties of Soils

- 3-86. Bovee, B. B., and C. C. Ladd, M.I.T. Plane Strain Device, Research in Earth Physics, Phase Report No. 12, Dept. of Civil Eng. Res. Report R70-24, MIT, 1970.
- 3-87. Isenberg, J. and A. K. Bhaumik, Stress/Strain Distribution in Triaxial Compression Tests on a Sand, DASA 2553, Agabian-Jacobsen Associates, Oct. 1970.

SECTION 4

GENERAL MATHEMATICAL MODELS OF MATERIAL PROPERTIES

This section discusses mathematical equations of state for earth materials. These equations of state usually express the pressure or the stress state of a material in terms of the relative density or strain, specific internal energy, and previous history of loading. Since a wide range of states is encountered in ground shock phenomena, it is understandable that no single theory of material behavior adequately describes all ranges.

There are several requisites in deriving an equation of state:

- a. It is desirable for the form of the mathematical equation of state to reflect physical processes.
- b. The equation of state should be consistent with physical laws such as conservation of energy and increase of entropy in a closed cycle.
- c. If possible, the form of the equation of state should apply to a range of materials so that a general equation can be programmed for a computer code. Calculations for different media can then be made merely by changing parameters through input data.

An equation of state for a material consists of a set of rules interrelating the thermodynamic and/or constitutive properties of the material such as pressure, density, internal energy, stress, and strain. If the material is fluid (gas and/or liquid), only two independent thermodynamic variables are required to specify completely its state. In the present discussion, the independent variables are the compression ($\eta = \rho/\rho_0$) or excess compression ($\mu = \eta - 1$) and the internal energy (e). Thus, the pressure (P) in a fluid is uniquely defined by specifying its compression and energy regardless of the path taken to reach this state. By contrast, if the material is a solid, the pressure or mean stress may depend on its previous history in addition to the current values of η

and e . Furthermore, since a solid is able to support deviatoric stresses, six strains (ϵ_{ij}) must be specified to define the state. The shear or rigidity modulus (G), a yield criterion and a flow rule, which together relate the deviatoric stresses and strains, are regarded as part of the equation of state.

Equations of state for fluids have been proposed in various forms which have various degrees of theoretical basis. Briefly discussed below are the Mie-Gruneisen and Tillotson forms, which are related to each other. The Tillotson form has an additional empirical term and is more widely used for earth materials.

Equations of state for isotropic solids are also put in several different forms. All of these use at least two independent stiffness parameters such as bulk and shear moduli. In the so-called variable modulus model, each modulus is allowed to vary with the state, intensity, and previous history of stress. An alternative is to use the theory of plasticity to define onset of inelastic deformation and to compute plastic strain increments as functions of the stress and stress increments. Hybrid models combining aspects of the variable modulus and plasticity approaches have also been proposed.

The first step in fitting a mathematical model to the properties of a specific site is to consider the available laboratory data. In most cases, the maximum amount of available data will be that illustrated in Figures 4-1 and 4-2 (Reference 4-30). These data include the principal hysteresis and several release adiabats, as shown in Figure 4-1. In the opinion of some workers in this field, the fluid equations of state need only mirror the main features of the hysteresis and the low-pressure release adiabats. Exact representation of release adiabats from the high-pressure regime, which may involve melting or vaporization, are presently considered strongly to influence only the crater formation.

Data which are usually available for developing solid equations are shown in Figure 4-2. The two principal dissipative mechanisms are volumetric hysteresis and inelasticity in shear. It is usually

General Mathematical Models of Material Properties

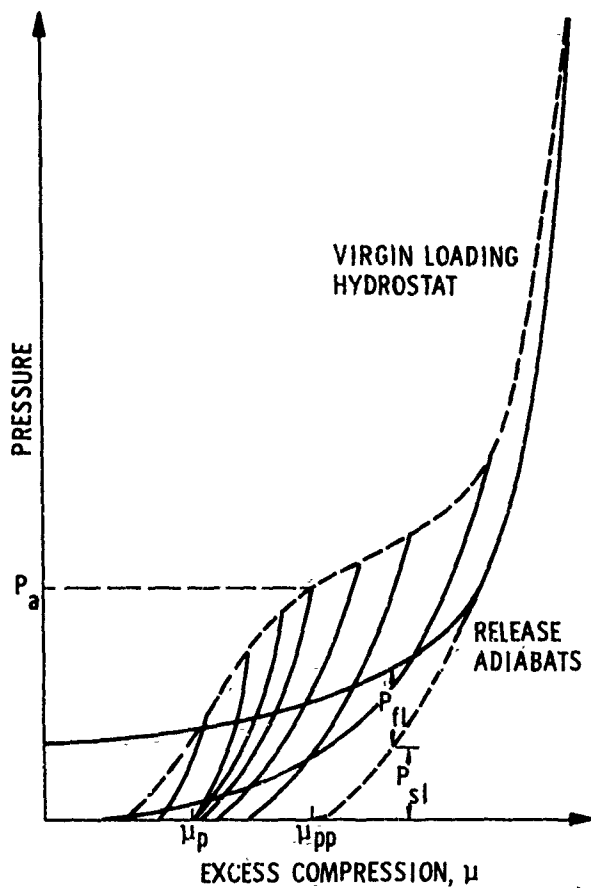


FIGURE 4-1. IDEALIZED HYDROSTAT AND RELEASE ADIABATS ILLUSTRATING THE EFFECT OF HYSTERETIC COMPACTION ON P_{sl}

possible to derive several different models which, by means of stress/strain relations, accurately represent these mechanisms for at least one cycle of loading and unloading. In selecting the best model, attention is given to the relation between axial stress and lateral stress for the case of uniaxial strain, Figure 4-2(a) through (c). Failure to represent this behavior accurately will result in significant errors in computing horizontal (parallel to surface) ground shock effects. Another criterion which is used to select the best model of a material exhibiting dilatancy is ability to represent the unloading/reloading behavior of the pressure/volumetric-strain relationship.

Following the derivation from laboratory data, mathematical models may further be evaluated by using them in a calculation of a field test. In some cases it is possible to certify a model through a calculation of a small field test. In other cases however, especially those involving late-time, low-amplitude motion following the initial shock, only comparison with a large-scale test is adequate.

Finally, the incorporation of a complicated model into a computer program can be checked for errors by comparing the predictions of the program with semianalytic solutions (References 4-31 to 4-34).

GENERAL EQUATIONS OF STATE (FLUID)

The equation of state of a fluid is a relationship among pressure (P), specific volume (V), or relative density (η), and specific internal energy (e):

$$P = f(\eta, e) \quad (4-1)$$

One relationship, which has been widely used for metals, is the Mie-Grüneisen equation of state (Reference 4-1), which may be written in the form

$$P - P_K = \frac{\gamma}{V}(e - e_K) \quad (4-2)$$

where

γ = Grüneisen ratio (assumed to be a function of volume)

P_K, e_K = Pressure and specific internal energy at 0° Kelvin

Since γ is a function only of volume, differentiating Equation 4-2 with respect to e at constant V leads to

$$\gamma = - \frac{V}{C_p} \left(\frac{\partial P}{\partial V} \right)_T \left(\frac{\partial V}{\partial T} \right)_N \quad (4-3)$$

where C_p is the specific heat and subscripts T, N denote constant temperature and entropy. Thus, at zero pressure, γ can be evaluated from experimental data for bulk modulus $(\partial P / \partial V)_T$, thermal expansion $(\partial V / \partial T)_N$ and the specific heat.

Another method of calculating γ is due to Dugdale and MacDonald, who proposed that a relation, originally due to Slater, be modified to

$$\gamma = - \frac{V}{2} \frac{\partial^2 (PV^{2/3}) / \partial V^2}{\partial (PV^{2/3}) / \partial V} - \frac{1}{3} \quad (4-4)$$

Using a known hughoniot curve $P_H(V)$, γ can be evaluated at a variety of states, and empirical expressions

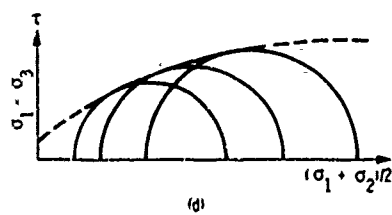
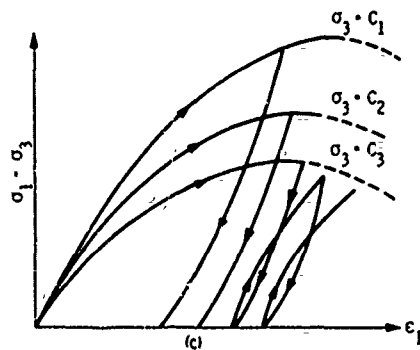
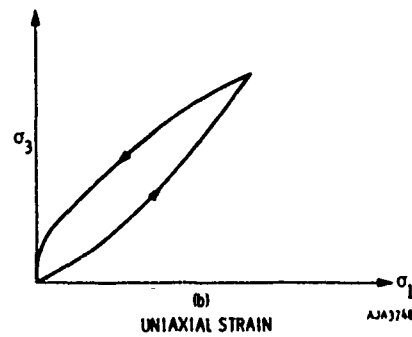
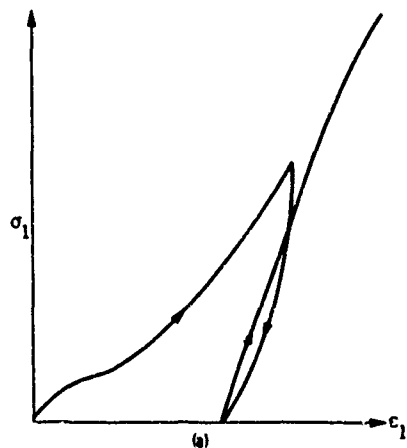
$$\gamma = \gamma_0 + \sum_{n=1}^N (a_n \mu)^n \quad (4-5)$$

where

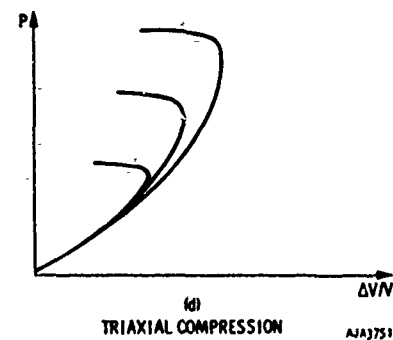
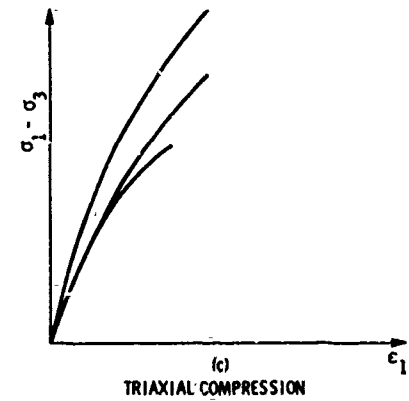
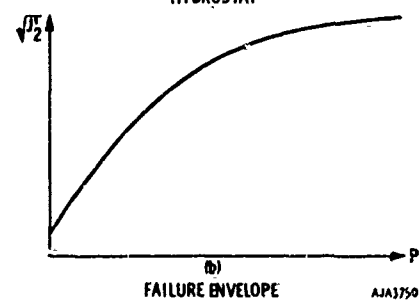
$$\mu = \rho / \rho_0 - 1$$

$$\gamma_0 = \gamma \text{ at } 0^\circ K$$

General Equations of State (Fluid)



(a) TYPICAL EXPERIMENTAL RESULTS, SOIL



(b) TYPICAL EXPERIMENTAL RESULTS, ROCK

FIGURE 4-2. TYPICAL LABORATORY DATA ON SOIL AND ROCK FROM WHICH MODELS OF SOLID STATE BEHAVIOR ARE DERIVED

General Mathematical Models of Material Properties

can be obtained. Equation 4-5 can then be substituted into Equation 4-2 to calculate states adjacent to the hughoniot.

A second form of fluid equation of state was first proposed by Tillotson (Reference 4-2) and applied to geologic materials by Allen (Reference 4-39) as follows:

$$P = \left(a_0 + \frac{b_1}{\frac{e}{e_0 \eta^2} + 1} \right) \rho e \quad (4-6a)$$

Under conditions of low density and high internal energy, Equation 4-6(a) tends to:

$$P = a_0 \rho e \quad (4-6b)$$

which is the familiar equation for a low-density perfect gas in which $a_0 = r - 1$, where r is the ratio of specific heats at constant pressure and volume. In many applications a_0 is assumed to remain constant in spite of experimental evidence that it varies with P , ρ and e (Reference 4-3). The value of b_1 is selected such that Equation 4-6 matches hughoniot data at pressures of several hundred kilobars. The value of e_0 is chosen so that Equation 4-6 approximates the Thomas-Fermi-Dirac description of highly compressed material at high energy densities.

The following modification to Equation 4-6 has been proposed (Reference 4-4) for earth materials

$$P = \left[a_0 + \left(b_2 + \frac{b_1}{\frac{e}{e_0 \eta^2} + 1} \right) \exp Z \right] \rho e^* \quad (4-7)$$

where

	Criterion	Material State
$Z = \begin{cases} 0 & \mu \geq 0 \\ b_3 \left(\frac{\mu}{\eta} \right) & \mu < 0 \end{cases}$	$\mu \geq 0$	Liquid or compressed gas
	$\mu < 0$	Expanded gas
$e^* = \begin{cases} 0 & e \leq e_m \\ e - e_m & e > e_m \end{cases}$	$e \leq e_m$	Cold solid
	$e > e_m$	Fluid with specific internal energy greater than that required for melting

The factor $\exp Z$ provides a smooth transition from the compressed state to that of an ideal gas. The role of e^* is to provide a smooth transition from the fluid state to the solid state by causing P in Equation 4-7 to tend toward zero as the material tends toward the solid state. The pressure or mean stress

in the solid state is computed by a different type of expression, which accounts for the effects of previous loading history. This is discussed below.

GENERAL EQUATIONS OF STATE (SOLID)

The solid state is characterized by six independent strain components and the specific internal energy. Usually the main task in characterizing the solid state is to determine the stress increment from the states of stress, strain and their previous history, internal energy, and strain increment.

The two types of mathematical models commonly used to do this are the so-called variable modulus approach and the theory of plasticity.

VARIABLE MODULUS

The variable modulus approach represents a "hypoelastic" (References 4-35 and 4-36) material in which the stress increment tensor ($d\sigma_{ij}$) is expressed in terms of the strain increment tensor ($d\epsilon_{ij}$) as follows:

$$d\sigma_{ij} = K d\epsilon_{kk} \delta_{ij} + 2G \left(d\epsilon_{ij} - \frac{1}{3} d\epsilon_{kk} \delta_{ij} \right) \quad (4-8)$$

where

$$d\epsilon_{kk} = \text{Linear dilatation} (= d\epsilon_{11} + d\epsilon_{22} + d\epsilon_{33})$$

$$\delta_{ij} = \text{Kronecker Delta} (= 1 \text{ if } i = j, = 0 \text{ if } i \neq j)$$

$$K, G = \text{Bulk and shear moduli, respectively}$$

Since only two independent elastic coefficients K and G appear in Equation 4-8, it is implied that the material is isotropic (Reference 4-5). The first term on the right side of Equation 4-8 computes the mean stress increment. The second term on the right side computes the deviatoric stress increment.

The constitutive equations of variable modulus models, Equation 4-8, are a set of first-order differential equations with variable coefficients K and G . These moduli are assumed to be scalar functions of stress and strain components and to depend on the history of stress and strain. The integration of Equation 4-8 for a given set of initial conditions and stress path leads to stress/strain relations, which is the outcome of the variable modulus approach. Evidently, the stress/strain relations so determined depend on the initial conditions and the stress path. Thus a variable modulus model cannot be considered a nonlinear elastic material for which a unique, path-independent stress/strain relationship would exist.

BULK MODULUS

In a linearly elastic material, K and G are

assumed to be constant. Since the bulk and shear properties of earth materials cannot be accurately represented by constant K and G , the variable modulus approach allows them to vary as functions of stress, strain, and previous history of loading. Theoretical guidance as to appropriate functions for K and G is slim. The main contribution in this area is due to Walsh (References 4-6, 4-7) whose theory is based on the behavior of rocks. Walsh postulates that the effective modulus differs from the intrinsic modulus of the consolidated material due to cracks and pores. The results of Walsh's work contain parameters related to the shapes of voids which are not retained in the empirical expressions for the effective bulk modulus as shown in Equation 4-9.

$$K = K_m - (K_m - K_o) \exp\left(\frac{-\mu}{\mu^*}\right) \quad (4-9)$$

where

K = Initial bulk modulus

K_m = Intrinsic bulk modulus of consolidated material

μ^* = Empirical constant

The intrinsic bulk modulus may be constant or may be assumed to vary with specific internal energy as follows:

$$K_m = K_{\max} \left[1 - \left(c \frac{e}{e_m} \right) \right] \quad (4-10)$$

where

K_{\max} = Intrinsic bulk modulus at room temperature

$e_m = e_{mo} (1 + s\eta)$, specific internal energy at which melting occurs

e_{mo} = Energy required to melt the material at normal density

c, s = Empirical constants

Equation 4-9 applies to the case of virgin loading, which is defined by

$$\mu \geq \mu_m \quad (4-11)$$

where μ_m is the previous maximum excess compression. If $\mu < \mu_m$, the material is unloading or reloading and a different expression for K is used which accounts for the irreversible compaction which may occur during hydrostatic loading and unloading. One way to represent the unloading/reloading bulk modulus is to define the permanent compaction μ_z as

a function of the maximum excess compression μ_m . The reloading curve is required to pass through the point on the loading curve (μ_m, P_m) at which unloading begins. An expression for K is obtained by integrating Equation 4-9 over the limits $\mu = 0$ to $\mu = \mu_m + \beta e$ (β is the coefficient of volumetric thermal expansion per unit of specific internal energy) to obtain an updated value of the initial bulk modulus:

$$K'_o = K_m - \frac{[P_m - K_m(\mu_m - \mu_z + \beta e)]}{[\mu^* \{1 - \exp[-(\mu_m - \mu_z + \beta e)/\mu^*]\}]} \quad (4-12)$$

K'_o then replaces K_o in Equation 4-9.

For rocks, experimental data (References 4-8, 4-9, and 4-10) show that μ_z increases with increasing peak pressure until all of the cracks and voids are apparently closed. Further moderate increases in compaction do not increase the permanent compaction until very high pressures are reached when phase changes of constituent minerals may cause μ_z to increase once more. Computation of μ_z may be performed as follows:

Criterion

$$\mu_z = \begin{cases} P_m d & P_m < \mu_p/d \\ \mu_p & \mu_p/d \leq P_m \leq P_a \\ \mu_p + (P_m - P_a)d & P_a < P_m < \frac{\mu_{pp} - \mu_p}{d} + P_a \\ \mu_{pp} & \frac{\mu_{pp} - \mu_p}{d} + P_a \leq P_m \end{cases} \quad (4-13)$$

μ_p is the excess compression at which all the voids are closed. The density $\rho_p (= \rho_o (1 + \mu_p))$ must be less than or equal to the crystal density of the rock. P_a is the minimum pressure at which a phase change can occur and $\rho_{pp} (= \rho_o (1 + \mu_{pp}))$ is the crystal density of the rock after the phase change is completed. The assumption of linear dependence of μ_z on pressure (d is the proportionality constant) is crude, but the meager unloading data and the large scatter within that data does not justify further refinements at this time.

Although this discussion has been presented as if fluid and solid states were distinctly separated, there is a smooth transition between them. This is achieved in the variable modulus model described above by computing the pressure as the sum of contributions from fluid and solid states:

$$P = P_{sf} + P_{fl} \quad (4-14)$$

General Mathematical Models of Material Properties

P_{sf} is computed by integrating Equation 4-9 over the loading path. P_{fl} is computed by Equation 4-7. The term e^* in Equation 4-7 provides a smooth transition from fluid to solid. An illustration of this model, showing both fluid and solid contributions to the pressure, is given in Figure 4-1.

Although the development of a variable bulk modulus described above might be applicable to some soils, as well as to rocks, many investigators prefer instead to use empirical relationships whose physical meaning is less easily identified. Some features of variable bulk moduli for soils are nonetheless similar to the rock model described above.

A model for soil subjected to hydrostatic stress is reported in Reference 4-26. The virgin loading relation is a polynomial of the form

$$P = \sum_{n=0}^N K_n \mu^n \quad (4-15)$$

where

K_n = Empirical coefficient in n^{th} term of the polynomial

μ = Excess compression

n = Number of a term in the polynomial expansion

N = Number of terms (usually 5 to 8)

The bulk modulus is the derivative of Equation 4-15:

$$K_l = \sum_{n=1}^N n K_n \mu^{n-1} \quad (4-16)$$

The model provides for hysteresis by prescribing that permanent compaction increases with increasing pressure until a certain pressure level, P_l is reached, Figure 4-3. This is assumed to correspond to the pressure at which air voids have either been removed from the soil or have become entirely filled with water. Loading to pressures higher than P_l produces no additional permanent compaction until very high pressures, not covered by the present model, are reached. Hysteresis is limited in the model by providing that at $P > P_l$ the virgin loading modulus becomes equal to the unloading/reloading modulus.

The unloading/reloading moduli may be prescribed by the following set of equations

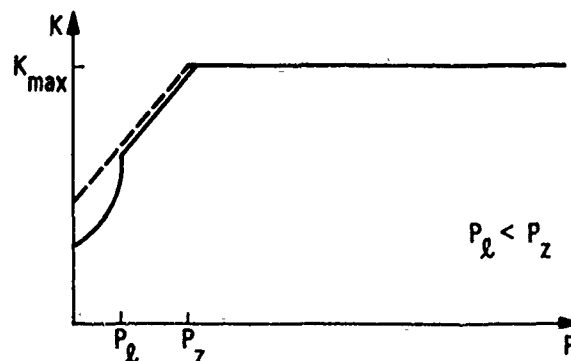
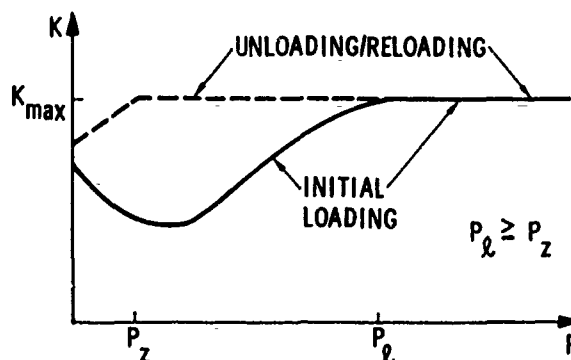
$$K_u = K_{ou} + K_{lu} P \quad P \geq P_z \quad (4-17a)$$

$$K_u = K_{\max} \quad P < P_z \quad (4-17b)$$

In order to prevent generation of energy during a cycle of loading, unloading, and reloading, which would violate thermodynamic principles, the unloading bulk modulus must always be greater than or equal to the loading modulus:

$$K_u \geq K_l$$

The physical meaning of the parameter P_z is not clear, but, empirically, it is associated with a change in slope of the unloading curve which is often observed in experimental data. This model implies that the soil has a maximum bulk modulus, K_{\max} . This may be a satisfactory approximation in some pressure ranges, but is not necessarily adequate in all ranges. Another limitation on this model is that there is no provision for the effect of changes in the specific internal energy. These limitations reflect the fact that this model is intended for use at pressures not exceeding a few kilobars. These are not inherent limitations, and the model could be extended.



AJA3752

FIGURE 4-3. BULK MODULUS (K) VERSUS PRESSURE (P) FOR A COMPACTING SOIL

The type of pressure/volumetric strain relation provided by this model is illustrated in Figures 4-3 and 4-4. Since shock heating does not contribute to the pressure, the unloading relation never crosses the loading relation, as it does for two release adiabat paths in the rock model shown in Figure 4-1.

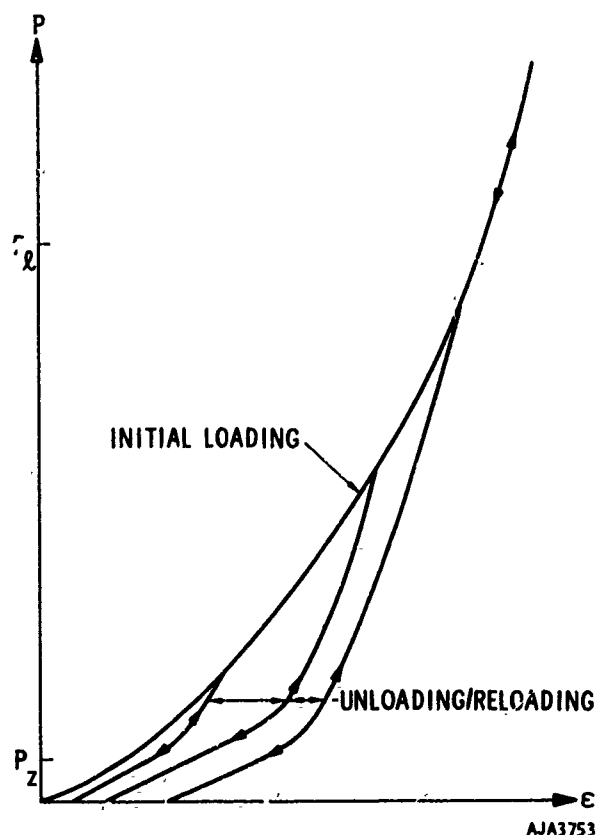


FIGURE 4-4. PRESSURE VERSUS VOLUMETRIC STRAIN FOR A COMPACTING SOIL

SHEAR MODULUS

As in the case of the variable bulk modulus, the mathematical forms of variable shear moduli are different depending on whether they have been developed for rock or soil and whether they are used with a yield criterion and flow rule. If a variable G is to be used together with a yield criterion and a flow rule, which govern the maximum shear stresses, variations in G need only to reflect changes in void space and in temperature. For rock, models of the shear modulus are inspired by the idea that G varies from an initial value, G_0 , at normal density to the intrinsic value, G_{\max} , as cracks and pores are closed. The expression

$$G_l = G_u = G_{\max} - (G_{\max} - G_0) \exp \frac{-\mu}{\mu_G^*} \quad (4-18)$$

is analogous to Equation 4-9 for the bulk modulus,

where

G_0 = Initial shear modulus

G_{\max} = Intrinsic shear modulus of consolidated material

μ_G^* = Empirical constant

For highly fractured rock, experimental data (References 4-11 and 4-12) suggest that G_0 is close to zero. However, as the material becomes compacted (represented in the model by increasing μ) G approaches the intrinsic value much more rapidly than does K . This is consistent with the concept that the effective bulk modulus is strongly influenced by the closing of pores, whereas the effective shear modulus is influenced mainly by the closing of cracks. Reference 4-6 shows that cracks are more readily closed than pores.

Specifying that G increases with increasing μ raises the possibility that energy might be extracted from the material by hydrostatically compressing it, shearing it at high pressure, releasing the pressure and then releasing the shear. This danger is avoided by assuming that friction prevents cracks from reopening during unloading so that the largest value of G reached on loading is retained during subsequent unloading/reloading. Under these restrictions, a material may dissipate energy in shear during loading and unloading cycles but can never produce additional energy.

Data on the temperature dependence of material strength (Reference 4-13) clearly indicate that the shear strength of several rocks decreases almost linearly with increasing temperature. By analogy, a similar dependence is assumed for the shear modulus. As the temperature rises to the melting point, G tends towards zero as specified in the following equation:

$$G_l = G_u = \left[G_{\max} - (G_{\max} - G_0) \exp \frac{-\mu}{\mu_G^*} \right] \left(1 - \frac{e}{e_m} \right) \quad (4-19)$$

For $e > e_m$, the rock is assumed to be melted and unable to support shear stress, in which case G is zero.

Simpler relationships are also used. The following relation, which is derived from the theory of linear elasticity, expresses the shear modulus in terms of the bulk modulus and Poisson's ratio, ν :

$$G = \frac{3}{2} K \frac{1-2\nu}{1+\nu} \quad (4-20)$$

General Mathematical Models of Material Properties

K is assumed to be variable as described above. The term ν may be a constant for loading and a different constant for unloading. Hence, G is proportional to K and undergoes the same type of variation with volumetric strain as does K.

Neither of the variable shear modulus models noted above account for inelasticity and fracture due to shear stress. A yield criterion and a flow rule, which are ideas from plasticity theory, are used to represent this aspect of shear behavior. The resulting model is referred to as "hybrid" because it combines features from the variable modulus and plasticity theory approaches. Yield criteria and flow rules are discussed in the following section on models based on plasticity theory.

If the variable modulus approach is used without explicitly including a yield criterion, the loading shear modulus G_l must tend toward zero as the shear stress approaches the shear strength of the material. The following formulas illustrate two possible ways to do this:

for

$$\sqrt{J_2'} \geq 0$$

$$G_l = G_{0l} + G_{1l}P + G_{2l}P^2 + G_{3l}\sqrt{J_2'}$$

(Reference 4-26)

(4-21a)

$$G_l = \left[G_{0l} + G_{1l} \left(\frac{P}{P + G_{2l}} \right) \right] \left[1 - \frac{G_{3l}\sqrt{J_2'}}{\alpha J_1 + A_0} \right]$$

(Reference 4-25)

(4-21b)

In each case, the term G_{0l} represents the shear modulus at zero confining pressure (Reference 4-14). The coefficient of G_{1l} accounts for increase in shear modulus with confining pressure. The remaining terms cause G_l to tend toward zero as the shear stress (represented by $\sqrt{J_2'}$) approaches the yield criterion (represented by $\alpha J_1 + A_0$ in Equation 4-21 (b)). Typical shear stress/strain relations obtained from models of this kind are compared with experimental data in Figure 4-5.

The unloading shear modulus can be represented by an expression similar to 4-21(a), as follows:

for

$$\sqrt{J_2'} < 0$$

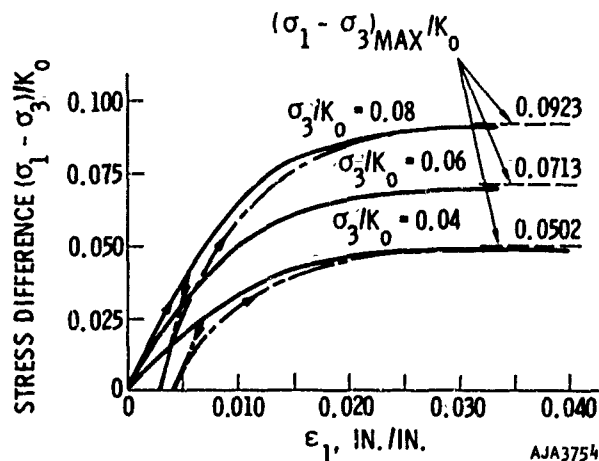
$$G_u = G_{0u} + G_{1u}P + G_{2u}P^2 + G_{3u}\sqrt{J_2'}$$

(Reference 4-26)

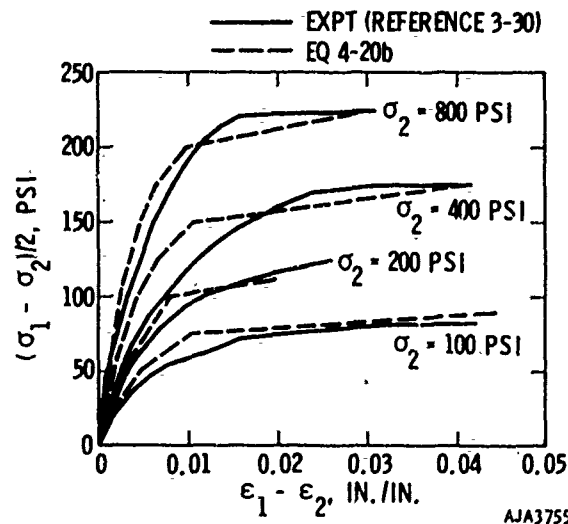
(4-22)

in some cases, the coefficients such as G_{0l} in Equations 4-21 and 4-22 vary with pressure level.

Reloading moduli may involve even more complicated expressions (Reference 4-26).



(a) TRIAXIAL COMPRESSION TEST COMBINED VARIABLE MODULI MODEL NORMALIZED TO K_0 , THE INITIAL VALUE OF K (REFERENCE 4-26)



(b) COMPARISON OF CANDIDATE MODEL WITH TRIAXIAL COMPRESSION DATA (REFERENCE 4-25)

FIGURE 4-5. VARIABLE MODULI MODELS VERSUS DATA

The main theoretical objection (Reference 4-30) to using different shear moduli in loading and unloading is illustrated in Figure 4-6. Point A lies on the surface $J'_2 = \text{const}$. Paths AB and AB' lie arbitrarily close to each other but on opposite sides of the surface. On AB, G_L applies while on AB', G_U applies. The effect is a finite difference in strain along the two paths even when B and B' are separated by an infinitesimal distance. This property violates continuity in neutral loading $J'_2 = \text{constant}$ in the manner similar to that discussed in Reference 4-37.

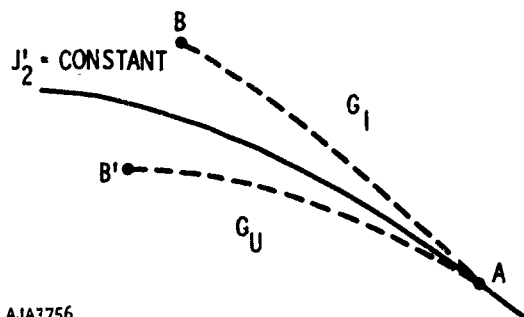


FIGURE 4-6. CONTINUITY CONDITION APPLIED TO A VARIABLE MODULUS MODEL WITH DIFFERENT SHEAR MODULI IN LOADING AND UNLOADING

PLASTICITY THEORY

The mathematical theory of plasticity is used in free field and ground shock calculations to restrict or limit shear stresses and to represent a particular type of inelasticity. Plasticity theory was used in early calculations because of its generality in representing all components of the stress and strain tensors. Also, there is at least one version of the theory which guarantees stability of the material and uniqueness of the stress and strain states. The theory is also capable of incorporating certain broad features of experimental data, including the dependence of shear strength on mean stress. As more experimental data have become available, limitations on the applicability of the early theory to rock and soil have appeared. For example, the version of plasticity theory which uses the plastic potential flow rule may, in some circumstances, produce plastic volumetric expansion or dilatancy. While dilatancy is observed in some earth materials, the theory tends to predict greater dilatancy than is observed, and in some cases the theory may lead to an indefinitely large amount of dilatancy, which is physically implausible. To remedy some of these faults, the application of the theory of plasticity to ground shock problems has been recently extended and is now capable of an improved representation of

material behavior while still retaining the desirable features of uniqueness and stability.

The main features of plasticity theory, as it is used in ground shock and soil/structure interaction calculations, are as follows:

- A yield criterion defines the onset of plastic deformation. The initial yield criterion is usually assumed to be exclusively a function of stress invariants, which implies that the material is isotropic and is insensitive to temperature changes and strain rate.
- A hardening rule defines the yield criterion after plastic deformation has developed. So-called "subsequent" yield surfaces are usually defined as functions of plastic strain or plastic work, as well as of stress. Perfect plasticity is a special case in which hardening is absent and the initial criterion applies throughout.
- A flow rule defines the increment of plastic strain accompanying an increment of stress after the yield criterion is satisfied. It is often convenient to write the plastic strain increment as a plastic strain rate. However, in the discussion which follows, no strain rate dependence is implied.

Many details of the following discussion of plasticity theory can be obtained from References 4-15 and 4-16.

The yield criterion f for a strain-hardening material is of the form

$$f(\sigma_{ij}, \epsilon_{ij}^p) = 0 \quad (4-23)$$

for which the plastic loading criteria are

$$\frac{\partial f}{\partial \sigma_{ij}} \dot{\sigma}_{ij} \stackrel{\text{def}}{=} 0 \text{ for } \begin{cases} \text{loading} \\ \text{neutral loading} \\ \text{unloading} \end{cases} \quad (4-24)$$

When $f < 0$, and during unloading or neutral loading, $\dot{\epsilon}_{ij}^p = 0$ (the dot denoting an increment) and Equation 4-8 is used to determine the (purely elastic) strain changes. The prescription that neutral loading produces no plastic strain is called the continuity condition and its satisfaction leads to coincidence of elastic and plastic laws during neutral loading, Reference 4-17.

General Mathematical Models of Material Properties

Drucker, References 4-18 and 4-19, introduced a postulate which requires that

$$(\sigma_{ij} - \sigma_{ij}^0) \dot{\epsilon}_{ij}^P \geq 0 \quad (4-25)$$

and

$$\dot{\sigma}_{ij} \dot{\epsilon}_{ij}^P \geq 0 \quad (4-26)$$

in which σ_{ij}^0 is an arbitrary stress state satisfying $f < 0$. In a six-dimensional space, the first of these equations requires the vector $\underline{\sigma} - \underline{\sigma}^0$ to form an acute angle with $\dot{\underline{\epsilon}}^P$ for any stress point, defined by σ^0 , within the yield surface $f = 0$, from which it follows that the yield surface is convex and the plastic strain rate vector corresponding to a point on it is in the direction of an outward drawn normal. The second inequality is referred to as Drucker's stability postulate in the small.

The theoretical restriction that initial and subsequent yield surfaces should be convex to the origin can usually be reconciled with experimental data. Common forms of yield criteria which can be adapted to onset of inelastic deformation in rocks and soils are illustrated in Figure 4-7. The von Mises yield criterion, illustrated in Figure 4-7(a), applies to materials whose yield properties are independent of mean stress. The criterion originally was intended for metals such as mild steel and aluminum and appears to be an acceptable approximation for some earth materials such as clay. The von Mises criterion may be written as

$$f = \sqrt{J_2} - A_0 \leq 0 \quad (4-27)$$

To account for the fact that the shear stress required to cause yielding in many earth materials increases with increasing mean stress, Prager and Drucker (Reference 4-20) proposed the criterion illustrated in Figure 4-7(b). This equation can be written as

$$f = \sqrt{J_2} - \alpha J_1 - A_0 \leq 0 \quad (4-28)$$

With A_0 set to zero, Equation 4-26 is sometimes referred to as a Coulomb yield criterion. If α is set equal to zero, Equation 4-26 reduces to the von Mises criterion.

Some materials exhibit different yielding properties in different pressure regions. Figure 4-7(c) illustrates a criterion in which the yield stress increases with mean stress up to some value above which yield stress is independent of mean stress. In rock, this type of transition is sometimes associated

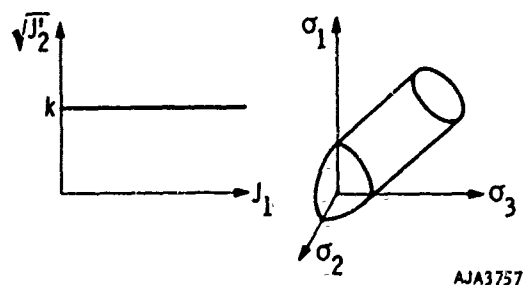
with a transition in the mode of yielding from slip between grains to fracture and slip within grains. In soils it is related to saturation of voids. A yield criterion representing a gradual transition is illustrated in Figure 4-7(c) and its equation is

$$f = \sqrt{J_2} - A_0 - \alpha J_1 \left(1 - \frac{J_1}{2A_2}\right) \quad 0 < J_1 \leq A_2 \quad (4-29a)$$

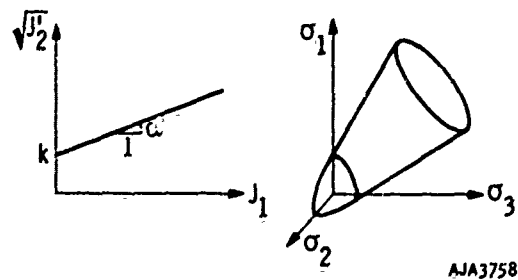
and

$$f = \sqrt{J_2} - k - \frac{\alpha}{2} A_2 \quad J_1 > A_2 \quad (4-29b)$$

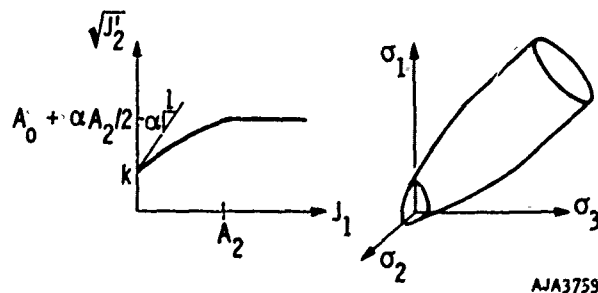
Expressions such as those in Equations 4-25 through 4-27, while convenient mathematically, do not represent failure in a number of earth materials,



(a) VON MISES YIELD CRITERION



(b) PRAGER-DRUCKER CRITERION

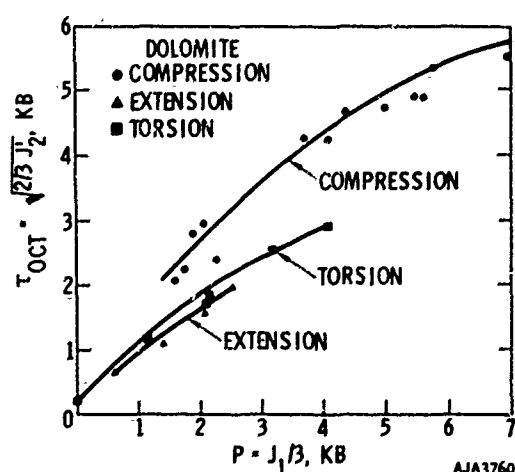


(c) MODIFIED PRAGER-DRUCKER CRITERION

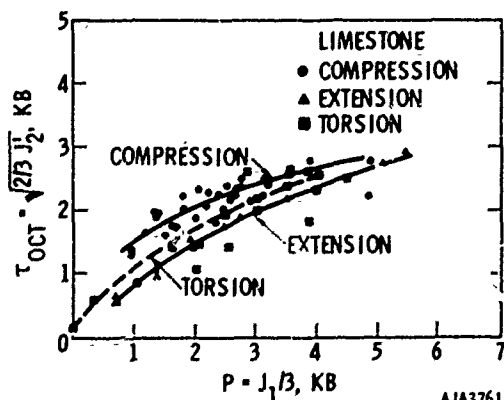
FIGURE 4-7. YIELD CRITERIA

especially brittle rocks. Their shortcomings are not apparent unless data from several different types of tests, such as triaxial compression ($|\sigma_1| > |\sigma_2| = |\sigma_3|$) and triaxial extension ($|\sigma_1| < |\sigma_2| = |\sigma_3|$), are performed on the same material and compared. Figure 4-8 illustrates that there is no unique function of J_1 and J_2 which accounts for all of the fracture data for a dolomite and a limestone. To remedy this, a fracture criterion has been proposed (Reference 4-27) which employs J_1 , J_2 , J_3 , and J_3' , where J_3 and J_3' are the third invariants of the stress and stress deviator tensors, respectively. The proposed fracture parameter is Y :

$$Y = \frac{3}{4} \left[\sqrt{3J_2'} + \frac{J_3}{|J_3|} \left(\frac{|J_3'|}{2} \right)^{1/3} \right] \quad (4-30)$$



(a) OCTAHEDRAL SHEAR STRESS VERSUS MEAN STRESS FOR DOLOMITE



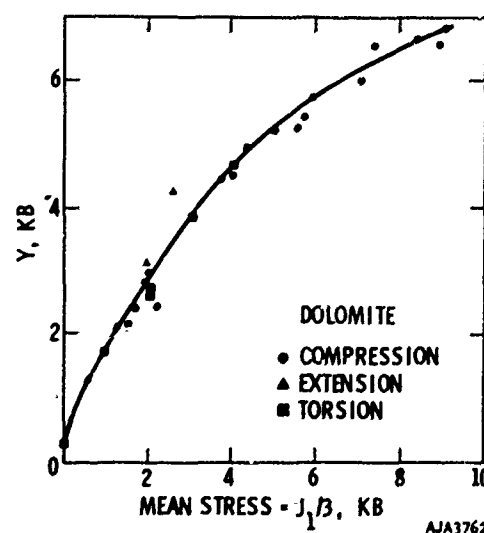
(b) OCTAHEDRAL SHEAR STRESS VERSUS MEAN STRESS IN TWO ROCKS (REFERENCE 4-27)

FIGURE 4-8. OCTAHEDRAL SHEAR STRENGTH IS NOT UNIQUELY RELATED TO MEAN STRESS IN TWO ROCKS (REFERENCE 4-27)

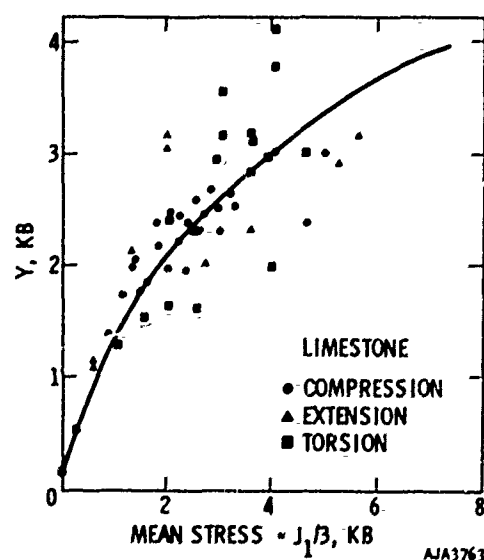
and the fracture criterion is expressed by

$$Y - f(J_1) = 0 \quad (4-31)$$

The effect of introducing J_3 in Equation 4-30 is to account automatically for stress states in which the principal stresses do not all have the same sign. Comparison between Figures 4-8 and 4-9 shows that Y is a much better parameter for representing all



(a) Y VERSUS MEAN STRESS FOR DOLOMITE



(b) Y VERSUS MEAN STRESS FOR LIMESTONE

FIGURE 4-9. PARAMETER Y , CONTAINING J_2' , J_3' AND J_3 AT FRACTURE, IS UNIQUELY RELATED TO MEAN STRESS FOR TWO ROCKS

General Mathematical Models of Material Properties

the available fracture data on dolomite and limestone than is $\sqrt{J_2}$. The ability to reconcile data from tests where the principal stresses have the same sign with data from tests where the signs differ is the major advantage claimed for the model.

A possible difficulty, caused by the specific form of Equation 4-28, is that the value of $\dot{\gamma}$ is discontinuous when one or more principal stresses equals zero. This occurs because, under these circumstances, $J_3 = 0$ but J_3 may not be zero. The consequences of this discontinuity are discussed in Reference 4-28.

In practical calculations involving earth materials, the criteria illustrated in Figure 4-7 usually represent "failure" or maximum combined stress rather than the onset of stable plastic deformation implied by Equations 4-23 and 4-24. The alternative of using such criteria to define the onset of inelasticity, a series of nested, subsequent yield surfaces, as illustrated in Figure 4-10, and a fracture criterion is not widely used. This is because the small amount of data available on which to base a rule of hardening and hypothesis of postfracture deformation is considered not to justify the added complexity. As a result, most investigators assume implicitly that Equations 4-23 and 4-24 apply as well to a fracture criterion as to yield criterion and that perfect plasticity adequately describes postfracture deformation. This assumption appears to be more reasonable for ductile fracture and to be less reasonable for brittle fracture.

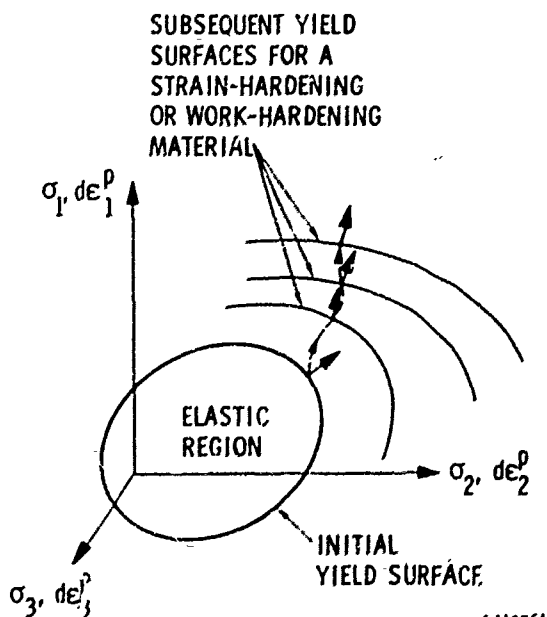


FIGURE 4-10. HARDENING MATERIAL HAVING NESTED, SUBSEQUENT YIELD SURFACES

The flow rule which satisfies Equations 4-24 through 4-26 expresses the plastic strain rate as a function of the yield criterion as follows:

$$\dot{\epsilon}_{ij}^P = \Lambda \frac{\partial f}{\partial \sigma_{ij}} \quad (4-32)$$

where Λ is a scalar function. An alternative derivation is offered in Reference 4-21. This is known as an associated flow rule in which the yield function appears as a plastic potential. The geometrical interpretation of Equation 4-30 is that the plastic strain increment vector is normal to the yield surface. This is illustrated in Figure 4-7 for a hardening material having nested subsequent yield surfaces. One of the attractive features of the hypothesis expressed by Equations 4-24 through 4-26, which culminate in the flow rule of Equation 4-32, is that they are sufficient to ensure uniqueness.

Substituting Equation 4-32 into the total differential form of Equation 4-23 results in the following relation between the plastic strain rate and the stress rate.

$$\dot{\epsilon}_{ij}^P = \left(\frac{1}{\frac{\partial f}{\partial \sigma_{mn}} \frac{\partial f}{\partial \epsilon_{mn}}} \frac{\partial f}{\partial \sigma_{kl}} \dot{\sigma}_{kl} \right) \frac{\partial f}{\partial \sigma_{ij}} \quad (4-33)$$

where the term in brackets () equals Λ .

Equations 4-26 and 4-32 are fairly stringent conditions in that the selection of a yield criterion automatically imposes restrictions on the plastic stress/strain relations. Although one of the main motives for imposing such restrictions is to obtain a mathematical assurance of uniqueness, this does not guarantee that all aspects of the model agree with experimental data. An important consequence of the associated flow rule in which f in Equation 4-32 is the yield function, when used with a Prager-Drucker type yield criteria, Figure 4-4(b), is that it predicts plastic volumetric expansion. Although many materials which obey a Prager-Drucker type of yield criterion also exhibit dilatancy, few materials exhibit as much dilatancy as Equation 4-33 predicts. Under some conditions, sand undergoes a plastic volumetric decrease during shear failure.

Partly to try to reconcile such differences, some investigators have employed a nonassociated flow rule in which the yield function f in Equation 4-32 is replaced by another potential function $F(\sigma_{ij}, \epsilon_{ij}^P)$. Equation 4-32 is replaced by the analogous equation

$$\dot{\epsilon}_{ij}^P = \Lambda \frac{\partial F}{\partial \sigma_{ij}} \quad (4-34)$$

and Equation 4-31 becomes

$$\epsilon_{ij}^P = \frac{1}{\frac{\partial F}{\partial \sigma_{mn}} \frac{\partial F}{\partial \sigma_{kl}}} \frac{\partial F}{\partial \sigma_{ij}} \frac{\partial F}{\partial \sigma_{kl}} \dot{\sigma}_{kl} \quad (4-35)$$

Recently, a model has been proposed which answers some of the objections raised against the models discussed above (References 4-15 and 4-22). This model employs a yield surface illustrated in Figure 4-11, which combines both ideal plasticity and strain hardening. The ideally plastic modified Drucker-Prager criterion is intended to represent the ultimate shear strength of the material, and in laboratory experiments it is associated with fracture or sustained plastic flow. The form of the equation may be similar to Equation 4-29(a) and is denoted by

$$f_1(J_1, J_2) = 0 \quad (4-36)$$

The strain-hardening cap expands or contracts as the plastic volumetric strain increases or decreases, respectively. It is denoted by

$$f_2(J_1, J_2, \epsilon^P) = 0 \quad (4-37)$$

The elastic behavior is assumed to be governed by Equations 4-8 with constant shear modulus and with bulk modulus as a function of pressure.

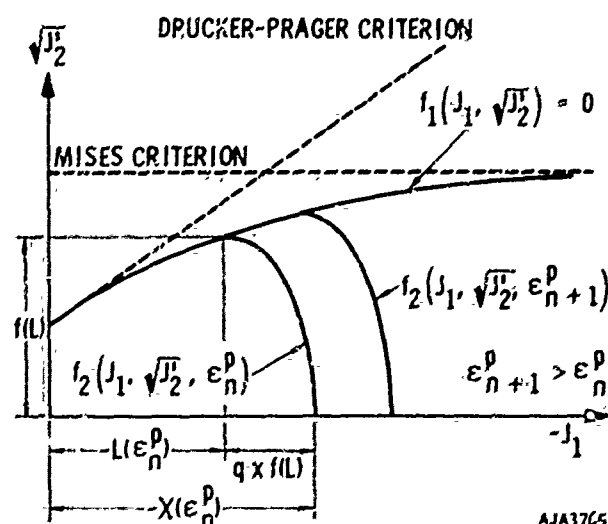


FIGURE 4-11. MATHEMATICAL MODEL HAVING A FIXED FRACTURE OR FAILURE CRITERIA (f_1) AND A MOVABLE OR STRAIN-HARDENING CAP (f_2) (REFERENCE 4-15)

In the adaptation of the model to soils (Reference 4-15), the movement of the cap is controlled by the increase or decrease of plastic volumetric strain. Hence, strain hardening can be reversed. This may happen if, after plastic compaction, elastic changes take place such that the stress point falls on the modified Drucker-Prager yield curve some distance below the cap. At such a stress point, the associated flow rule requires plastic dilatation, leading to a contraction of the cap back towards the point. This reversal in the motion of the cap can continue only until the cap reaches the stress point. When this occurs, the point becomes a corner of the contracted yield surface, permitting clockwise rotation of the plastic strain rate vector. If the loading is such that the stress point remains fixed once it has become a corner, the plastic strain rate vector parallel to the J_2' axis remains thus preventing further plastic volumetric strain. In this way the amount of dilatancy is controlled. Also, in this model, shear strength is independent of pressure for high pressure levels, hysteresis in hydrostatic loading-unloading is possible, the continuity condition is enforced, and Drucker's postulate is satisfied, ensuring uniqueness.

In the adaptation of the model to rock (Reference 4-22), the cap is constrained to move only in the direction away from the origin. The cap can move out on loading (increasing J_1, J_2') but does not move in if yielding takes place on unloading. In this way, dilatancy is not limited, and the plastic volume increase accompanying fracture of rocks is properly represented.

There are several methods of incorporating plasticity theory into computer programs (References 4-23 through 4-25 and 4-29). One method (Reference 4-25), which is appropriate for both finite element and finite difference methods, and which possesses desirable convergence properties, expresses the material properties as a matrix of coefficients, C (generalized tangent moduli) relating incremental stress and strain components. In cylindrical coordinates (r, z, θ),

$$\begin{Bmatrix} d\sigma_{rr} \\ d\sigma_{zz} \\ d\sigma_{\theta\theta} \\ d\sigma_{rz} \end{Bmatrix} = \begin{bmatrix} & & & \\ & & & \\ & & & \\ & & & \end{bmatrix} C \begin{Bmatrix} d\epsilon_{rr} \\ d\epsilon_{zz} \\ d\epsilon_{\theta\theta} \\ d\epsilon_{rz} \end{Bmatrix} \quad (4-38)$$

where

$d\sigma_{rr}$, etc. = Stress increments

$d\epsilon_{rr}$, etc. = Strain increments (γ_{rz} , the engineering shear strain is equal to twice the tensorial shear strain)

General Mathematical Models of Material Properties

In either finite difference or finite element applications, the equations of motion are solved for the displacement field at the end of the current time step. The displacements are then converted into strains and strain increments. The latter are substituted into Equation 4-38 from which stresses are computed. The equations of motion are then solved for the next time step. The coefficients of [C] are listed below.

$$[C] = \begin{bmatrix} \lambda + 2G - \frac{\lambda F + 2Gf_r}{\lambda F^2 + 2GX - R} & \lambda - \frac{(\lambda F + 2Gf_\theta)(\lambda F + 2Gf_r)}{\lambda F^2 + 2GX - R} & \lambda - \frac{(\lambda F + 2Gf_z)(\lambda F + 2Gf_r)}{\lambda F^2 + 2GX - R} & -2Gf_{rz} \frac{\lambda F + 2Gf_r}{\lambda F^2 + 2GX - R} \\ & \lambda + 2G - \frac{(\lambda F + 2Gf_\theta)^2}{\lambda F^2 + 2GX - R} & \lambda - \frac{(\lambda F + 2Gf_\theta)(\lambda F + 2Gf_z)}{\lambda F^2 + 2GX - R} & -2Gf_{rz} \frac{\lambda F + 2Gf_\theta}{\lambda F^2 + 2GX - R} \\ & & \lambda - \frac{(\lambda F + 2Gf_z)^2}{\lambda F^2 + 2GX - R} & -2Gf_{rz} \frac{\lambda F + 2Gf_z}{\lambda F^2 + 2GX - R} \\ & & & G - \frac{4G^2 f_{rz}^2}{\lambda F^2 + 2GX - R} \end{bmatrix} \quad (4-39)$$

Symmetrical

where

$$F = f_r + f_z + f_\theta = f_{kk}$$

$$X = f_r^2 + f_z^2 + f_\theta^2 + 2f_{rz}^2 = f_{ij} f_{ij}$$

f_r , etc. = Derivatives of the yield function f with respect to stress components (plastic potential flow rule). Subscripts r , z , and θ indicate differentiation with respect to r , z , and θ components of stress while subscript rz indicates differentiation with respect to shear stress

$$R = H' f_{ij}$$

$$H' = \frac{\partial f}{\partial H} \frac{\partial H}{\partial \epsilon_{ij}^p} \quad \text{Where } H \text{ is the strain-hardening function. For non-strain-hardening materials, this quantity is zero.}$$

The same matrix of coefficients applies to stresses in a rectangular coordinate system when appropriate changes in subscript notation are made.

Formulation of the C matrix in Equations 4-38 is useful to illustrate how stresses and strains are related in nonlinear materials. Furthermore, in finite element applications C must be formed not

only to relate stress to strain but also to compute the element stiffness matrices.

Finite difference formulations of nonlinear stress/strain relations differ from those described above for finite element. A representative finite difference method is described in Reference 4-29. Unlike the finite element approach where stresses are obtained from strains which are found initially from a displace-

ment field, the finite difference approach of Reference 4-29 computes stresses from strain rates which are found initially from particle velocity. In cylindrical coordinates, the component of the strain rate tensor at time $n+1$ and point ξ, η are found from the velocities as follows:

$$(\dot{\epsilon}_{rr})_{\xi, \eta}^{n+1} = \delta_r (\dot{u}_r)_{\xi, \eta}^{n+1} = \frac{1}{\Delta r} \left[(\dot{u}_r)_{\xi, \eta}^{n+1} + \frac{1}{2} - (\dot{u}_r)_{\xi, \eta}^{n+1} + \frac{1}{2} \right] \quad (4-40a)$$

$$(\dot{\epsilon}_{\theta\theta})_{\xi, \eta}^{n+1} = \frac{1}{r\xi} (\dot{u}_r)_{\xi, \eta}^{n+1} \quad (4-40b)$$

$$(\dot{\epsilon}_{zz})_{\xi, \eta}^{n+1} = \delta_z (\dot{u}_z)_{\xi, \eta}^{n+1} = \frac{1}{\Delta z} \left[(\dot{u}_z)_{\xi, \eta}^{n+1} + \frac{1}{2} - (\dot{u}_z)_{\xi, \eta}^{n+1} + \frac{1}{2} \right] \quad (4-40c)$$

$$(\dot{\epsilon}_{rz})_{\xi, \eta}^{n+1} = \delta_z (\dot{u}_r)_{\xi, \eta}^{n+1} + \delta_r (\dot{u}_z)_{\xi, \eta}^{n+1} \quad (4-40d)$$

where

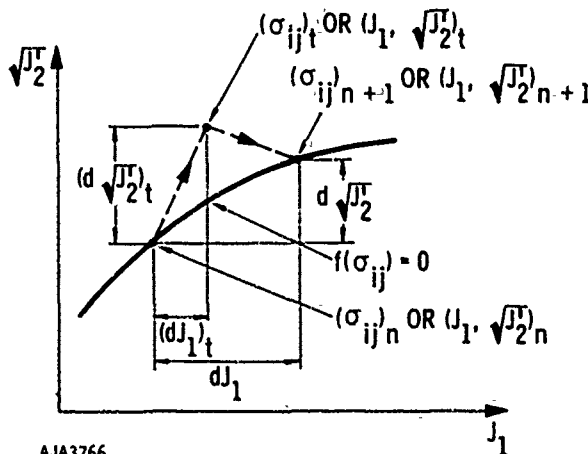
\dot{u}_r, \dot{u}_z = Particle velocity components in r, z directions at mesh points ξ, η

δ_r, δ_z = Central difference operators

$\Delta r, \Delta z$ = Radial and axial dimensions of the finite difference zone at whose center is the point ξ, η

r, z = Coordinates of the point ξ, η

The next step is to compute stresses from the strain rates. The procedure is illustrated in Figure 4-12 for an elastic/perfectly plastic material.



AJA3766

FIGURE 4-12. METHOD OF CORRECTING FINAL STRESS STATE FROM A TRIAL STATE

Assuming the stress increment to be entirely elastic, a trial stress increment and a new trial stress, denoted by subscript t , are computed in terms of deviatoric and hydrostatic components for the point ξ, η .

$$(\sigma'_{ij})_t^{n+1} = (\sigma'_{ij})_t + 2G(\dot{\epsilon}'_{ij})^{n+1} \Delta t \quad (4-41a)$$

$$(\sigma'_{kk})_t^{n+1} = (J_1)_t^{n+1} = (\sigma'_{kk})_t + 3K(\dot{\epsilon}'_{kk})^{n+1} \Delta t \quad (4-41b)$$

The trial deviatoric components $(\sigma'_{ij})_t^{n+1}$ are converted into a trial value of $(J_2)_t^{n+1}$ and the trial stress point $(J_2)_t^{n+1}$ is compared with the yield criterion. If the total stress falls inside the yield criterion, the stress components in Equation 4-41 are correct. If the trial stress falls outside the yield criterion (as is the case in Figure 4-12), the stress increment is corrected such that the new total stress lies exactly on the yield criterion. The method of correcting the stress depends on the flow rule. There are two types of flow rules in common use:

- In a nonassociated flow rule where $\sqrt{J_2}$ is used as a potential function (Prandtl-Reuss flow rule), the correction is made along a

line perpendicular to the J_1 axis. This procedure, which is equivalent to the associated flow rule when the yield criterion depends only on $\sqrt{J_2}$ (Mises yield criterion), produces no plastic volume change due to plastic flow.

- In an associated flow rule, where the yield criterion is used as a potential function, the correction is made as illustrated in Figure 4-12. The deviation of dJ_1 and $d\sqrt{J_2}$ is given below.

The mathematical statement that the final stress point (superscript $n+1$) must lie on the yield surface is

$$df = \frac{\partial f}{\partial \sigma_{ij}} d\sigma_{ij} = 0 = f_{ij} d\sigma_{ij} \quad (4-42a)$$

or

$$df = \frac{\partial f}{\partial J_1} dJ_1 + \frac{\partial f}{\partial \sqrt{J_2}} d\sqrt{J_2} = 0 \quad (4-42b)$$

Following Equation 4-8 and 4-32

$$dJ_1 = (dJ_1)_t - 9K\Lambda f_{kk} \quad (4-43a)$$

$$d\sqrt{J_2} = (d\sqrt{J_2})_t - 2G\Lambda \sigma'_{ij} f'_{ij} \quad (4-43b)$$

The remaining task is to find Λ . Defining

$$f_{kk} = \frac{\partial f}{\partial \sigma_{kk}} = f_I$$

$$f'_{ij} = \frac{\partial f}{\partial \sigma'_{ij}} = \frac{\partial f}{\partial \sqrt{J_2}} \frac{\partial \sqrt{J_2}}{\partial \sigma'_{ij}} = f_{II} \frac{\sigma'_{ij}}{2\sqrt{J_2}}$$

Substituting these definitions into Equations 4-43 and substituting the result into Equation 4-42, the result is

$$f_I [(dJ_1)_t - 9K\Lambda f_I] + f_{II} (d\sqrt{J_2})_t - \frac{G\Lambda \sigma'_{ij} \sigma'_{ij} f_{II}}{2J_2} = 0 \quad (4-44)$$

Equation 4-44 may also be expressed by

$$9K\Lambda f_I^2 + G\Lambda f_{II}^2 = f_I (dJ_1)_t + f_{II} (d\sqrt{J_2})_t \quad (4-45)$$

General Mathematical Models of Material Properties

The expression on the right-hand side of Equation 4-45 is considered to equal the difference between the trial state and the surface $f = 0$. The geometrical interpretation is given in Figure 4-12.

Thus

$$f[(J_1)_t, (\sqrt{J_2})_t] > 0 = f_I(dJ_1)_t + f_{II}(d\sqrt{J_2})_t \quad (4-46)$$

is then computed from the expression

$$\Lambda = \frac{f[(J_1)_t, (\sqrt{J_2})_t]}{9Kf_I^2 + Gf_{II}^2} \quad (4-47)$$

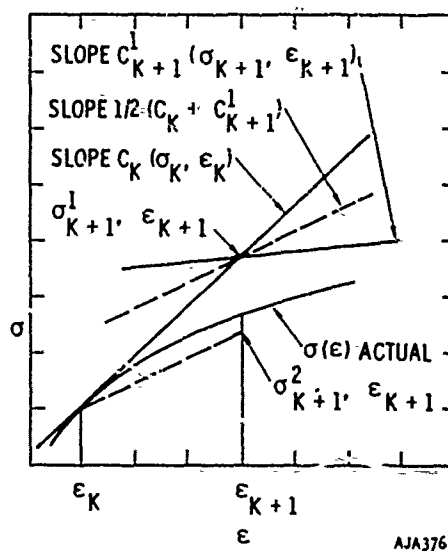
Inspection of the C matrix, Equation 4-39, reveals that each term has an elastic part ($\lambda + 2G$, λ or G) and a plastic correction. This is the matrix equivalent of steps performed in Equations 4-41 through 4-47.

Equations 4-39 and 4-43 through 4-47 contain terms which depend on the value of the stresses and plastic strains. Theoretically, the values of stress and strain which should be used to evaluate these equations differ only infinitesimally from the values being sought. In practical situations, state n where stresses and plastic strains are known may differ appreciably from state $n + 1$. To be sure that equations such as Equation 4-41 and its correction Equation 4-43 converge in spite of such differences, the following techniques are used.

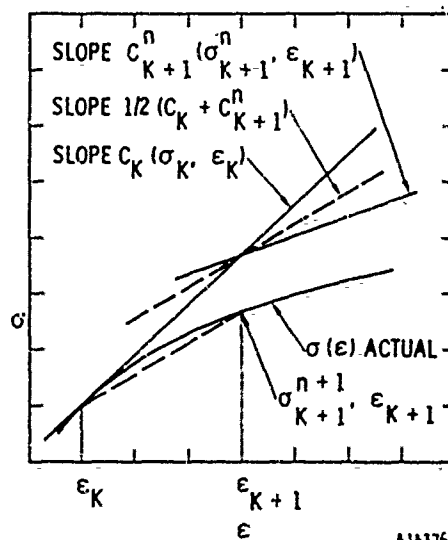
- The integration time step is kept small such that stress and strain increments are small compared with total stresses and strains. Although this is usually a necessary precaution, it may be insufficient. For example, at the start of a calculation, stress and strain increments are necessarily comparable to total stresses and strains. Also, in the event of large shear flows as occur in calculations of cratering, the time step may have to be so small that the calculation becomes uneconomical.
- The strain increment resulting from an integration step (finite element) or the time step (finite difference) may be subdivided into a number of smaller steps. From each small strain increment or step the corresponding stress and plastic strain increments are computed, and the quantities in the C matrix or the stresses are updated before taking the next small step. This process is repeated until the accumulated small strain increments or small time steps equal the total strain increment or total Δt produced during the

integration step. This procedure is approximately as accurate as decreasing the integration time step but is much more efficient. It may still be costly, since a significant percentage of total solution time in finite difference calculations is spent in the material property subroutines.

- An iterative procedure can be used. As an example, Euler's predictor-corrector formulas are applied to determine the slope (corresponding to the C matrix) and function value (corresponding to stress) of the $\sigma(\epsilon)$ curve in Figure 4-13.



(a) INITIAL ITERATION



(b) nTH ITERATION

FIGURE 4-13. ITERATION SCHEME TO EVALUATE STRESSES

The first iteration uses the slope C_K at K to obtain a trial stress increment $d\sigma_{K+1}$ which is added to the initial stress σ_K to obtain an estimate of σ_{K+1}^1 . The Superscript 1 denotes iteration Number 1.

$$|d\sigma_{K+1}| = [C_K] |d\epsilon_{K+1}| \quad (4-48)$$

$$|\sigma_{K+1}^1| = |\sigma_K| + |d\sigma_{K+1}| \quad (4-49)$$

From σ_{K+1}^1 , ϵ_{K+1} is estimated. A new trial slope for the second iteration is then obtained by averaging as follows.

$$C_{K+1}^2 = [C_K + C_{K+1}^1]/2 \quad (4-50)$$

This procedure is repeated until the change in a pre-determined function of stress components is stationary within a prescribed tolerance.

SUMMARY

An equation of state is a relationship among the pressure or stress, relative density or strain, specific internal energy, and previous history of loading. Although it would be desirable to have a single equation which applies to all ranges of these variables, no such relation has yet been derived. Instead, ranges of behavior are defined according to the pressure or relative density and the specific internal energy. At high relative density and specific internal energy, the material is assumed to act as a fluid. At low relative density and high specific internal energy, the material is considered to be a hot gas. The Mie-Gruneisen and Tillotson equations are widely used to describe such states.

The material is assumed to be in a solid state if the relative density and specific internal energy do not differ greatly from the in situ state. Several forms of solid equations of state are available. An extension of the theory of linear elasticity whereby the moduli are allowed to vary with intensity and history of stress and strain is known as the variable modulus model. A second type of solid equation of state is based on plasticity theory, which includes a yield criterion,

hardening rule, and flow rule. Combinations of variable modulus and plasticity theory models are often used to try to match the experimental data on a specific material. Such hybrid models may match experimental data better than either variable modulus or plasticity theory models alone. However, use of variable modulus models often makes it impossible to prove uniqueness of stress and strain states for arbitrary stress paths. To overcome this disadvantage, strain hardening models have recently been developed whereby hysteresis in the pressure/volume relation is introduced within the framework of classical plasticity theory.

Table 4-1 summarizes the advantages and disadvantages of the types of models presently in use. Although the elastic, ideally plastic model is the simplest to fit to some experimental data, it is unable to match stress/strain data from triaxial compression experiments. When used with an associated flow rule and either constant shear modulus G or G which varies with maximum pressure P_m , the resulting stress/strain relations are unique. Other adaptations, such as an explicitly variable $G(P)$ or an implicitly variable G through a variable bulk modulus and constant Poisson's ratio can generate energy along some paths. To use different G on loading and unloading is objectionable from the standpoint of continuity. To try to overcome the tendency of elastic ideally plastic models to produce too much dilatancy when they are used with a Prager-Drucker type yield criterion and associated flow rule, non-associated flow rules which suppress dilatancy are sometimes used. These have not been proved to be rigorously correct, even though available work (Reference 4-38) indicates no uniqueness difficulties arise.

Variable moduli models give the best overall fit to the type of laboratory data which are usually available. This model is the only one discussed above which is capable of producing repeated hysteretic effects under cyclic loading within the failure envelope. It is therefore attractive for use in cases of low-amplitude loading in layered media where energy dissipation during many cycles of loading and unloading/reloading is important. For problems where neutral loading ($J_2 = \text{const.}$) or near neutral loading occurs, the variable modulus model may result in discontinuous stress/strain relations. For proportional loading (principal stresses in fixed ratio), it satisfies the rigorous theoretical requirements.

The cap models were developed in an attempt to obtain a satisfactory model from the viewpoint of uniqueness while providing a reasonably good fit of all available experimental data. In its application to rock and soil, the cap model controls dilatancy more effectively than the elastic, ideally plastic model with an associated flow rule. The cap model is the most difficult to fit of the models described above.

General Mathematical Models of Material Properties

TABLE 4-1. ADVANTAGES AND DISADVANTAGES OF EACH MODEL

Advantages	Disadvantages
A. Elastic-Ideally Plastic	
Simplest to fit Approximates most features of data $G = \text{Const. } G = G(P_m)$ and associated flow rule theoretically correct	May not fit all available data Cannot match triaxial test Other treatments of G can lead to possible paths of energy generation For nonassociated flow rule no general uniqueness theorem
B. Variable Moduli	
Best fit of data Only model with repeated hysteresis within failure envelope Ideal for finite element Computationally simple Relatively easy to fit	Restricted to near-proportional loading (in shear) For nonproportional loading paths no uniqueness theorem Additional quantity F_m must be stored at each grid point
C. Soil-Cap Model	
Satisfies all rigorous theoretical requirements Reasonable good fit of data	Indirect approach needed to fit data Relatively complicated
Note: Elastic-Ideally Plastic model with $K_U \neq K_L$ may be considered a special case	
D. Rock-Cap Model (Same as C)	
Effective control of dilatancy	Additional quantity, the strain hardening parameter must be stored at each grid point

REFERENCES

- | | |
|---|---|
| <p>4-1. Rice, M. H., et al., "Compression of Solids By Strong Shock Waves," <u>Solid State Physics</u>, Vol. 6, Chapter IV, "Equation of State," Eds. F. Seitz and D. Turnbull, Academic Press, Inc., New York and London, 1958.</p> <p>4-2. Tillotson, J., <u>Metallic Equations of State for Hypervelocity Impact</u>, GA-3216, General Atomic Division, General Dynamics Corporation, July 1962.</p> <p>4-3. Butkovitch, T. R., <u>The Gas Equation of State for Natural Materials</u>, UCRL-14729, Lawrence Radiation Laboratory, January 1967.</p> | <p>4-4. Schuster, S. H., and J. Isenberg, <u>Free Field Ground Motion for Beneficial Siting, Volume 2--Equation of State for Geologic Media</u>, SAMSO-TR-70-88, June 30, 1970.</p> <p>4-5. Love, A. E. H., <u>A Treatise on the Mathematical Theory of Elasticity</u>, Dover Publications, New York, 1944.</p> <p>4-6. Walsh, J. B., "The Effect of Cracks on the Compressibility of Rock," <u>J. Geophys. Res.</u>, Vol. 70, No. 2, January 15, 1965.</p> <p>4-7. Walsh, J. B., "The Effect of Cracks on Poisson's Ratio," <u>J. Geophys. Res.</u>, Vol. 70, No. 2, October 15, 1965.</p> |
|---|---|

References

- 4-8. Stephens, D. R., and E. M. Lilley, Static PV Curves of Cracked and Consolidated Earth Materials to 40 Kilobars, UCRL-14711, Lawrence Radiation Laboratory, March 1966.
- 4-9. LaMori, P. N., Compressibility of Three Rocks, (A) Westerly Granite and Solenhofen Limestone to 40 Kilobars at 300°C, (B) Cedar City Tonalite to 40 Kilobars at Room Temperature, DASA-2151, Defense Atomic Support Agency, August 1968.
- 4-10. Army Corps of Engineers, Missouri River Division Laboratory, Tests for Strength Characteristics of Rock, Pile Driver Project, MRDL 64/90, 1964.
- 4-11. Stephens, D. R., Elastic Constants of Fractured Granodiorite, UCIK-15369, Lawrence Radiation Laboratory.
- 4-12. Calhoun, D. E., Project Mine Shaft Material Properties, Preliminary Report, Eric H. Wang Civil Engineering Research Facility, December 1968.
- 4-13. Towle, L. C., and R. E. Riecker, "The Pressure and Temperature Dependence of the Shear Strength of Minerals," J. Appl. Phys., Vol. 39, No. 10, September 1968, p. 4807.
- 4-14. Domaschuk, L., and N. H. Wade, "A Study of Bulk and Shear Moduli of a Sand," Proc., ASCE, Soil Mechanics and Foundation Division, Vol. 95, No. SM2, March 1969, pp. 561-581.
- 4-15. DiMaggio, F. L., and I. Sandler, Material Model for Soils, DASA-2521, Paul Weidlinger Consulting Engineer, April 1970.
- 4-16. Fung, Y. C., Foundations of Solid Mechanics, Prentice-Hall Englewood Cliffs, New Jersey, 1965.
- 4-17. Handelman, G. H., et al., "On the Mechanical Behavior of Metals in the Strain Hardening Range," Quart. Appl. Math., Vol. 4, 1947, pp. 397-407.
- 4-18. Drucker, D. C., "A More Fundamental Approach to Stress-Strain Relations," Proc., 1st U. S. Congress Appl. Mech., ASME, 1950, pp. 487-491.
- 4-19. Drucker, D. C., "Some Implications of Work Hardening and Ideal Plasticity," Quart. Appl. Math., Vol. 7, 1950, pp. 411-418.
- 4-20. Drucker, D. C., and Prager, W., "Soil Mechanics and Plastic Analysis or Limit Design," Quart. Appl. Math., Vol. 10, No. 2, July 1952, pp. 157-165.
- 4-21. Hill, R., The Mathematical Theory of Plasticity, Oxford, 1950.
- 4-22. Sandler, I., and F. E. Dimaggio, Material Model for Rocks, DASA-2595, Paul Weidlinger Consulting Engineer, October 1970.
- 4-23. Isenberg, J., Material Properties for AFTON Code, DASA 2178, Agabian-Jacobsen Associates, December 1968.
- 4-24. Isenberg, J., and L. C. Lee, Material Properties for ELK Code, DASA 2344, Agabian-Jacobsen Associates, October 1969.
- 4-25. Isenberg, J., and A. K. Bhaumik, Stress/Strain Distribution in Triaxial Compression Tests on a Sand, DASA 2553, Agabian-Jacobsen Associates, October 1970.
- 4-26. Nelson, I., et al., Mathematical Models for Geological Materials for Wave Propagation Studies, DASA 2672, Paul Weidlinger Consulting Engineer, March 1971.
- 4-27. Cherry, J. T., et al., "A Unique Description of the Failure of a Brittle Material," Int. J. of Rock Mech. and Min. Sci., Vol. 5, Pergamon Press, 1968, p. 455-463.
- 4-28. Baron, M. L., Summary of Investigations on the Response of Soil and Rock Materials to Nuclear Bursts, Paul Weidlinger, Consulting Engineer, June 1969.
- 4-29. Baron, M. L., et al., "Investigation of Ground Shock Effects in Nonlinear Hysteretic Media," Computational Approaches in Applied Mechanics, ASME, Computer Conference, IIT, June 1969.
- 4-30. Nelson, I., et al., "Mathematical Models for Geological Wave-Propagation Studies," Shock Waves and the Mechanical Properties of Solids, Syracuse Univ. Press, 1971.
- 4-31. Matthews, A. T., and H. H. Bleich, Stresses in an Elastic-Plastic Half-Space Due to a Superseismic Step Load, Technical Report No. 4, Paul Weidlinger, Consulting Engineer, Ballistics Research Laboratory, Aberdeen Proving Ground, March 1966.
- 4-32. Bleich, H. H., and A. T. Matthews, "Step Load Moving with Superseismic Velocity on the Surface of an Elastic-Plastic Half-Space," Int. J. Solids Structures, 3, 1967, pp. 819-852.

General Mathematical Models of Material Properties

- 4-33. Bleich, H. H. and A. T. Matthews, Exponentially Decaying Pressure Pulse Moving with Superseismic Velocity on the Surface of a Half-Space of a von Mises Elasto-Plastic Material, Report AFWL-TR-68-46, Paul Weidlinger, Consulting Engineer, August 1968.
- 4-34. Matthews, A. T., et al., Investigation of Ground Shock Effects in Nonlinear Hysteretic Media - Report 4 - Effect of a Step Load Moving with Constant Superseismic Velocity on a Half-Space of a Variable Modulus Material, Report S-68-1, Paul Weidlinger, Consulting Engineer, Army Engineer Waterways Experiment Station, March 1970.
- 4-35. Prager, W., Introduction to Mechanics of Continua, Chap. VIII, Ginn and Co., 1961.
- 4-36. Truesdell, C., "Hypo-Elasticity," J. Rat. Mech. Analysis, 4, 1955, p. 83.
- 4-37. Handelman, G. H., Lin, C. C., and W. Prager, "On the Mechanical Behavior of Metals in the Strain-Hardening Range," Quart. Appl. Math., 4, 1947, pp. 397-407.
- 4-38. Bleich, H. H., On the Use of a Special Nonassociated Flow Rule for Problems of Elasto-Plastic Wave Propagation, DASA-2635, Paul Weidlinger, Consulting Engineer, October 1970.
- 4-39. Allen, R. T., Equation of State of Rocks and Minerals, General Atomic Division of General Dynamics, GAMD-7834, March 1967.

SECTION 5

SPECIFIC MATHEMATICAL MODELS OF SELECTED EARTH MATERIALS

INTRODUCTION

Mathematical models for a variety of rock and soil types have been derived as part of studies of free field ground shock and soil/structure interaction. Some of these models, which are summarized below, are considered to be the best presently available. Among the rocks included in the summary are Nevada Test Site granite, Cedar City tonalite, a soft limestone, an anorthosite, a sandstone, and basalt. Among the soils are a typical alluvium, a silty clay from Suffield Experiment Station, Canada, and a silty sand from McCormick Ranch in New Mexico. Each model is based on the results of laboratory experiments, but the amount of supporting data varies from one material to another. Field tests and calculations have been performed for some of the materials considered, such as NTS granite (Pile Driver event), Cedar City tonalite (Mine Shaft series), and Suffield silty clay (Operations Distant Plain and Prairie Flat). For these materials, the mathematical model has been somewhat validated through comparison with actual field test data followed, in some instances, by modification of the model. The models that have not been compared with field data should be regarded as preliminary.

MATHEMATICAL MODELS FOR SEVEN ROCKS

This subsection describes mathematical models for fluid and solid phases of NTS granite, Cedar City tonalite, Laramie anorthosite, Banded Mountain limestone, Coconino sandstone, porous and dense basalt, and NTS tuff. The following discussion describes how experimental data are used to derive a model for NTS granite and gives a table of coefficients for the other materials in the list above from tonalite through basalt. These models are derived within the framework of the general model described in Section 4. An alternative model for the solid phase of Cedar City tonalite, which includes a strain-hardening cap, is given subsequently.

NTS GRANITE (GRANODIORITE)

The mathematical model of NTS granite described here is reported in Reference 5-1. The general mathematical model is described by Equations 4-7, 4-14, 4-19, 4-26, and 4-29. The high-pressure equation of state is based on a modified Tillotson form. The bulk and shear moduli are based on Walsh's concept of an effective modulus that tends toward an intrinsic modulus as cracks and pores are closed. The shear modulus is assumed to decrease as the melting temperature is approached. A Drucker-Prager yield criterion with a von Mises limit at high pressure are used together with an associated flow rule.

The density of granitic rocks may vary from 2.5 to 2.8 gm/cm³, while samples from the region of interest, Area 15 of the Nevada Test Site (NTS), vary between 2.62 and 2.70 gm/cm³. Densities are usually determined from measurements on small, competent samples and, hence, represent an upper limit to the average density of the rock in a volume comparable to that in the much larger finite difference zones. With this in mind, an initial density of 2.65 gm/cm³ was selected to represent the granodiorite under consideration.

The calculation of mean stress P for granite, a solid exhibiting hysteresis, requires the evaluation of nine constants: β , K_{\max} , K_0 , μ^* , c , d , μ_p , μ_{pp} , and P_a .

The first, β , is the coefficient of volume expansion per unit internal energy and can be derived from the ratio of the coefficient of volume expansion per degree Centigrade and the specific heat. Using values of 25 $\mu\text{in./in.}$ and 0.192 cal/gm (Reference 5-2) for the two above-mentioned quantities, β equals 3.0 (Mb-cc/gm)⁻¹. Although neither the specific heat nor the coefficient of volume expansion is constant over the range of pressure and temperature of interest, both tend to increase linearly with temperature, and it is assumed here that their ratio does not change. A more elaborate representation of β is unwarranted

Specific Mathematic Models of Selected Earth Materials

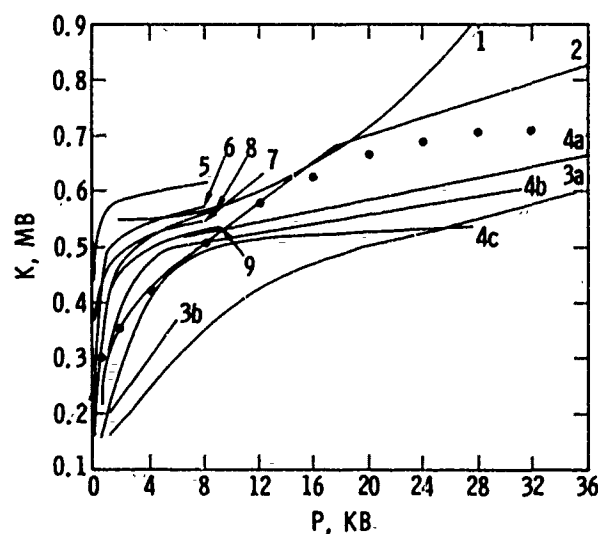
since β_e is usually small relative to the compression unless the material is subjected to pressure of the order of hundreds of kilobars.

The values of K_{max} , K_0 , and μ^* for NTS granite can be determined directly from experimental data for pressures below 100 kb. Using a hydrostatic press, Stephens (References 5-3 and 5-4) has obtained loading and unloading pressure/volume data on several NTS rocks for pressures up to 40 kb. In addition, La Mori's measurements (Reference 5-5) of the hydrostats of Westerly granite and tonalite and Birch's data (Reference 5-6) on the compressional wave speed in various granites prestressed up to 10 kb provide useful information on possible variations in the hydrostat. Triaxial compression tests in which all of the stress-strain components were measured (References 5-7 and 5-8) have been performed at pressures less than 1 kb, and these provide a further check. In an attempt to correlate these experiments, $dP/d\mu$ was calculated from the data reported and plotted against P . Curves representing the data obtained are compared with the model in Figure 5-1. The variations among the measurements are so large that it is not possible to choose a single value for the "intrinsic" bulk modulus, K_{max} , for all granites. While all of the curves tend toward values between 0.6 and 1.0 Mb, the data vary too much to be fit by a single value of K_{max} . Differences in mineral content are probably responsible for the measured variations in this parameter. A value of 0.8 Mb is chosen as representative of the most recent data on NTS granodiorite (Reference 5-4). Similarly, although K_0 ranges between 0 and 0.7 Mb for the variety of granites examined, a value of 0.225 Mb appears appropriate for the NTS material.

The parameter μ^* determines the rate at which the bulk modulus rises from K_0 to K_{max} , while the constant c is used to decrease the bulk modulus at high temperatures to match the hugoniot data in the transition region between solid and fluid. Values of 0.0375 and 0.35 for these two parameters complete the description of the loading hydrostat. In Figure 5-2, calculated hydrostat and hugoniot curves are compared with data for several granites for pressures in the range 0 to 45 kb. Since the hugoniot measurements are performed on small samples of highly competent material, most of those data lie above the curve calculated for the in situ material. However, the upper curve, which was calculated by assuming a constant shear modulus appropriate to consolidated granite, fits the data well up to 35 kb. At higher pressures, the measurements on Westerly granite fall below the calculation. This is not expected as the bulk modulus (curve 4a, Figure 5-1) for Westerly granite and, therefore, its hydrostat, are also less than those of NTS granite at these pressures.

The parameters, d , μ_p , μ_{pp} , and P_a are used in describing the unloading behavior of solid material.

CURVE	MATERIAL	REFERENCE
1	NTS GRANODIORITE	5-3
2	NTS GRANODIORITE	5-4
3a, b	CEDAR CITY TONALITE	5-5
4a	WESTERLY GRANITE 24°C	5-5
4b	WESTERLY GRANITE 160°C	5-5
4c	WESTERLY GRANITE 313°C	5-5
5	ROCKPORT GRANITE	5-6
6	STONE MT. & WESTERLY GRANITE	5-6
7	PORTERVILLE GRANITE	5-6
8	STONE MT. GRANITE	5-8
9	WESTERLY GRANITE	5-8
•	NTS GRANITE MODEL	



AJA3769

FIGURE 5-1. TANGENT BULK MODULI FOR VARIOUS GRANITES AND A MODEL FOR NTS GRANITE (REFERENCE 5-1)

Walsh (Reference 5-12) has shown that the pressure necessary to close a crack is linearly related to the dimensions of the crack. If there are many randomly sized small cracks contributing to the initial porosity, it is reasonable to expect an irreversible change in porosity, which varies inversely with peak-loading pressure until all cracks are closed. No further permanent change in porosity is then exhibited until the pressure is so high that either the pores break down or an irreversible phase change occurs. This behavior is modeled by Equation 4-13, where d is the constant of proportionality between the loss of porosity and the pressure, μ_p is the total change in compression when all the cracks are closed, P_a is the pressure above which pore breakdown and/or phase change is possible, and μ_{pp} is the maximum irreversible change in compression due to pore breakdown of phase change. Typical unloading paths from the granite hydrostat are shown in Figure 5-3.

NTS Granite (Granodiorite)

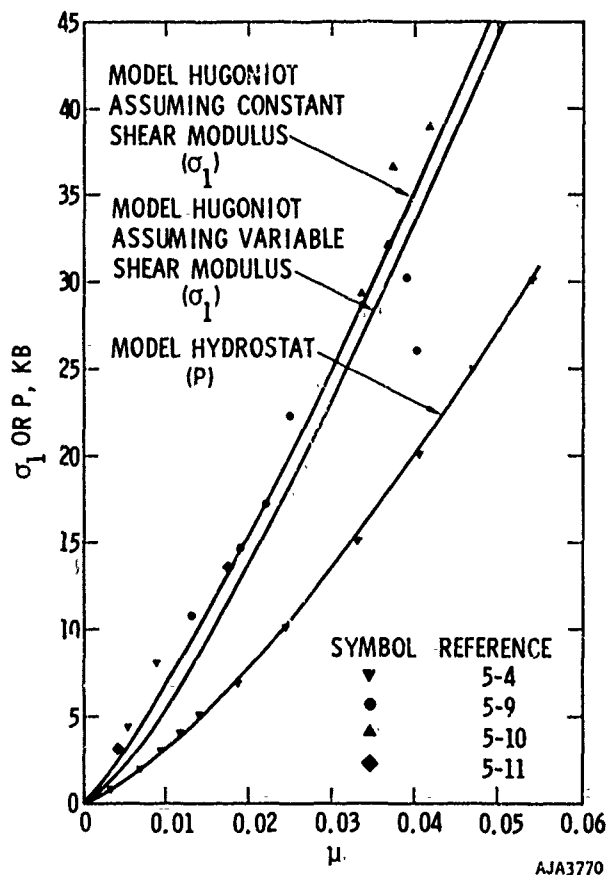


FIGURE 5-2. MODEL HUGONIOT AND HYDROSTAT FOR NTS GRANITE COMPARED WITH DATA (REFERENCE 5-1)

At pressures above 400 kb, enough internal energy is present in the material so that the fluid pressure P_{fl} is not zero. The unloading path from these high pressures drops very sharply until the contribution of P_{fl} to the total pressure dominates. Beyond that point, the pressure diminishes so slowly that the material may not actually return to zero pressure until it has expanded beyond the initial solid density. Such behavior has been seen experimentally in the release adiabats of anorthosite and quartz (Reference 5-13).

Evaluating the parameters for P in Equation 4-7 is all that remains to define the behavior of the mean stress in NTS granite. At low densities, the exponential expression $\exp Z$ damps out everything but the $a_0 \rho e^*$ term. Hence, a_0 is the equivalent of $r - 1$ in the perfect gas law. Calculations (Reference 5-14) show that $r - 1$ asymptotically approaches a value between 0.04 and 0.14 for several rock media at low densities for pressures below 10 kb. Therefore, a_0 is assumed to be 0.1. The coefficient b_3 of μ/η in the exponential is assumed to be 5, consistent with

the studies on metals by Tillotson (Reference 5-15) and on rocks by Allen (Reference 5-16). For compressed material at energies considerably greater than the vaporization energy, the term

$$\frac{b_1}{\frac{e}{e_0} \eta^2 + 1}$$

becomes negligible, and the coefficient of ρe^* becomes $a_0 + b_2$. The term b_2 was set at 0.4 so that the sum equaled 0.5, again consistent with Tillotson and Allen. This model differs from Tillotson's formulation in that the term P_{fl} is set to zero at energy densities less than that required to melt the material. For granite, which melts a temperature of about 1400°C, the minimum energy density for melting, e_{m0} , is assumed to be 0.0115 Mb-cc/gm. Since the melting temperature in most materials increases with compression, the energy density at melting, e_m , is allowed to increase linearly to a

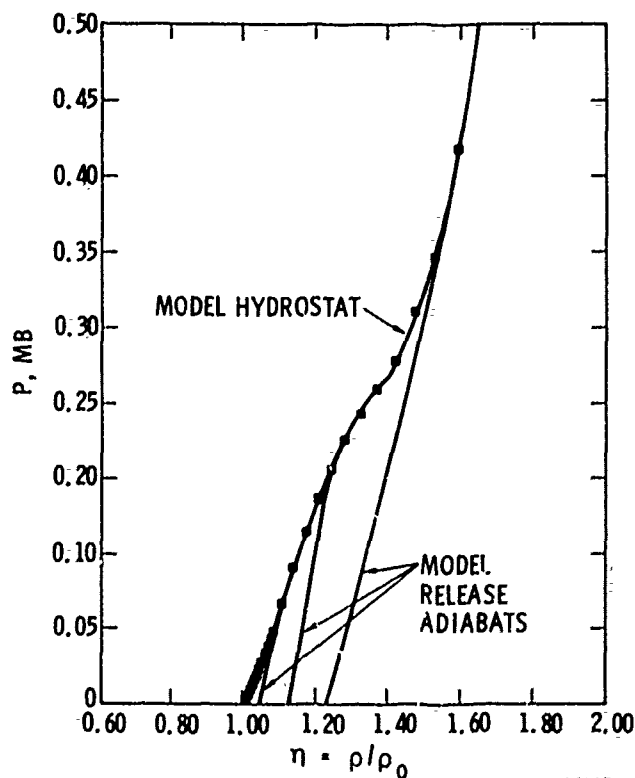


FIGURE 5-3. MODEL HYDROSTAT AND RELEASE ADIABATS FOR NTS GRANITE (REFERENCE 5-1)

Specific Mathematical Models for Selected Earth Materials

maximum, e_{mm} , equal to 0.035 Mb-cc/gm in granite, so that

$$e_{mo} < e_m = e_{mo} (1 - s\eta) < e_{mm} \quad (5-1)$$

where s is 1.7. In Figure 2-40 the calculated principal hugoniot is compared with experimental data up to 1 Mb. Data for several rocks with mineral contents similar to NTS granite are included. Above 100 kilobars, all of these rocks behave alike, suggesting that their basic chemical composition--rather than initial density, porosity, or physical structure--largely determines their behavior at high pressures.

The mean stress behavior of NTS granite is now determined, and attention is shifted to the parameters influencing its deviatoric characteristics. Except for Simmons' work (Reference 5-22) on the shear wave velocities of rocks under hydrostatic pressures up to 10 kb, there is little data from which to determine the shear modulus, G , of granite. Recently improved techniques in triaxial testing (Reference 5-12) show considerable promise as a means of determining G , but the work is still preliminary. Stephens (Reference 5-23) recently measured the shear modulus for consolidated and cracked NTS granodiorite; his data, the wave speed measurements of Simmons, and the model are presented in Figure 5-4. The values of G_0 , G_{max} , and μ^*G (Equation 4-19) match Stephens' data for the cracked granodiorite.

Data on the yield strength of granite as a function of mean stress are presented in Figure 5-5. Several Mohr-Coulomb surfaces are also plotted for comparison. The equation for these surfaces is

$$f = \left\{ \sqrt{J_2} - \text{minimum of} \begin{bmatrix} (A_0 + \alpha P) \\ (A_3) \end{bmatrix} \right\} \leq 0 \quad (5-2)$$

The large differences between the various experiments are attributable to the initial condition of the rock, since preexisting cracks and pores or variations in the water content and pore pressure can severely affect the strength of the rock. For intact, competent granite, the data are best fit by choosing $A_0 = 0.0005$ Mb and $\alpha = 1.10$. The measurements made on jointed and cracked samples from the Pile Driver site in NTS Area 15 lead to $A_0 = 0.0001$ Mb and $0.5 < \alpha < 0.7$ (References 5-7 and 5-24). Finally, recent unpublished LRL data (Reference 5-25) from presumably cracked, wet NTS granite suggest that α may be as low as 0.3.

Since the small samples used in the experiments are generally more competent than in situ material, the measured yield strengths have been treated as upper bounds to the values to be expected in the field, and values of $A_0 = 0.0001$ Mb and $\alpha = 0.3$ are used in the model. For similar reasons, the von Mises surface, A_2 , is set at 0.017 Mb, although comparison

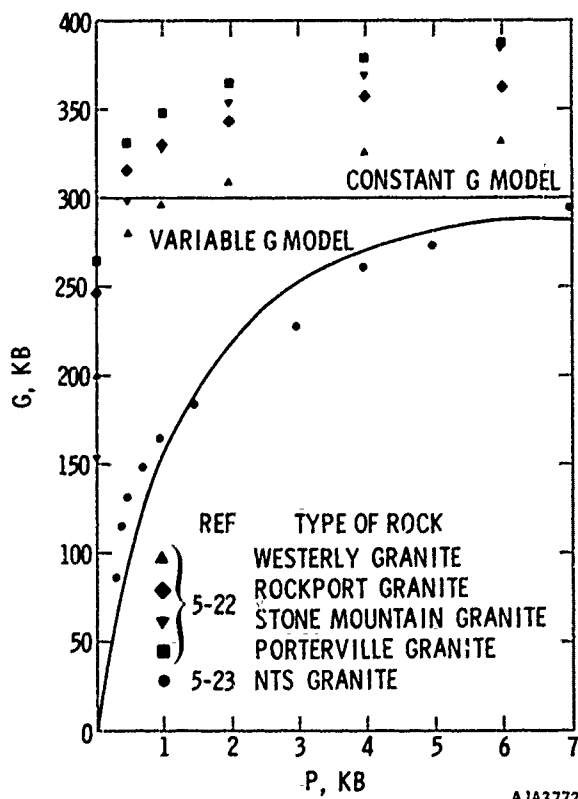


FIGURE 5-4. SHEAR MODULUS AS A FUNCTION OF PRESSURE FOR NTS GRANITE (REFERENCE 5-1)

of the data near the hugoniot elastic limit with the calculated hydrostat would suggest a value of A_3 as high as 0.020 Mb.

Material models having the same form for a number of other rocks have been derived. The experimental data on which these are based are discussed in Reference 5-1. A summary of the empirical parameters in models for Cedar City tonalite, Laramie anorthosite, Banded Mountain limestone, Coconino sandstone, and porous and dense basalt is given in Table 5-1.

Cedar City Tonalite

An alternate model for the solid phase stress/strain properties of Cedar City tonalite has been proposed in Reference 5-26.* Theoretical aspects of this model are described in Section 4. The bulk and shear moduli are, respectively:

$$K = 7500 (1 - 0.07e^{0.005J_1}) \text{ ksi} \quad (5-3)$$

$$G = 3300 \text{ ksi} \quad (5-4)$$

*In this model, compressive stresses are negative.

NTS Granite (Granodiorite)

The fracture surface f_1 and strain hardening cap f_2 are defined as follows:

$$f_1 = J_2' - 152 + 145e^{0.0029J_1} \leq 0 \quad (5-5)$$

$$f_2 = \left(\frac{J_1 - J_c}{Z^2} \right)^2 + J_2' - Q = 0 \quad (5-6)$$

where

$$J_c = J_{1F} - Z^2 \sqrt{J_{2F}} \left(\frac{\partial f_1 / \partial J_1}{\partial f_1 / \partial \sqrt{J_2'}} \right) \quad (5-7)$$

$$Q = J_{2F} \left[1 + Z^2 \left(\frac{\partial f_1 / \partial J_1}{\partial f_1 / \partial \sqrt{J_2'}} \right)^2 \right] \quad (5-8)$$

$$J_{2F} = 152 - 145e^{0.0029J_{1F}} \quad (5-9)$$

$$J_{1F} = -450\kappa \quad (5-10)$$

$$Z = 4e^{-0.05J_{1F}} \quad (5-11)$$

$$\kappa = \sum_{n=1}^N -f_1 \sqrt{(d\epsilon_{11}^P)^2 + (d\epsilon_{22}^P)^2 + (d\epsilon_{33}^P)^2} \quad (5-12)$$

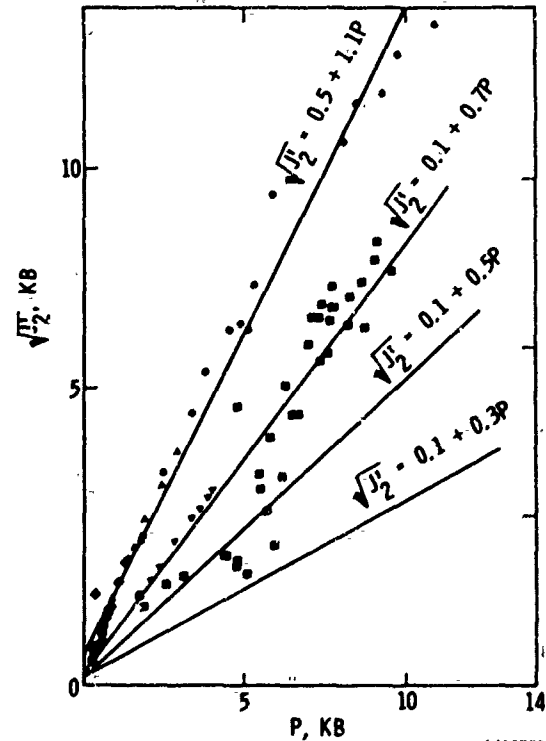
As illustrated in Figure 5-6, J_c is the value of J_1 at the center C of the elliptical cap, Z is the ratio of the major to minor axes of the ellipse and Q is the value of J_2' on the cap when $J_1 = J_c$. At the junction F, f_1 and f_2 have equal slopes. If the stress point lies on f_1 , strain hardening is zero. The functions of the yield criterion used in the C matrix, Equation 4-37, are computed from f_1 and the R terms are zero. If the stress point lies on f_2 , strain hardening occurs. Functions of the yield criterion are computed from f_2 . The R term of the coefficient matrix is as follows:

$$R = f_1 f_{1\kappa} (f_r^2 + f_0^2 + f_z^2)^{1/2} \quad (5-13)$$

where $f_{1\kappa} = \partial f_1 / \partial \kappa$ which can be obtained by applying the chain rule to the expression for f_2 above.

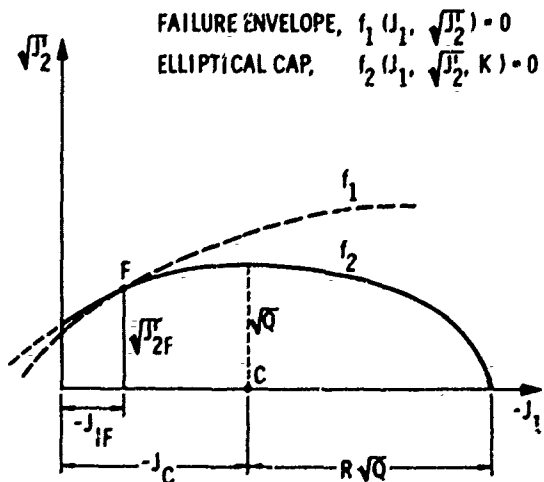
SYMBOL REFERENCE

- 5-27
- ▲ COMPRESSION 5-29
- ▼ EXTENSION 5-29
- 5-28
- ◆ 5-7



AJA3773

FIGURE 5-5. MODELS FOR YIELD STRENGTH OF GRANITE AS A FUNCTION OF MEAN STRESS (VARIOUS STATES OF STRESS AND DEGREES OF INITIAL CRACKING)



AJA3774

FIGURE 5-6. ROCK CAP MODEL

Specific Mathematical Models for Selected Earth Materials

TABLE 5-1. EQUATION-OF-STATE PARAMETERS AND VARIABLES

Quantity	Units	NTS Granite	Cedar City Tonalite	Laramie Anorthosite	Banded Mountain Limestone	Coconino Sandstone	Basalt Porous	Basalt Dense	Description
a_0	--	0.1	0.1	0.1	0.1	0.1	0.1	0.1	Coefficients in perfect gas equation (Eq. 4-7)
b_2	--	0.4	0.4	0.4	0.4	0.4	0.4	0.4	
b_1	--	1.3	1.3	1.3	1.3	0.8	1.0	1.0	Empirical constant (Eq. 4-7)
c	--	0.35	0.2	0.35	0.2	0.	0.35	0.2	Empirical constant (Eq. 4-10)
d	Mb ⁻¹	1.0	1.0	--	0.855	5.	1.0	--	Empirical constant (Eq. 4-13)
e	Mb-cc/gm	--	--	--	--	--	--	--	Specific internal energy, an independent state variable
e_m	Mb-cc/gm	--	--	--	--	--	--	--	Specific internal energy necessary to reach the melting point (Eq. 4-7, 4-10)
e_{mo}	Mb-cc/gm	0.0115	0.010	0.0115	0.0007	0.015	0.012	0.0075	Specific energy of melted material at normal density (Eq. 4-10)
e_{mm}	Mb-cc/gm	0.035	0.035	0.035	0.025	0.035	0.035	0.035	Specific energy at complete melting (Eq. 19)
e_0	Mb-cc/gm	0.160	0.160	0.160	0.100	0.03	0.16	0.16	Empirical constant (Eq. 4-6)
s	--	1.7	1.0	1.7	1.7	0.8	0.	0.	Empirical constant (Eq. 4-10)
G	Mb	--	--	--	--	--	--	--	Shear modulus (Eq. 4-8)
G_{max}	Mb	0.3	0.1	0.315	0.2	0.045	0.2	0.2	Intrinsic shear modulus of consolidated rock (Eq. 4-18)
G_0^t	Mb	0.	--	--	--	--	--	--	Initial shear modulus of porous rock at zero pressure (Eq. 4-18)
K	Mb	--	--	--	--	--	--	--	Bulk modulus (Eq. 4-8)
K_{max}	Mb	0.8	0.525	0.8	0.6	0.8	0.5	0.65	Intrinsic bulk modulus at room temperature (Eq. 4-10)
K_m	Mb	--	--	--	--	--	--	--	Intrinsic bulk modulus (function of temperature) (Eq. 4-9)
K_0	Mb	0.225	0.075	0.6	0.25	0.04	0.15	0.65	Initial bulk modulus of porous rock at zero pressure (Eq. 4-9)
K_0'	Mb	--	--	--	--	--	--	--	Unloading bulk modulus of porous rock at zero pressure (Eq. 4-12)
A_0	Mb	0.0001 [†]	0.0001	0.0001	0.0001	0.00005	0.0001	0.0001	Yield strength (cohesion) at zero pressure
α	--	0.3	0.3	0.5	0.45	0.75	0.5	0.5	Coefficient of P_1 , tangent of the angle of internal friction
A_2	Mb	0.017 [†]	0.00525	0.017	0.003	0.003	0.017	0.017	Maximum yield strength (von Mises limit)
P_a	Mb	0.050	0.050	0.050	--	0.15	1.0	1.0	Empirical constant (Eq. 4-13)

[†]Since a constant shear modulus is used in the most calculations G_0 and μ_g were evaluated only for NTS granite

Mathematical Models for Several Soils

TABLE 5-1. EQUATION-OF-STATE PARAMETERS AND VARIABLES (CONTINUED)

Quantity	Units	NTS Granite	Cedar City Tonalite	Laramie Korthosite	Banded Mountain Limestone	Coconino Sandstone	Basalt Porous	Basalt Dense	Description
P_{fl}	Mb	--	--	--	--	--	--	--	Contribution to P of the fluid (Eq. 4-14)
P_m	Mb	--	--	--	--	--	--	--	Maximum solid pressure attained (Eq. 4-12)
P_{sl}	Mb	--	--	--	--	--	--	--	Contribution to P of the solid (Eq. 4-14)
T	$^{\circ}K$	--	--	--	--	--	--	--	
T_m	$^{\circ}K$	--	--	--	--	--	--	--	
β	$(Mb\text{-cc/gm})^{-1}$	3.0	3.0	3.0	2.0	3.0	2.0	2.0	Volume coefficient of thermal expansion (Eq. 4-12)
r	--	--	--	--	--	--	--	--	Ratio of specific heats
η	--	--	--	--	--	--	--	--	Compression (ρ/ρ_0)
μ	--	--	--	--	--	--	--	--	Excess compression ($\eta-1$)
μ_m	--	--	--	--	--	--	--	--	Maximum excess compression (Eq. 4-12)
μ_p	--	0.005	0.05	0.	0.011	0.25	0.16	0.	Irreversible compaction in the material resulting from the closing of all void spaces (Eq. 4-13)
μ_{pp}	--	0.4	0.4	0.4	0.011	0.9	0.16	0.16	Maximum irreversible compaction resulting from phase change (Eq. 4-13)
μ_2	--	--	--	--	--	--	--	--	Irreversible compaction due to loading (Eq. 4-12)
μ^*	--	0.03	0.0275	0.03	0.04	1.5	0.05	--	Empirical constant (Eq. 4-9)
$\mu_G^{(1)}$	--	0.005	--	--	--	--	--	--	Empirical constant (Eq. 4-18)
ρ	gm/cc	--	--	--	--	--	--	--	Density
ρ_0	gm/cc	2.65	2.55	2.72	2.66	2.0	2.5	2.9	Initial density of material

(1) See G_0

MATHEMATICAL MODELS FOR SEVERAL SOILS

This section describes mathematical models for fluid and solid phases of Middle Gust alluvium and Suffield silty clay. The method of translating experimental data into the mathematical model is also indicated.

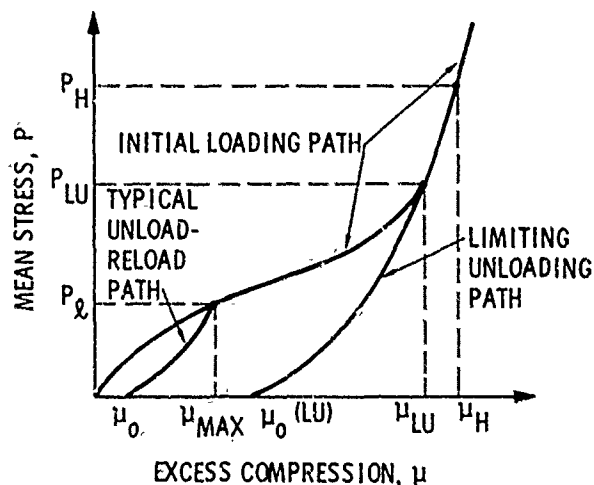
Middle Gust Sandy Clay

The mathematical model of Middle Gust alluvium described here is reported in Reference 5-30. The general mathematical model for the high-pressure energy-dependent hydrostat is given by Equation 4-7. The model for the low-pressure hydrostat is indicated by the curve in Figure 5-7. This curve is defined by

a table of experimental results stored by the computer. Interpolation between values is done by means of cubic splines to avoid the numerical difficulties of fitting high-order polynomials to the experimental data. The shear modulus is calculated from the instantaneous bulk modulus and the Poisson's ratio by means of Equation 4-20. The Poisson's ratio may be different in loading and unloading. A yield criterion which varies with mean normal stress is used, together with an associated plastic potential flow rule.

The density of Middle Gust sandy clay varies from 2.08 gm/cm³ to 2.16 gm/cm³ within a layer. An initial density of 2.10 gm/cm³ is assumed to represent the layer under consideration.

Specific Mathematical Models for Selected Earth Materials



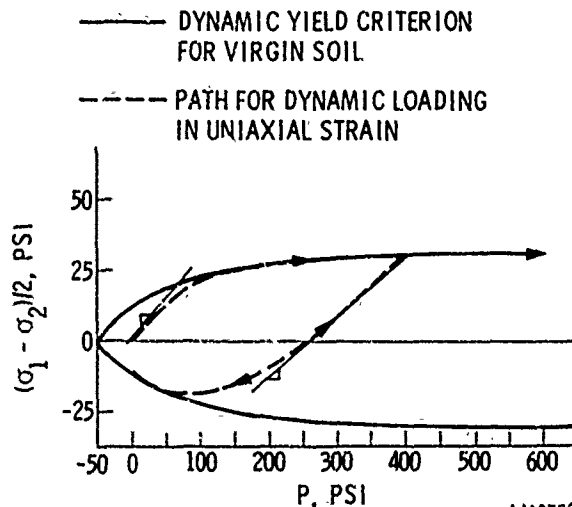
- μ_{MAX} = VALUE OF μ AT WHICH AN ARBITRARY UNLOADING PATH INTERSECTS THE VIRGIN LOADING PATH
- μ_{LU} = μ_{MAX} FOR THE LIMITING UNLOADING PATH; ALSO, VALUE OF ABOVE WHICH NO FURTHER PERMANENT COMPACTION IS ALLOWED
- μ_0 = PERMANENT SET FOR AN ARBITRARY UNLOADING PATH
- $\mu_0(LU)$ = μ_0 FOR THE LIMITING UNLOADING PATH
- μ_H = VALUE OF μ AT WHICH A CHANGE TAKES PLACE IN THE FORM OF THE ALGEBRAIC FUNCTION THAT DEFINES THE VIRGIN LOADING PATH

AJA3775

FIGURE 5-7. TYPICAL BEHAVIOR OF A COMPACTIBLE MATERIAL UNDER HYDROSTATIC LOADS

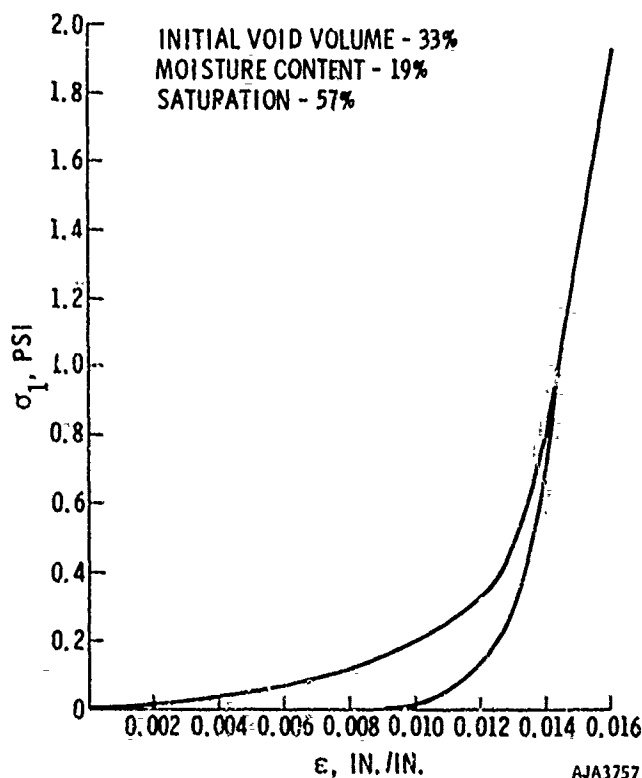
The solid phase hydrostat is defined by constructing a table of P/μ values from the data of Figures 5-8 and 5-9. The first step is to determine from Figure 5-9 the relation between axial stress and mean stress for loading and unloading/uniaxial stress paths. Using this information, the ordinate of Figure 5-8 can be converted from axial stress to mean stress, which enables Figure 5-8 to be regarded as a preliminary hydrostat for both loading and unloading/reloading.

The second step is to define Poisson's ratios for loading and unloading/reloading. This is done by examining in Figure 5-8 the slopes of the several loading and unloading/reloading paths in $(\sigma_1 - \sigma_3)/P$ plane for uniaxial strain. By idealizing a segment of a path as linear, an equivalent Poisson's ratio may



AJA3756

FIGURE 5-8. SHEAR STRESS VERSUS MEAN STRESS UNDER UNIAXIAL STRAIN FOR LAYER 3 OF EVENT MIDDLE GUST 1 (ALLUVIUM)



AJA3757

FIGURE 5-9. STRESS/STRAIN RELATIONS UNDER UNIAXIAL STRAIN FOR LAYER 3 OF EVENT MIDDLE GUST 1 (ALLUVIUM)

Mathematical Models for Several Soils

be found from the following expression for that segment:

$$\frac{\Delta(\sigma_1 - \sigma_3)}{\Delta P} = 3 \frac{1 - 2\nu}{1 + \nu} \quad (5-14)$$

It is usually assumed that ν is constant on loading and may be a different constant on unloading.

The third step is to define the yield criterion from triaxial compression data on maximum deviator stresses as a function of confining stress as shown in Figure 5-8. This completes the preliminary model.

The final step is to compute typical stress/strain paths and make adjustments to improve agreement with data. For example, the procedure described above for constructing the hydrostat omits the effect of plastic dilatation. If the final model includes this effect, some adjustment of the preliminary hydrostat is necessary. For the soil, in Figures 5-8 and 5-9, the adjustment for plastic dilatation is small because, in uniaxial strain, yielding occurs in a portion of the yield surface when according to the plastic potential flow rule plastic dilatation is slight.

Table 5-2 defines the virgin loading part of the solid phase hydrostat. If $\mu \geq \mu_m$ (where μ_m equals the previous maximum value of μ), the mean stress P is found by entering Table 5-2 with the current value of μ and interpolating between appropriate rows using cubic splines. Tables 5-3 and 5-4 define the unloading/reloading hydrostat.

If $\mu < \mu_m$, Table 5-3 defines μ_z (the value of μ at which the mean normal stress is zero) as a function of μ_m . Table 5-4 then defines the unloading/reloading hydrostat which connects the states (μ_z, P_m) and (μ_m, P_m) .

TABLE 5-2. LOADING HYDROSTAT FOR MIDDLE GUST ALLUVIUM, LAYER 2 (REFERENCE 5-30)

μ	P , psi
0.00000-2	0.000
0.57529-2	48.917
0.83634-2	106.404
1.04031-2	185.640
1.15724-2	252.080
1.24511-2	327.594
1.30378-2	423.697
1.36251-2	591.894
1.42132-2	815.877
1.45075-2	960.000

TABLE 5-3. PERMANENT EXCESS COMPRESSION AS A FUNCTION OF MAXIMUM EXCESS COMPRESSION FOR MIDDLE GUST ALLUVIUM, LAYER 2 (REFERENCE 5-30)

μ_m	μ_z
0.00000-3	0.00000-3
1.74909-3	1.12426-3
3.19165-3	2.06338-3
4.64240-3	2.89455-3
6.09315-3	3.61871-3
7.25375-3	4.20057-3
8.70450-3	5.00024-3
9.96510-3	5.63060-3
10.73555-3	6.11605-3
11.89615-3	6.88892-3
13.34690-3	7.67814-3
14.50750-3	8.00000-3

TABLE 5-4. UNLOADING HYDROSTAT FOR MIDDLE GUST ALLUVIUM, LAYER 2 (REFERENCE 5-30)

μ , (10^{-2})	P , psi
0.80000	0.000
1.02704	48.1
1.14749	100.9
1.21100	150.
1.26000	200.
1.29000	250.
1.31000	300.
1.34000	400.
1.36600	500.
1.38600	600.
1.41400	750.
1.45075	960.

Specific Mathematical Models for Selected Earth Materials

For pressure above the limit of the data, an expression explained by Equations 4-9 through 4-14 replaces the tables.

$$P = P_{fl} + K_m(\mu_m - \mu_z) - (K_m - K_o) \mu^* \left(1 - \exp - \frac{(\mu_m - \mu_z)}{\mu} \right) \quad (5-15)$$

Table 5-5 lists specific parameters for Middle Gust sandy clay.

The yield criterion is defined by Table 5-6. The allowable value of $\sqrt{J_2}$ is found by entering the table with the current value of P and interpolating between appropriate rows by using cubic splines.

The Poisson's ratios found from Figure 5-8 are

$$\nu_{load} = 0.35$$

$$\nu_{unload-reload} = 0.4$$

An alternative model used for the Middle Gust site is a capped model as described above for tonalite and in Section 4 (Reference 5-32). The site is considered to have layers, each of which is represented by a separate set of material constants.

The yield criteria are represented by the following expression:

$$\sqrt{J_2} = A_0 + A_1 e^{-\alpha J_1} \quad (5-16)$$

where A_0 , A_1 , and α are material constants, J_1 is the first invariant of the stress tensor (compression positive), and J_2 is the second invariant of the deviatoric stress. The equation of the cap is

$$(L - J_1)^2 + q^2 J_2 - (L - \chi)^2 = 0 \quad (5-17)$$

in which the functions L and χ are related to a plastic strain parameter κ

$$W(e^{D\chi} - 1) = \kappa \quad (5-18)$$

$$L - q(A_0 - A_1 e^{\alpha L}) = \chi \quad (5-19)$$

The geometrical meanings of L , χ , and q are shown in Figure 4-11, and q , W , and D are material constants. κ is assumed to be equal to the plastic volumetric compaction. The elastic portion of the model is represented by a constant shear modulus G and a bulk modulus K given by

$$K = K_m (1 - K_1 e^{-K_2 J_1}) \quad (5-20)$$

in which K_m , K_1 , and K_2 are constants. Specific values of constants for each layer are given in Table 5-7. In Figures 5-10 and 5-11 the model for Layer 5 is compared with experimental data for the case of uniaxial strain.

TABLE 5-5. HYDROSTAT FOR MIDDLE GUST ALLUVIUM AT PRESSURES ABOVE LABORATORY DATA (REFERENCE 5-30) 5-30)

$K_m = 1.0 \times 10^7$ psi
$K_o = 5.83 \times 10^5$ psi
$\mu^* = 0.25$
$P_L = 960$ psi

TABLE 5-6. YIELD STRENGTH OF MIDDLE GUST ALLUVIUM, LAYER 3

P, psi	$\sqrt{J_2}$, psi
0.00	25.0
-10.0	20.0
25.0	32.0
50.0	37.0
75.0	41.0
100.	44.5
150.	50.0
200.	54.0
250.	57.0
300.	59.0
400.	60.0
500.	60.0

Mathematical Models for Several Soils

TABLE 5-7. MATERIAL PARAMETERS FOR CAPPED MODEL OF MIDDLE GUST SITE

Layer	A_0 , ksi	α , ksi^{-1}	A_1 , ksi	D , ksi^{-1}	W	Layer	q	K_m , ksi	K_1	K_2 , ksi	G , ksi
1 (0-2 ft)	0.0346	6.5	0.0266	3.2	0.0555	1 (0-2 ft)	3.0	400.0	0.9	0.5	12
2 (2-4 ft)	0.052	6.3	0.0375	2.1	0.022	2 (2-4 ft)	3.0	500.0	0.9	0.5	15
3 (4-9 ft)	0.0231	10.0	0.0168	3.0	0.0089	3 (4-9 ft)	3.0	530.0	0.86	1.0	15
4 (9-15 ft)	0.0866	7.0	0.0289	3.3	0.0075	4 (9-15 ft)	3.0	400.0	0.80	1.0	30
5 (15-23 ft)	0.289	3.6	0.196	1.7	0.0054	5 (15-23 ft)	3.5	500.0	0.62	0.5	60
6 (23-45 ft)	0.577	2.0	0.45	0.62	0.0024	6 (23-45 ft)	3.0	700.0	0.64	0.3	150
7 (45-125 ft)	1.44	0.833	1.27	0.65	0.00081	7 (45-125 ft)	4.0	700.0	0.50	0.3	250

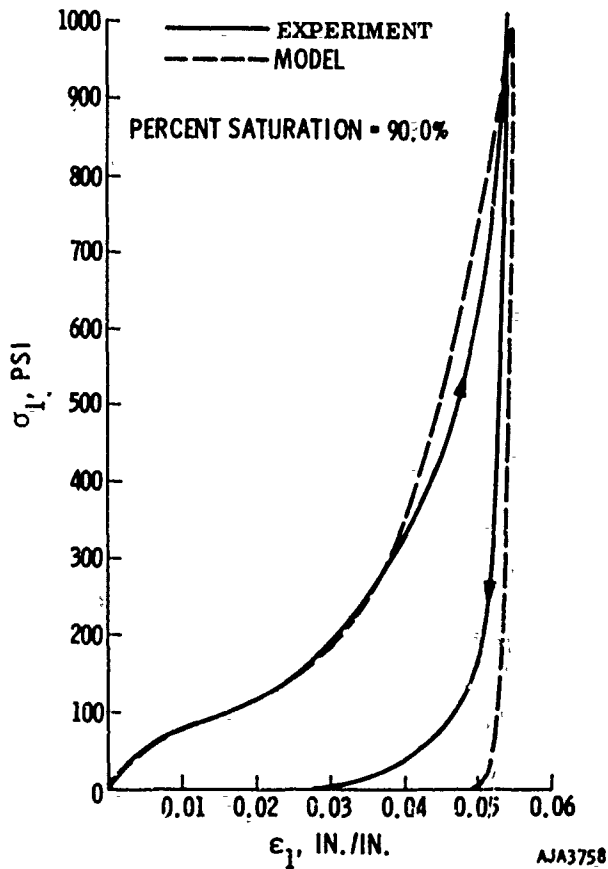


FIGURE 5-10. EVENT 1A, OPERATION DISTANT PLAIN, LAYER III, WET SAND, SILT, SUBJECTED TO UNIAXIAL STRAIN (REFERENCE 5-31)

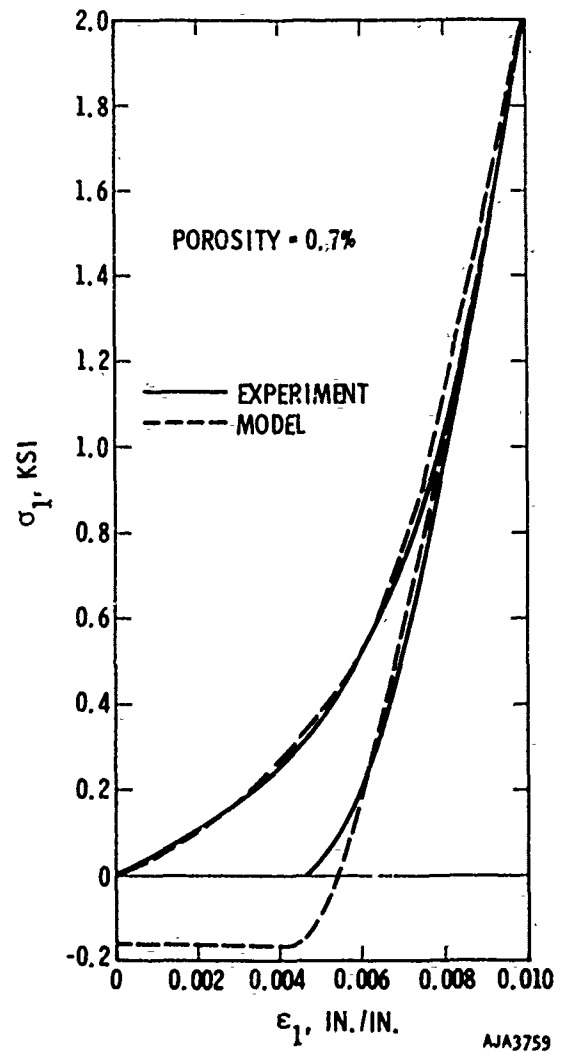


FIGURE 5-11. CAPPED MODEL FOR LAYER 5 OF MIDDLE GUST SITE SUBJECTED TO UNIAXIAL STRAIN (REFERENCE 5-32)

Specific Mathematical Models for Selected Earth Materials

Distant Plain Alluvium

The mathematical model for the alluvium at the site of Event 1A Operation Distant Plain is reported in Reference 5-31. The ground shock from this event was induced by air blast only so that it was unnecessary to develop fluid or energy-dependent equations of state. The main features of the model include a variable bulk modulus of the form suggested in Equation 4-16 and Figure 4-3. Hysteresis in bulk is provided by different moduli for loading and unloading/reloading. The shear modulus is assumed to be a constant on loading and a different constant on unloading/reloading. The yield criterion prescribes maximum allowable shear strength as a function of confining pressure. A nonassociated flow rule is used, such that plastic dilatation is zero.

For computational purposes, four materials are defined in horizontal layers as shown in Table 5-8. Data were obtained mainly from stress/strain relations under uniaxial strain and maximum combined stress under triaxial compressive stress for each layer.

TABLE 5-8. SOIL LAYERS AT SITE OF EVENT 1A, OPERATION DISTANT PLAIN

Layer	Depth, ft	Type of Soil
1	0 to 4	Dry clay
2	4 to 20	Dry sandy silt
3	20 to 34	Wet sandy silt
4	34 to 74	Saturated clay

The bulk modulus for virgin loading, where $P \leq P_m$ (compression negative) is prescribed by the following equation:

$$K = K_0 - K_1(J_1 + K_3) + K_2(J_1 + K_3)^2 \quad (5-21)$$

where K_0 , K_1 , K_2 , and K_3 are material constants for each layer. As shown in Figure 4-3, the loading bulk modulus decreases with (algebraically) decreasing J_1 until a minimum is reached at

$$J_1 = -K_3/2$$

and then increases again, reaching

$$K = K_0$$

at

$$J_1 = -K_3$$

The bulk modulus for unloading/reloading, defined by

$$P > P_m \text{ (compression negative)}$$

is a constant

$$K = K_{un} = \text{constant}$$

The shear modulus for virgin loading is assumed to be a constant:

$$G = G_0 = \text{constant}$$

The shear modulus for unloading/reloading is a constant

$$G = G_{un} = \text{constant}$$

The yield criterion is as follows

$$f = \sqrt{J_2} - \left[A_0 - \alpha J_1 \left(1 + \frac{J_1}{2A_1} \right) \right] \leq 0 \quad (5-22)$$

where A_0 , A_1 , and α are material constants for each layer.

The material constants for each layer are given in Table 5-9. The experimental stress/strain curves in uniaxial strain are compared with the model for Layer 2 in Figure 5-12.

TABLE 5-9. MATERIAL CONSTANTS--DISTANT PLAIN 1A MODEL

Layer	I	II	III	IV
α	0.148	0.18	0.16	0.0
A_0 (psi)	10.0	3.0	1.5	12.7
A_1 (ksi)	3.45	3.44	1.42	(Not Applicable)
ρ_0 (gm/cm ³)	1.402	1.49	1.829	1.875
K_1	7.5	9.8	49.0	400.0
K_2 (/ksi)	-0.55	0.6	-15.0	-280.0
K_3 (ksi)	0.7762	0.3440	0.4118	0.810
G_0 (ksi)	2.0	4.2	3.3	33.33
K_{un} (ksi)	166.7	266.7	244.0	270.0
G_{un} (ksi)	25.0	100.0	90.0	36.0

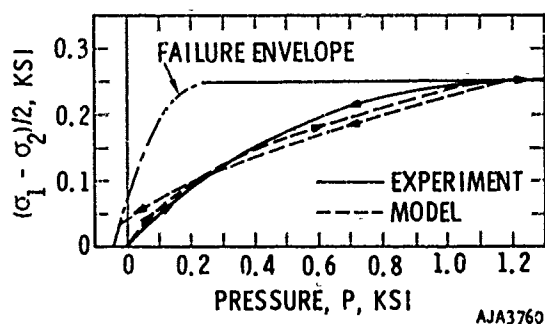


FIGURE 5-12. CAPPED MODEL FOR LAYER 5 OF MIDDLE GUST SITE SUBJECTED TO UNIAxIAL STRAIN (REFERENCE 5-32)

REFERENCES

- 5-1. Schuster, S. H., and J. Isenberg, Free Field Ground Motions for Beneficial Facility Siting, Volume 2--Equations of State for Geologic Media, SAMSO-TR-70-88, ATI-AJA, June 30, 1970.
- 5-2. Handbook of Chemistry and Physics, Chemical Rubber Publishing Company, 36th Ed., 1955, pp. 2061-2103.
- 5-3. Stephens, D. R., and E. M. Lilley, Static PV Curves of Cracked and Consolidated Earth Materials to 40 Kilobars, UCRL-14711, Lawrence Radiation Laboratory, March 1966.
- 5-4. Private Communication from D. R. Stephens (Lawrence Radiation Laboratory), 1968.
- 5-5. LaMori, P. N., Compressibility of Three Rocks, (A) Westerly Granite and Solenhofen Limestone to 40 Kilobars at 300°C, (B) Cedar City Tonalite to 40 Kilobars at Room Temperature, DASA-2151, Defense Atomic Support Agency, August 1968.
- 5-6. Birch, F., "Velocity of Compressional Waves in Rocks to 70 Kilobars, Part 1," J. Geophys. Res., Vol. 6b, No. 4, 1960, p. 1083.
- 5-7. Army Engineer District, Omaha, Tests for Strength Characteristics of Rock, Pile Driver Project, MRDL 64/70 U. S. Army Corps of Engineers, Missouri River Division Laboratory, 1964.
- 5-8. Brace, W. F., "Some New Measurements of Linear Compressibility in Rocks," J. Geophys. Res., Vol. 70, No. 2, 1965, p. 391.
- 5-9. Jones, A. H., and N. H. Froula, Uniaxial Strain Behavior of Four Geological Materials to 50 Kilobars, DASA-2209, March 1969.
- 5-10. Grine, D. R., Equations of State of Granite and Salt, UCRL-13004, Lawrence Radiation Laboratory, May 1961.
- 5-11. Ainsworth, D. L., and B. R. Sullivan, Shock Response of Rock at Pressures Below 30 Kilobars, WES TR-6-802, U. S. Army Engineer Waterways Experiment Station, November 1967.
- 5-12. Walsh, J. B., "The Effect of Cracks on the Compressibility of Rock," J. Geophys. Res., Vol. 70, No. 2, January 15, 1965.
- 5-13. Ahrens, T. J., et al., Dynamic Properties of Rocks, DASA-1868, Stanford Research Institute, September 1966.
- 5-14. Butkovitch, T. R., The Gas Equation of State for Natural Materials, UCRL-14729, Lawrence Radiation Laboratory, January 1967.
- 5-15. Tillotson, J., Metallic Equations of State for Hypervelocity Impact, GA-3216, General Atomic Division, General Dynamics Corporation, July 1962.
- 5-16. Allen, R. T., Equation of State of Rocks and Minerals, GAMD-7834, General Atomic Division, General Dynamics Corporation, 1967.
- 5-17. Bass, R. C., et al., Hugoniot Data for Some Geological Materials, SC-4903(RR), Sandia Corporation, June 1963.
- 5-18. Shipman, F. H., et al., High Pressure Hugoniot Measurements for Several Nevada Test Site Rocks, DASA-2214, March 1969.
- 5-19. Lombard, D. B., The Hugoniot Equation of State of Rocks, UCRL-6311, Lawrence Radiation Laboratory, February 1961.
- 5-20. Bass, R. C., Additional Hugoniot Data for Geological Materials, SC-RR-66-548, Sandia Corporation, October 1966.
- 5-21. McQueen, H. G., et al., "Hugoniot Equation of State of Twelve Rocks," J. Geophys. Res., Vol. 72, No. 20, 1967, p. 4999.
- 5-22. Simmons, G., "Velocity of Shear Waves in Rocks to 10 Kilobars, Part 1," J. Geophys. Res., Vol. 69, No. 6, 1964, p. 1123.
- 5-23. Stephens, D. R., Elastic Constants of Granodiorite, UCID-15369, Lawrence Radiation Laboratory (to be published).
- 5-24. Byerlee, J. D., "Frictional Characteristics of Granite Under High Confining Pressure," J. Geophys. Res., Vol. 72, No. 14, 1967, p. 3639.

Specific Mathematical Models for Selected Earth Materials

- 5-25. Private Communication from H. Heard (Lawrence Radiation Laboratory) via D. R. Stephens (Lawrence Radiation Laboratory), 1968.
- 5-26. Sandler, I., and F. L. Dimaggio, Material Model for Rocks, DASA-2595, Paul Weidlinger Consulting Engineer, October 1970.
- 5-27. Brace, W. F., et al., "Dilatancy in the Fracture of Crystalline Rocks," J. Geophys. Res., Vol. 71, No. 16, August 15, 1966.
- 5-28. Giardini, A. A., et al., "Triaxial Compression Data on Nuclear Explosion Shocked, Mechanically Shocked and Normal Granodiorite from the Nevada Test Site," J. Geophys. Res., Vol. 73, No. 4, February 15, 1968, p. 305.
- 5-29. Mogi, K., "Effect of the Intermediate Principal Stress on Rock Failure," J. Geophys. Res., Vol. 72, No. 20, October 1967, p. 5117.
- 5-30. Schuster, S. H., Private Communication, 1972
- 5-31. McCormick, J. M., et al., Studies on the Distant Plain 1A Event, DASA 2213, Paul Weidlinger, Consulting Engineer, July 1968.
- 5-32. Sandler, I. S., Private Communication, 1972

SECTION 6

CONCLUSION

There is some evidence that present capability can predict ground shock parameters in a field test within a factor of 2 to 3 of field measurements. This factor depends somewhat on the quantities being considered. Pressure and particle velocity close to the source might be predicted more accurately while permanent displacements might be less accurate. Further, there are uncertainties in the field measurements which may magnify or shrink the apparent differences between calculations and measurements. After weighing these considerations against the expenditures required to make further progress, it still appears that there is advantage in refining the measurement and mathematical representation of material properties.

Although opinions vary on the relative importance of each of the following areas, it is agreed that they are profitable for further work:

- a. In partially and fully saturated soils and rocks, it would be an improvement to compute the effective stress separately from the total stress. In this way, information on properties expressed as a function of effective stress could be used. Then, all laboratory data could be expressed in terms of effective stress, and ambiguity arising from varying degrees of saturation could be avoided.
- b. A method of accounting for inhomogeneity in properties would enable dispersion in waves to be more accurately computed. Inhomogeneity arises not only from such obvious sources as cracks, grains of different sizes and properties and irregular layering, but also from the in situ state of stress which varies with depth of overburden and with tectonic stresses.
- c. A method of distinguishing between brittle and ductile modes of fracture might help efforts to calculate block motion effects, which are a form of large-scale brittle fracture. The present practice of representing all types of fractures by a form of theory appropriate to homogeneous flow has its critics, who have proposed various alternative schemes. However, there has been no systematic attack on this problem by both experimental and theoretical groups.

To these areas, a fourth may be added which is less specific and less easily defined. In some problems there is a special need for physical understanding of material behavior to be included in the mathematical representation. One example is ground shock computations for the antiballistic missile system, which involves propagation of low level stresses for great distances. In this instance, minor variations or uncertainties in properties can accumulate to become large discrepancies at the target point. Rethinking the assumptions on which materials parameters are measured and represented mathematically does not guarantee success, of course, but it helps to give proper perspective. Details of stress/strain behavior which are rightfully ignored at several kilobars may dominate behavior at several bars.

In addition to these major areas for future work, several lesser areas should also be explored. Among these is the need for computational studies to guide experimental programs. One such study is to distill the most important stress paths from the output of ground shock calculations. This information could be used to guide experimental programs to measure properties along the most important stress paths.

INDEX

- Adhesion, p. 13
- Anisotropy in rock masses, p. 29
- Anorthosite, p. 124, Table 5-1
- Atterburg limits, p. 62
- Basalt, p. 124, Table 5-1
- Bore hole direct shear test, p. 94, Fig. 3-58
- Biaxial compression testing in rock, p. 35
- Brittleness of rock, p. 24
- Boston blue clay, Fig. 3-32
- Brittle-ductile transition, p. 24
- Bulk Modulus, p. 4
 - partially saturated clay, Fig. 3-42
 - rock, Figs. 2-1 through 2-8
 - sand, Figs. 3-13 through 3-15
 - variable modulus model, p. 104
- Cap model, p. 113
- Carbonate rock, Fig. 2-5
- Clastic, rock pp. 10, 13
- Clay
 - Weald, Chicago, London, Fig. 3-35
 - Watching Hills, Figs. 3-36, 3-37, 3-38, 3-42, 3-43
 - Hope, N. Dakota, Fig. 3-41
 - Jordan Buff, Fig. 3-45
- Crystalline, p. 10
- Coefficient of earth pressure, p. 80
- Coefficient of friction,
 - in rock, p. 32
 - in soil, p. 67
- Conservation of mass momentum, energy, p. 7
(Rankin-Hugoniot Equations)
- Consolidation of clay, Fig. 3-5
- Dilatation wave, p. 6
 - in soil, pp. 75, 86
 - in rock, pp. 32, 39
- Dilatancy
 - in rocks, p. 16ff, Figs. 2-1 through 2-8
 - in sand, p. 59
- Diorite, Table 2-5
- Direct shear test,
 - in rock, p. 37
 - in soil, p. 94
- Dispersed Clay, p. 62
- Dolomite
 - Dunham, Figs. 2-10, 2-14, 2-17
- Ductility
 - of rocks, Fig. 2-14, p. 22
- Effective stress
 - in rocks, Figs. 2-19, 2-27
 - in soil, p. 63
- Equation of state
 - general fluid, p. 102
 - Mie-Gruneisen, p. 102
 - Tillotson, p. 104
 - general solid, p. 104
- Excess compression, p. 101
- Faulting, p. 30
- Flocculated clay, p. 62
- Flow rule, p. 112
- Grain ductility, pp. 13, 14
- Grain strength, pp. 13, 14
- Granite, pp. 19, 121
 - Nevada Test Site, p. 121, Fig. 2-40
 - Westerly, Figs. 2-8, 2-9, 2-16, 2-18
 - Cedar City, Fig. 2-4, p. 124
- Hugoniot Curve
 - general, p. 7
 - in rock, Fig. 2-40
- Hypoelastic material, p. 104
- Igneous rock, p. 10
- Internal energy, p. 7
- In situ properties
 - of rock masses, pp. 43, 50
- Intermediate principal stress, Fig. 2-16
- Invariant, pp. 1 through 4
- Light gas gun, p. 39
- Limestone
 - banded mountain, Table 5-1
 - solenhofen, Figs. 2-5, 2-39
- McCormick Ranch Sandy Clay, pp. 74, 80
- Marble, Figs. 2-6, 2-30
- Metamorphic rock, p. 12
- Middle gust alluvium, p. 128
- Modulus, (bulk, shear, Young's, constrained), p. 4
- Penetration test, p. 93
- Permeability
 - in rocks, p. 13
 - in soil, p. 63
- Pore pressure
 - effect on rocks, p. 21ff
 - effect on soil, p. 63ff
- Plasticity theory, p. 109
 - adapted to finite element methods, p. 113
 - adapted to finite difference methods, p. 114
- Plate jacking test
 - in rock, p. 48
 - in soil, p. 93
- Plasticity index, p. 62
- Porosity
 - in rocks, p. 13
 - measured by conductivity, p. 46
- Pressure meter test, Fig. 3-5
- Pressure chamber test, p. 49
- Quartzite, Figs. 2-13, 2-14
- Radial jacking test, p. 49

- Rate of loading effects
 - fine-grained soil, p. 85
 - coarse-grained soil, p. 74
 - rocks, Figs. 2-13, 2-21
- Rayleigh line, p. 7
- Rayleigh Wave
 - in soil, p. 95
- Relative density, p. 59
- Release adiabats, p. 8
- Riemann integral, p. 7
- Rock quality designation, p. 45
- Sand
 - Sacramento River, Fig. 3-3
 - Hope, No. Dakota, Fig. 3-14
 - Ottawa, Figs. 3-15, 3-27
 - Minnesota, Fig. 3-23
- Sandstone, Fig. 2-22
 - Coconino, Fig. 2-3, Table 5-1
 - Nugget, Figs. 2-2, 2-35
 - Berea, Figs. 2-11, 2-19
- Sandy clay/sandy silt
 - McCormick Ranch, Figs. 3-16, 3-24
- Sedimentary rock, p. 11
- Secant modulus
 - in clay, Fig. 3-33
- Seismic survey, p. 45
- Shear modulus, p. 4
 - partially-saturated clay, p. 81
 - saturated clay, p. 79
 - rock, Figs. 2-1, 2-2, 2-4 through 2-7
 - sand, Fig. 3-19
- Shale
 - Green River, Figs. 2-1, 2-31, 2-32
- Shear wave, p. 6
 - in soil, p. 94
 - in rock, Figs. 2-27, 2-29
- Soil
 - coarse grained, p. 59
 - fine grained, p. 60
- Split Hopkinson bar, Fig. 2-46
- Strain, p. 3
 - volumetric, p. 3
 - deviatoric, p. 4
- Stick-slip, p. 25
- Strength
 - effect of temperature, strain rate, pore pressure on (rock), p. 21ff
 - of joints, p. 30ff
- Stress, p. 1ff
- Triaxial compression testing
 - in rock, p. 35
 - in soil, p. 89ff
- Temperature
 - effect on rocks, p. 21
- Texture, rock, p. 13
- Tuff
 - Nevada test site, Fig. 2-41
- Uniaxial strain
 - in soil (experimental) p. 89ff
- Uniaxial compression test
 - large scale, in rock, p. 50
- Uniaxial jacking test, p. 49
- Variable moduli model, p. 104
- Vane shear test, p. 94
- Void ratio
 - critical, p. 60
- Watching Hill clay, p. 81
- Wave velocity
 - in rocks, Figs. 2-38, 2-39, 2-55
 - coarse grained soils, Fig. 3-27
 - fine grained soils, p. 86ff
- Yield strength
 - of rocks, p. 22